In situ FTIR Measurements of the Kinetics of the Aqueous CO_2-Monoethanolamine Reaction

by

Neo Motang

Thesis presented in partial fulfillment
of the requirements for the Degree

of

MASTER OF ENGINEERING
(CHEMICAL ENGINEERING)

in the Faculty of Engineering
at Stellenbosch University

Supervisor
Dr. L.H. Callanan

Co-Supervisor
Prof. A.J. Burger

March 2015

Declaration

By submitting this thesis electronically, I declare that the entirety of the work contained therein is my own, original work, that I am the sole author thereof (save to the extent explicitly otherwise stated), that reproduction and publication thereof by Stellenbosch University will not infringe any third party rights and that I have not previously in its entirety or in part submitted it for obtaining any qualification.

Date: 23 February 2015

Abstract

The reaction between carbon dioxide (CO_2) and monoethanolamine (MEA) is used in industry to capture CO_2 from flue gas streams. When the reaction is conducted in water, a large amount of energy is required to regenerate free MEA. The regeneration energy required can be reduced through more efficient design of CO_2 absorption processes. Among others, accurate reaction rate equations would be needed for the design. These rate equations can be obtained by conducting reaction kinetics experiments. Previous research shows that published rate equations are inconsistent, and that the proposed reaction mechanisms are contradictory. In order to improve the accuracy of both the rate equations and the reaction mechanisms, individual reactive species may be monitored during the reaction.

In this work, the aqueous CO_2-monoethanolamine (MEA) reaction was investigated over the temperature range 20-30°C in a semi-batch reactor. Equilibrium and kinetic experiments were conducted. In the equilibrium experiments, CO_2 was added incrementally to 0.33 mol/L MEA solutions up to a CO_2 loading of 0.6 mol CO_2/mol MEA. In the kinetic experiments, MEA solutions were pumped into 0.02 mol/L CO_2 solutions. Two settings for the MEA concentrations were used, and the MEA concentration in the reactor was either 0.26 or 0.52 mol/L at the end of the reaction. The reaction was monitored using *in situ* Fourier Transform Infrared (FTIR) spectroscopy, giving novel insight into the aqueous reaction CO_2-MEA at low MEA concentrations.

In the equilibrium experiments, the absorbances of chemical species in the reaction mixture were measured at CO_2 loadings between 0.0 and 0.6 mol CO_2/mol MEA. The measured absorbances were converted to concentrations using carbamate calibration calculations based on 100% conversion of CO_2 to carbamate product ($CH_2CH_2OHNH_2COO$) at CO_2 loadings less than 0.3 mol CO_2/mol MEA. MEA and CO_2 reacted in a 2:1 ratio at loadings less than 0.3 mol CO_2/mol MEA, with carbamate and protonated MEA products forming. HCO_3^- formation became significant from 0.3 mol CO_2/mol MEA. Carbamate concentration reached a maximum at 0.4 mol CO_2/mol MEA and thereafter decreased, whereas HCO_3^- concentration continued increasing.

These observations confirm a two-part mechanism for the aqueous CO_2-MEA reaction: carbamate formation at CO_2 loadings less than 0.4 mol CO_2/mol MEA, and HCO_3^- formation accompanied by carbamate consumption beyond 0.4 mol CO_2/mol MEA. The HCO_3^- formation becomes significant from around 0.3 mol CO_2/mol MEA. As these trends in species concentrations vs. CO_2 loading are similar to species concentration trends in 5 mol/L MEA solutions as seen from literature, the reaction mechanism is likely to be valid in both low and high MEA concentration solutions.

In the kinetic experiments, only CO_2 and MEA absorbances were measured. Products species absorbances could not be measured due to measurement limitations. The reagent species-time profiles confirmed that the aqueous CO_2- MEA reaction is rapid, with the CO_2 reaching

essentially 100% conversion within 10 s of reaction initiation. The stoichiometric ratio of reacting MEA to CO_2 achieved was essentially 2.

The reagent species-time data collected were modelled using published reaction models, considering only the forward rate expression. The proposed carbamate-HCO_3^- mechanism could not be evaluated since it depended on knowledge of the carbamate and HCO_3^- product concentrations. Optimized rate constants obtained from the second order and termolecular model fits were in general agreement with literature values within the rate constant confidence interval specified, thus verifying the use of a semi-batch experimental setup for investigating the aqueous CO_2-MEA reaction. The second order, third order and termolecular models represented the CO_2 and MEA data equally well.

Opsomming

Die reaksie tussen koolstofdioksied (CO_2) en mono-etanolamien (MEA) word in die industrie gebruik om die CO_2 uit uitlaatgas strome te vang. As die reaksie in water plaasvind, word ‘n groot hoeveelheid energie verbruik om vry MEA te regenereer. Die nodige regenerasie energie kan deur meer effektiewe ontwerp van die CO_2 absorpsieproses, verminder word. Akkurate reaksietempo vergelykings is deel van die stel inligting wat nodig is vir die ontwerp. Dié vergelykings word uit resultate van reaksiekinetika eksperimente bepaal. ’n Literatuurstudie het bevestig dat gepubliseerde reaksietempo vergelykings uit vorige navorsing van mekaar verskil en dat die voorgestelde reaksiemeganismes teenstrydig is. Om die akkuraatheid van beide die reaksietempo vergelykings en reaksiemeganismes te verbeter, kan individuele reaktiewe spesies tydens die reaksie opgespoor word.

In hierdie studie is die waterige CO_2-MEA reaksie oor die temperatuurgebied 20-30°C in ‘n semi-enkelladingsreaktor ondersoek. Ewewig en kinetiese eksperimente is uitgevoer. Tydens die ewewigseksperimente, is die CO_2 in klein hoeveelhede by 0.33 mol/L MEA oplossings bygevoeg tot en met CO_2 ladings van 0.6 mol CO_2/mol MEA. Tydens die kinetiese eksperimente is MEA oplossings in 0.02 mol/L CO_2 oplossings ingespuit. Twee stellings vir die MEA konsentrasies is gebruik en die MEA konsentrasie in die reaktor was óf 0.26 of 0.52 mol/L teen die einde van die reaksie. Die reaksie is gemonitor deur gebruik te maak van *in situ* Fourier Transform Infrarooi (FTIR) spektroskopie, wat nuwe insig verskaf het in terme van die waterige CO_2-MEA reaksie by lae MEA konsentrasies.

In die ewewigseksperimente is die absorbansies van chemiese spesies in die reaksiemengsel gemeet by CO_2 ladings tussen 0.0 en 0.6 mol CO_2/mol MEA. Die absorbansies wat gemeet is, is omgeskakel na konsenstrasies deur gebruik te maak van karbamaat kalibrasie berekeninge. Die berekeninge is gebaseer op 100% omskakeling van CO_2 na karbamaat produk ($CH_2CH_2OHNH_2COO$) by CO_2 ladings minder as 0.3 mol CO_2/mol MEA. MEA en CO_2 het gereageer in ‘n 2:1 verhouding by ladings minder as 0.3 mol CO_2/mol MEA met karbamaat en geprotoneerde MEA as die produkte wat gevorm word. HCO_3^- formasie het beduidend geword vanaf 0.3 mol CO_2/mol MEA. Die karbamaat konsentrasie het ‘n maksimum by 0.4 mol CO_2/mol MEA bereik en daarna het dit afgeneem, terwyl die HCO_3^- konsentrasie aangehou het om te vermeerder.

Hierdie waarnemings bevestig ‘n tweedelige meganisme vir die waterige CO_2-MEA reaksie: karbamaat formasie by CO_2 ladings minder as 0.4 mol CO_2/mol MEA, en HCO_3^- formasie wat gepaard gaan met karbamaat inname na 0.4 mol CO_2/mol MEA. Die HCO_3^- formasie raak beduidend vanaf 0.3 mol CO_2/mol MEA. Omdat hierdie tendense in spesies konsentrasies vs. CO_2 ladings soortgelyk is aan die spesies konsentrasie tendense in 5 mol/L MEA oplossings soos gesien in die literatuur, is die reaksie meganisme waarskynlik geldig in beide lae en hoë MEA konsentrasie oplossings.

Slegs CO_2 en MEA absorbansies is gemeet tydens die kinetiese eksperimente. Die absorbansie van die produk spesies kon nie gemeet word nie as gevolg van beperkings tydens meting. Die reagense spesies-tyd profiele bevestig dat die waterige CO_2-MEA reaksie vinnig is, aangesien die CO_2 omtrent 100% omskakeling bereik binne die eerste 10 s vanaf die aanvang van die reaksie. Die stoigiometriese verhouding tussen reagerende MEA en CO_2 is omtrent 2.

Die reagense spesie- en tyd-data wat versamel is, is gemodelleer deur gebruik te maak van gepubliseerde reaksie modelle waar slegs die voorwaartse reaksietempo se uitdrukkings in ag geneem is. Die voorgestelde karbamaat-HCO_3^- meganisme kon nie geëvalueer word nie aangesien dit afhanklik was van die kennis van karbamaat en HCO_3^- produk konsentrasies. Geoptimaliseerde reaksiekonstantes, soos verkry van die tweede orde en driemolekulêre modelvooruitskattings, was in algemene ooreenkoms met literatuur waardes binne die gespesifiseerde vertrouensinterval. Dít verifieer die gebruik van ‘n semi-enkelladingsreaktor om die waterige CO_2-MEA reaksie na te vors. Die tweede orde, derde orde en driemolekulêre modelle het die CO_2 en MEA data ewe goed voorgestel.

Acknowledgements

This work is based on the research supported in part by the National Research Foundation of South Africa (Grant specific unique reference number (UID) 83966) and Sasol Technology (Pty) Ltd. The authors acknowledge that opinions, findings and conclusions or recommendations expressed in any publication generated by the NRF supported research are that of the authors, and that the NRF sponsors accepts no liability whatsoever in this regard.

This project also would not have been possible without the help of the following people. Your input was highly appreciated.

- My supervisory team: Dr. L.H. Callanan, Prof. A.J. Burger and Dr. L.J. du Preez
- The staff at the Process Engineering Department: Mrs. F. Layman, Mrs. J. Steyl, Mrs. L. Bresler, Mrs. H. Botha, Dr. J.P. Barnard, Dr. L. Auret, Mr. A. Petersen, Mr. L. Mzayifani, Mr. J. Weerdenburg, Mr. J. Barnard and Mr. A. Cordier
- Fellow postgrad students at the Process Engineering Department
- My family, for your patience and understanding
- My friends, who were always there when I needed a shoulder to cry on, or someone to celebrate milestones with
- Jesus – none of this could have happened without You.

Table of Contents

List of figures

List of tables

Abbreviations, nomenclature and glossary

Abbreviations

ATR ..... Attenuated Total Reflectance
B ..... Base
BH^+ ..... Protonated base
$Carb^-$ or Carb ..... Carbamate salt
CCS ..... Carbon Capture and Sequestration
CO_3^{2-} or CO_3 ..... Carbonate ion
DEA ..... Diethanolamine
FTIR ..... Fourier Transform Infrared
Ge ..... Germanium
H^+ ..... Hydronium ion
HCO_3^- or HCO_3 ..... Bicarbonate ion
IR ..... Infrared
MEA ..... Monoethanolamine
$MEACOO^-$ ..... Carbamate salt from MEA
MEACOOH ..... Zwitterion from MEA
$MEAH^+$ or MEAH ..... Protonated MEA
MSE ..... Mean sum of squared errors
NaOH ..... Sodium hydroxide
NMR ..... Nuclear magnetic resonance
ODE ..... Ordinary differential equation
OH^- ..... Hydroxide ion
PSSH ..... Pseudo steady state hypothesis
R ..... Organic functional group
R_1R_2HN ..... Primary or secondary alkanolamine
R_1R_2HNCOO ..... Zwitterion from R_1R_2HN
$R_1R_2NCOO^-$ ..... Carbamate salt from R_1R_2HN
R_1R_2NCOOH ..... Carbamic acid from R_1R_2HN
$R_1R_2R_3N$ ..... Tertiary alkanolamine
$R_1R_2R_3NH^+$ ..... Protonated tertiary alkanolamine
RLS ..... Rate-limiting step
SNR ..... Signal-to-noise ratio
ZnSe ..... Zinc selenide

Symbols

A ..... Absorbance
A ..... Arbitrary chemical species
A [L/mol.s] ..... Arrhenius constant
A_{x_i} ..... Absorbance of species i at wavenumber x
$A_{x_{sol}}$ ..... Absorbance of solution at wavenumber i
B ..... Arbitrary chemical species

C..... Arbitrary chemical species
C_i [mol/L] ..... Molar concentration of species i
D ..... Arbitrary chemical species
D_i [m^2/s] ..... Diffusion coefficient of dissolved gas i
E [J/mol]..... Activation energy
$f(i)$ ..... Arbitrary function of i
$F_{B_{in}}$ [mol/L]..... Inlet molar flow rate of B
F_{MEA} [mol/L]..... Inlet molar flow rate of MEA
i ..... Chemical species i
I ..... Emitted radiation intensity
I_0 ..... Incident radiation intensity
k..... Reaction rate constant
k_1 [L/mol.s] ..... Zwitterion formation forward rate constant
k_{-1} [s^{-1}] ..... Zwitterion formation reverse rate constant
k_2 [L/mol.s]..... Second order rate constant
k_3 [L^2/mol^2.s] ..... Third order rate constant
k_{app} [s^{-1}]..... Apparent first order reaction rate constant
k_f [various units]..... Forward reaction rate constant
k_B [L/mol.s]..... Zwitterion deprotonation rate constant
k_{H_2O} [L^2/mol^2.s] ..... Termolecular rate constant for H_2O
k_{MEA} [L^2/mol^2.s] ..... Termolecular rate constant for MEA
k_r [various units]..... Reverse reaction rate constant
$k_{R_1R_2HN}$ [L^2/mol^2.s]..... Termolecular rate constant for R_1R_2HN
k_{x_i} ..... Lambert-Beer's law calibration constant of species i at wavenumber x
K_{eq} [L/mol] ..... Carbamate-HCO_3 thermodynamic equilibrium constant
K_i [various units]..... Thermodynamic equilibrium constant for reaction i
n..... Order of reaction with respect to alkanolamine
N ..... Number of data points used to calculate an average value
N_i [mol] ..... Number of moles of species i
r [mol/L.s]..... Reaction rate
$-r_{CO_2}$ [mol/L.s]..... Rate of consumption of CO_2
r_f [mol/L.s]..... Rate of forward reaction
r_i [mol/L.s] ..... Rate of formation of species i
$-r_i$ [mol/L.s] ..... Rate of consumption of species i
r_r [mol/L.s]..... Rate of reverse reaction
R [J/mol.K]..... Universal gas constant, 8.314 J/mol.K
t [s]..... Time
T [°C] or [K]..... Temperature
V [L] ..... Reactor volume
V_0 [L] ..... Initial reactor volume
v_{in} [L/s]..... Inlet volumetric flow rate

x ..... Arbitrary parameter
x [m] ..... Distance below liquid surface
x [cm^{-1}] ..... Wavenumber
x_{CO_2} ..... CO_2 conversion
x_{MEA} ..... MEA conversion
α_i ..... Order of an elementary reaction with respect to species i
σ ..... Standard deviation
$[i]$ [mol/L] ..... Molar concentration of species i

Glossary

Artefact – false signal in the absorbance spectrum that is caused by the presence of chemical species that do not absorb IR radiation at the particular wavenumber, or extended processing of the recorded spectrum.

Attenuated – of reduced intensity.

CO_2 loading – ratio of moles of CO_2 added to a solution to moles of MEA added to the solution.

Evanescent – quickly decaying or decreasing in amplitude (for waves).

Heterogeneous – containing more than one phase (of matter), e.g. solid and liquid.

Homogeneous – containing only one phase (of matter).

Sequestration – removal of a chemical component from a mixture by reaction with another chemical, forming a product that becomes unavailable for further reaction.

Spectroscopy – study of matter through observing its interaction with radiation.

Zwitterion – a neutral molecule containing a positive and a negative electrical charge, with the charges occurring at different parts of the molecule.

1. Introduction

1.1 Background

The reaction between carbon dioxide (CO_2) and monoethanolamine (MEA) is an industrially important reaction which is used to capture CO_2 from flue gas streams. Capturing the CO_2 prevents its release into the atmosphere, where it would otherwise contribute to global warming. The CO_2 is captured from the flue gas by reactively absorbing it into an aqueous MEA solution in an absorption column. Other solvents that can be used to absorb CO_2 are diethanolamine (DEA) and ammonia. The process produces a clean gas stream and a loaded liquid stream. The clean gas is released into the atmosphere while the liquid is passed to a regenerating column. In the regenerating column, the liquid is stripped with low pressure steam to remove the CO_2. The regenerated solvent is returned to the absorption column while the CO_2 is captured for storage (Kohl & Nielsen, 1997).

The lean MEA stream entering the absorption column usually contains 0.1 to 0.2 mol CO_2/mol MEA, and the loaded stream entering the regenerating column contains 0.4 to 0.5 mol CO_2/mol MEA. A 30 wt % MEA -70 wt % water solution is used in the absorption column. The absorption column is operated at 20 to 60°C under atmospheric pressure, and the regeneration column at 90 to 120°C at 1.5 to 2 atm. At these conditions, 85% of the CO_2 entering the absorption column can be recovered as a relatively pure gas stream (Freguia & Rochelle, 2003).

Although MEA is effective at absorbing CO_2, the high energy input required to regenerate the lean MEA stream reduces the energy efficiency of the overall process (National Energy Technology Laboratory, 2007). Hence much research is being done on amine absorption. The research effort is two-fold: design MEA processes that are energetically more efficient, and develop new solvents that work as effectively as MEA without requiring as large an energy input for solvent regeneration.

Designing new absorption processes requires vapour-liquid-equilibrium and mass transfer data of the chemical species, as well as the kinetics of the reaction under consideration. Although published data on the kinetics of the aqueous CO_2- MEA reaction dates back to the 1950s, there are still uncertainties regarding the details of the kinetics: the published rate constants show a large degree of scatter, and the reaction mechanisms are inconsistent.

1.2 Motivation

Experimental work investigating the reaction has been conducted at the Department of Process Engineering at Stellenbosch University. The work entailed investigating the CO_2-

MEA reaction in both aqueous and non-aqueous environments. In the aqueous environment, the reaction was shown to be rapid, reaching completion within 10 s (Machinga, 2012). Conductivity was initially used to monitor the reaction in a batch reactor, where pure MEA was added to a CO_2 solution. However, because MEA is very viscous, it was not instantly mixed into the solution and concentration gradients in solution were observed for the first 5-15 s of the reaction. The experimental setup was therefore changed to a semi-batch configuration.

In the semi-batch configuration, MEA pre-dissolved in water was pumped slowly into the CO_2 solution (Motang, 2012). The change in reactor configuration slowed down the reaction, and eliminated MEA concentration gradients. However, using conductivity to monitor the reaction only gave an indication of the overall reaction rate. The recorded conductivity-time plots suggested that the overall reaction is made up from multiple independent reactions. An alternative to monitoring the reaction using conductivity was to use Fourier Transform Infrared (FTIR) spectroscopy coupled to an Attenuated Total Reflectance (ATR) element.

ATR-FTIR spectroscopy has been used successfully to monitor the kinetics of the CO_2-MEA reaction in non-aqueous solvents such as n-propanol (du Preez, 2014). This analytical method was also used to monitor the equilibrium of the CO_2-DEA reaction in water by Diab *et al.* (2012). In this project, ATR-FTIR spectroscopy will be used to generate new kinetic and equilibrium data for the aqueous CO_2-MEA reaction, and the kinetics will be studied in a semi-batch reactor. The data will then be used to determine kinetic rate constants from existing reaction models and to propose a mechanism for the reaction.

1.3 Objectives

The aim of this project is to investigate the kinetics of the aqueous CO_2-MEA reaction by performing the following:

1. Collect equilibrium species distribution data at low MEA concentrations over varying CO_2 loadings in order to compare with published data from high MEA concentrations.
2. Monitor the reaction and collect reaction kinetics data over a range of temperatures and MEA concentrations.
3. Fit reaction model parameters to the reaction kinetics data collected in order to determine the appropriate rate expression and the corresponding reaction mechanism.

1.4 Thesis structure

Chapter 2 of this thesis is a review of the literature on aqueous CO_2-MEA reaction kinetics. Mechanisms that have been proposed for general CO_2-amine reactions are described, as well as kinetic rate constants and equilibrium species distributions for the CO_2-MEA reaction. The

third chapter describes the experimental setup and procedure used to generate data in this study. The results from the experimental data are discussed in Chapters 4 to 6. Chapter 4 describes the error and repeatability in absorbance measurements. Chapter 5 describes absorbance- CO_2 loading profiles that were measured during equilibrium experiments and the species concentrations that were derived from these. A carbamate- HCO_3^- equilibrium constant calculated from the species concentrations is discussed at the end of the chapter. Chapter 6 describes kinetic measurements in the form of absorbance- and molar amount-time profiles. Kinetic rate constants fitted to the molar amount-time profiles are discussed in the same chapter. Conclusions and recommendations from the work are given in Chapter 7.

2. Literature review

Absorption of CO_2 into aqueous solutions of MEA in industry faces many challenges. Some of these challenges are equipment corrosion by concentrated MEA solutions, degradation of the MEA, and a requirement for a high energy input to regenerate free MEA once the CO_2 has been absorbed. The regenerated MEA is reused in the absorption column to absorb more CO_2. To decrease the extent of equipment corrosion, corrosion inhibitors may be added to the solution. This would decrease the costs associated with replacing damaged equipment. Degradation of the MEA is caused by fly ash, O_2, SO_2 and heat. Fly ash is typically encountered in flue gas from electric power plants. Degradation through heat takes place during regeneration of free MEA, where temperatures as high as 120°C are encountered (Kohl & Nielsen, 1997; Bhown & Freeman, 2011).

Replacement of MEA lost in the process due to degradation increases operating costs for a CO_2 absorption plant. However, regeneration of the MEA has a more significant impact on the operating costs. The cost to produce steam for regeneration and strip the liquid can account for up to 70% of the absorption plant's operating costs (Aaron & Tsouris, 2005). When considering an existing power plant, adding a MEA-based CO_2 absorption unit could decrease the power plant's energy output by as much as 30% (National Energy Technology Laboratory, 2007). This 30% decrease represents the energy used to produce steam for regeneration of free MEA.

One way to reduce the energy penalty when using CO_2 capture units, is to reduce the amount of energy required for amine regeneration (National Energy Technology Laboratory, 2007). This can be achieved by using amines that require less energy for regeneration or designing more efficient MEA-based processes. A better understanding of the CO_2-MEA chemistry will allow more efficient process design. The aqueous CO_2-MEA reactions are described next with reference to the mechanisms that have been proposed for general CO_2-alkanolamine reactions.

2.1 Mechanisms proposed for CO_2-alkanolamine reactions

Alkanolamines are organic molecules that contain an amine functional group and at least one alcohol functional group. The amine functional group is the main group that reacts with CO_2. Both amine and alcohol functional groups interact with water molecules to dissolve the alkanolamines in water. CO_2 can react with water to form bicarbonate (HCO_3^-) according to Equations 1 and 2. The hydroxide (OH^-) reacting in Equation 2 is formed from the dissociation of water (Equation 3). HCO_3^- can also dissociate into carbonate (CO_3^{2-}) and a proton (Equation 4). However, CO_2 is consumed primarily through direct reaction with an alkanolamine (Versteeg *et al*., 1997).

$$CO_2 + H_2O \rightarrow HCO_3^- + H^+ \quad (1)$$

$$CO_2 + OH^- \rightarrow HCO_3^- \quad (2)$$

$$H_2O \rightarrow OH^- + H^+ \quad (3)$$

$$HCO_3^- \rightarrow CO_3^{2-} + H^+ \quad (4)$$

Primary and secondary alkanolamines have at least one hydrogen atom attached to the amine-nitrogen, while in tertiary alkanolamines the nitrogen is bound to three organic groups (Figure 1). The different alkanolamine types also react differently with CO_2. For example, the reaction is first order with respect to primary alkanolamines in water but shows fractional orders between 1 and 2 for the secondary alkanolamine, diethanolamine (DEA). For all alkanolamine types the reaction is first order with respect to CO_2 (Versteeg *et al*., 1996; Vaidya & Kenig, 2007).

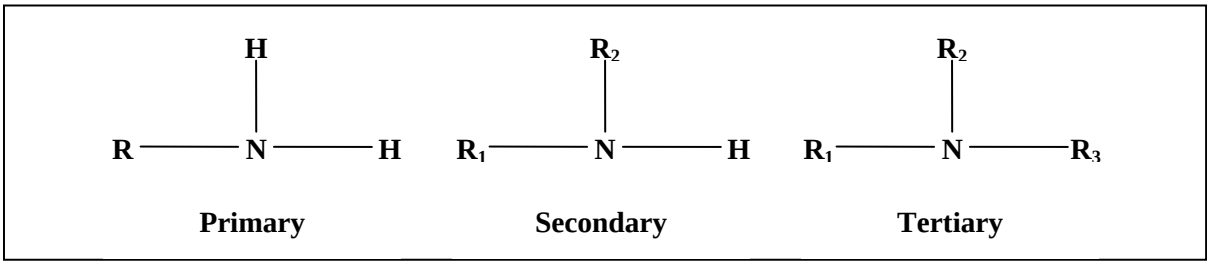

Figure 1 : General structure of primary, secondary and tertiary alkanolamines; R_i denotes organic groups

The primary alkanolamine, monoethanolamine (MEA), is one of the most widely used alkanolamines for CO_2 capture (Kohl & Nielsen, 1997). Most kinetic studies on MEA favour the zwitterion mechanism for describing the CO_2-MEA reaction. The aqueous reaction is said to be of first order with respect to both CO_2 and MEA (Versteeg *et al*., 1996; Vaidya & Kenig, 2007). Recent studies, however, indicate that the termolecular mechanism introduced by Crooks & Donnellan (1989) describes the reaction better at some conditions (Aboudheir *et al*., 2003; Luo *et al*., 2012). A carbamic acid mechanism proposed by Arstad *et al*. (2007) has also been successfully used to describe the reaction (McCann *et al*., 2009; Conway *et al*., 2011). The reaction mechanisms are described next.

2.1.1 Zwitterion mechanism

The zwitterion mechanism is the most quoted mechanism for describing the reaction of CO_2 with primary or secondary alkanolamines. A zwitterion is a neutral molecule containing both a positive and a negative electrical charge, with the two charges occurring at different parts of the molecule. The zwitterion mechanism was initially proposed by Caplow (1968) for alkyl amines, and then later reintroduced by Danckwerts (1979) for alkanolamines. According to Danckwerts (1979), the alkanolamine (R_1R_2HN) and CO_2 react to form a zwitterion (R_1R_2HNCOO) intermediate (Equation 5). The zwitterion structure is shown in Figure 2; the positive charge is on the N atom, and the negative on the upper O atom.

$$R_1R_2HN + CO_2 \underset{k_{-1}}{\overset{k_1}{\rightleftarrows}} R_1R_2HNCOO \quad (5)$$

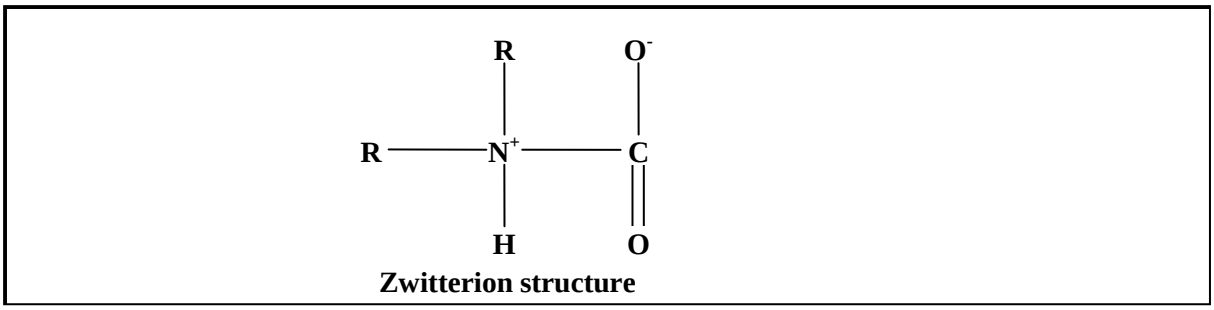

Figure 2 : Structure of a zwitterion molecule

The zwitterion intermediate is deprotonated by a base (B), producing a carbamate product ($R_1R_2NCOO^-$) and a protonated base (BH^+) (Equation 6). Any base present in the solution (e.g. water, alkanolamine, and hydroxide) can act as deprotonating base. The deprotonation step is essentially instantaneous, while the zwitterion formation step is rate-limiting.

$$R_1R_2HNCOO + B \xrightarrow{k_B} R_1R_2NCOO^- + BH^+ \quad (6)$$

If the pseudo steady-state hypothesis (see Section 2.2.2.) is applied on the concentration of the zwitterion, the rate expression for the forward reaction is given by Equation 7 (Danckwerts, 1979):

$$-r_{CO_2} = \frac{k_1[CO_2][R_1R_2HN]}{1 + \frac{k_{-1}}{\sum k_B[B]}} \quad (7)$$

If $\frac{k_{-1}}{\sum k_B[B]} << 1$, the expression simplifies to Equation 8 which is the typically reported second order rate equation (Versteeg *et al.*, 1996; Vaidya & Kenig, 2007).

$$-r_{CO_2} = k_1[CO_2][R_1R_2HN] \quad (8)$$

If $\frac{k_{-1}}{\sum k_B[B]} >> 1$, the expression simplifies to Equation 9.

$$-r_{CO_2} = k_1[CO_2][R_1R_2HN] \cdot \frac{\sum k_B[B]}{k_{-1}} \quad (9)$$

Equation 9 shows third order kinetics with an order of two in the alkanolamine if the alkanolamine is the only deprotonating base. Fractional orders in the alkanolamine between one and two are seen if other bases also deprotonate the zwitterion.

2.1.2 Termolecular mechanism

The termolecular mechanism introduced by Crooks and Donnellan (1989) suggests that the reaction is a single step, termolecular reaction between CO_2, alkanolamine and a base. Collision of the CO_2 and alkanolamine molecules produces weakly-bonded encounter complexes. Most of these complexes break up to form the initial reagents, while some react with a base molecule to form the carbamate and protonated base (BH^+) (Figure 3). The base is usually water or the alkanolamine (Crooks & Donnellan, 1989).

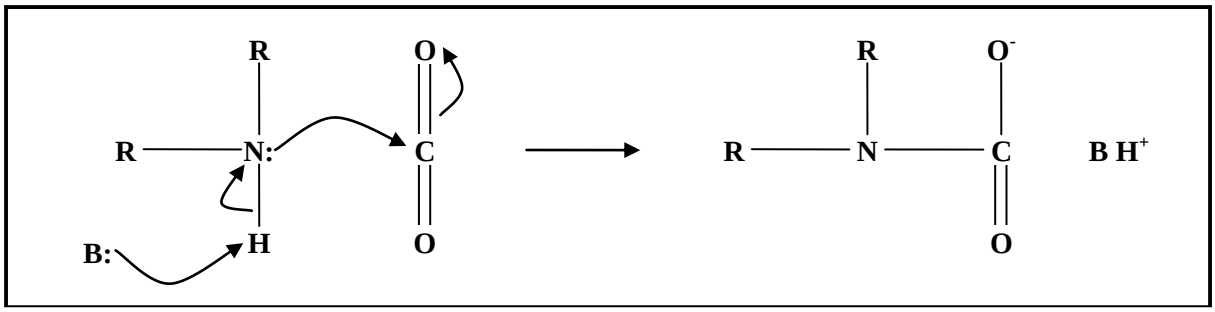

Figure 3: Termolecular reaction mechanism illustrated (adapted from Crooks and Donnellan (1989))

The forward rate expression for the mechanism is given in Equation 10 (Crooks & Donnellan, 1989). This rate expression has the same form as the second limiting case of the zwitterion mechanism when water and alkanolamine are the only deprotonating bases (Equation 9).

$$-r_{CO_2} = [CO_2][R_1R_2HN] \cdot (k_{R_1R_2HN}[R_1R_2HN] + k_{H_2O}[H_2O]) \quad (10)$$

2.1.3 Carbamic acid mechanism

The carbamic acid mechanism proposed by Arstad *et al*. (2007) describes the intermediate product of the reaction between CO_2 and alkanolamine as a carbamic acid (R_1R_2NCOOH) instead of zwitterion (Equation 11). The carbamic acid forms from an alkanolamine-CO_2 complex, when water or a second alkanolamine molecule catalyses the transfer of a hydrogen atom from nitrogen to an oxygen atom in the $-CO_2$ group. Figure 4 compares the zwitterion and carbamic acid structures.

$$R_1R_2HN + CO_2 \underset{\leftarrow}{\overset{\text{cat}}{\rightarrow}} R_1R_2NCOOH \quad (11)$$

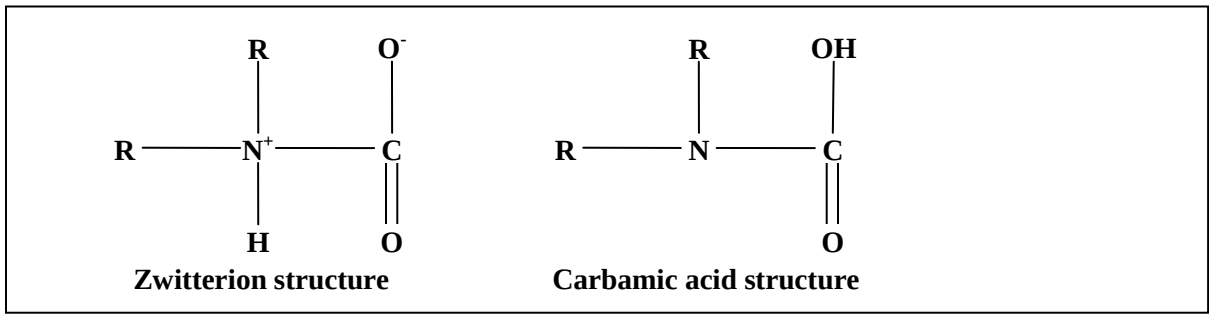

Figure 4 : Comparison of the zwitterion and carbamic acid structures

Carbamate is formed when the carbamic acid is deprotonated (Equation 12). The forward rate expression for the mechanism is a second order equation such as in Equation 8 (McCann *et al.*, 2009).

$$R_1R_2NCOOH + B \underset{\leftarrow}{\rightarrow} R_1R_2NCOO^- + BH^+ \quad (12)$$

2.1.4 Base-catalysed hydration mechanism

The absence of a hydrogen atom bonded to nitrogen in tertiary alkanolamines ($R_1R_2R_3N$) means they do not form carbamates. Instead they act as Brønsted bases and catalyse the hydration of CO_2 as given in Equation 13 (Sharma & Danckwerts, 1963). The reaction takes

place between a hydrogen-bonded water-amine complex and a free CO_2 molecule to produce bicarbonate (HCO_3^-) (Donaldson & Nguyen, 1980).

$$R_1R_2R_3N + CO_2 + H_2O \rightarrow R_1R_2R_3NH^+ + HCO_3^- \quad (13)$$

The zwitterion, termolecular and carbamic acid mechanisms primarily explain the formation of a carbamate salt ($R_1R_2NCOO^-$) from CO_2 and MEA. However, they do not describe the formation of HCO_3^- as observed by Jakobsen *et al*. (2005), Böttinger *et al*. (2008) and Richner and Puxty (2012). A base-catalysed hydration mechanism can explain the formation of HCO_3^- (Donaldson & Nguyen, 1980). This suggests that the overall mechanism for the reaction is a combination of a carbamate formation mechanism (either zwitterion, termolecular or carbamic acid) and the base-catalysed hydration mechanism. The basic theory on reaction kinetics and semi-batch kinetics is described in the next two sections.

2.2 Reaction kinetics fundamentals

The rate expression of an elementary reaction indicates how the reaction rate (r) depends on the temperature (T) and species concentrations (C_i) in a reactor (Equation 14). The expression can be assumed to contain two terms: a temperature dependent term and a concentration dependent term (Equation 15). The temperature dependence is given by the rate constant and takes the form of the Arrhenius equation (Equation 16). The constants A and E can be determined by linearizing Equation 16 to obtain a straight line that can be fitted to measured data (Equation 17) (Roberts, 2009):

$$r = f(T, \text{all } C_i) \quad (14)$$

$$r = f_1(T) \cdot f_2(\text{all } C_i) \quad (15)$$

$$f_1(T) = k = Ae^{\left(\frac{-E}{RT}\right)} \quad (16)$$

$$\ln(k) = \ln(A) - \frac{E}{R} \cdot \frac{1}{T} \quad (17)$$

The concentration dependence has the form given in Equation 18. The exponent of each concentration term (α_i) is the order of the reaction with respect to species i. These exponents can be estimated for elementary reactions, or determined experimentally for non-elementary reactions (Roberts, 2009).

$$f_2(\text{all } C_i) = \prod_i C_i^{\alpha_i} \quad (18)$$

2.2.1 Elementary reactions

An elementary reaction is defined as a reaction that proceeds on the molecular level precisely as it is written in a single step. For the elementary reaction in Equation 19, the forward reaction's rate expression with respect to species A is given in Equation 20.

$$A + B \underset{k_r}{\overset{k_f}{\rightleftarrows}} C \quad (19)$$

$$r_f = k_f C_A C_B \quad (20)$$

A feature of elementary reactions shown in Equation 20 is that the order of the reaction with respect to each species is equal to the molecularity of the species in the balanced chemical equation. The rate expression for the reverse reaction is given in Equation 21.

$$r_r = k_r C_{\mathrm{C}} \quad (21)$$

The net rate of consumption of the reactant A is given by Equation 22. When the reaction reaches chemical equilibrium, $-r_{\mathrm{A}} = 0$ and the equilibrium constant (K_{eq}) can be calculated from Equation 23.

$$-r_{\mathrm{A}} = r_f - r_k = k_f C_{\mathrm{A}} C_{\mathrm{B}} - k_r C_{\mathrm{C}} \quad (22)$$

$$K_{eq} = \frac{k_f}{k_r} = \frac{C_{\mathrm{C}}}{C_{\mathrm{A}} C_{\mathrm{B}}} \quad (23)$$

2.2.2 Non-elementary reactions

Non-elementary reactions can be broken down into steps of elementary reactions. Roberts (2009) presents criteria for determining whether a given reaction is elementary or not. A typical indication that a reaction is not elementary is if some species in the experimentally determined rate expression have reaction orders that are different to their molecularity in the balanced chemical equation.

Suppose the reaction given in Equation 19 proceeded on the molecular level in two steps (Equations 24 and 25). The net rate of consumption of species A and D would then be Equations 26 and 27, respectively.

$$\mathrm{A} + \mathrm{B} \underset{k_{-1}}{\overset{k_1}{\rightleftarrows}} \mathrm{D} \quad (24)$$

$$\mathrm{D} \underset{k_{-2}}{\overset{k_2}{\rightleftarrows}} \mathrm{C} \quad (25)$$

$$-r_{\mathrm{A}} = k_1 C_{\mathrm{A}} C_{\mathrm{B}} - k_{-1} C_{\mathrm{D}} \quad (26)$$

$$-r_{\mathrm{D}} = k_{-1} C_{\mathrm{D}} + k_2 C_{\mathrm{D}} - k_1 C_{\mathrm{A}} C_{\mathrm{B}} - k_{-2} C_{\mathrm{C}} \quad (27)$$

To derive a rate expression for $-r_{\mathrm{A}}$ that does not include the intermediate species term (C_{D}), the pseudo steady state hypothesis (PSSH) and the rate-limiting step (RLS) approximation can be used. The PSSH is used if the net rate of formation of the intermediate species is very small compared to the net rates of formation of other species in solution. The rate expression from using the PSSH is derived by setting the net rate of formation of the intermediate equal to zero. Applying the PSSH on species D gives Equations 28 to 30 (Roberts, 2009).

$$-r_{\mathrm{D}} = k_{-1} C_{\mathrm{D}} + k_2 C_{\mathrm{D}} - k_1 C_{\mathrm{A}} C_{\mathrm{B}} - k_{-2} C_{\mathrm{C}} = 0 \quad (28)$$

$$\therefore C_{\mathrm{D}} = \frac{k_1 C_{\mathrm{A}} C_{\mathrm{B}} + k_{-2} C_{\mathrm{C}}}{k_{-1} + k_2} \quad (29)$$

$$\Longrightarrow -r_{\mathrm{A}} = k_1 C_{\mathrm{A}} C_{\mathrm{B}} - k_{-1} \cdot \frac{k_1 C_{\mathrm{A}} C_{\mathrm{B}} + k_{-2} C_{\mathrm{C}}}{k_{-1} + k_2} \quad (30)$$

If the forward and reverse reaction rates of one elementary reaction in the reaction scheme are significantly lower than other elementary reactions' rates, the elementary reaction may be assumed to be the RLS in the mechanism. All other elementary reactions are assumed to be at chemical equilibrium. Making Reaction 24 the RLS gives Equations 31 to 33 (Roberts, 2009).

$$r_{\mathrm{C}} = k_2 C_{\mathrm{D}} - k_{-2} C_{\mathrm{C}} \approx 0 \quad (31)$$

$$\therefore C_{\mathrm{D}} = \frac{k_{-2} C_{\mathrm{C}}}{k_2} = \frac{C_{\mathrm{C}}}{K_2} \quad (32)$$

$$\Longrightarrow -r_{\mathrm{A}} = k_1 C_{\mathrm{A}} C_{\mathrm{B}} - k_{-1} \cdot \frac{C_{\mathrm{C}}}{K_2} \quad (33)$$

Once a rate expression for a proposed mechanism has been developed, it can only be verified by experimental measurements.

2.3 Semi-batch kinetics

In a semi-batch reactor setup, some reagents flow at a constant flow rate into a stirred reaction mixture with no product flowing out. This setup can be used either to slow down a reaction for better control and monitoring, or to improve selectivity of one product over another (Roberts, 2009). Suppose the reaction in Equation 19 was performed by initially adding a solution of A into the reactor and then slowly pumping in a solution of B. Mass balance equations for all three compounds (A, B and C) would be given by Equations 34 to 36, and the reactor volume by Equation 37.

$$\mathrm{A} + \mathrm{B} \underset{k_r}{\overset{k_f}{\rightleftarrows}} \mathrm{C} \quad (19)$$

A balance:

$$\frac{dN_{\mathrm{A}}}{dt} = r_{\mathrm{A}} V \quad (34)$$

B balance:

$$\frac{dN_{\mathrm{B}}}{dt} = r_{\mathrm{B}} V + F_{\mathrm{B}_{in}} \quad (35)$$

C balance:

$$\frac{dN_{\mathrm{C}}}{dt} = r_{\mathrm{C}} V \quad (36)$$

Reactor volume:

$$V = V_0 + v_{in} t \quad (37)$$

2.4 Typical experimental methods used to study the MEA-CO_2 reaction

The different experimental methods that have been used to study the aqueous CO_2-MEA reaction can be classified as either heterogeneous or homogeneous. In heterogeneous methods gaseous CO_2 is reactively absorbed into a liquid solution of MEA. In homogeneous methods, liquid solutions of both CO_2 and MEA are reacted. Vaidya and Kenig (2007b) present a review of some of the heterogeneous experimental methods, while Danckwerts (1970) discusses the analysis of reaction kinetics data collected from heterogeneous methods. Examples of both heterogeneous and homogeneous methods are discussed below, as well as advantages and disadvantages of both methods.

2.4.1 Heterogeneous methods

Heterogeneous experimental methods involve the reaction between CO_2 in the gaseous phase and MEA in the liquid phase. The reaction takes place at the contact area between the two phases. The contact area is defined by the geometry of the experimental setup. Use of the heterogeneous methods requires incorporating the absorption of gas molecules into a liquid (mass transfer) as well as the chemical reaction between the liquid and gas molecules into the data analysis. This is done by solving Equation 38 (Danckwerts, 1970) which represents the variation over time and distance of the concentration of the gas molecules (C_i) in the liquid. In the equation, D_i is the diffusion coefficient of the gas, x is the distance below the liquid surface, t is time, and $-r_i$ is the rate of consumption of the gas molecules at time t and distance x below the liquid surface. The rate at which gas molecules are absorbed into the liquid is dependent on the solubility of the gas into the liquid and the contact area between the gas and liquid.

$$D_i \frac{\partial^2 C_i}{\partial x^2} = \frac{\partial C_i}{\partial t} - r_i(x,t) \qquad (38)$$

2.4.1.1. Advantages

When using heterogeneous methods the concentration of CO_2 and MEA can be chosen such as to represent typical values used in industrial absorption columns (5 mol/L MEA and 2 to 2.5 mol/L CO_2). Aboudheir *et al*. (2003), Luo *et al*. (2012) and Luo *et al*. (2014) were able to reach these concentrations in their experiments. With most heterogeneous methods, a solution of MEA is prepared and then brought into contact with a gaseous stream of CO_2. CO_2 is absorbed into the solution, and its concentration in solution increases up to the saturation limit at the temperature considered.

Once reagent concentrations that are more representative of industrial conditions are achieved, it becomes possible to derive kinetic and equilibrium reaction data that are relevant to industrial absorption process conditions. Results obtained by using heterogeneous experimental methods have led to the following contributions: 1) published concentrations of carbamate and HCO_3^- products forming over time (Yang *et al*., 2009); 2) published

equilibrium reagent and product concentrations at different CO_2 loadings (Jakobsen *et al*., 2005; Böttinger *et al*., 2008; Richner & Puxty, 2012); and 3) modelling of kinetic reaction rate from data collected in conditions representative of industrial absorption columns (Aboudheir *et al*., 2003; Luo *et al*., 2012; Luo *et al*., 2014).

2.4.1.2. Disadvantages

Physicochemical properties such as the solubility and diffusion coefficient of the gas in the liquid are required for analysis of reactive gas-liquid mixtures. However, the solubility and diffusivity coefficient for reactive mixtures cannot be determined directly. This is due to the inherent combination of the absorption with the reaction. For the CO_2-MEA system, the solubility and diffusivity of CO_2 in MEA is typically estimated using the CO_2- N_2O analogy (Clarke, 1964; Laddha & Danckwerts, 1981). However, the analogy has been shown to have limited accuracy over a wide range of amine concentrations (Kreulen *et al*., 1993).

Analytical and numerical solutions of Equation 38 exist for various types of reactions. One of the simplest analytical solutions is for the irreversible first order reaction, where the reaction rate of only the gas molecules needs to be accounted for. If the CO_2-MEA reaction is conducted with a large excess of MEA, a small fraction of the MEA is consumed in the reaction and the reaction becomes a pseudo-first order reaction. At these conditions the reaction is essentially irreversible and the irreversible first order solution of Equation 38 becomes applicable. This has been the basis for most of the kinetic rate constants reported in the literature based on heterogeneous methods. The rate constants are discussed in Section 2.5.1.

Although conducting the reaction under pseudo-first order conditions allows the use of simple analytical solutions to Equation 38, the absorption process in industry is not conducted under pseudo-first order conditions. The CO_2 loading typical of such absorption processes is 0.4 to 0.5 mol CO_2/mol MEA. Pseudo-first order conditions are satisfied when there is negligible consumption of MEA and so pseudo-first order conditions can be assumed to correspond to CO_2 loadings of 0.1 mol CO_2/mol MEA or less. A CO_2 loading of 0.1 mol CO_2/mol MEA would give 20% conversion of MEA for a 2:1 MEA: CO_2 reaction stoichiometry. Therefore, the CO_2 loading in CO_2-MEA solutions that satisfy pseudo-first order conditions is much less than the CO_2 loadings encountered in industrial absorption columns. Simple kinetic models determined at CO_2 loadings between 0-0.4 mol CO_2/mol MEA have been shown to predict with increasing error above 0.3 mol CO_2/mol MEA (Luo *et al*., 2014). This suggests that the results from pseudo-first order conditions will have limited accuracy at typical absorption column conditions. Some examples of typical heterogeneous experimental methods used in kinetic studies are described next.

2.4.1.3. Laminar jet absorber

The laminar jet absorber consists of two tubes arranged vertically in a gas chamber with a gap in between the tubes. CO_2 gas flows continuously through the chamber. The top tube directs

MEA solution down into the chamber and the solution forms a jet that flows into the bottom receiving tube. The receiving tube's diameter is larger than the top tube's diameter (Danckwerts, 1970). Aboudheir *et al.* (2003, 2004) monitored the reaction by using a soap film meter to measure the outlet gas flow rate.

2.4.1.4. Wetted wall column

The wetted wall column setup consists of a cylinder placed in a gas chamber. The MEA solution flows down in a thin film over the cylinder. CO_2 gas enters through the bottom of the chamber and leaves at the top (Danckwerts, 1970). The reaction can be monitored from knowledge of the gas flow rate, as well as the inlet and outlet gas concentrations if a gas mixture is used (Vaidya & Kenig, 2007b).

2.4.1.5. Stirred cell reactor

In the stirred cell reactor, the reaction is conducted in a batch mode of operation (Vaidya & Kenig, 2007b). The reactor is initially loaded with MEA solution, and then CO_2 gas is added to the gas space above the liquid. The change in gas pressure over time is recorded and the pressure profile is used to determine the extent of reaction. The reaction takes place at the gas-liquid interface. Both the liquid and gas phases are stirred. Baffles are included in the liquid side to prevent vortex formation and maintain a constant liquid level.

2.4.1.6. Membranes

Membrane reactors that use tracer compounds to monitor the reaction were introduced by Donaldson and Quinn (1974; 1975). Donaldson and Nguyen (1980) used this type of reactor to monitor the CO_2-MEA reaction. A membrane containing MEA was placed in a diffusion cell. The cell contained a gaseous mixture of CO_2 and nitrogen and the gas was brought to equilibrium on both sides of the membrane. A small amount of tagged $^{14}CO_2$ was then introduced to one side of the membrane. The reaction rate was determined by monitoring the flux of the $^{14}CO_2$ through the membrane.

2.4.2 Homogeneous methods

In homogeneous experimental methods, aqueous solutions of CO_2 and MEA are reacted. The reaction is conducted in the absence of a vapour space, preventing the desorption of dissolved CO_2 into the vapour space. A common feature in the homogenous methods described below is mixing of the reaction solution, whereas not all heterogeneous methods require mixing (e.g. laminar jet absorber).

2.4.2.1. Advantages

When using homogeneous methods, aqueous solutions of both CO_2 and MEA are reacted. Because the two reactants are in the same phase, mass transfer effects are eliminated. It is

therefore not necessary to have values of the solubility and diffusion coefficient of the chemical species in the system. Therefore, the use of the CO_2- N_2O analogy to estimate physicochemical properties is not required.

The concentrations of both CO_2 and MEA in the system are often low. Therefore, the reaction mixture can be approximated as an ideal solution with negligible error. When the reaction mixture is assumed to be an ideal solution only the individual pure component chemical properties are needed and interaction between the different chemical species does not need to be taken into account. At high concentrations, activity coefficient models are necessary to account for interactions between molecules in the solution (Aboudheir *et al*., 2003; Luo *et al*., 2014).

2.4.2.2. Disadvantages

Analysis of results from homogeneous methods assumes that the reaction mixture is well mixed. However, the solution is likely to be well mixed only if low MEA concentrations are used. MEA has a viscosity higher than water, and at high MEA concentrations MEA concentration gradients are likely to be present when MEA solutions are mixed with dilute CO_2 solutions. CO_2 solutions will usually be dilute as a result of the solubility limit of CO_2 in water. The solubility limit of CO_2 in water restricts the range in CO_2 concentrations that can be used in homogeneous experimental methods. At 25°C and atmospheric pressure, the solubility limit of CO_2 in water is to 0.033 mol/L (Perry & Green, 2008).

The low concentrations of CO_2 in solution have another important consequence besides possible MEA concentration gradients when mixing with concentrated MEA solutions. In industrial applications, the typical total CO_2 absorbed into MEA solutions is 2 to 2.5 mol/L (Freguia & Rochelle, 2003). These concentrations are two orders of magnitude greater than the maximum concentration of CO_2 in water at 25°C and atmospheric pressure of 0.033 mol/L (Perry & Green, 2008). Reagent concentrations have been shown to have a significant effect on the rate of the reaction (Aboudheir *et al*., 2003). Therefore, kinetic models determined at low CO_2 concentrations will have limited accuracy for industrial applications. Examples of homogeneous experimental methods used in kinetic studies are described next.

2.4.2.3. Rapid mixing

The rapid mixing method was developed by Hartridge and Roughton (1923). The following description is based on work by Hikita *et al.* (1977). Aqueous solutions of both CO_2 and MEA were pumped at constant flow rates into a mixing chamber. The solutions entered the chamber as jets and were rapidly mixed and pushed up an observation tube. The reaction took place as the mixture moved up the tube. The product solution flowed out at the top of the tube. Once steady operation was achieved, the temperature profile along the observation tube was used to derive the extent of reaction using the heat of reaction.

2.4.2.4. Stopped flow

The stopped flow method was introduced by Roughton (1934). It is a variation of the rapid mixing method where equal volumes of two solutions are quickly introduced into the mixing chamber. Most researchers who have used this method inject the solutions into the chamber using syringes. The CO_2-MEA reaction has been monitored in the stopped flow setup using conductivity (Alper, 1990) and spectrophotometry (Conway *et al.*, 2011).

2.4.2.5. Batch reactor

In the batch reactor CO_2 is initially dissolved in water. A small volume of pure MEA is then injected into the reactor. The reactor contents are stirred at all times. The reaction can be monitored using conductivity (Machinga, 2012). Due to the higher viscosity of MEA when compared to the viscosity of water, MEA concentration gradients have been encountered during the first few seconds of the reaction (Machinga, 2012).

2.4.2.6. Semi-batch reactor

In a semi-batch reactor, a solution of MEA is pumped slowly into a solution containing dissolved CO_2. This allows the rapid reaction to be effectively slowed down for better monitoring. Reactions performed in this type of reactor have been monitored using conductivity (Motang, 2012) as well as Fourier Transform Infrared (FTIR) spectroscopy (du Preez, 2014).

2.5 Results from previous work

2.5.1 Reaction rate constants

Second order rate constants (k_2) are given for various temperatures, MEA concentrations and experimental methods in Table 1 and Figures 5 and 6. The corresponding rate equation is first order in both CO_2 and MEA. Data points collected from experiments in laminar jet absorbers and wetted wall columns are plotted in Figure 5, while data points collected from experiments in membrane, stirred cell and stopped flow reactors are plotted in Figure 6. The models given in Table 1 are plotted in both figures. A consistent data set would be indicated by the data points and model curves lying on one straight line with little scatter. However, there is significant scatter in the data. For example, at T = 298 K, the data points range from k_2 = 3630 L/mol.s for a stirred cell (Mimura *et al.*, 1998) (Figure 6) to k_2 = 8400 L/mol.s for a laminar jet absorber (Sada *et al.*, 1976b) (Figure 5).

Aboudheir *et al.* (2003) have proposed reasons for the discrepancies in the data. Some of the reasons are problems encountered when using heterogeneous gas-liquid type reactors. These include the use of the CO_2-N_2O analogy and the assumption of pseudo-first order reaction kinetics (Section 2.4.1.2), may explain why data points from the laminar jet absorber have values that are consistently higher than data points from other reactors. Data points from other

heterogeneous reactors (wetted wall column, stirred cell) have values that are neither consistently higher nor lower than data points from other reactors.

The zwitterion mechanism is the mechanism mostly used to describe the reaction rate data for MEA (Versteeg *et al.*, 1996; Vaidya & Kenig, 2007). Conway *et al.* (2011) however, interpreted their results using the carbamic acid mechanism. In both mechanisms, MEA can act as the main deprotonating base. Both mechanisms produce an overall second order rate expression, making it difficult to distinguish between them. Neither the zwitterion nor carbamic acid intermediate species has yet been detected experimentally. Analysis of the zwitterion, carbamic acid and termolecular mechanisms using criteria for elementary reaction steps by Roberts (2009) indicates that the zwitterion mechanism is likely to be the correct mechanism.

Table 1: Second order rate constants found in literature

Reference	T **[K]**	[MEA] **[mol/L]**	k_2 **[L/mol.s]**	**Experimental Method**
Astarita (1961)	294.5	0.25-2.0	5400	Laminar jet abs.
Clarke (1964)	298	1.6-4.8	7500	Laminar jet abs.
Sharma (1965)	298	1	7600	Laminar jet abs.
Sada *et al.* (1976a)	298	0.2-1.9	8400	Laminar jet abs.
Sada *et al.* (1976b)	298	0.2-1.9	7140	Laminar jet abs.
Hikita *et al.* (1977)	278.6-308.4	0.0152-0.177	$9.77 \times 10^{10} \mathrm{e}^{\left(\frac{-4955}{T}\right)}$	Rapid mixing
Alvarez-Fuster *et al.* (1980)	293.15	0.2-2.02	4300	Wetted wall col.
Donaldson & Nguyen (1980)	298	0.03-0.08	6000	Membranes
Laddha & Danckwerts (1981)	298	0.49-1.71	5870	Stirred cell
Penny & Ritter (1983)	278-303	0-0.060	$1.23 \times 10^{11} e^{\left(\frac{-5078}{T}\right)}$	Stopped flow
Sada *et al.* (1985)	303	0.5-2.0	7740	Stirred cell
Barth *et al.* (1986)	293	0.02-0.05	3600	Stopped flow
Barth *et al.* (1986)	298	0.02-0.05	4700	Stopped flow
Alper (1990)	278-298	0-0.45	$8.51 \times 10^{11} e^{\left(\frac{-5617}{T}\right)}$	Stopped flow
Littel *et al.* (1992)	318	0-3.2	10400	Stirred cell
Littel *et al.* (1992)	333	0-3.2	25700	Stirred cell
Versteeg *et al.* (1996)[1]	278-313	–	$4.4 \times 10^{11} e^{\left(\frac{-5400}{T}\right)}$	–
Mimura *et al.* (1998)	298	0.9-2.5	3630	Stirred cell
Kucka *et al.* (2003)	293-324	3.3	$4.495 \times 10^{11} e^{\left(\frac{-5405}{T}\right)}$	Stirred cell
Ali (2005)	298-313	0.005-0.035	$8.36 \times 10^{11} e^{\left(\frac{-5613}{T}\right)}$	Stopped flow
McCann *et al.* (2009)	303	0.002-0.006	6110	Stopped flow
Puxty *et al.* (2010)	283	5	2634	Wetted wall col.
Conway *et al.* (2011)	288-318	0.001-0.016	$5.8 \times 10^{10} e^{\left(\frac{-4872}{T}\right)}$	Stopped flow
Ying & Eimer (2013)	298-323	0.5-12	$4.14 \times 10^{11} e^{\left(\frac{-5399}{T}\right)}$	Stirred cell
Luo *et al.* (2014)	298-343	1	$8.87 \times 10^{8} e^{\left(\frac{-3458}{T}\right)}$	Wetted wall col. & String of discs
Luo et al. (2014)	298-343	5	$4.396 \times 10^{9} e^{\left(\frac{-3693}{T}\right)}$	Wetted wall col. & String of discs

[1] Rate-constant expression based on published data up to 1992

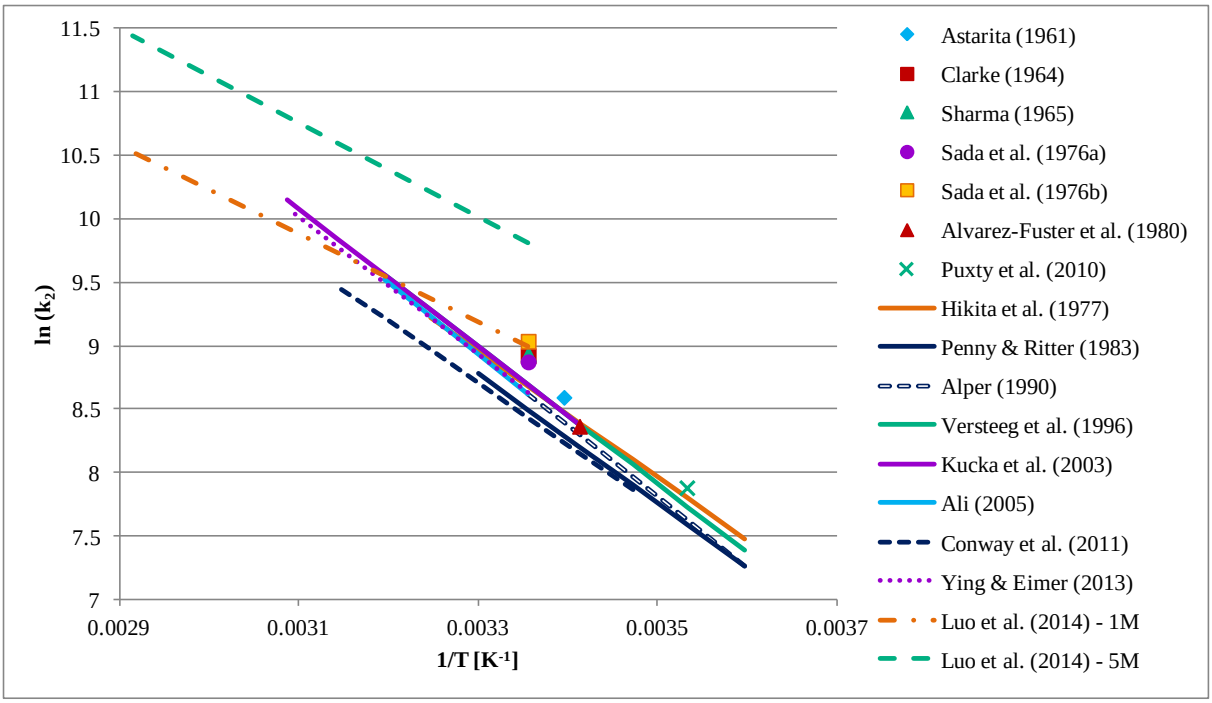

Figure 5 : Second order rate constants found in literature – data points are from laminar jet absorbers and wetted wall columns; all models given in Table 1 are plotted

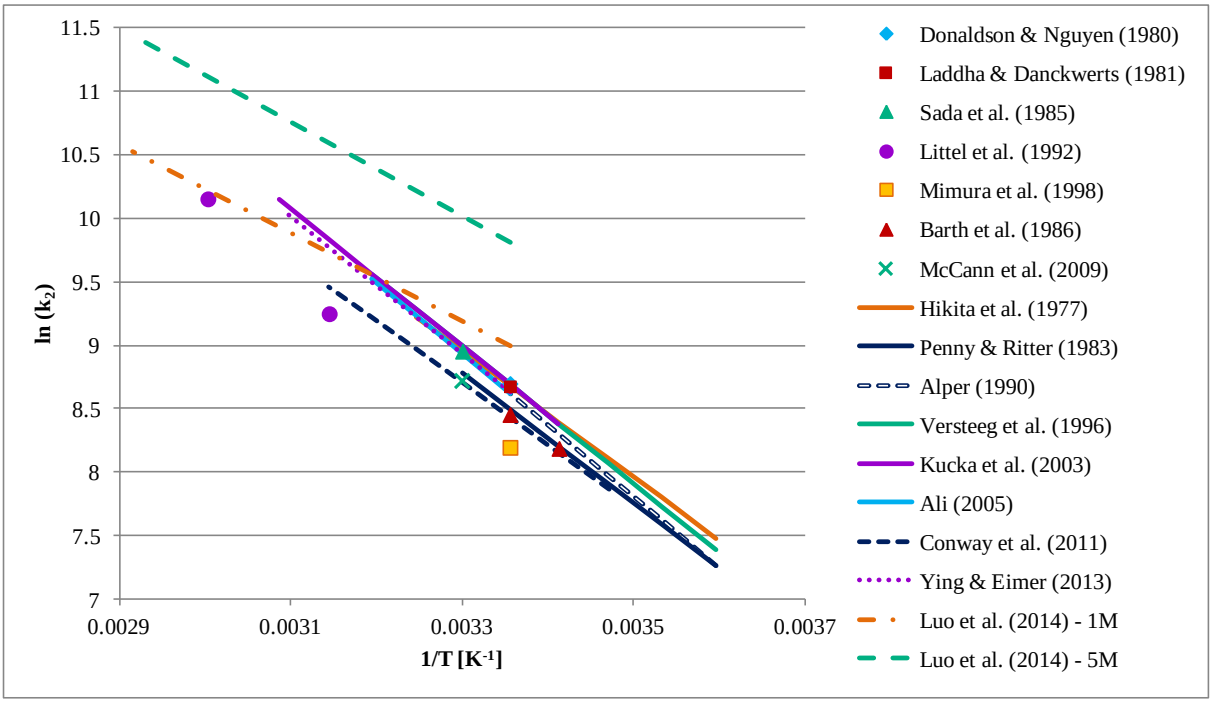

Figure 6: Second order rate constants found in literature – data points are from membrane, stirred cell and stopped flow reactors; all models given in Table 1 are plotted

For the rate constants given in Table 1, only Puxty *et al.* (2010) and Luo *et al.* (2014)'s results were determined at CO_2 loadings representative of CO_2 loadings used in industrial absorption columns. Puxty *et al.* (2010) worked at 0-0.5 mol CO_2/mol MEA, and Luo *et al.* (2014) worked at 0 to 0.4 mol CO_2/mol MEA. Absorption columns are usually operated at maximum CO_2 loadings between 0.4 to 0.5 mol CO_2/mol MEA (Freguia & Rochelle, 2003). Both groups of researchers used the wetted wall column, and could achieve CO_2 loadings in solutions with

an initial MEA concentration of 5 mol/L, a concentration similar to that used in absorption columns. Puxty *et al*. (2010), however, conducted their experiments at only one temperature, 283 K, which is outside the temperature range typically found in absorption columns (313-333 K).

Luo *et al*.'s (2014) results were determined at two MEA solution concentrations, 1 and 5 mol/L. Their results show large deviation from other results reported in literature. The reasons for the deviation may be that their experiments were conducted at relatively high MEA concentrations, using both unloaded and loaded MEA solutions. In loaded MEA solutions, CO_2 gas was pre-dissolved into the MEA solution before being used in a kinetic experiment. The CO_2 loading of the solutions with pre-dissolved CO_2 was known. The reported rate constants summarize the results found in both unloaded and loaded MEA solutions. In the range of CO_2 loadings considered (0 to 0.4 mol CO_2/mol MEA), the second order rate constants predicted systematic deviations in the reaction rate at CO_2 loadings above 0.3 mol CO_2/mol MEA (Luo *et al*., 2014).

The CO_2 loadings used in experiments of other researchers are not representative of the CO_2 loadings in industrial absorption columns. Researchers who worked with heterogeneous experimental methods worked under pseudo-first order conditions. Under pseudo-first order conditions, an insignificant amount of MEA is consumed. At these conditions, it can be assumed that the maximum CO_2 loading in solution is approximately 0.1 mol CO_2/mol MEA. 0.1 mol CO_2/mol MEA corresponds to 20% consumption of MEA for 2:1 MEA: CO_2 reaction stoichiometry.

The CO_2 loadings from experiments conducted in homogeneous experimental methods by other researchers could not be determined accurately. This is because the researchers only report the range of CO_2 and MEA concentrations that were used while not reporting the CO_2-MEA ratios used in each experiment. However, the concentrations used were not representative of concentrations in industrial absorption columns. The CO_2 concentrations used were much lower than CO_2 concentration found in absorption columns (Section 2.4.2.2). Therefore most heterogeneous experimental results were determined at CO_2 loadings not representative of CO_2 loadings in industrial absorption columns, and most homogeneous experimental results were determined at CO_2 concentrations not representative of CO_2 concentrations in industrial absorption columns.

The effect of CO_2 loading on the reaction rate is more significant than the effect of other variables during the experiments (Setameteekul *et al*., 2008). Up to date, the most investigated variables have been the reaction temperature and MEA concentration, as can be seen in Table 1. The effect of CO_2 loading on the reaction rate will be discussed shortly with reference to the results of Luo *et al*. (2014). The effect of CO_2 loading effect on the apparent order of the reaction with respect to MEA is discussed first.

The apparent order of the reaction with respect to MEA is given by n in Equation 39. The equation allows a fractional order (n) in MEA. Alper (1990) found values of n between 1.04-1.07 and concluded that the values were sufficiently close to 1. A value of 1 supports the common assumption that the reaction is an overall second order reaction. Aboudheir *et al.* (2003) and Luo *et al.* (2012), however, calculated values between 1.04-1.36 and 1.37-1.52, respectively. The calculated reaction orders were shown to increase with temperature, suggesting a reaction mechanism more complex than just overall second order kinetics. Both Aboudheir *et al.* (2003) and Luo *et al.* (2012) conducted their experiments at CO_2 loadings between 0.1 and 0.49, and 0 and 0.4 mol CO_2/mol MEA, respectively; Alper (1990)'s experiments were conducted at 0.05 mol CO_2/mol MEA, suggesting a dependence of the mechanism on the CO_2 loading in solution.

$$-r_{CO_2} = k[CO_2][R_1R_2HN]^n \quad (39)$$

Aboudheir *et al.* (2003) and Luo *et al.* (2012) fitted their experimental results successfully to the termolecular model. The published termolecular rate constants are given in Table 2. The MEA deprotonation constants are plotted in Figure 7, and the water deprotonation constants are plotted in Figure 8. Aboudheir *et al.* (2003) report an inconsistency between Crooks and Donnellan (1989)'s results and two other sets of results published at low MEA concentrations (Hikita *et al.*, 1977; Laddha & Danckwerts, 1981). Aboudheir *et al.* (2003) and Luo *et al.* (2012)'s results were determined at high MEA concentrations. Both groups of researchers report their models can correctly predict published results determined at low MEA concentration. However, Luo *et al.* (2014)'s results suggest that experimental results determined at CO_2 loadings different from those in industrial absorption columns will have limited accuracy when applied to the modelling of these absorption columns.

Table 2: Termolecular rate constants found in literature

Reference	T **[K]**	[MEA] **[mol/L]**	k_{MEA} **[L²/mol².s]**	k_{H_2O} **[L²/mol².s]**	**Exp. Method**
Crooks & Donnellan (1989)	298	0.1-1	52600	24	Stopped flow
Aboudheir *et al.* (2003)	293-333	3-9	$4.61 \times 10^9 e^{\left(\frac{-4412}{T}\right)}$	$4.55 \times 10^6 e^{\left(\frac{-3287}{T}\right)}$	Laminar jet
Luo *et al.* (2012)	298-343	0.5-5	$8.07 \times 10^9 e^{\left(\frac{-4503}{T}\right)}$	$3.51 \times 10^6 e^{\left(\frac{-3055}{T}\right)}$	Wetted wall & String of discs
Luo *et al.* (2014) - c	298-343	1&5	$2.003 \times 10^{10} e^{\left(\frac{-4742}{T}\right)}$	$4.147 \times 10^6 e^{\left(\frac{-3110}{T}\right)}$	Wetted wall & String of discs
Luo *et al.* (2014) - a	298-343	1&5	$1.844 \times 10^{10} e^{\left(\frac{-4112}{T}\right)}$	$2.064 \times 10^5 e^{\left(\frac{-1766}{T}\right)}$	Wetted wall & String of discs

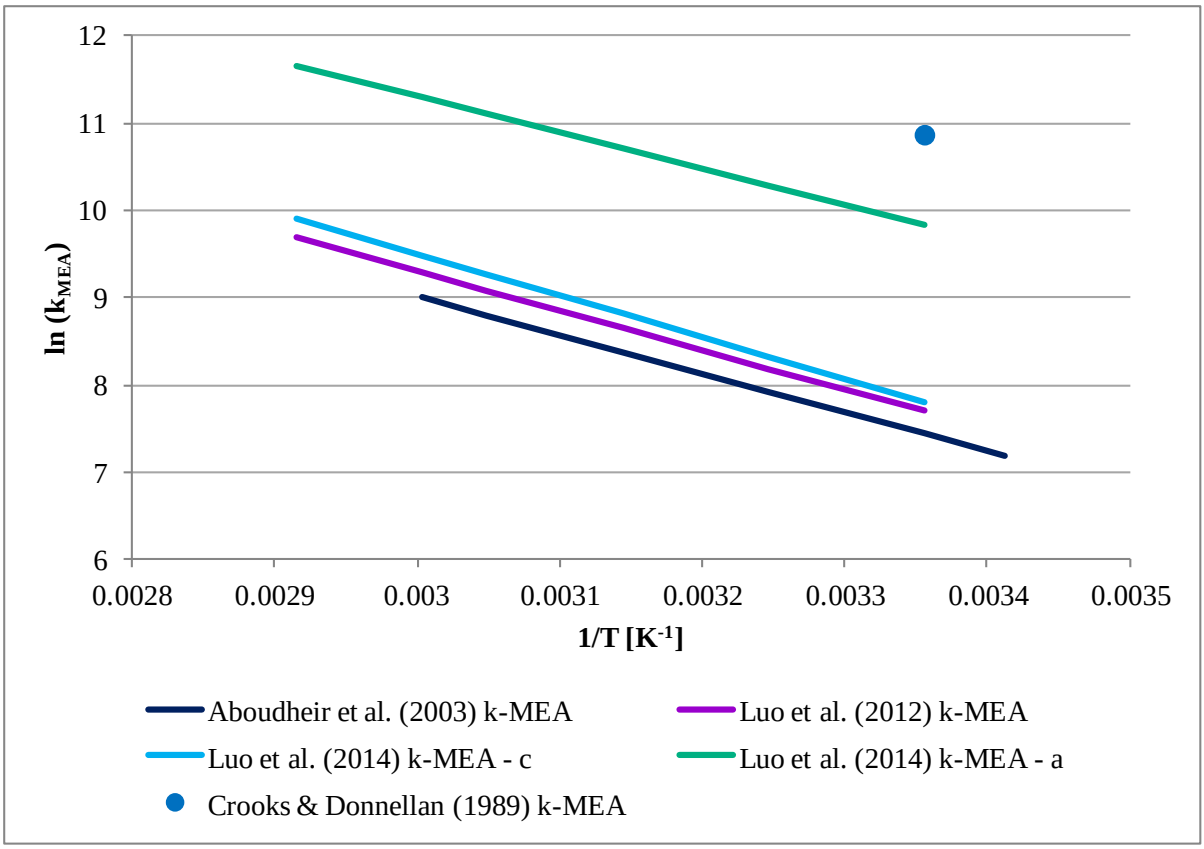

Figure 7: Literature termolecular rate constants – MEA deprotonation constant (k_{MEA})

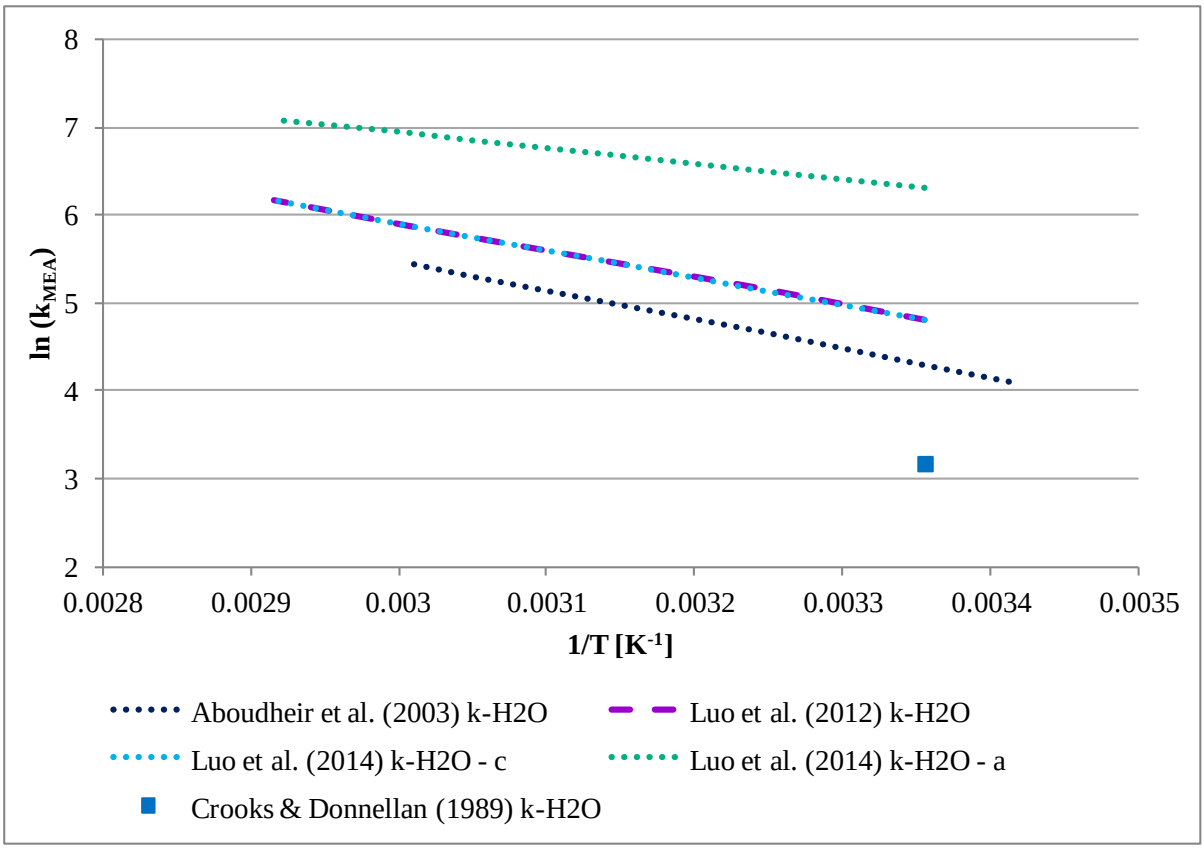

Figure 8: Termolecular rate constants found in literature – H_2O deprotonation constant (k_{H2O})

Concentration- ($k_{\mathrm{MEA}} - \mathrm{c}$ and $k_{\mathrm{H_2O}} - \mathrm{c}$) and activity coefficient-based ($k_{\mathrm{MEA}} - \mathrm{a}$ and $k_{\mathrm{H_2O}} - \mathrm{a}$) termolecular rate constants were determined by Luo *et al.* (2014). The concentration-based model provided a model fit similar to the second order model given in Table 1. The model fits experimental data well at CO_2 loadings below 0.3 mol CO_2/mol MEA, but predicted systematic deviations in the reaction rate above CO_2 loadings of 0.3 mol CO_2/mol MEA. The activity coefficient-based termolecular model fit the data well over the entire range of CO_2 loadings considered (0 to 0.4 mol CO_2/mol MEA).

The apparent reaction rate constant (k_{app}) as defined in Equation 40 has been shown to decrease with increasing CO_2 loading (Aboudheir *et al*., 2003). The absorption rate of gaseous CO_2 into MEA solutions also decreases with increasing CO_2 loading (Astarita *et al*., 1964; Luo *et al*., 2014). These observations illustrate the importance of taking CO_2 into account when investigating the kinetics of the CO_2-MEA reaction.

$$-r_{CO_2} = k_{app}[CO_2] \qquad (40)$$

CO_2 loading has also been shown to have a significant effect on the distribution of product species at equilibrium. Plots of product species concentration against CO_2 loading suggest that the mechanism of the aqueous CO_2-MEA reaction is a function of the solution CO_2 loading as well. These concentration measurements are discussed next.

2.5.2 Equilibrium species concentration measurements

Equilibrium species concentration measurements by Jakobsen *et al.* (2005), Böttinger *et al.* (2008) and Richner and Puxty (2012) show the trends in Figure 9 when plotted against CO_2 loading. Similar plots have been generated using vapour-liquid equilibrium models developed by, among others, Austgen *et al.* (1989). In the following discussion, data from Fan *et al.* (2009) are not included because the concentration of HCO_3^- at CO_2 loadings where HCO_3^- formation would be significant was not calculated.

From Figure 9, low CO_2 loadings give rise to protonated MEA ($MEAH^+$) and carbamate concentrations that are approximately equal. The two concentrations add up to the amount of MEA consumed. Carbamate concentration is a maximum at 0.5 mol CO_2/mol MEA, where MEA is nearly completely consumed. At higher CO_2 loadings, carbamate concentration decreases and $MEAH^+$ and HCO_3^- concentrations increase. Carbonate (CO_3^{2-}) concentration is negligible at all CO_2 loadings.

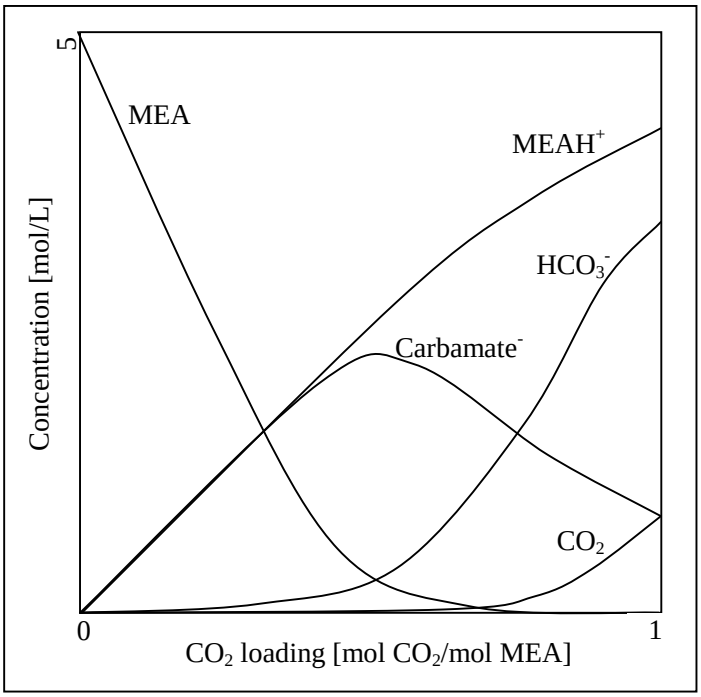

Figure 9 : Species concentrations at various CO_2 loadings in the aqueous CO_2-MEA mixture at 40°C (redrawn from Austgen *et al*., 1989)

Further analysis of the figure at high CO_2 loadings (>0.5 mol CO_2/mol MEA) suggests that for every CO_2 molecule added and consumed, one carbamate molecule is also consumed. In addition one $MEAH^+$ molecule and two HCO_3^- molecules are produced. The zwitterion, termolecular and carbamic acid mechanisms cannot explain HCO_3^- formation. Base-catalysed hydration can, but it does not explain carbamate formation. The correct mechanism must therefore be a combination of the carbamate formation and base-catalysed hydration mechanisms.

Danckwerts and McNeil (1967) suggest that the formation of HCO_3^- from carbamate takes place through hydrolysis of the carbamate (Equation 41). However, equilibrium concentration measurements suggest a reaction such as in Equation 42. This reaction may take place through the steps in Equations 43 to 48 (Astarita *et al*., 1964).

$$\text{Carbamate}^- + H_2O \rightarrow \text{MEA} + HCO_3^- \quad (41)$$

$$CO_2 + \text{Carbamate}^- + 2H_2O \rightarrow MEAH^+ + 2HCO_3^- \quad (42)$$

Reaction steps for HCO_3^- formation with carbamate decomposition, which occur when excess CO_2 is added to the reaction mixture:

$$\text{Step 1: } 2H_2O \rightarrow 2OH^- + 2H^+ \quad (43)$$

$$\text{Step 2: } CO_2 + OH^- \rightarrow HCO_3^- \quad (44)$$

$$\text{Step 3: } \text{Carbamate}^- + H^+ \rightarrow \text{Zwitterion} \quad (45)$$

$$\text{Step 4: Zwitterion} \rightarrow \text{MEA} + CO_2 \quad (46)$$

$$\text{Step 5: } \text{MEA} + H^+ \rightarrow MEAH^+ \quad (47)$$

$$\text{Step 6: } CO_2 + OH^- \rightarrow HCO_3^- \quad (48)$$

Yang *et al*. (2009) have measured the changes in species distribution over time as CO_2 is absorbed into MEA solutions. The measurements were made using ^{13}C NMR spectroscopy.

The concentration profiles from these measurements indicate that initially, only carbamate forms as the CO_2-containing reaction product. The carbamate concentration then reaches a maximum, and starts decreasing as HCO_3^- begins to form. These results support the combined carbamate formation-base-catalysed hydration mechanism.

2.5.3 Effect of pH on observed kinetics

Bicarbonate formation accompanied by carbamate consumption seems to only appear at high CO_2 loadings (Astarita *et al*., 1964), which corresponds to low pH solutions. The solution pH decreases as the CO_2 loading increases. The rate of carbamate consumption has been shown to decrease with increasing pH through a proposed mechanism that involves a zwitterion intermediate (Johnson & Morrison, 1972).

For individual amine solutions from amines with different base strengths, bicarbonate formation-carbamate consumption takes place more readily in solutions of less basic amines (Johnson & Morrison, 1972; Ewing *et al*., 1980). This is demonstrated in the case of alkanolamines through comparison of equilibrium species distributions from MEA and diethanolamine (DEA) solutions. MEA is more basic than DEA. For these two systems, Böttinger *et al*. (2008) and Richner and Puxty (2012) confirmed that more carbamate forms for MEA and more bicarbonate forms for DEA relative to the initial amount of alkanolamine.

The studies presented in Table 1 agree on the order of MEA in Equation 39 being $n = 1$. Most of these studies were conducted at relatively low CO_2 loadings (≤0.1 mol CO_2/mol MEA). Aboudheir *et al*. (2003) and Luo *et al*.'s (2012) research at higher CO_2 loadings give $1 < n < 2$. Experimental work on DEA also reports the order of the reaction with respect to DEA being $1 < n < 2$ (Versteeg *et al*., 1996; Vaidya & Kenig, 2007). Fractional orders between 1 and 2 could be as a result of the low pH that is encountered in DEA solutions compared to MEA solutions, as well as in MEA solutions with high CO_2 loading compared to low CO_2 loading solutions. At the low pH, carbamate consumption and bicarbonate formation are expected to take place more readily.

The CO_2 loading of MEA solutions has been shown to be the most influential parameter on the mass transfer in an absorption column (Setameteekul *et al*., 2008). The effect of pH on the absorption process can therefore be accounted for by correctly incorporating the species distribution data at each CO_2 loading. Diab *et al*. (2013) have shown that incorporating such species distribution data for a DEA solution improves modelling of absorption column operation.

2.5.4 Insight into the reaction mechanism from theoretical studies

A number of authors have used computational methods to investigate the aqueous CO_2-MEA reaction. Quantum chemistry methods such as *ab initio* and density-functional theory calculations have limited accuracy though because water is represented implicitly using solvation models (Levine, 2009). Studies based on these methods agree that a zwitterion formed during the reaction has a short lifetime (da Silva & Svendsen, 2004; da Silva &

Svendsen, 2007; Shim *et al*., 2009; Xie *et al*., 2010). Xie *et al*. (2010) estimate zwitterion deprotonation to take place within 3 picosecond (ps), where the zwitterion would have an equilibrium concentration of 10^{-11} mol/L at 5 mol/L MEA and 0.03 mol/L CO_2.

Unlike *ab initio* and density-functional theory methods, molecular dynamics simulations represent solvent molecules explicitly (Levine, 2009). Results from such simulations indicate that a zwitterion can be deprotonated within approximately 1 ps (Xie *et al*., 2010; Han *et al*., 2011). The activation energy for zwitterion deprotonation by the MEA is calculated to be 1.3 kcal/mol (Xie *et al*., 2010; Han *et al*., 2011). Deprotonation by water has a higher activation energy of 6–8 kcal/mol (Guido *et al*., 2013), indicating that deprotonation by MEA is kinetically more favourable. Activation energies of zwitterion formation and breakdown are 9.85–11.2 kcal/mol (Hikita *et al*., 1977; Alper, 1990) and 6–8 kcal/mol (Guido *et al*., 2013), respectively.

Iida and Sato (2012), who used a hybrid electronic structure theory-statistical mechanics method, confirmed that MEA is the more favourable deprotonating base. Regarding base-catalysed hydration, Da Silva and Svendsen (2007) stated that any amine can act as base. The carbamate stability-base strength relationship mentioned by Da Silva and Svendsen (2007) can be understood in terms of the effect of pH on the observed kinetics, i.e. a strong base results in a high pH, favouring the formation of a stable carbamate.

2.6 Fourier Transform Infrared Spectroscopy and Attenuated Total Reflectance

Fourier Transform Infrared (FTIR) spectroscopy is an analytical method that can be used to identify molecular species in a solution. This is done by detecting the infrared (IR) radiation absorbed by the chemical bonds in each species. The chemical bonds can be detected because they vibrate at different characteristic wavenumbers and so absorb IR radiation at these wavenumbers. The radiation absorbed is quantified by calculating absorbance (A) from the incident (I_0) and emitted (I) radiation intensities (Equation 49) (Hsu, 1997).

$$A = -\log\left(\frac{I}{I_0}\right) \quad (49)$$

In a solution the absorbance is related to the number of chemical bonds present and therefore the concentration of the chemical species containing the bonds of interest. The absorbance at a wavenumber x due to the presence of chemical species i (A_{x_i}) and the species' concentration (C_i) are related through Equation 50 (Lambert-Beer's law). The calibration constant k_{x_i} can be determined for species i at wavenumber x by recording the absorbances at x from a number of solutions of known i concentrations (Hsu, 1997).

$$A_{x_i} = k_{x_i} C_i \quad (50)$$

Absorbance is an additive property, so that the absorbance of a solution at a wavenumber x is the sum of the absorbances of all species in solution at x (Equation 51). The absorbance

spectrum of the solution ($A_{x_{sol}}$) is obtained by recording the absorbance over a range of wavenumbers (Hsu, 1997).

$$A_{x_{sol}} = \sum_i A_{x_i} = \sum_i k_{x_i} C_i \quad (51)$$

For calibration purposes wavenumbers can be selected such that only one species in a mixture absorbs radiation at particular wavenumbers. Any absorbance at a specific wavenumber can then be attributed to the presence of the corresponding species in solution. The concentration of this species is calculated from the measured absorbance and a pre-determined calibration factor through Equation 50. This is the basis for the analysis in this work.

The use of an Attenuated Total Reflectance (ATR) element allows the FTIR method to be used *in situ*, with the ATR element placed inside the reaction vessel. The element is a crystal made from a material with a refractive index higher than the refractive index of the solution in the reaction vessel, e.g. zinc selenide or germanium (Hsu, 1997). The ATR-FTIR method was chosen in this work to monitor the aqueous CO_2-MEA reaction because of its success in qualitatively (Jackson *et al.*, 2009) and quantitatively (Diab *et al.*, 2012; Richner & Puxty, 2012) monitoring the aqueous CO_2-alkanolamine system. The method has been incorporated into a semi-batch reactor setup for use in monitoring reaction kinetics by du Preez (2014).

Monitoring of a liquid sample using an ATR crystal is illustrated in Figure 10. An IR beam travels from the spectrometer to the crystal (I_0). At the interface between the crystal and sample, part of the IR beam is transmitted into the sample as an evanescent wave. The portion of the IR beam not transmitted into the sample is reflected into the crystal and travels back to the spectrometer (I). The ratio of intensities of the outgoing and incoming beams gives absorbance as calculated by Equation 49.

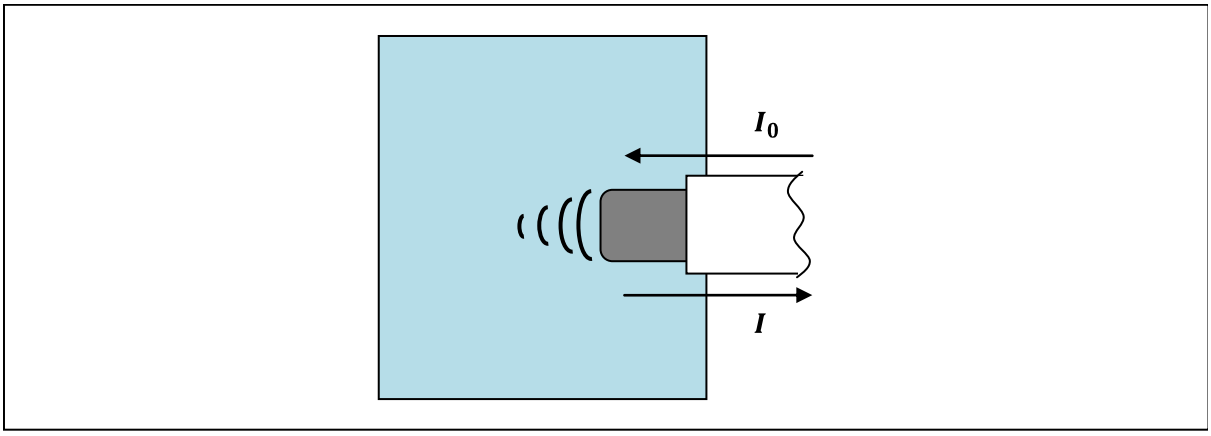

Figure 10 : Evanescent wave emitted into a liquid sample from an ATR element

2.7 Conclusion and motivation for study

From the previous discussion, it is clear that monitoring the chemical species that form during the aqueous CO_2-MEA reaction is necessary for understanding the kinetics of the reaction. Published literature shows that there is disagreement with regards to the kinetics and mechanism of the reaction. A combined carbamate and HCO_3^- formation mechanism may be more appropriate for describing the reaction over a range of CO_2 loadings. This range of CO_2 loadings would include the loadings commonly found in industrial absorption columns (0-0.5 mol CO_2/mol MEA).

In this project the reaction will be conducted in a homogeneous reactor, simplifying data analysis by eliminating the effects of mass transfer. A semi-batch reactor will used for this purpose. Equilibrium and kinetics experiments will be conducted and the reaction will be monitored using ATR-FTIR spectroscopy. For the kinetics experiments, semi-batch operation will be achieved by pumping in MEA solutions into well-mixed CO_2 solutions. This configuration will allow: 1) detection of various chemical species during reaction; 2) varying of the CO_2 loading in solution between 0.1 and 1 mol CO_2/mol MEA; and 3) elimination of MEA concentration gradients.

In the equilibrium experiments, chemical species in the CO_2-MEA reaction mixture will be recorded at various CO_2 loadings. Lower MEA concentrations than reported in equilibrium distributions from published literature will be used. The results from low MEA concentrations will be compared to results from higher concentrations to compare the reaction mechanism at high MEA concentrations to the mechanism at low concentrations. Agreement between the results from both low and high MEA concentration solutions will validate the applicability of the combined carbamate and HCO_3^- formation mechanism at low concentration solutions as well.

The hypotheses proposed for this work are the following:

1. The reaction between CO_2 and MEA in water proceeds via a two-part mechanism consisting of carbamate formation through a zwitterion intermediate, and base-catalysed hydration of CO_2 accompanied by carbamate consumption.
2. At CO_2 loadings less than 0.5 mol CO_2/mol MEA, free CO_2 is consumed predominantly through carbamate formation; at CO_2 loadings greater than 0.5 mol CO_2/mol MEA, free CO_2 is consumed predominantly through base-catalysed hydration.

3. Materials and methods

3.1 Experimental setup

All experiments were conducted in the FTIR-semi-batch reactor setup designed by du Preez (2014). The setup is shown in Figure 11. The setup consisted of a cylindrical reactor, a syringe, a peristaltic pump and an ATR-FTIR probe for monitoring the reaction.

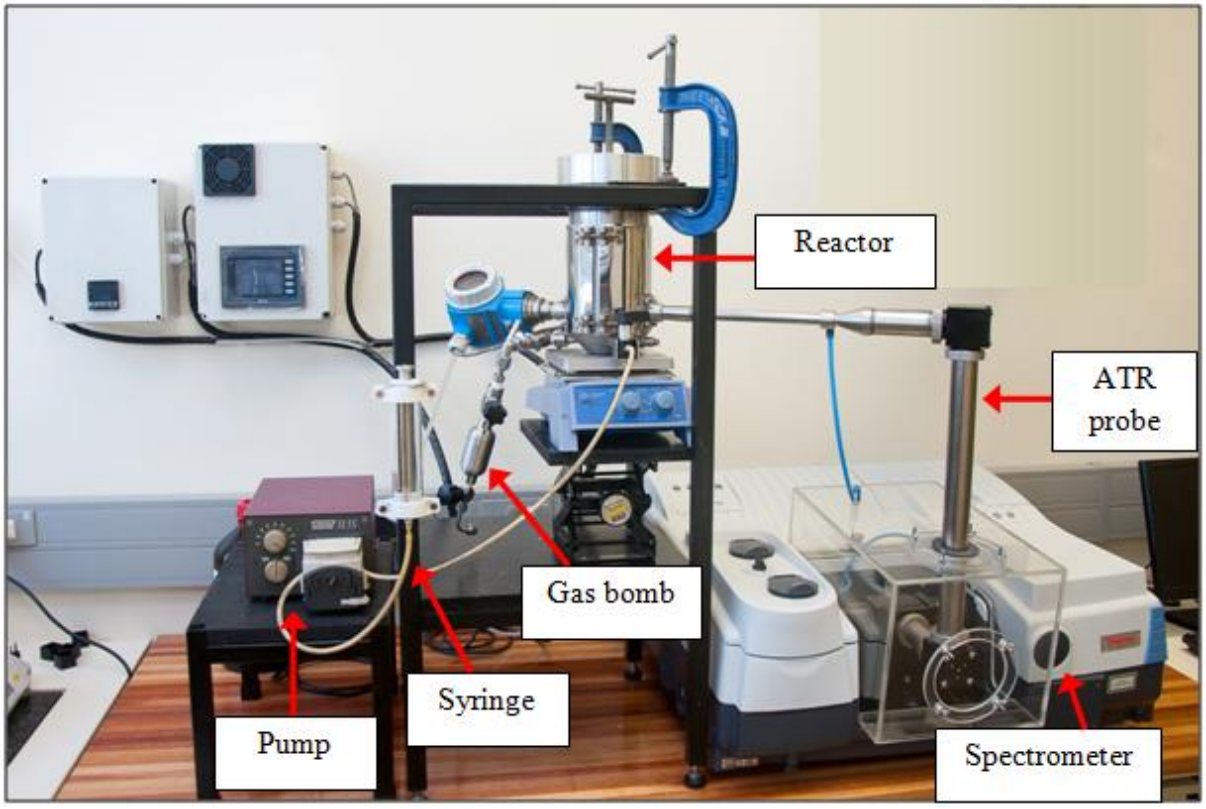

Figure 11 : Semi-batch reactor setup with FTIR spectrometer

3.1.1 Reactor configuration and assembly

The reactor was a 1 L vessel made from 316 stainless steel. It had dimensions of 200 mm for height, 100 mm for internal diameter and 2 mm for the wall thickness. The reactor was constructed at the Process Engineering Department at Stellenbosch University. The steel used to make the reactor was supplied by Macsteel VRN Cape Town, Republic of South Africa. Stainless steel was chosen as the material of construction due to the corrosive nature of MEA.

The reactor had a piston assembly that could be used to change the internal reactor volume. The piston head was a 316 stainless steel disk with a silicone rubber lip seal fitted to the bottom edge. The rubber seal had a diameter of 100 mm and thickness of 10 mm. The disk had a ball valve on top. A steel cap rested on the piston head, and could be pushed down by steel rod. A screw-on steel disk with a threaded hole was placed on top of the reactor, and the

rod moved through the hole. A schematic diagram of the piston assembly is shown in Figure 12.

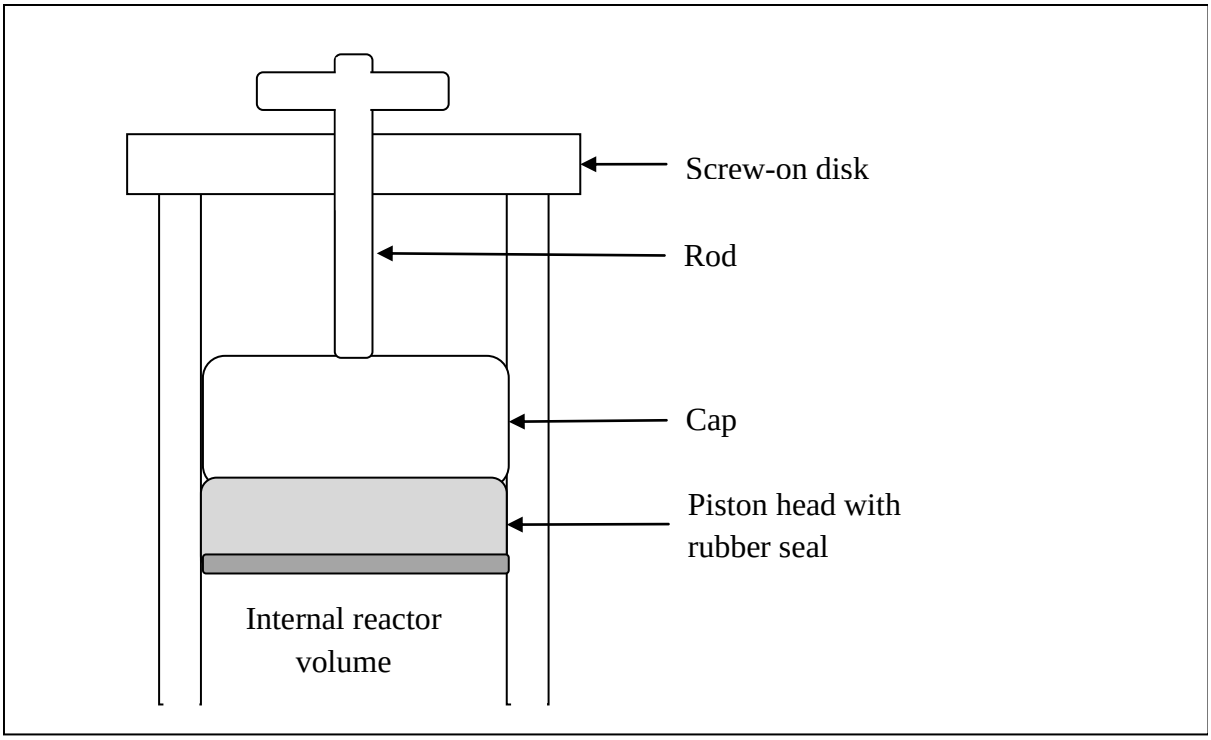

Figure 12 : Reactor piston assembly

Turning the rod by its handle clockwise pushed the cap downwards, thereby lowering the reactor piston and reducing the volume of the reactor. The metal pieces in the piston assembly were constructed at the Process Engineering Department at Stellenbosch University. The rubber seal was from IMAC Hydraulics Somerset West, Republic of South Africa.

The reactor's temperature was regulated using a fitted thermal jacket. The jacket had a power rating of 500 W, diameter of 115 mm and length of 150 mm. It was supplied by UNITEMP Cape Town, Republic of South Africa. A Stuart magnetic stirrer (CB162 model) was used to stir the contents of the reactor. The stirrer bar used had dimensions of 6 mm in diameter and 30 mm in length.

A Watson Marlow 313S peristaltic pump was used to pump aqueous MEA solutions into the reactor. The solutions flowed from a 100 mL gas tight syringe (Hamilton 1000 series) through a two-way valve into the reactor. CO_2 was fed to the reactor using a gas bomb. The gas bomb was a 50 mL 316SS cylindrical chamber (304L-HDF4-50) with two needle valves (SS-16DKM-F4 and SS-16DKM-F4) attached as indicated in Figure 13. The chamber, valves and fittings indicated in the figure were Swagelok components supplied by Johannesburg Valve & Fitting Co. (Pty) Ltd. Specifications of the valves and fittings are given in Appendix A. The pipe segment and bush fitting indicated were modifications done by the Technical Workshop at the Department of Process Engineering, Stellenbosch University.

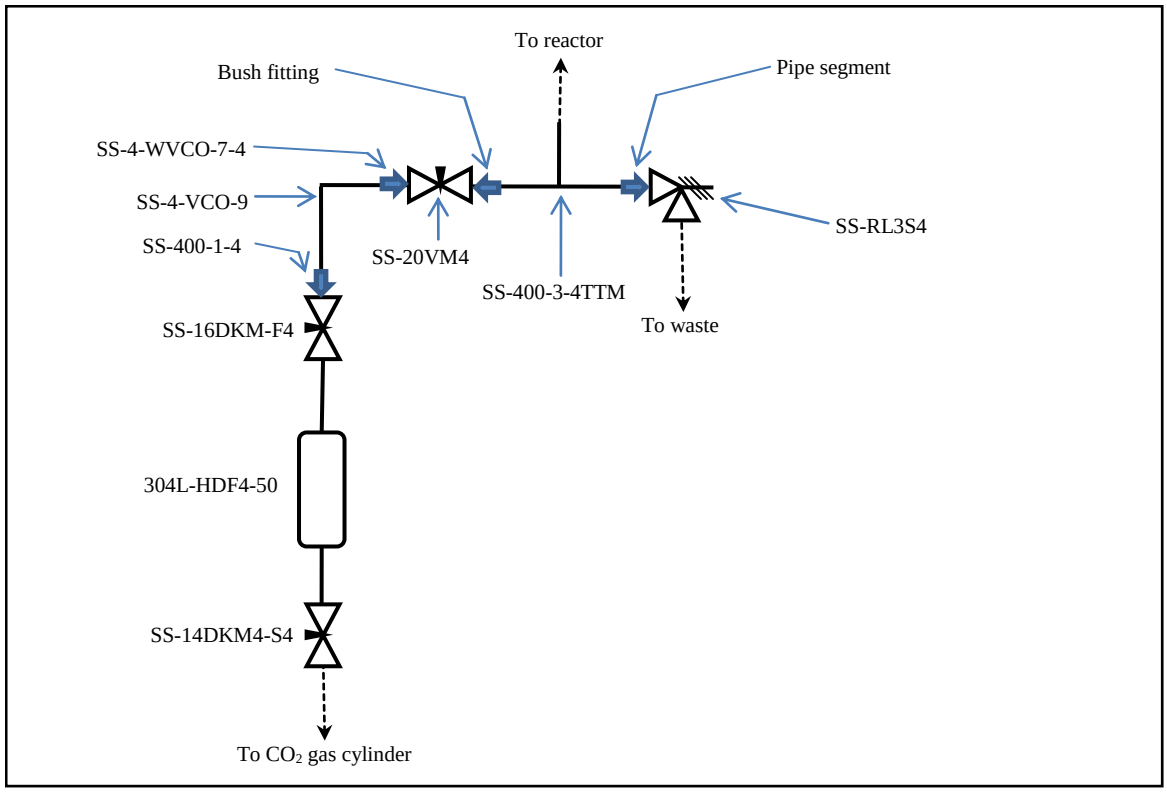

Figure 13 : Gas feed section with gas bomb attached

A relief valve (SS-RL3S4) was installed at the gas inlet of the reactor. In the event of pressure build-up in the reactor during loading of gas, the valve would open and release some of the reactor contents to waste, thereby reducing the reactor pressure. The valve set pressure was initially set to 2 bar abs. However, the relief valve would be actuated during loading of CO_2, releasing some of the reagents to waste. The set pressure was therefore changed to 3 bar abs. The reactor pressure never exceeded the higher set pressure during CO_2 loading.

The FTIR spectrometer used in this work was the Thermo Scientific^{TM} Nicolet 6700 model. It was fitted with an ATR probe accessory containing an ATR element. The probe was the DPR-207 model, and both probe and ATR element were supplied by Axiom Analytical. The spectrometer environment was continuously purged with either baseline grade N_2 gas or dried compressed air to remove water and CO_2 contamination from recorded spectra. Water and CO_2 from the compressed air were removed by a PG28L purge gas generator supplied by Peak Scientific. To improve stability of the purged environment, a purge hood made from Perspex was fitted onto the spectrometer's sample compartment. Liquid N_2 used for cooling the MCT detector was supplied by the Department of Chemistry, Stellenbosch University.

Two ATR elements were available for use in the FTIR-ATR setup: a Ge element and a zinc selenide (ZnSe) element. The Ge and ZnSe materials have different properties that should be considered when choosing an ATR element for experimental use. A Ge element has a typical evanescent wave penetration depth of 0.6 µm, while a ZnSe element has a typical penetration depth of 2 µm (PIKE Technologies, 2011). The higher penetration depth of ZnSe allows the evanescent wave to penetrate deeper into a sample solution, and allows a higher fraction of

the wave to be attenuated by the sample. This leads to higher accuracy in measurements when compared to measurements made using a Ge element. However, the Ge element can withstand solution pHs in the range of 1 to 14 pH units, whereas the ZnSe is recommended for use only between 5 to 9 pH units (PIKE Technologies, 2011).

In the experiments conducted, the solution pH was estimated to vary from 4 pH units in CO_2-water mixtures (Chuang & Johannsen, 2009), to 11 pH units for MEA-water mixtures (Kohl & Nielsen, 1997). Therefore, it was necessary to use the Ge ATR element to avoid chemical attack from the reaction solution.

3.1.2 Reaction monitoring and analysis

The temperature in the reactor was monitored using a PT-100 temperature probe with an accuracy of ±0.5°C. During the experiments, fluctuations in the reactor temperature due to reaction were always within 0.5 C of the reactor set point temperature. Pressure was monitored using a Endress and Hauser® Cerebar S Pressure sensor, with an accuracy of 0.075% in the displayed value. The mass of reagents was weighed on a Precisa® EP 920M balance with a capacity of 920 g and accuracy of ±0.001 g.

IR spectra were collected and analysed using the Thermo Scientific™ OMNIC™ Software Suite. A resolution of 16 cm^{-1} was used, and provided sufficient clarity of absorption bands in the region 1600-1000 cm^{-1}. Background spectra and equilibrium sample spectra were created from 256 scans of the reactor solution. Kinetic sample spectra were created from 1 scan each using the Series add-on module of OMNIC™. At 1 scan per spectrum, spectra from the kinetic experiments could be collected every 0.13 s. The rapid data collection ensured many data points were collected during the transient phase of the reaction. Automatic atmospheric suppression as configured by the software was used on all spectra. 2-level zero filling, Happ-Genzel apodization and Mertz phase correction were also used on the spectra. Baseline correction of sample spectra was not used.

3.2 Reagent chemicals

The MEA used in experiments was the ACS reagent grade (>99% purity) supplied by Sigma-Aldrich. CO_2 was supplied by Afrox. Demineralised water produced by a reverse osmosis process was used to make up all solutions. The densities of MEA and water at the temperatures considered in this work are given in Table 3.

Table 3 : MEA and H_2O densities at the temperatures considered in this work

T [°C]	20	25	30
ρ_{MEA} [g/L]	1016.7	1011.9	1008.0
ρ_{H_2O} [g/L]	998.2	997.0	995.6
Reference:	Tseng & Thompson (1964)	Han *et al.* (2012)	

Because both CO_2 and MEA were used at low concentrations in the experiments, the reaction solution could be approximated as an ideal liquid solution. Dissolution of CO_2 in water increased the liquid volume, and this was accounted for by the partial volume of CO_2 in water. The partial volume of CO_2 is not a strong function of temperature (Parkinson & de Nevers, 1969). A value of 0.0339 L/mol CO_2 determined at 25°C (Moore *et al.*, 1982) was used for the CO_2 partial volume at all temperatures.

3.3 Experimental procedure

Data collected in this work was either from monitoring the kinetics or the equilibrium of the reaction. The wavenumbers at which chemical species in the aqueous CO_2-MEA reaction mixture absorb IR radiation were identified, and calibration factors were derived for the reagent species at their respective wavenumbers. The calibration factors were used to calculate reagent concentrations from absorbance measurements made during the kinetic experiments.

3.3.1 Species identification

The wavenumbers at which chemical species in the reaction mixture absorb IR radiation were identified using two methods. The first was through gradually adding MEA to an aqueous solution of CO_2. The second was through adding CO_2 to a MEA solution. In both cases, sample spectra were recorded and the wavenumbers at which absorbance peak activity appeared were noted. Reagent species were identified from sample spectra of the initial CO_2 or MEA solution, processed using a background spectrum of water. Product species were identified from sample spectra of the reaction mixture, processed using a background spectrum of the initial CO_2 or MEA solution. Both reagent and species wavenumbers are given in Section 5.1.

3.3.2 Reagent species FTIR calibration

Calibration curves in the form of Equation 52 were obtained for CO_2 and MEA. In the equation, C_i is the concentration of species i, A_j is the absorbance at wavenumber j, and $k_{i,j}$ is the calibration factor for species i at wavenumber j.

$$C_i = k_{i,j} A_j \qquad (52)$$

Each value of absorption recorded was the average of Series kinetic measurements recorded in a solution of either CO_2 or MEA dissolved in water. Data were collected over 30 s. A total of 230 data points were collected, and the average and standard deviation in the measurements were calculated.

Positive peak height was used during kinetic experiments to measure MEA absorbance, and negative peak height was used for CO_2 absorbance. During a kinetic reaction experiment, the

MEA peak would grow more positive as the concentration of MEA in solution increases. Since a background spectrum of CO_2 in water was used to process sample spectra collected in the kinetic experiments, the CO_2 peak would grow more negative as the concentration of CO_2 in solution decreased. The calibration results described next refer to the positive MEA peak height and the negative CO_2 peak height.

3.3.2.1 CO_2 calibration

In analyzing data from the kinetic experiments, the background spectrum used to process sample spectra was that of the initial CO_2 solution. As MEA was added to the reactor, CO_2 was consumed by reacting with MEA and the CO_2 absorbance peak activity appeared as a negative peak in the sample spectrum. Calibration factors were obtained for the negative absorbance peak by adding excess MEA to CO_2 solutions and then recording the resulting sample spectra. The CO_2 absorbance was recorded at 2342 cm^{-1}.

In each experiment, 0.5 g CO_2 was loaded and dissolved in 0.5 L demineralised water. The actual amount of CO_2 added was weighed. This would give a concentration of approximately 0.02 mol/L, well below the solubility limit of CO_2 in water which is 0.038 to 0.26 mol/L between 20 to 35°C (Perry & Green, 2008). The CO_2 loading procedure is given in Section 3.3.5. A background spectrum of the CO_2 solution was recorded and then pure MEA was added. The amount of MEA added was enough to achieve a MEA: CO_2 molar ratio of 100:1. The excess MEA ensured close to 100% conversion of the CO_2. The absorbance recorded from the CO_2-MEA solution was plotted against the concentration of consumed CO_2. The actual CO_2 concentration in the reactor in a kinetic experiment could then be calculated from the concentration of consumed CO_2 and the initial amount of CO_2 added to the reactor.

The CO_2 calibration factor was determined at each temperature from at least three calibration points measured as described above. A wide range of CO_2 concentrations was not used to construct a calibration curve for CO_2 absorbance due to large uncertainties in CO_2 absorbance at low CO_2 concentrations. However, a wide range of MEA concentrations was used during MEA calibration experiments. The MEA concentration-absorbance measurements obeyed Lambert-Beer's law, which states that the measured absorbance will be directly proportional to the concentration (Hsu, 1997). Therefore, CO_2 absorbance could also be assumed to obey Lambert-Beer's law because both MEA and CO_2 absorbances were measured using the same technique.

The calibration curve for CO_2 at 30°C is given in Figure 14, with error bars indicating the 95% confidence limit of the measured absorbance. The curve was forced through the origin in order to comply with Lambert-Beer's law. The data points in Figure 14 correspond to masses of CO_2 between 0.4 and 0.5 g, and the straight line generated passes through the absorbance range represented by each data point's 95% confidence interval. This validates assuming CO_2 obeys Lambert-Beer's law. The calibration factors for all three temperatures are given in Table 4, with the corresponding Pearson's R^2 values also given. The error and reliability of

the measured CO_2 absorbance is discussed in Chapter 4. Calibration curves for all three temperatures are given in Appendix B.

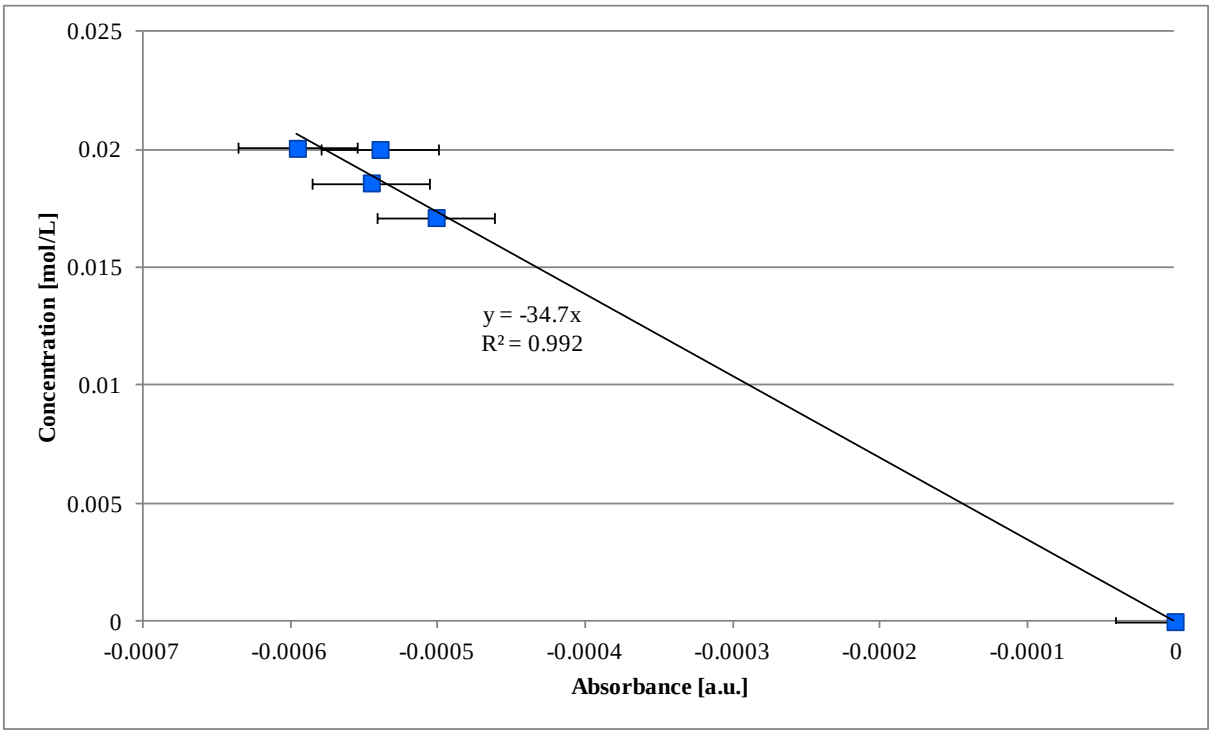

Figure 14 : FTIR CO_2 calibration data at 30°C; absorbance measured at 2342 cm^{-1}

Table 4 : CO_2 calibration factors at various temperatures

T [°C]	$k_{CO_2,2342}$	R^2
20	33.0	0.996
25	29.9	0.995
30	34.7	0.992

3.3.2.2 MEA calibration

For MEA calibration, pure MEA was added in small increments to 0.5 L demineralised water. Each increment was weighed, and up to between 20 and 24 g MEA was added in each calibration experiment. The increments were 1 to 2 g up to 10 g total MEA added and approximately 4 g for mass above 10 g total MEA added. The exact amount of MEA added was weighed. Sample spectra were recorded after adding each increment. The background spectrum used to process sample spectra was that of water. The calibration was performed three times at each reaction temperature. MEA absorbance was recorded at 1024 cm^{-1}.

The calibration curve for MEA at 30°C is given in Figure 15. The data points plotted are from measurements made in three different calibration experiments. The error bars are included for all the points, and these indicate good repeatability of the MEA absorbance measurements. Similar results were obtained at other temperatures. The MEA calibration curve was forced through the origin, and the data points plotted follow Lambert-Beer's law, where absorbance increases linearly with increasing concentration. The calibration factors determined for the

three temperatures are given in Table 5 with the corresponding Pearson's R^2 values. Accuracy and reliability of the measured MEA absorbance is discussed in Chapter 4. Calibration curves for all three temperatures are given in Appendix B.

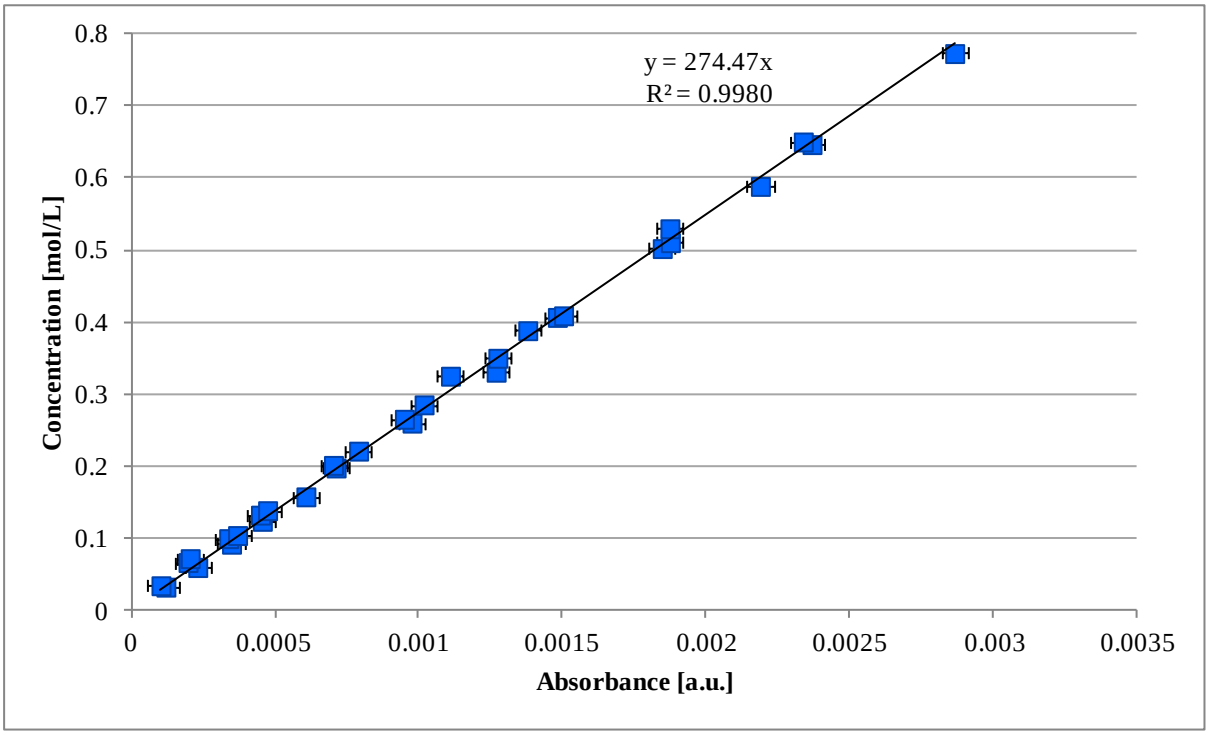

Figure 15 : FTIR MEA calibration data at 30°C; absorbance measured at 1024 cm^{-1}

Table 5 : MEA calibration factors at various temperatures

T [°C]	$k_{MEA,1024}$	R^2
20	284.80	0.9937
25	267.98	0.9922
30	274.47	0.9980

The validity of the MEA calibration was tested by adding known amounts of CO_2 to a MEA solution, and comparing the measured absorbance with the expected MEA concentration. The MEA absorbance was measured once CO_2 had been dissolved. Up to approximately 0.5 g CO_2 was added to the MEA solution. This is the same amount of CO_2 that was used in kinetic experiments.

The theoretical stoichiometric ratio of 2 was used to calculate the theoretical concentration of MEA left in solution once all CO_2 had reacted. This theoretical concentration is plotted against the measured MEA absorbance in Figure 16 as the data series [MEA*]. The data series [MEA] represents data from a calibration experiment at 30°C. The data plotted show that the MEA absorbance decreased once CO_2 was added to the MEA solution, and that absorbance moves along the MEA calibration curve. This validates the use of the absorption band at 1024 cm^{-1} to monitor MEA in solution.

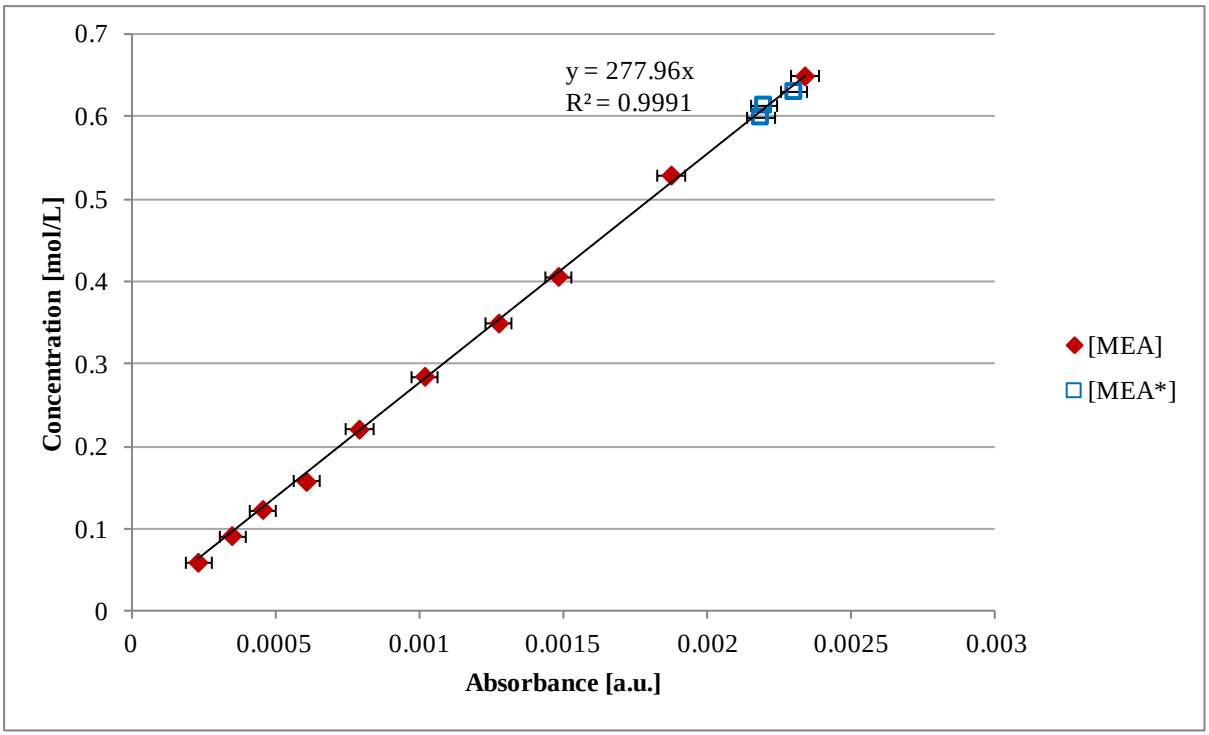

Figure 16 : MEA peak behaviour confirmation at 30°C

3.3.3 Equilibrium experiments

Equilibrium experiments were conducted so that the chemical species forming in the aqueous CO_2-MEA system could be monitored over various CO_2 loadings in low MEA concentration solutions. Measurements were made in 0.33 mol/L MEA solutions, at three temperatures. In each experiment, the CO_2 loading in solution was varied from 0 to 0.6 mol CO_2/mol MEA.
the chemical species distribution in the reaction mixture over CO_2 loadings from 0-0.6 mol CO_2/mol MEA were monitored.

The reactor was initially purged with N_2 gas to remove small droplets of solution from previous experiments. Demineralised water was weighed and added to the reactor. Once the water was in the reactor, the piston assembly described in Section 3.1.1 was used to seal off the portion of the reactor volume containing liquid: the piston head was lowered into the reactor with the ball valve open until the bottom of the metal disk was flush with the liquid in the reactor. At this point the ball valve was closed, the rest of the piston assembly replaced, and the water heated to the required temperature.

MEA was weighed and added to the reactor using a syringe. About 10 g of MEA was used in each experiment. Stirring of the reactor solution was then started, and the solution was left to return to the required temperature. This was because dissolving MEA would slightly increase the reactor temperature. Once the solution was at the required temperature, CO_2 gas was added in increments and dissolved under pressure. The procedure used to add CO_2 to the reactor is described in Section 3.3.5. Sample spectra of 256 scans each were recorded for the MEA solution, and after each increment of CO_2 had been dissolved. The background spectrum used to process sample spectra was of water at the required temperature.

3.3.4 Kinetic experiments

Kinetic experiments were conducted so that the CO_2-MEA reaction could be measured in real-time. The reaction was conducted by pumping a solution of MEA into a stirred solution of CO_2. Real-time kinetic measurements were used to model the kinetics of the reaction and determine kinetic rate constants.

The reactor was initially purged, and the water was added to the reactor and heated as described for the equilibrium experiments (Section 3.3.3). CO_2 was then loaded as described in Section 3.3.5 and dissolved under pressure. The MEA solution was made up by loading known amounts of MEA and demineralised water in the syringe at the required reaction temperature. The solution in the syringe was dissolved by shaking it until all the MEA had dissolved. Streaks of MEA would be seen swirling around in the syringe if not all the MEA was dissolved. 10 mL of the MEA solution was used to purge the tubing connecting the syringe and reactor before conducting the reaction. During the reaction, 80 mL of the solution was pumped into the reactor at a constant flow rate while recording sample spectra using the OMNIC^{TM} Series module. The mass of MEA solution added was determined by weighing the syringe before and after pumping the solution into the reactor.

The background spectrum used to process sample spectra was that of the CO_2 solution in the reactor before adding the MEA solution. The CO_2 solution background was used because it allowed a smaller time interval between recording of background and sample spectra. If a water background spectrum was used instead, the background spectrum would be recorded before dissolving CO_2, at least an hour before recording sample spectra.

3.3.5 Loading of CO_2 into gas bomb and reactor

CO_2 was loaded into the gas bomb through the bomb inlet valve (SS-14DKM4-S4, indicated in Figure 13). The inlet valve was connected to the outlet valve of a CO_2 gas cylinder. Both valves were then opened for a few seconds to allow some gas into the bomb. Once the gas was loaded, the two valves were closed and the bomb was disconnected from the cylinder. The mass of loaded gas was determined from the difference in mass between the loaded and unloaded bomb. Thereafter, some of the loaded gas was vented to the atmosphere through the bomb's outlet valve (SS-16DKM-F4) until the mass of loaded gas was approximately 1.5 g.

The gas was loaded into the reactor through a pipe section connected on the reactor. The bomb's outlet valve (SS-16DKM-F4) was connected to the section using the fitting SS-400-1-4. Once connected, the rod in the reactor's piston assembly was raised, and valve SS-16DKM-F4 quickly opened and closed to allow a small amount of gas into the pipe section. The needle valve SS-20VM4 was then opened briefly to allow the gas into the reactor. The gas was dissolved into the liquid in the reactor by lowering the reactor's piston head and pressurising the reactor. The mass of gas added to the reactor was determined by weighing the

gas bomb before and after loading gas into the reactor. More CO_2 was loaded into the reactor until the required mass was loaded.

3.4 Experimental design

The variables in the kinetic and equilibrium experiments were MEA concentration and reaction temperature. The operating pressure was kept at atmospheric pressure for all experiments. Because CO_2 was dissolved in water for the kinetic experiments, the maximum CO_2 concentration was limited by CO_2's solubility limit in water. For a temperature range of 20-30°C, 0.022 mol/L CO_2 was used. This concentration was well below the solubility limit of CO_2 in water. The maximum concentration of CO_2 that can dissolve in water decreases from 0.038 to 0.26 mol/L between 20 to 35°C (Perry & Green, 2008).

The concentration and temperature settings for the kinetic experiments are given in Table 6. Two MEA concentrations were chosen in order to determine the effect of the MEA concentration on kinetic rate constants. The concentrations could be achieved by pumping 80 mL of a 10 or 20 wt% MEA solution into the reactor. The same volumetric flow rate was used for both MEA concentrations, which led to two different molar feed flow rates. The MEA concentrations and the reaction temperatures were within the ranges of conditions used to generate some of the kinetic data published in literature (Section 2.5.1).

Table 6 : Kinetic experiments settings

	Low MEA	**High MEA**
C_{MEA} **[mol/L]**	0.26	0.52
N_{MEA} **[mol]**	0.13	0.26
F_{MEA} **[mol/s]**	0.005	0.01
C_{CO_2} **[mol/L]**	0.022	
N_{CO_2} **[mol]**	0.11	
T **[°C]**	20, 25, 30	

The combination of MEA concentrations and solution flow rates chosen also ensured kinetically limiting conditions as will be discussed in Section 6.1. Three experiments were conducted at each concentration-temperature setting, resulting in a total of 18 experiments. The experimental results are discussed in chapter 5.

The concentration and temperature settings for the equilibrium experiments are given in Table 7. Only one MEA concentration was considered. The equilibrium experiments were conducted at all three temperatures used in the kinetic experiments, with CO_2 loading in increments of 0.1 mol CO_2/mol MEA. The maximum CO_2 loading in each experiment was 0.6 mol CO_2/mol MEA, which was 0.1 mol CO_2/mol MEA more than the CO_2 corresponding to the theoretical reaction stoichiometric ratio of 2. The range of CO_2 loadings chosen would, therefore, allow measurements to be made at conditions of excess MEA as well as conditions near the stoichiometric ratio. Three experiments were performed at 25°C in order to evaluate the

repeatability of the measurements. The results of the equilibrium experiments are discussed in Chapter 5.

Table 7 : Equilibrium experiments settings

C_{MEA} **[mol/L]**	0.33
N_{MEA} **[mol]**	0.17
Max. CO_2 loading [mol CO_2/mol MEA]	0.6
T **[°C]**	20, 25, 30

4. Error and repeatability in absorbance measurements

The error and repeatability of the measurements made in the experiments are discussed in this chapter. Measurements from both kinetic and equilibrium experiments are considered. Interference from MEA and carbamate absorbances when measuring species absorbances is discussed at the end of the chapter.

4.1 Error

Error in measurements represents the uncertainty of the measured experimental values. The uncertainty can be quantified using the standard deviation in the measured values, with the standard deviation representing the average uncertainty in the measured values. When reported with the mean, the standard deviation gives the confidence interval of the calculated mean. One standard deviation gives the 68% confidence interval, which is the range of values wherein 68% of the measured values are likely to fall (Equation 53). Two standard deviations represent the 95% confidence interval (Equation 54) (Taylor, 1997).

$$68\%\ \text{confidence interval} = x_{mean} \pm \sigma \quad (53)$$

$$95\%\ \text{confidence interval} = x_{mean} \pm 2\sigma \quad (54)$$

The use of the standard deviation to represent uncertainty in the experimental measurements assumes the measured values follow a normal distribution. If the assumption of normally distributed data is valid, Equation 55 can be used to calculate the confidence interval of the mean (σ_N) based on how many values were used to calculate the mean (N) (Taylor, 1997; Montgomery, 2013). The equation was used to calculate the standard deviation of smoothed kinetic data using $N = 20$. The equation was also used to calculate the standard deviation of the equilibrium measurements. Each data point recorded in the equilibrium experiments represented the average of 256 spectra. Therefore $N = 256$ for the equilibrium measurements. The assumption of normal distribution is proved in Appendix C for data recorded during a MEA calibration experiment.

$$\sigma_N = \frac{\sigma}{\sqrt{N}} \quad (55)$$

4.1.1 Kinetic measurements

Experimental measurements from kinetic experiment 10-25-2 are given in Figures 17 and 18. The CO_2 absorbance is given in Figure 17 and the MEA absorbance is given in Figure 18. The experiment was conducted with 0.147 mol MEA, at a MEA flow rate of 0.00508 mol/s and 25°C. The standard deviation of the measured kinetic data was $3.0\text{x}10^{-4}$ a.u. for CO_2 absorbance and $3.5\text{x}10^{-5}$ for MEA absorbance. The kinetic absorbance measurements were made with the Series module of OMNIC™. Data points were recorded every 0.13 s, ensuring that many data points were recorded in the transient region of the reaction. However, the

small data collection time gave rise to large uncertainty in the measured values, as seen in Figures 17 and 18.

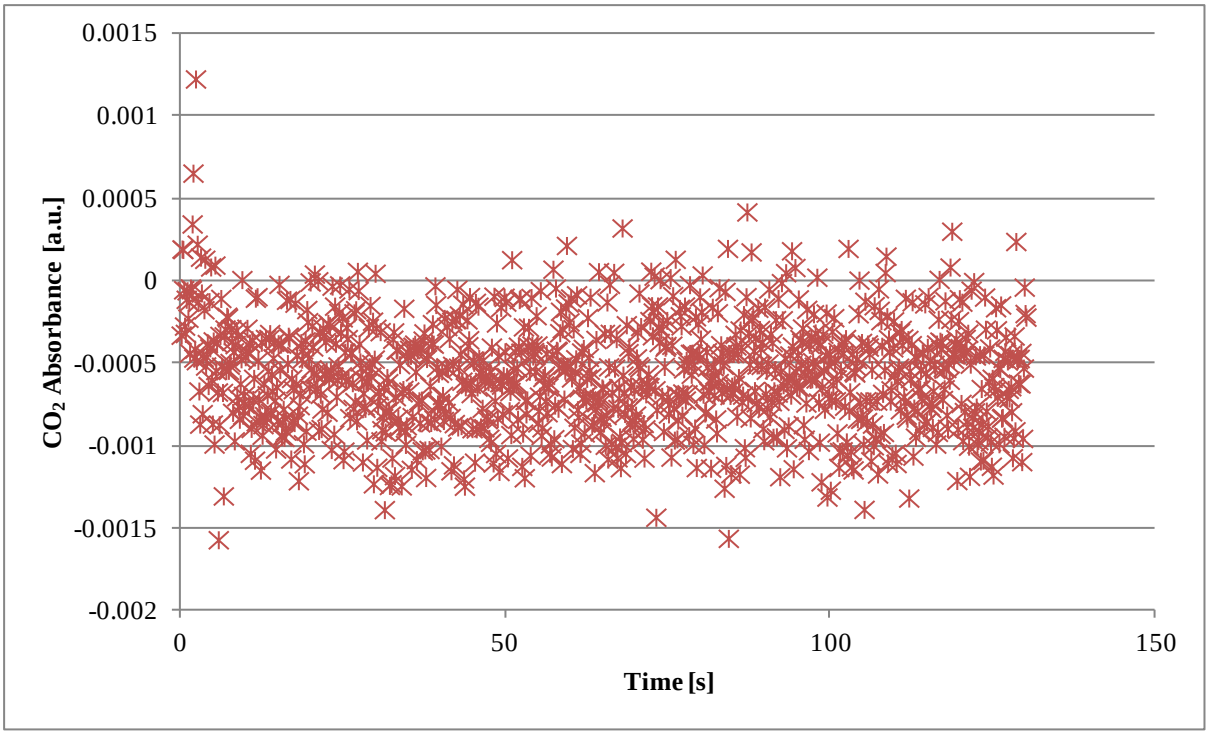

Figure 17 : CO_2 absorbance measured at 2342 cm^{-1} for experiment 10_25_2, conducted with 0.147 mol MEA at 0.00508 mol MEA/s and 25°C

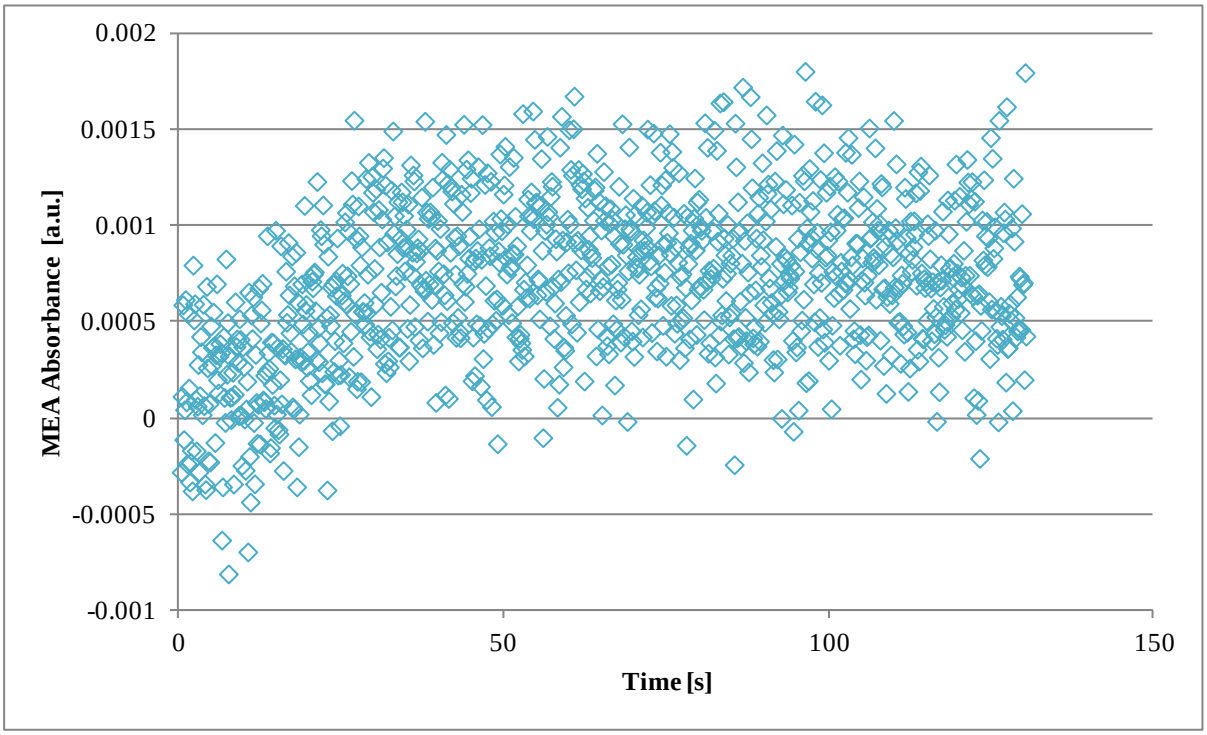

Figure 18 : MEA absorbance measured at 1024 cm^{-1} for experiment 10_25_2, conducted with 0.147 mol MEA at 0.00508 mol MEA/s and 25°C

The standard deviation of the measured absorbance for both CO_2 and MEA were calculated from values recorded over the region 60 to 130 s. The standard deviation was also calculated from measurements made in all kinetic experiments, as well as the calibration experiments. The values calculated for CO_2 and MEA were constant and were found to be independent of temperature as well as the purge gas composition.

Excessive noise such as indicated in the plots in Figures 17 and 18 conceals the trends in the measured species absorbance for the kinetic experiments. For example, although the reaction reaches completion in the region beyond 50 s, the trend in CO_2 absorbance is not clear. The trends in both CO_2 and MEA absorbance could be made clearer by reducing the uncertainty through reducing the noise in the measured data. The noise in the kinetic measurements was reduced by imposing a moving average to smooth the data. Smoothing the data using a moving average reduced the noise while maintaining the time spacing of 0.13 s between data points. Each data point in the smoothed data set was calculated from 20 data points.

For the experimental data shown in Figures 17 and 18, the measured and smoothed data are compared in Figures 19 and 20. From the smoothed profiles, it is easier to see the trends in species absorbance over time. The standard deviation for the smoothed data set is 6.7×10^{-5} a.u. for CO_2 and 7.8×10^{-5} a.u. for MEA. These values of the standard deviation are further discussed with respect to repeatability of measurements in the next section. Further absorbance and concentration profiles from kinetic data reported in this work are based on smoothed data.

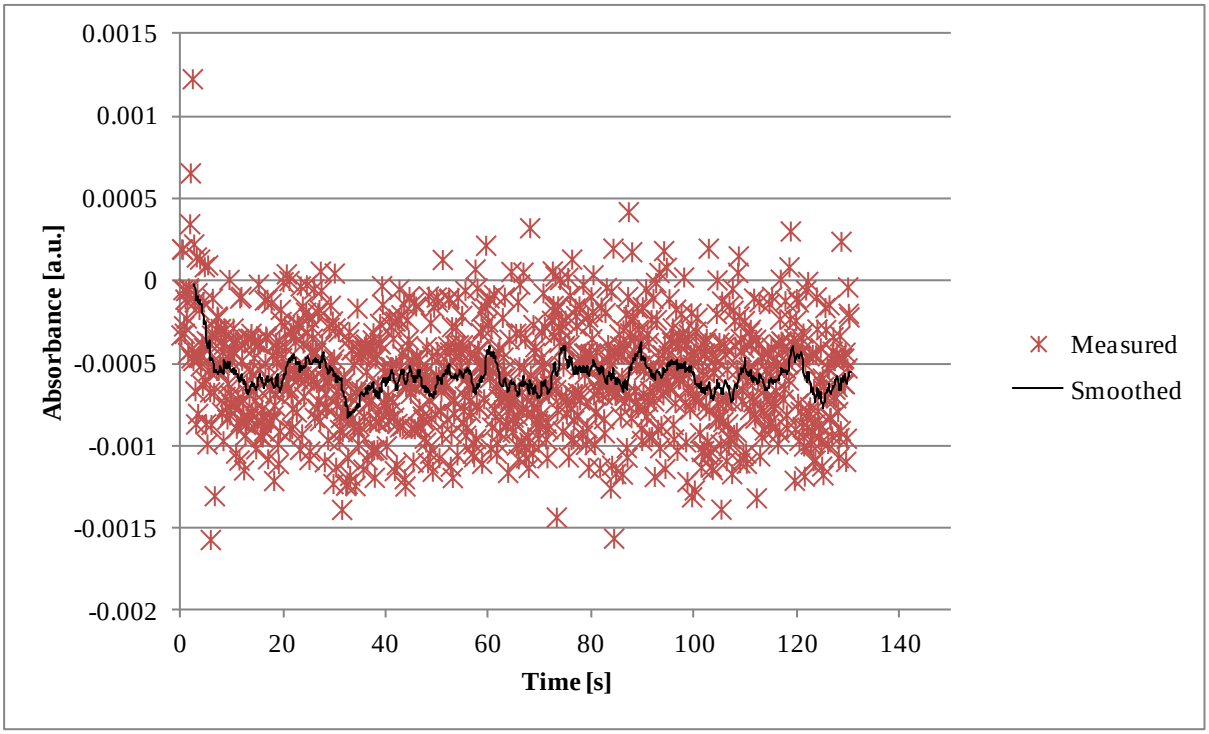

Figure 19 : Measured and smoothed CO_2 absorbance at 2342 cm^{-1} for experiment 10-25-2 conducted with 0.147 mol MEA at 0.00508 mol MEA/s and 25°C

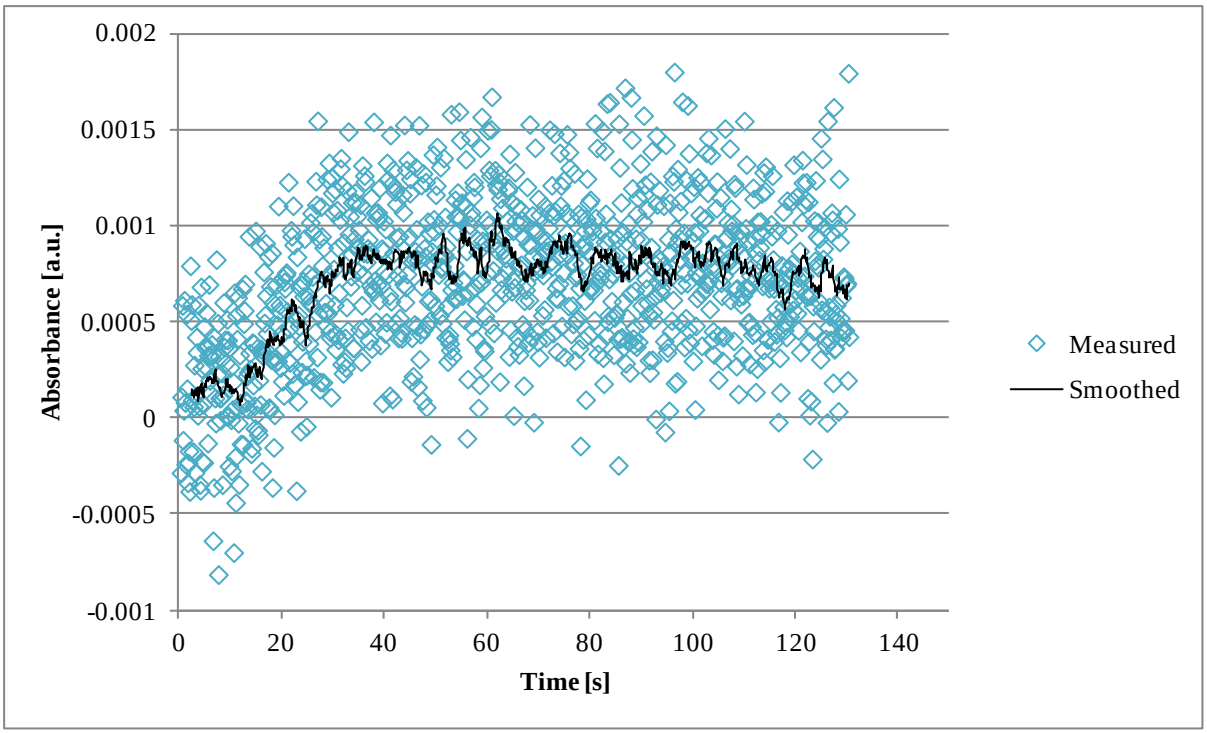

Figure 20 : Measured and smoothed MEA absorbance at 1024 cm^{-1} for experiment 10-25-2 conducted with 0.147 mol MEA at 0.00508 mol MEA/s and 25°C

4.1.2 Equilibrium measurements

Each data point recorded in the equilibrium experiments represented the average of 256 spectra. The standard deviation of the equilibrium absorbance measurements was estimated using Equation 55 with $N = 256$. Using the standard deviation for the kinetic measurements (3.0×10^{-4} a.u. for CO_2 absorbance and 3.5×10^{-5} for MEA absorbance), the standard deviation for the equilibrium measurements was 1.9×10^{-5} a.u. for CO_2 and 2.2×10^{-5} a.u. for MEA. For the product species, the standard deviation was assumed to be the same as the MEA absorbance standard deviation because the standard deviations had similar values for the kinetic experiments.

4.2 Repeatability

Repeatability of the experimental data can be shown by plotting data from several experiments conducted at the same conditions on one graph. When error bars are added to the plotted data points, good repeatability will be indicated when the error bars from different experiments coincide.

4.2.1 Kinetic measurements

For the settings of low MEA concentration and 20°C, data from three experiments are plotted in Figures 21 and 22. Figure 21 shows the measured CO_2 absorbance and Figure 22 the

measured MEA absorbance. Error bars representing 95% confidence intervals are included in both plots. Error bars are included for only one experiment, but both Figures 21 and 22 indicate good repeatability of the absorbance measurements during kinetic experiments.

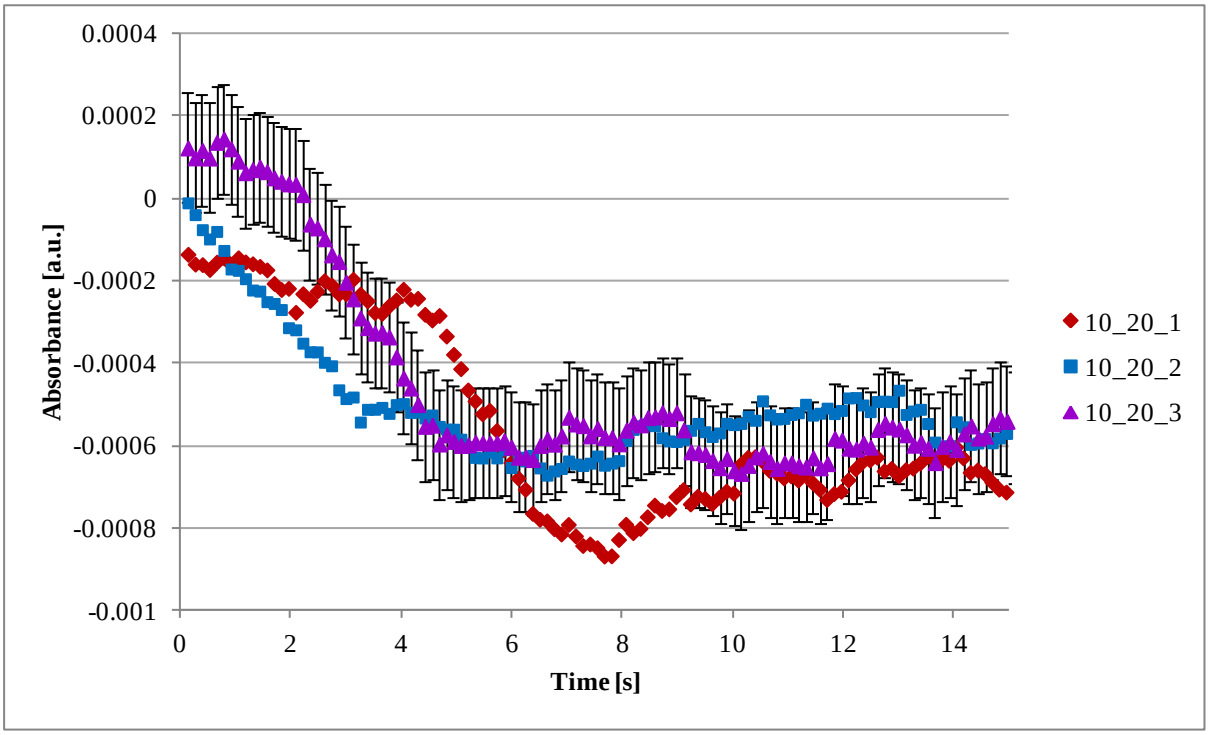

Figure 21 : Repeatability for kinetic experiments: CO_2 absorbance at 2342 cm^{-1} from experiments 10_20_1, 10_20_2 and 10_20_3 (0.13 mol MEA and 20°C)

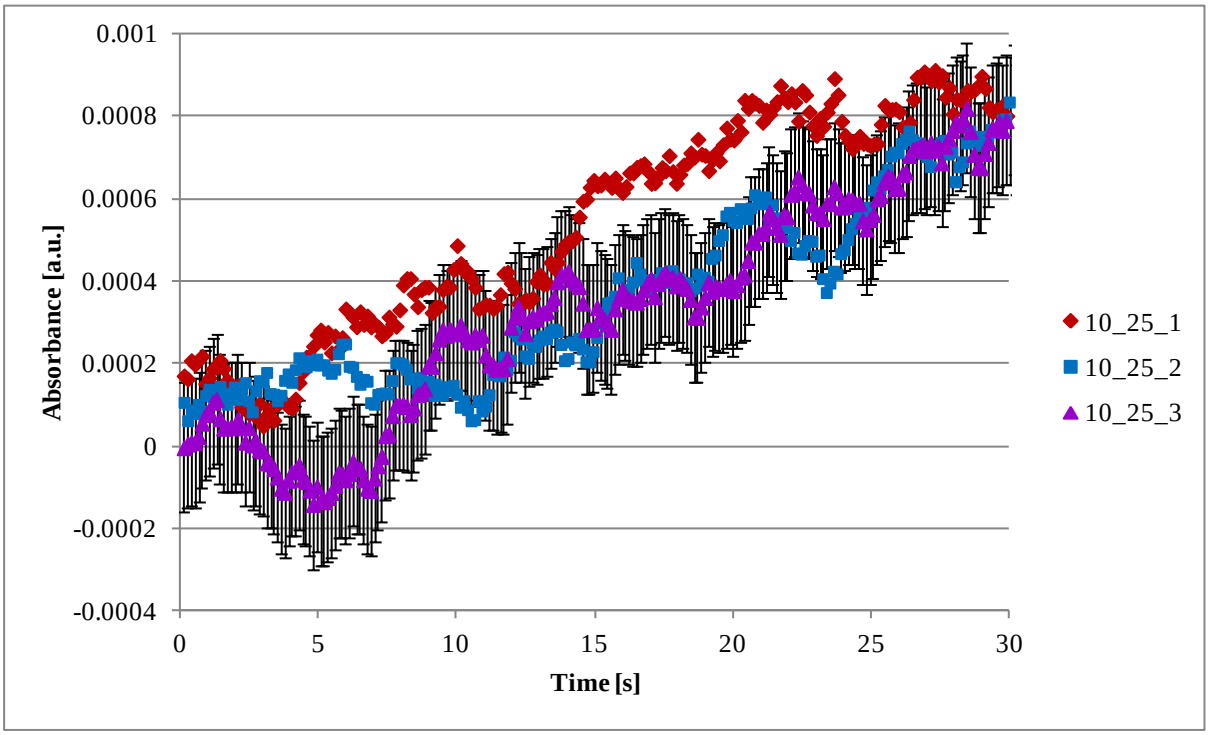

Figure 22 : Repeatability for kinetic experiments: MEA absorbance at 1024 cm^{-1} from experiments 10_20_1, 10_20_2 and 10_20_3 (0.13 mol MEA and 20°C)

4.2.2 Equilibrium measurements

Measured absorbance for three equilibrium experiments is plotted in Figures 23 to 27. In each experiment, CO_2 was added in increments to a solution of MEA at 25°C. CO_2 absorbance is plotted in Figure 23, with error bars indicating 95% confidence intervals included. The CO_2 measurements show good repeatability, with the data points oscillating around zero. Because the data points oscillate around zero, it can be assumed that a negligible amount of unreacted CO_2 remained in solution throughout each experiment. This suggests that all CO_2 was completely consumed up to CO_2 loadings in solution of 0.6 mol CO_2/mol MEA.

MEA absorbance is plotted in Figure 24, with error bars indicated. Carbamate is plotted in Figure 25, HCO_3^- in Figure 26 and protonated MEA in Figure 27. All the species absorbance measurements plotted show good repeatability, and also show trends similar to published species concentration measurements. The measured species concentrations are discussed in Chapter 5.

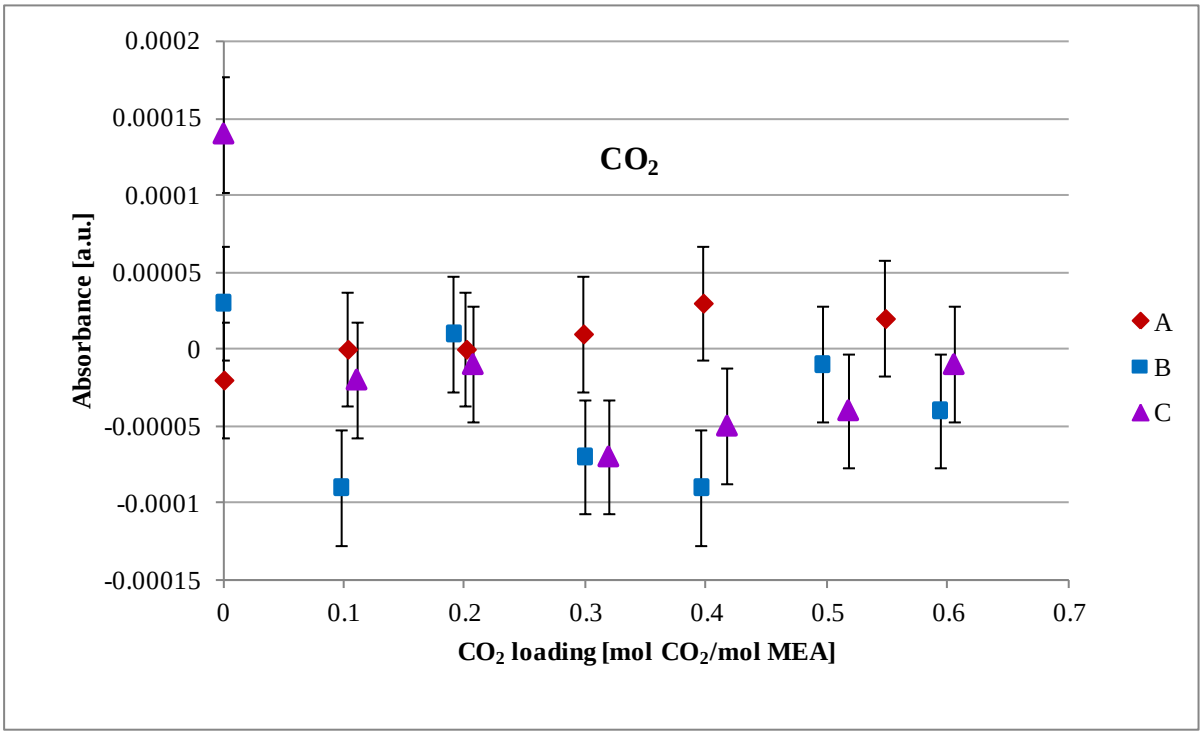

Figure 23 : Repeatability for equilibrium experiments: CO_2 absorbance at 2342 cm^{-1} from experiments 25_A, 25_B and 25_C (0.17 mol MEA and 25°C)

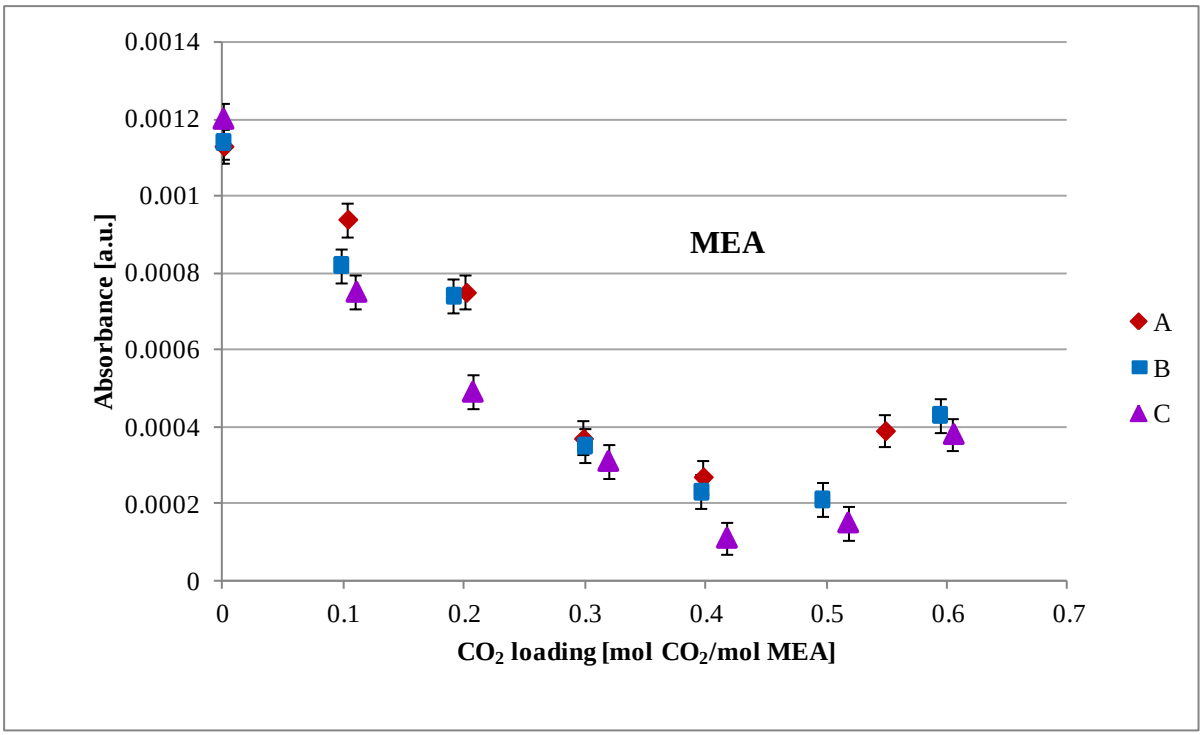

Figure 24 : Repeatability for equilibrium experiments: MEA absorbance at 1024 cm^{-1} from experiments 25_A, 25_B and 25_C (0.17 mol MEA and 25°C)

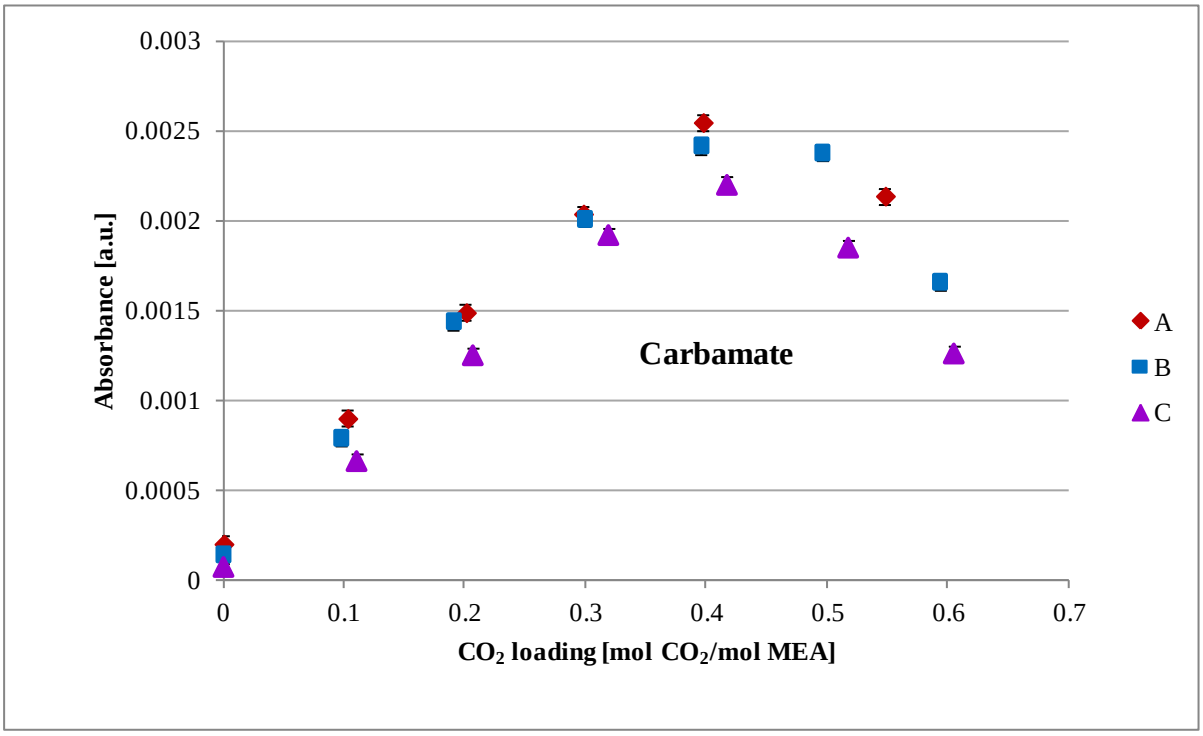

Figure 25 : Repeatability for equilibrium experiments: Carbamate absorbance at 1564 cm^{-1} from experiments 25_A, 25_B and 25_C (0.17 mol MEA and 25°C)

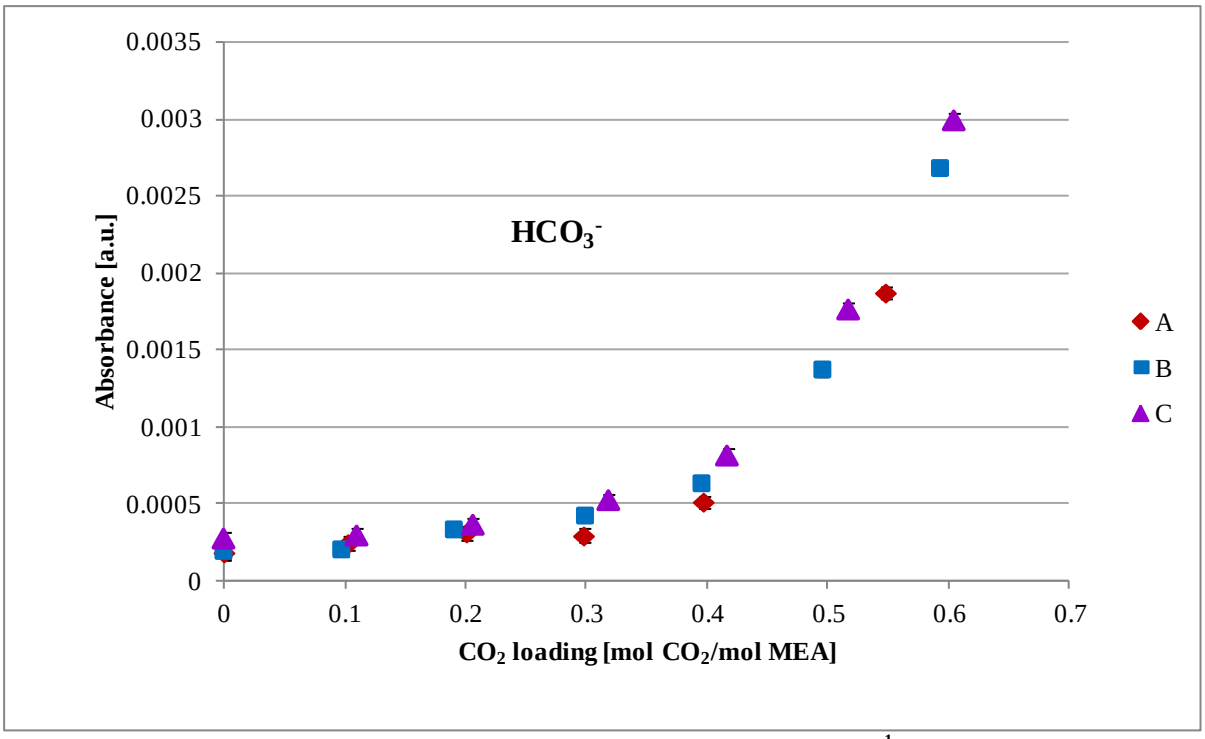

Figure 26 : Repeatability for equilibrium experiments: HCO_3^- absorbance at 1360 cm^{-1} from experiments 25_A, 25_B and 25_C (0.17 mol MEA and 25°C)

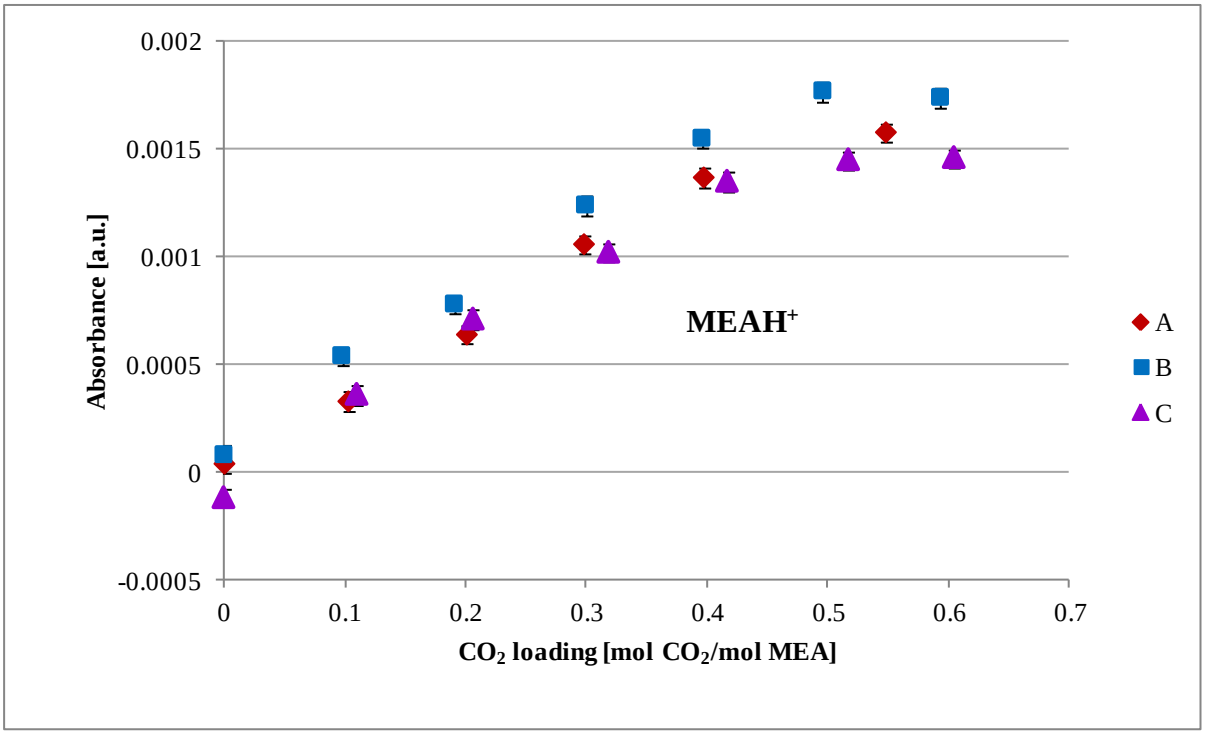

Figure 27 : Repeatability for equilibrium experiments: Protonated MEA absorbance at 1064 cm^{-1} from experiments 25_A, 25_B and 25_C (0.17 mol MEA and 25°C)

4.3 Interference of MEA absorption during kinetic experiments

Two kinetic experiments were conducted to investigate possible interference of MEA absorbance on the absorbance of CO_2 and product species. Interference of MEA absorbance on

product species absorbance has been noted before (du Preez, 2014). In one experiment, MEA solution was pumped into a CO_2 solution. In the other experiment, the MEA solution was pumped into a reactor containing only water. The amount of MEA added to the reactor during the experiments was 0.562 mol for the experiment in which CO_2 was present, and 0.507 mol for the experiment in which CO_2 was not present. In the first experiment, 0.0112 mol CO_2 was used, giving a MEA: CO_2 ratio of 50. The high MEA: CO_2 ratio is much greater than the theoretical reaction stoichiometric ratio of 2, and thus ensured essentially complete reaction of CO_2.

During both experiments, the absorbance of the reagent species, CO_2 (2342 cm^{-1}), MEA (1024 cm^{-1}), and the product species, carbamate (1564 cm^{-1}), HCO_3^- (1360 cm^{-1}) and protonated MEA (1064 cm^{-1}), were measured. The measured absorbances are shown in Figures 28 and 29. Figure 28 shows the data from the experiment where CO_2 was present, and Figure 29 shows the data from the experiment where CO_2 was not present.

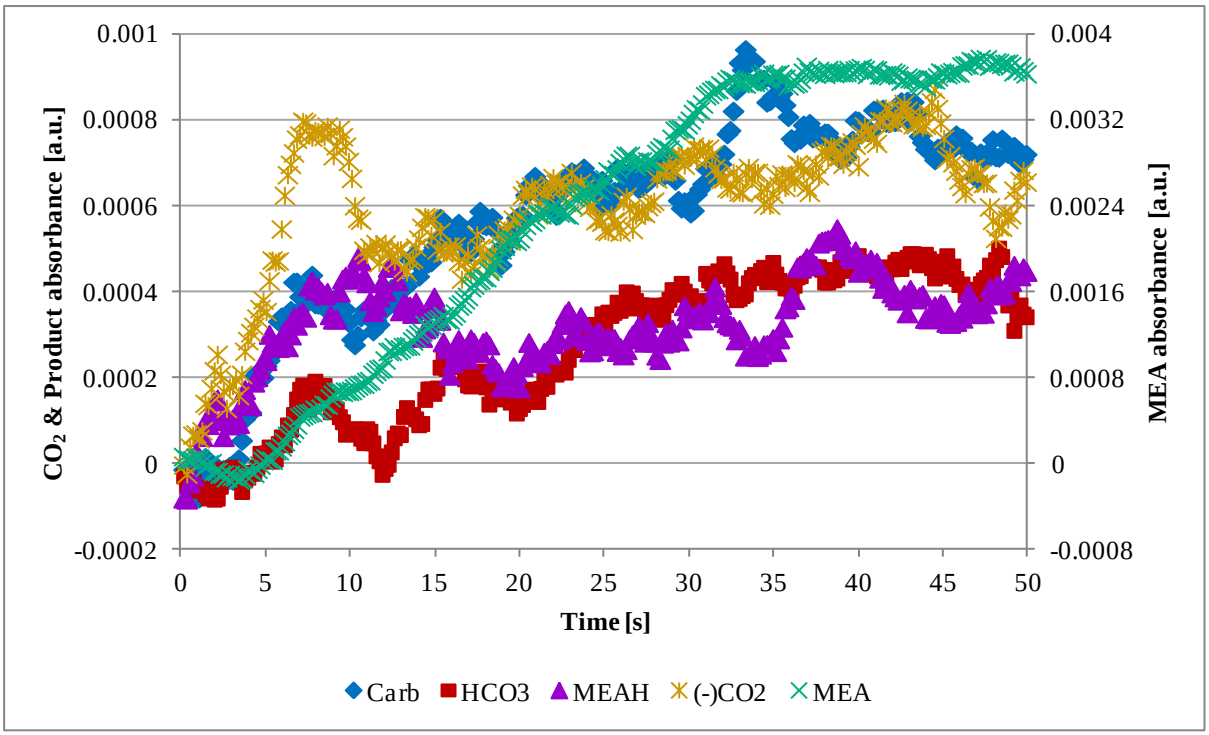

Figure 28 : Measured product and reagent species absorbance for carbamate (1564 cm^{-1}), HCO_3^- (1360 cm^{-1}) protonated MEA (1064 cm^{-1}), CO_2 (2342 cm^{-1}) and MEA (1024 cm^{-1}); the experiment was conducted with 0.562 mol MEA and 0.0112 mol CO_2 at 0.0192 mol MEA/s and 25°C

Because CO_2 is a reagent, it is consumed during the reaction. Its absorbance would therefore decrease. Product species absorbances are expected to increase as the concentrations of the respective products increases. In Figure 28, the CO_2 absorbance was inverted to facilitate comparison of the rate of CO_2 consumption and the rate of product species formation. MEA solution was added to the reactor from 0 s. The inverted CO_2 absorbance shows a rapid increase during the first 10 s, and thereafter oscillates around 0.0006 a.u. The rapid increase indicates that the CO_2 was quickly consumed once MEA entered the reactor. The CO_2 was completely consumed after 10 s.

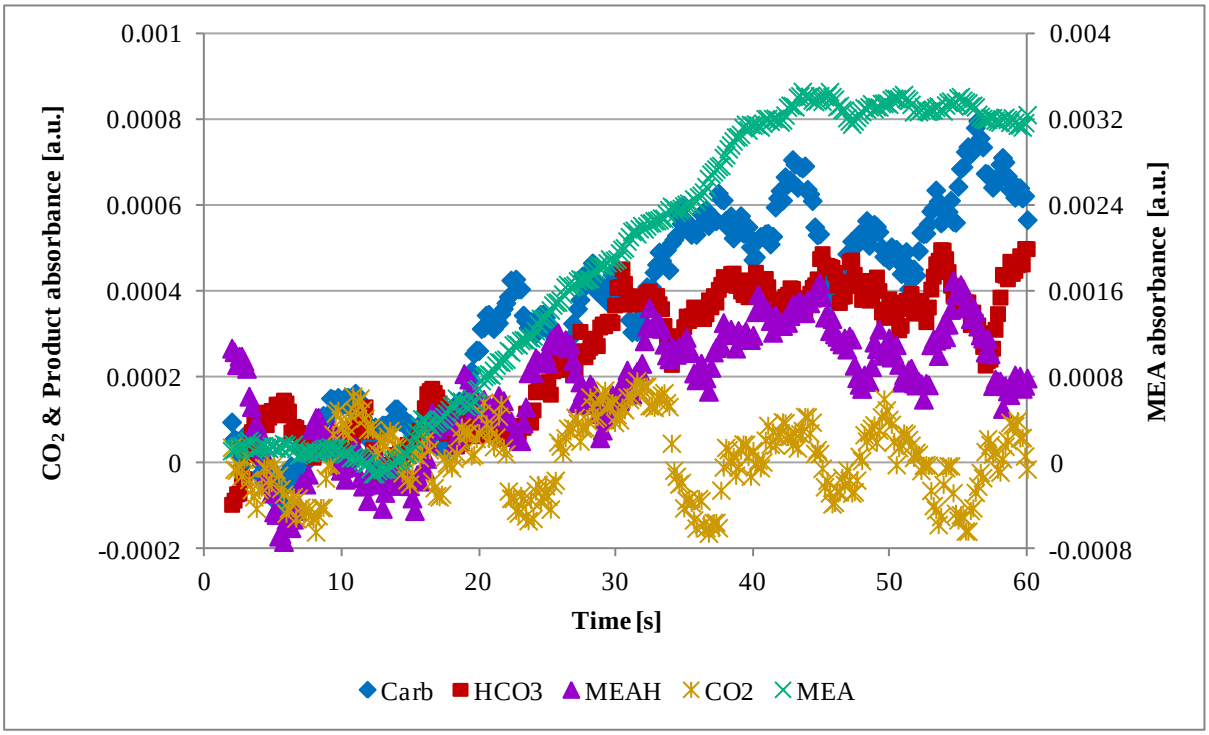

Figure 29 : Measured product and reagent species absorbance for carbamate (1564 cm^{-1}), HCO_3^- (1360 cm^{-1}) protonated MEA (1064 cm^{-1}), CO_2 (2342 cm^{-1}) and MEA (1024 cm^{-1}); the experiment was conducted with 0.507 mol MEA and no CO_2 at 0.0171 mol MEA/s and 25°C

Carbamate and protonated MEA absorbance also show a rapid increase during the first 10 s of adding MEA to the reactor. The slopes of the two species absorbance are similar, and are proportional to the slope of the negative CO_2 absorbance. The HCO_3^- absorbance does not show a similar rapid increase that is distinguishable from the experimental noise. This suggests that for the first 10 s of adding MEA to the reactor, CO_2 and MEA rapidly reacted to form carbamate and protonated MEA. This is consistent with a carbamate formation mechanism were MEA acts as the proton-accepting base. Beyond 10 s, carbamate and HCO_3^- absorbance continue increasing as the amount of MEA in solution increases.

Figure 29 shows the reagent and product species absorbance when no CO_2 was present in solution. As expected, the CO_2 absorbance oscillates around zero, indicating that no CO_2 is consumed as the amount of MEA in solution increases. However, carbamate, HCO_3^- and protonated MEA absorbance all increase as the amount of MEA increases. The increase in the product species absorbance is proportional to the increase in MEA absorbance. The protonated MEA absorbance is likely a result of protonated MEA forming from the dissolution of MEA in water.

Both carbamate and HCO_3^- can form only in the presence of CO_2 or another CO_2-containing species. However, the carbamate and HCO_3^- absorbance increased in the absence of CO_2, indicating formation of both carbamate and HCO_3^-. Since the product species absorbances increased at a rate proportional to the rate of increase of the MEA absorbance, the measured absorbances suggest MEA absorbance does interfere with carbamate and HCO_3^- absorbance.

MEA interference would also explain the increase in carbamate and HCO_3^- absorbance beyond 10 s in Figure 28.

Protonated MEA formed in both experiments due to the CO_2-MEA reaction as well as protonation of MEA from dissolving in water. The difference between the amounts of $MEAH^+$ formed in the two experiments is insignificant. Therefore, both CO_2-containing product species and protonated MEA could not be measured accurately during kinetic experiments.

4.4 Interference in CO_3^{2-} absorption during equilibrium experiments

CO_3^{2-} absorbs IR radiation at 1389 and 1431 cm^{-1}, and HCO_3^- absorbs at 1360 cm^{-1}. The corresponding absorption bands are indicated in Figure 30 below. Figure 30 gives sample spectra recorded in a solution of MEA in water with different amounts of dissolved CO_2. The CO_2 was added to the MEA solution in increments of approximately 0.1 mol CO_2/mol MEA. As the amount of dissolved CO_2 increased, the absorption band of HCO_3^- initially showed little activity. However, at CO_2 to MEA molar ratios of 0.394 to 0.590 mol CO_2/mol MEA, the HCO_3^- band grew and overlapped the CO_3^{2-} band at 1389 cm^{-1}. This gave inaccuracies when monitoring the amount of CO_3^{2-} in solution at 1389 cm^{-1}. Therefore, the CO_3^{2-} band at 1389 cm^{-1} was unsuitable for quantitative monitoring of the amount of CO_3^{2-} in solution. A similar result was found in all experiments where CO_2 was dissolved in MEA solutions.

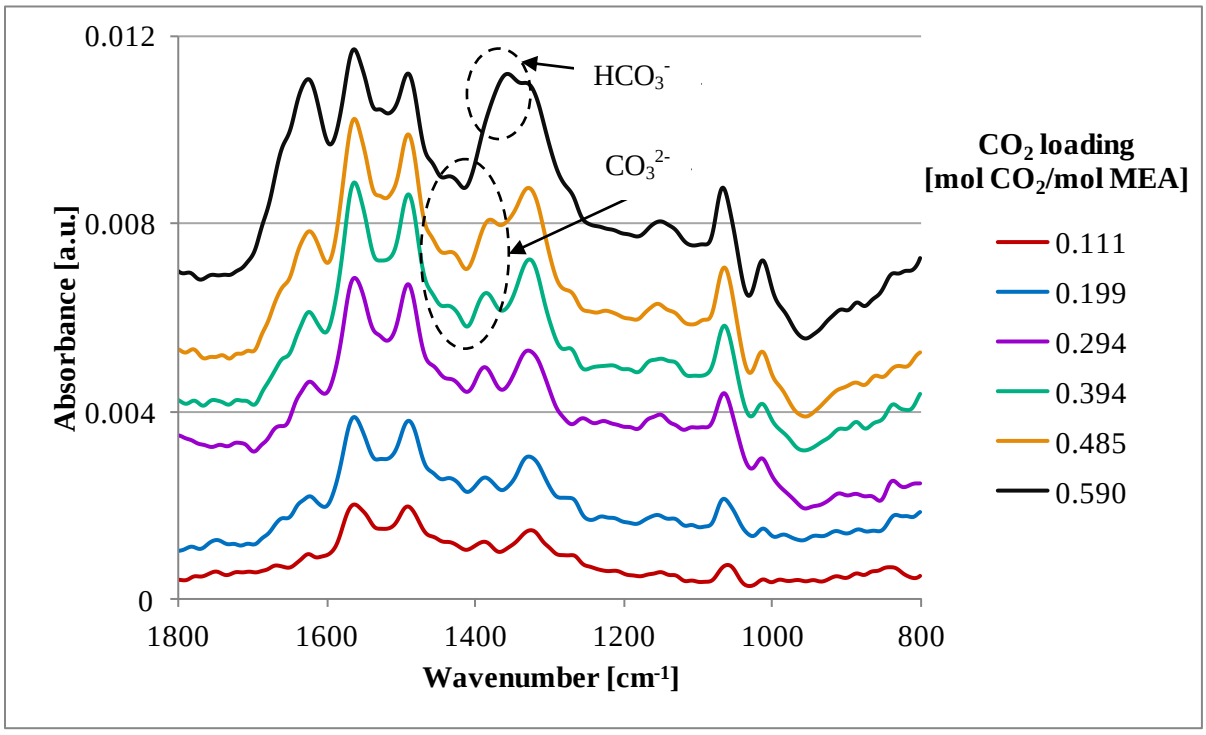

Figure 30 : HCO_3^--CO_3^{2-} overlap in sample spectra recorded at equilibrium – various amounts of CO_2 dissolved in 0.338 mol MEA/L at 25°C; sample spectra were processed with a baseline spectrum of water containing MEA

The CO_3^{2-} absorption band at 1431 cm^{-1} was not overlapped by other species' absorption bands. The peak height at 1431 cm^{-1} (baseline at 1446.350; 1415.495) was recorded during

three experiments conducted with 10 g MEA at 25°C. The peak heights are plotted in Figure 31 with error bars indicating 95% confidence intervals included. The plotted absorbances suggest that the concentration of CO_3^{2-} in solution initially increases from 0 mol CO_2/mol MEA, and then decreases from 0.4 mol CO_2/mol MEA. However, the CO_3^{2-} absorbances showed the same trend that was observed for carbamate absorbances. The CO_3^{2-} and carbamate absorbances are plotted together in Figure 32. Carbamate absorbance was recorded at 1564 cm^{-1}, with a baseline between 1652.696 and 1523.489 cm^{-1}.

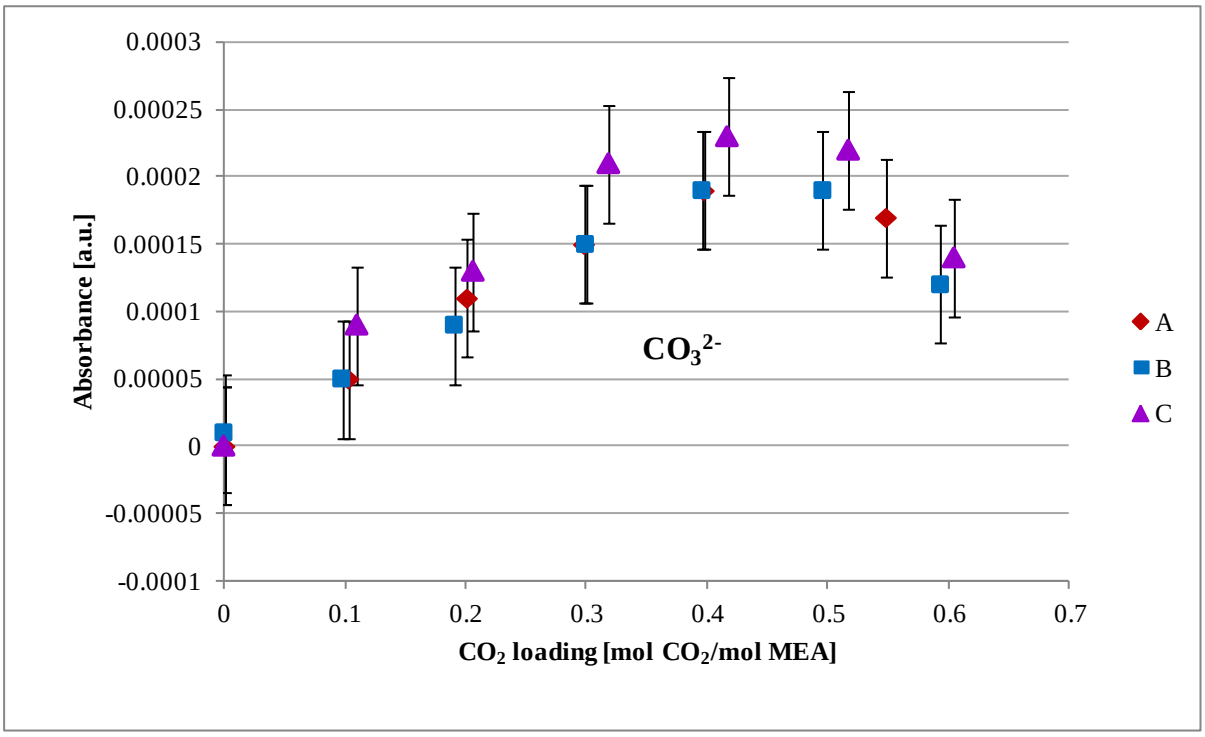

Figure 31 : CO_3^{2-} absorbance at 1431 cm^{-1} recorded during equilibrium experiments 25_A, 25_B and 25_C (0.17 mol MEA and 25°C)

The values of the data points plotted in Figure 32 indicate that the CO_3^{2-} absorbance is equal to approximately a tenth of the carbamate absorbance. This suggests that the absorbance measured at 1431 cm^{-1} is due to interference from carbamate absorbance. Other researchers who have monitored chemical species in aqueous CO_2-MEA mixtures report negligible CO_3^{2-} formation (Jakobsen *et al*., 2005; Böttinger *et al*., 2008; Richner & Puxty, 2012). Therefore, it is reasonable to assume negligible formation of CO_3^{2-} in the reaction mixtures, so that the assumption of carbamate interference at 1431 cm^{-1} is valid. The equilibrium experimental results reported in the next chapter do not include CO_3^{2-} absorbance.

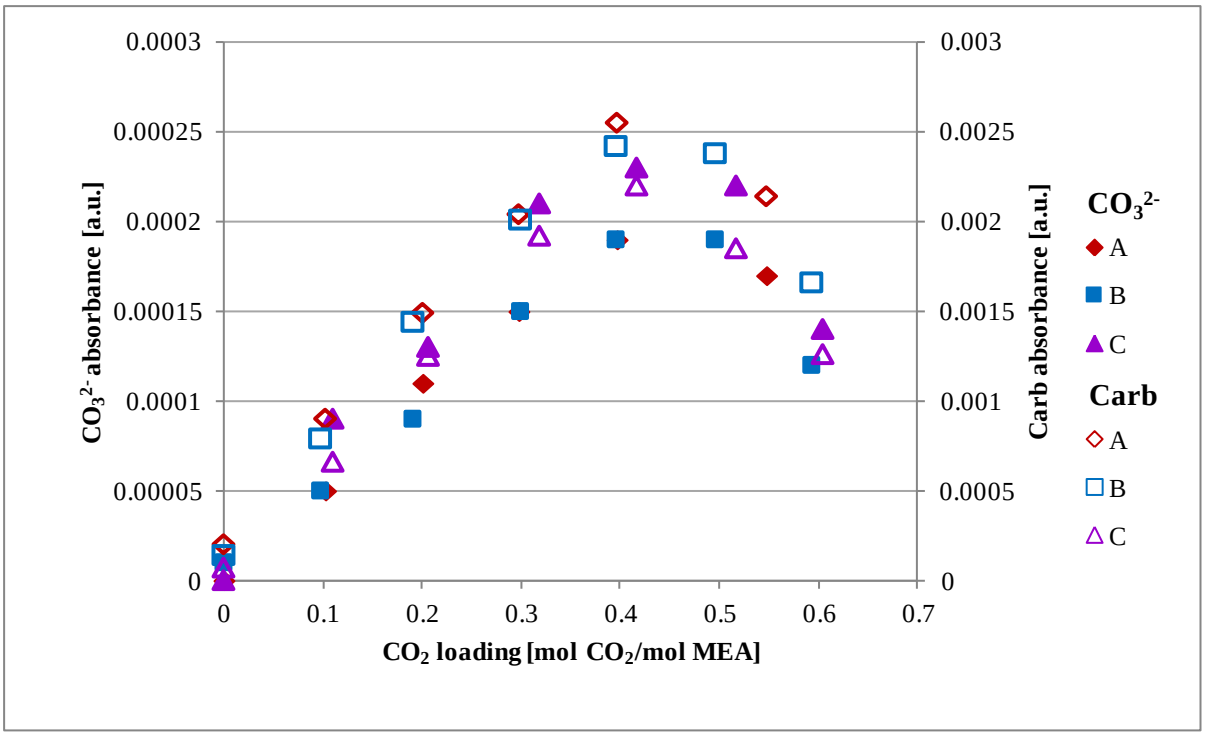

Figure 32 : CO_3^{2-} absorbance at 1431 cm^{-1} and carbamate absorbance at 1564 cm^{-1} recorded during equilibrium experiments 25_A, 25_B and 25_C (0.17 mol MEA and 25°C)

5. Equilibrium experimental results

In this chapter the wavenumbers at which species were monitored are presented. The absorbance measurements made during equilibrium experiments are also presented, followed by implicit calibration calculations that were used to generate species concentration. Plots of the species concentrations against the CO_2 loading in solution are discussed and compared to literature data. Measurements in this work were made at low MEA concentrations, whereas literature data are based on high MEA concentration solutions. Agreement between the low and high MEA concentration measurements indicated the same reaction mechanism at both conditions. The mass of reagents used in the experiments are given in Appendix D.

5.1 Species identification

Portions of the sample spectra showing the CO_2 and MEA absorbance bands are given in Figures 33 and 34, respectively. The two spectra in the figures, "CO_2 only" and "MEA added", were recorded from solutions of CO_2 in water and CO_2 and MEA in water, respectively. "CO_2 only" is a sample spectrum of a CO_2-water solution, processed with a background spectrum of water. "MEA added" is a sample spectrum recorded once MEA had been added to the CO_2 solution. The background spectrum used to process the "MEA added" sample spectrum was of the CO_2 solution. The CO_2 peak in this spectrum appears as an inverted peak, indicating a decrease in the CO_2 concentration in solution. The spectra were recorded during a CO_2 calibration experiment at 25°C. Three MEA absorption bands monitored are indicated in Figure 34. The bands appeared at 1074, 1024 and 966 cm^{-1}.

Product species in the aqueous CO_2-MEA reaction mixture were identified by gradually adding CO_2 to a solution of MEA. The sample spectra of these solutions at equilibrium were recorded. A background spectrum of the MEA solution was used to process sample spectra, and also reduce the interference of MEA absorption on protonated MEA absorption. Examples of the sample spectra between 1800-800 cm^{-1} are shown in Figure 35. The product absorption bands in the figure are at 1564, 1493, 1431, 1389, 1360, 1329, 1064 and 1014 cm^{-1}.

The assignment of absorption bands to chemical species is given in Table 8, where the wavenumbers found in this work are compared to published literature values. The values determined in this work are in agreement with the literature values.

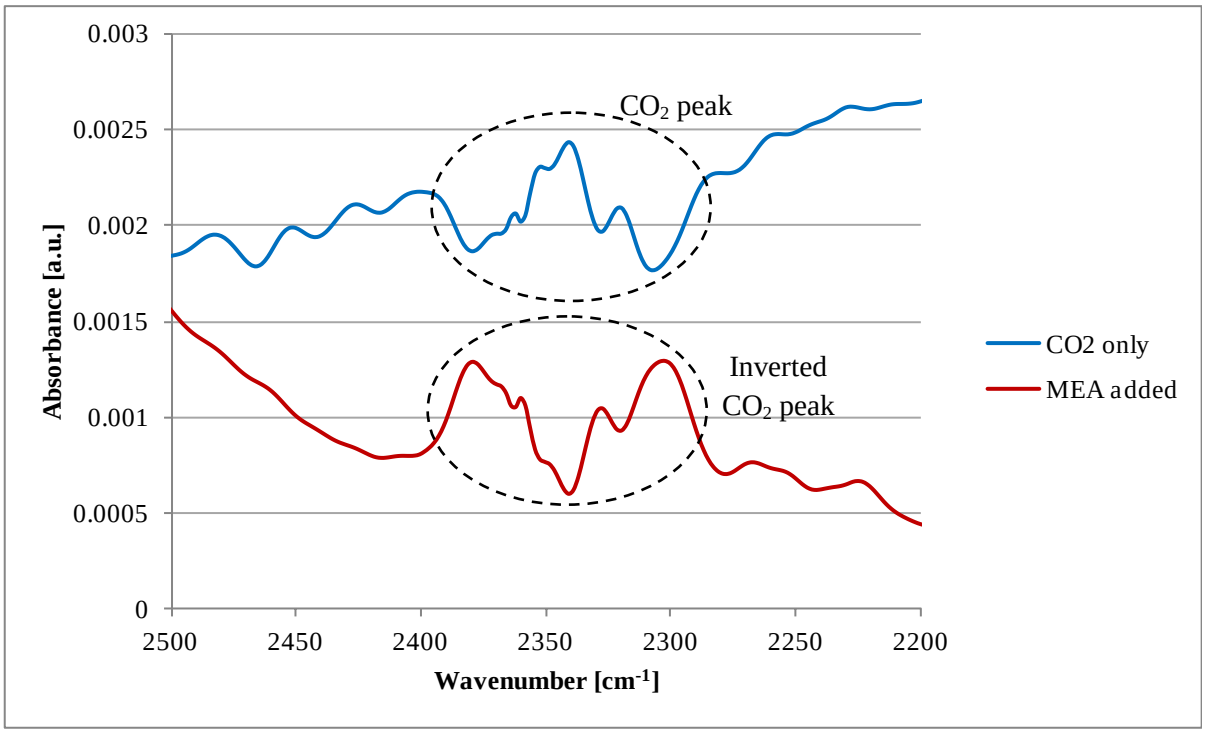

Figure 33 : CO_2 absorbance bands: "CO_2 only" is from a sample spectrum of a CO_2 solution processed with a water background spectrum; "MEA added" is from a sample spectrum of excess MEA added to a CO_2 solution, processed with a CO_2 solution background spectrum

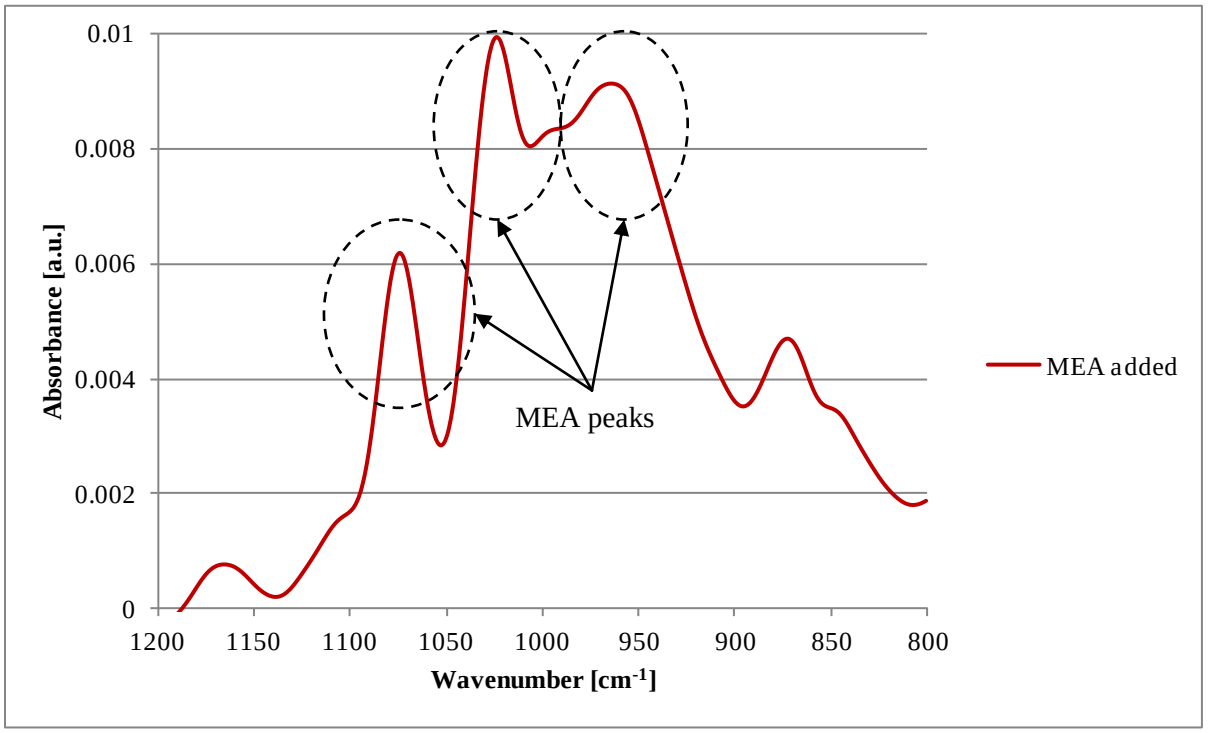

Figure 34 : MEA absorbance bands; sample spectrum was processed with a CO_2 solution background

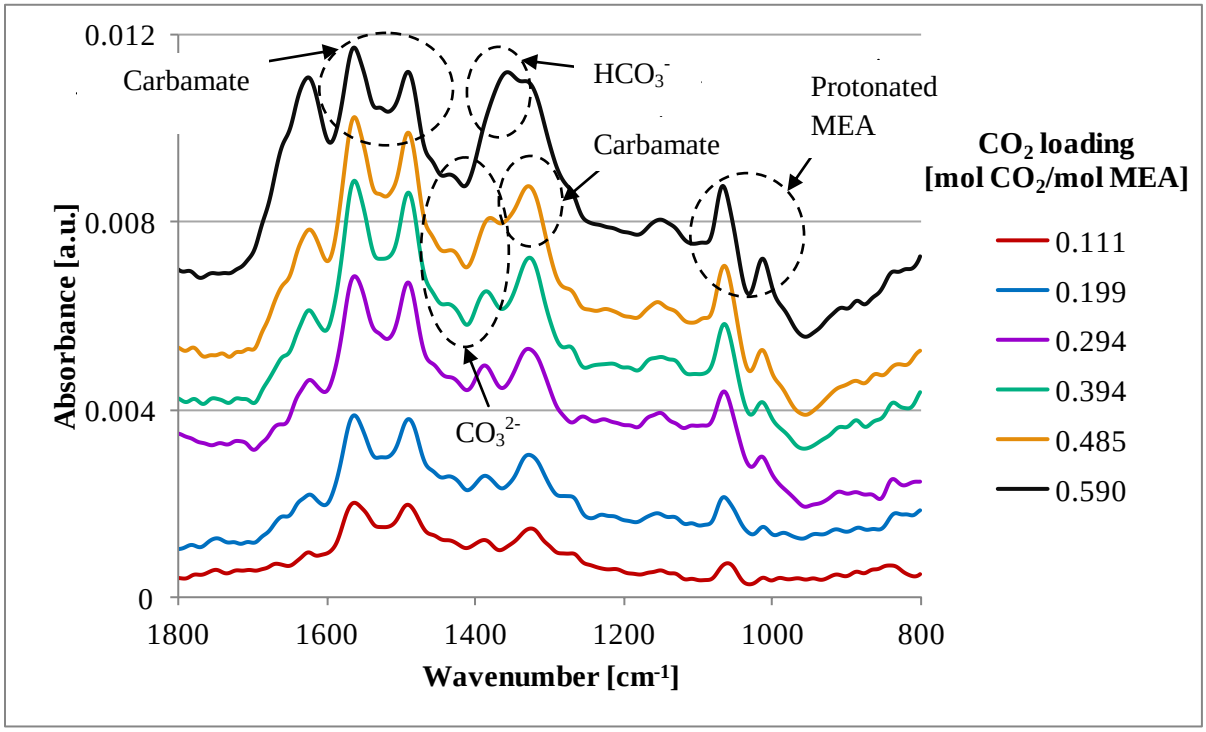

Figure 35 : Equilibrium species identification – various amounts of CO_2 dissolved in 0.338 mol MEA/L at 25°C; sample spectra were processed with a baseline spectrum of water containing MEA

Table 8 : Assignment of infrared absorption wavenumbers (in cm^{-1}) of chemical species in the reaction mixture

Species	Vibration	This work	Literature	References
CO_2	C-O asymmetric stretch	2342	2349	Nakamoto (1986); Aruldhas (2001)
			2342.9	Falk & Miller (1992)
			2342	Diab *et al.* (2012)
			2343	Richner & Puxty (2012)
MEA	C-N-H out-of-plane wag and C-NH_2 twist	966	955	Richner & Puxty (2012)
	C-O stretch	1024	1024	Richner & Puxty (2012)
	C-N stretch	1074	1076	Richner & Puxty (2012)
Carbamate	N-COO stretch	1329	1322	Jackson *et al.* (2009); Richner & Puxty (2012)
	COO symmetric stretch	1493	1486*	Richner & Puxty (2012)
	COO asymmetric stretch	1564	1568*	Richner & Puxty (2012)
HCO_3^-	-CO_2 symmetric stretch	1360	1355	Davis & Oliver (1972); Nakamoto (1986)
			1360	Falk & Miller (1992); Jackson *et al.* (2009); Diab *et al.* (2012); Richner & Puxty (2012)
$MEAH^+$	C-O stretch	1014	1013	Richner & Puxty (2012)
	C-N stretch	1064	1069	Richner & Puxty (2012)
CO_3^{2-}		1431	1430	Socrates (1994)
	asymmetric stretch	1389	1385	Falk & Miller (1992)
			1388	Richner & Puxty (2012)

* Ma *et al.* (2014) assign COO symmetric and asymmetric stretches to 1568 and 1486 cm^{-1}, respectively.

One wavenumber was chosen for monitoring each chemical species. The wavenumbers chosen for each species are given in Table 9 with the corresponding absorption band baseline positions. MEA was monitored at 1024 cm^{-1}, carbamate at 1564 cm^{-1} and protonated MEA at 1064 cm^{-1} because these wavenumbers showed greater peak activity than the other wavenumbers at which the species absorbed radiation. CO_3^{2-} was not monitored due to interference by carbamate and HCO_3^- absorption at 1431 cm^{-1} and 1389 cm^{-1}(Section 4.4).

Table 9 : Position of chemical species absorption bands chosen for monitoring reaction

Molecule	Wavenumber [cm^{-1}]	Baseline [cm^{-1}]
CO_2	2342	2379.728; 2304.518
MEA	1024	1051.014; 900.594
$Carbamate^-$	1564	1652.696; 1523.489
HCO_3^-	1360	1413.566; 1195.649
$MEAH^+$	1064	1103.083; 997.017

5.2 Species absorbance-CO_2 loading profiles

In each equilibrium experiment, approximately 10 g MEA was loaded into a reactor containing 0.5 L water. CO_2 was then added to the MEA solution in increments of known CO_2 loading. Sample spectra of the CO_2-MEA reaction mixture were recorded at the various CO_2 loadings. The peak heights of MEA and three reaction products (carbamate, HCO_3^- and $MEAH^+$) were plotted against the CO_2 loading of the solution. These plots are given in Figures 36 to 40 for 0.33 mol/L MEA at 20-30°C. CO_2 is not plotted in the figures because of negligible measured absorbance (Section 4.2.2).

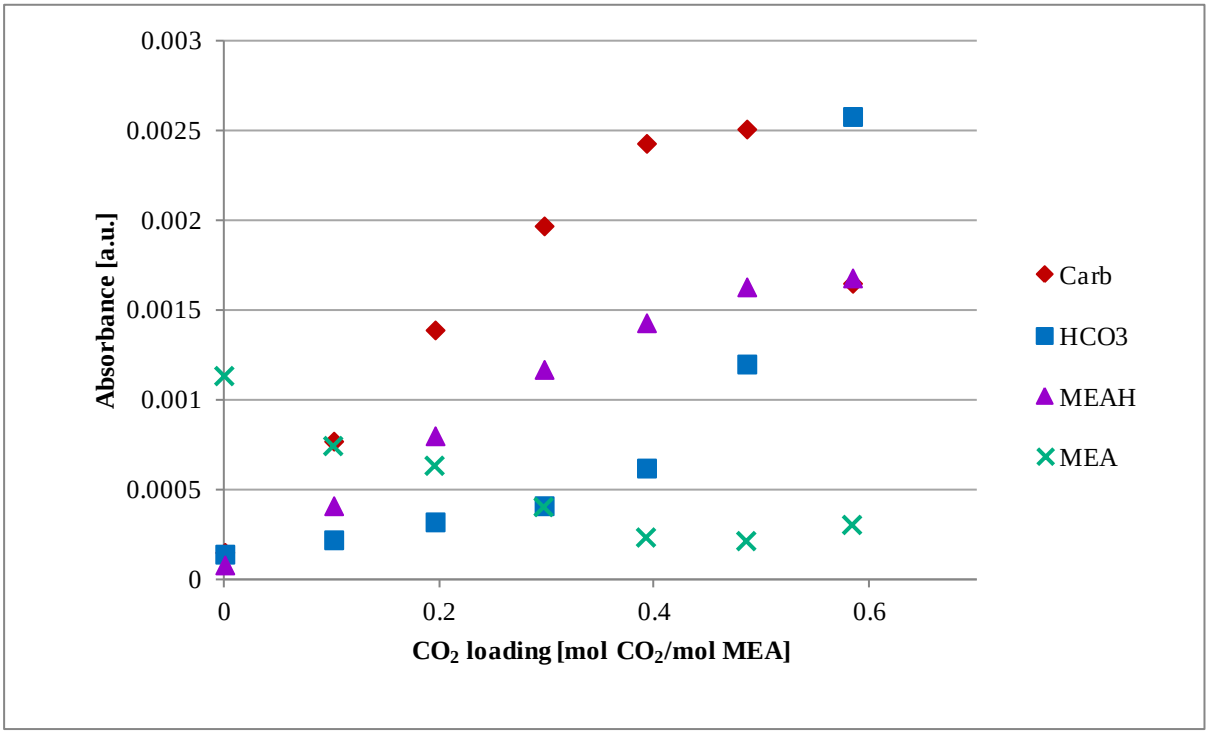

Figure 36 : Species absorbance as a function of CO_2 loading for 0.337 mol MEA/L at 20°C

During the kinetic experiments the absorbances recorded at 1564 (carbamate) and 1360 cm^{-1} (HCO_3^-) were a result of interference from MEA absorption (Section 4.3). In the equilibrium experiments the absorbances measured at these wavenumbers were due to the presence of actual product species due to two reasons. The first is that the absorbance at 1564 (carbamate), 1360 (HCO_3^-) and 1064 cm^{-1} ($MEAH^+$) have different trends over the range of CO_2 loading considered. If the absorbances measured at these wavenumbers were a result of interference from reagent species, the data plotted in Figures 36 and 40 would likely show similar trends as CO_2 loadings increases. This was the result found for kinetic measurements, where carbamate, HCO_3^- and $MEAH^+$ absorbance increased proportionally to the MEA absorbance. For the equilibrium measurements, absorption peak activity for the three product species is unique for each species, pointing to each species' unique involvement in the reaction at different CO_2 loadings.

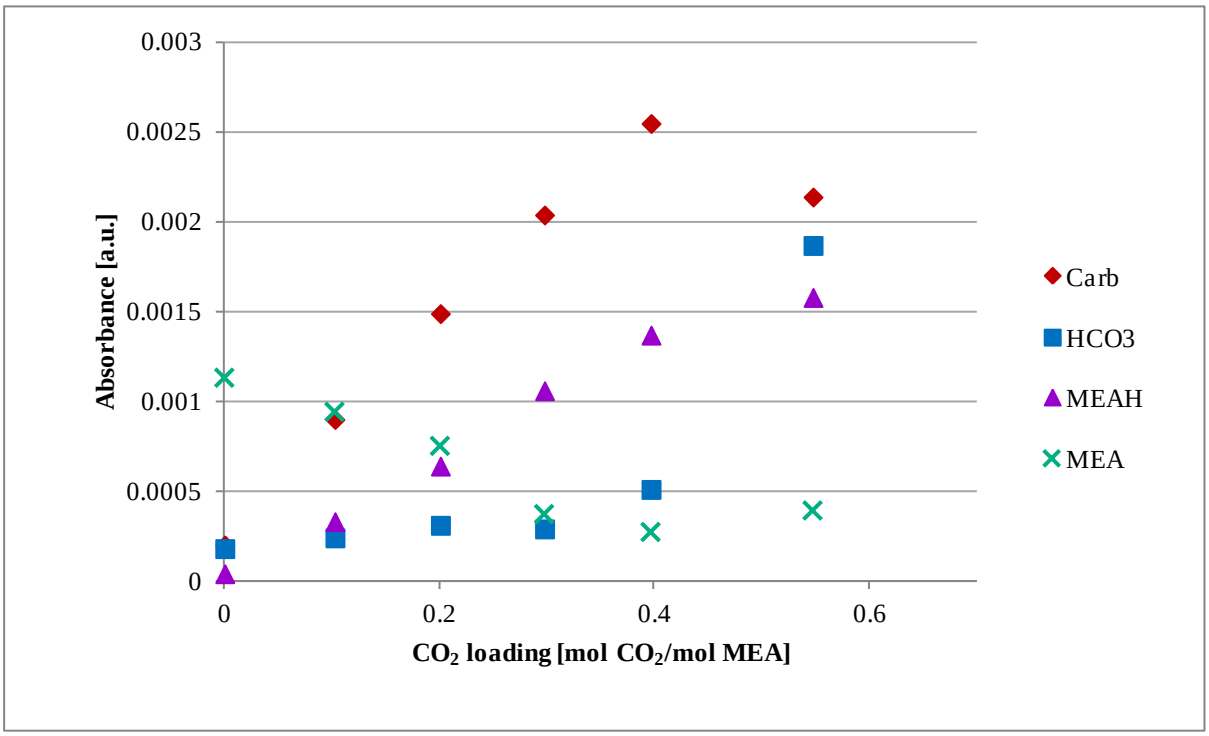

Figure 37 : Species absorbance as a function of CO_2 loading for 0.326 mol MEA/L at 25°C (25_A)

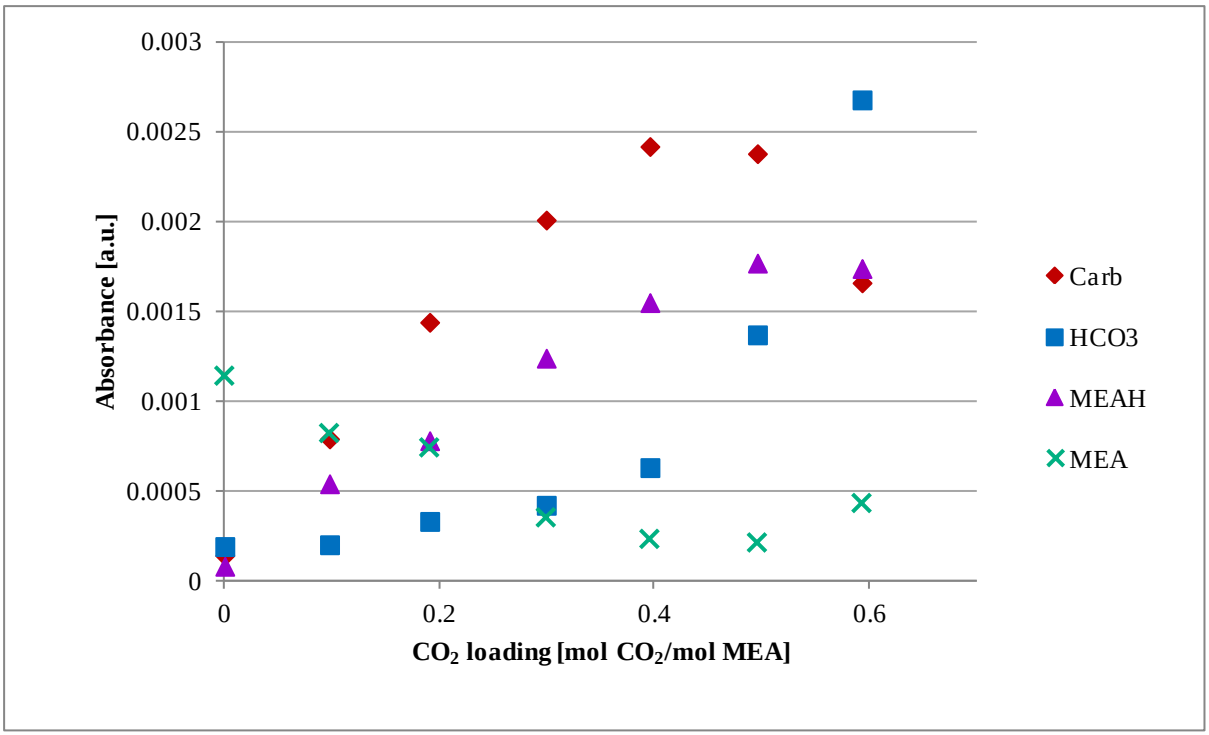

Figure 38 : Species absorbance as a function of CO_2 loading for 0.340 mol MEA/L at 25°C (25_B)

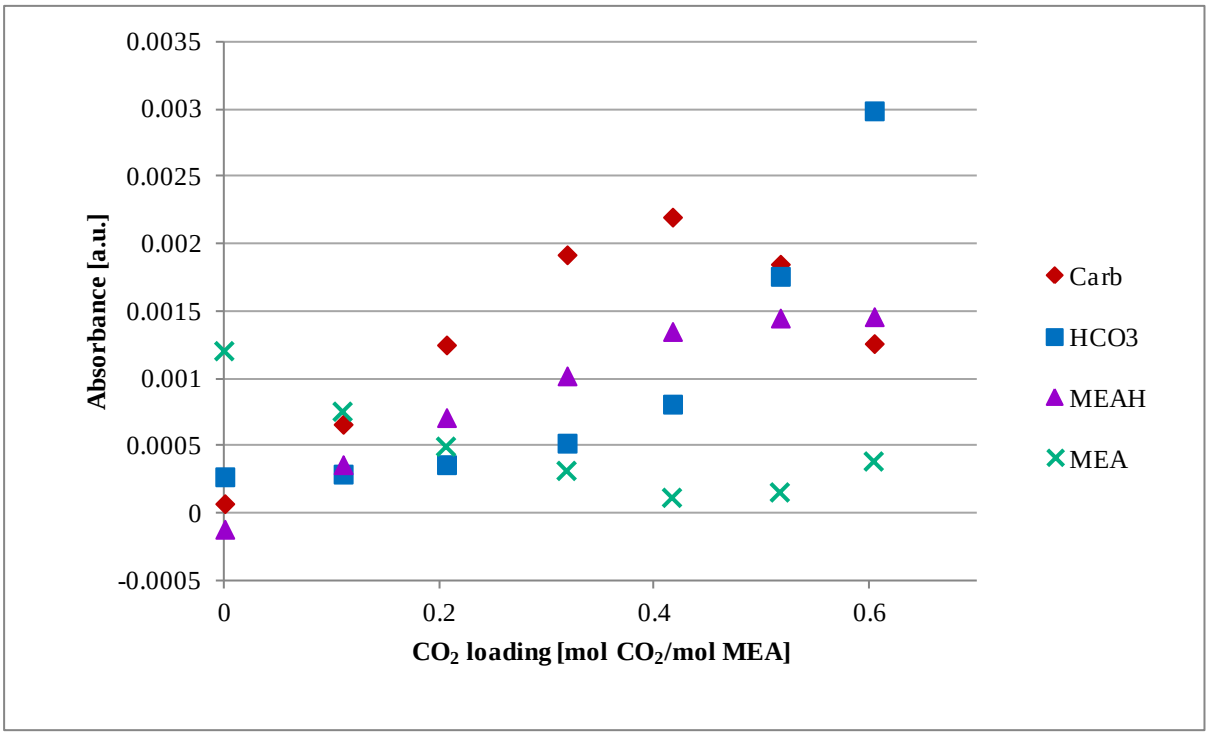

Figure 39 : Species absorbance as a function of CO_2 loading for 0.323 mol MEA/L at 25°C (25_C)

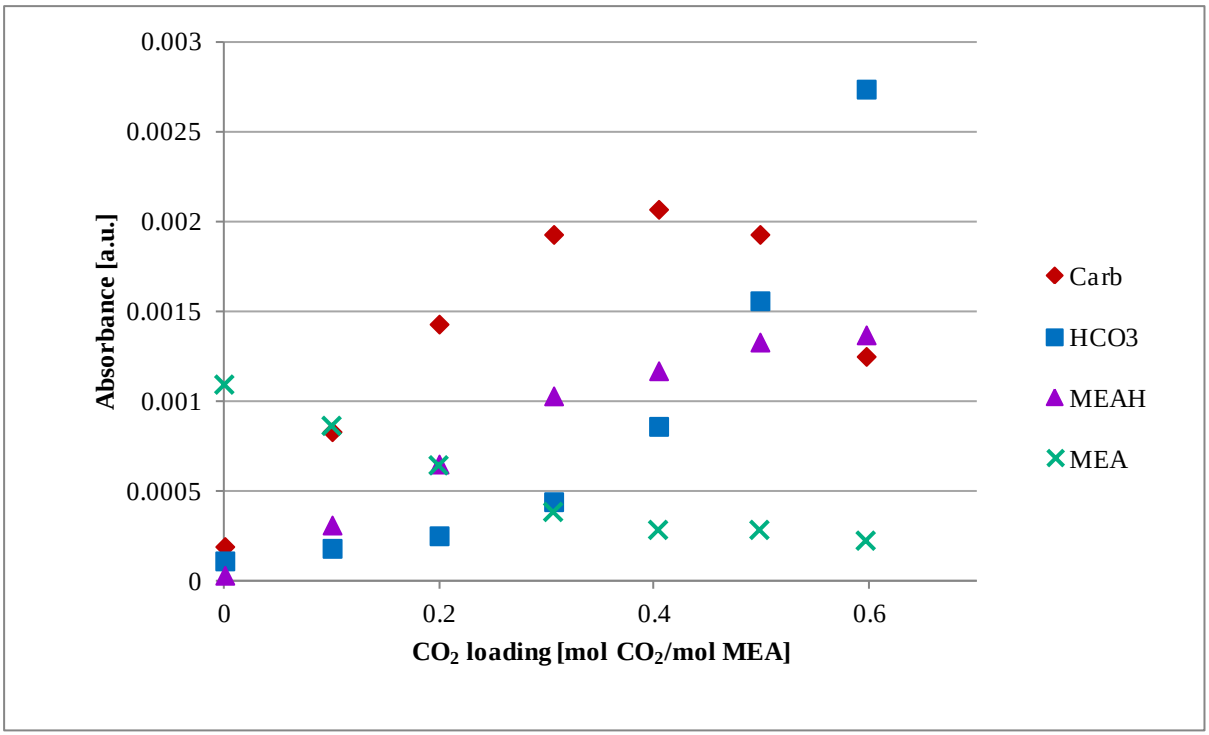

Figure 40 : Species absorbance as a function of CO_2 loading for 0.328 mol MEA/L at 30°C

The second reason the absorbance plotted in Figures 36 to 40 above would reflect actual product species concentrations is the correlation between the measured absorbance and published species concentration profiles: the absorbance vs. CO_2 loading profiles for absorbance at 1564, 1360 and 1064 cm^{-1} have trends similar to species concentration vs. CO_2 loading profiles for carbamate, HCO_3^- and $MEAH^+$. In the next section, the measured carbamate absorbance was used to calculate the concentration of each species in solution. The trends in the calculated species concentration profiles are compared to trends in published concentration profiles in Section 5.4.

5.3 Carbamate calibration calculations

Concentration profiles were generated for the species in the aqueous CO_2-MEA reaction mixture using implicit calibration calculations. In the calculations, a calibration factor for carbamate was determined based on an assumption of 100% CO_2 conversion. The assumption of 100% CO_2 conversion can be validated by Figure 41, where the CO_2 absorbance measured oscillates around a value of zero. It was also assumed that all reacting CO_2 would form either carbamate or HCO_3^-, and not CO_3^{2-}. The assumption of no CO_3^{2-} formation was based on an inability to accurately measure absorbance (Section 4.4) and reports of negligible CO_3^{2-} formation in published species concentration results (Jakobsen *et al.*, 2005; Böttinger *et al.*, 2008; Richner & Puxty, 2012).

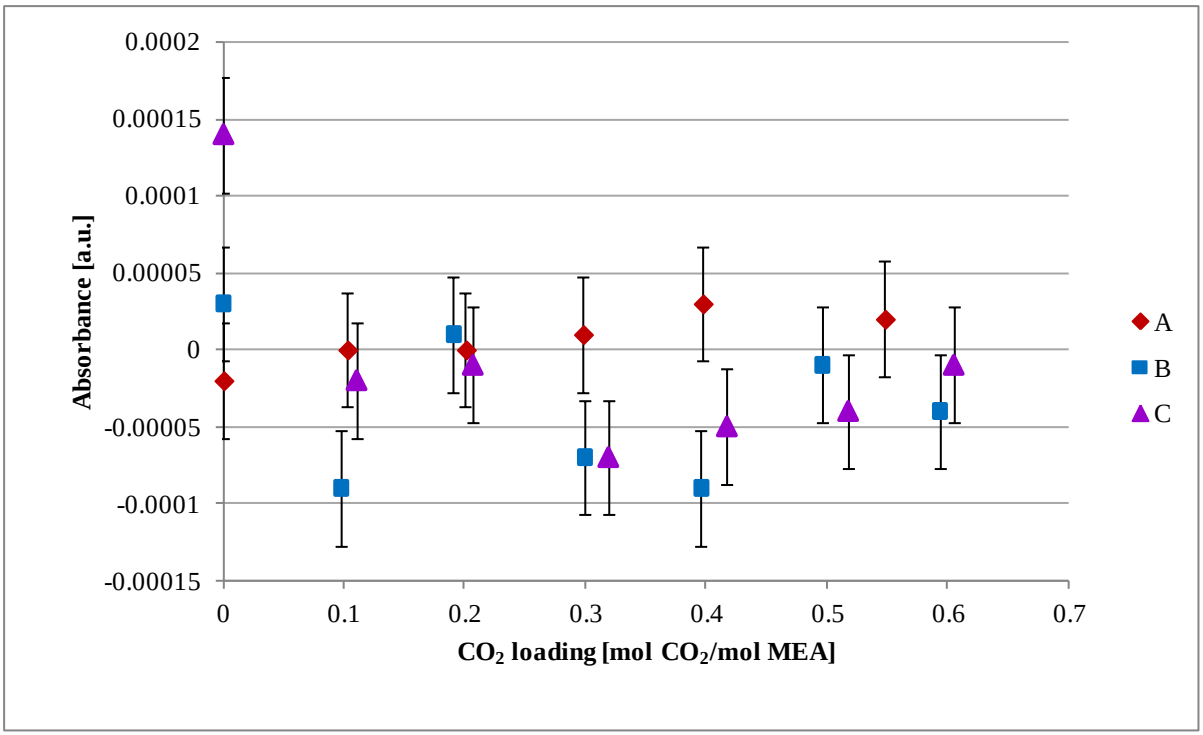

Figure 41 : Repeatability for equilibrium experiments: CO_2 absorbance at 2342 cm^{-1} from experiments 25_A, 25_B and 25_C (0.17 mol MEA and 25°C)

For the calibration calculation, all reacted CO_2 was assumed to convert to carbamate at CO_2 loadings less than 0.3 mol CO_2/mol MEA. This assumption was used to calculate the concentration of carbamate in solution. The calculated carbamate concentration is plotted against absorbance measured at 1564 cm^{-1} in Figure 42 for one of the experiments conducted at 25°C, shown as the series [Carb]. Fitting a straight line through the data points gives a calibration factor of 47.9 with a Pearson's R^2 value of 0.971. The straight line was forced through the origin, and the good fit of the data to the straight line is consistent with Lambert-Beer's law.

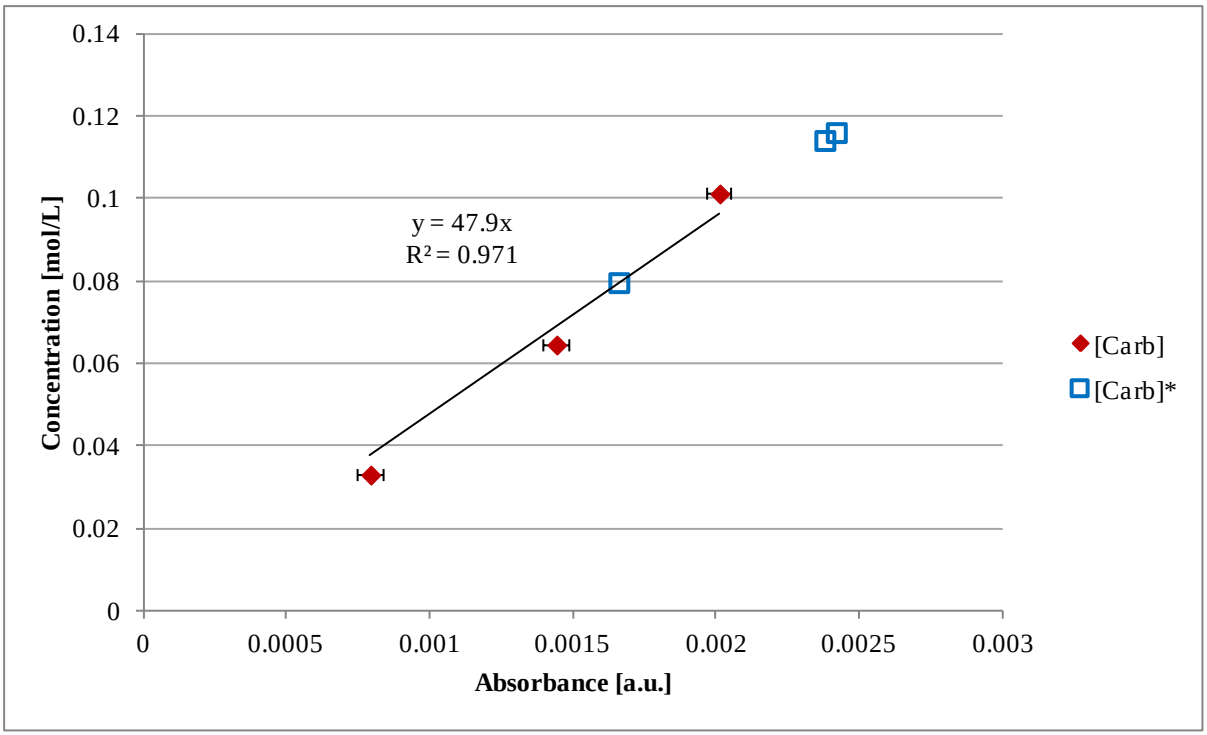

Figure 42 : Carbamate calibration curve for at 25°C; data recorded from experiment 25_B

The series $[Carb]^*$ plotted in Figure 42 is the predicted carbamate concentrations for absorbance measurements at CO_2 loadings greater than 0.3 mol CO_2/mol MEA. The concentrations were predicted using the calculated calibration factor. If the underlying assumption of 100% conversion of the CO_2 to carbamate at CO_2 loadings less than 0.3 mol CO_2/mol MEA was incorrect, the series $[Carb]^*$ would deviate systematically from the calibration curve. However the calculated concentrations lie along the calibration curve, verifying the assumption. Similar concentration-absorbance plots were generated at other experimental conditions. The calibration factors calculated are given in Table 10 with the corresponding Pearson's R^2 values.

Table 10 : Carbamate calibration factors from each equilibrium experiment

T [°C]	Calibration factor	Pearson's R^2
20	54.4	0.998
25 (25_A)	51.6	0.994
25 (25_B)	47.9	0.971
25 (25_C)	54.0	1.000
30	52.4	0.999

Two other carbamate calibration procedures have been published in literature. One was use to determine carbamate calibration factors in the absence of a solvent (Diab *et al*., 2012), and the other was used to determine the calibration factors in non-aqueous solvents (du Preez, 2014). In the work of Diab *et al*. (2012), the calibration factors were determined from mixtures of CO_2 and pure DEA without any water present. The calibration factors were then used to analyse data collected from the reaction conducted in water. This introduced uncertainty as

the wavenumber at which carbamate absorbs IR radiation shifted from 1548 cm^{-1} with no solvent to 1530 cm^{-1} in water.

In non-aqueous reaction mixtures carbamate is the only anionic product forming. The negative charge on carbamate is balanced by $MEAH^+$. Therefore, the concentration of $MEAH^+$ in solution would be the same as the concentration of carbamate. This assumption was the basis for the calibration procedure used by du Preez (2014) for work in non-aqueous solvents. The $MEAH^+$ concentration was determined using conductometric titrations as described by Cummings *et al*. (1990).

The conductometric titration procedure could not be used in the current work because more than one anionic product formed. The negative charge on HCO_3^- was also balanced by the positive charge on $MEAH^+$. Therefore, the concentration of $MEAH^+$ could not be assumed to be equal to the carbamate concentration. Also, at concentrations where little HCO_3^- and CO_3^{2-} may form, the concentration of $MEAH^+$ would be influenced by dilution of a reaction solution with an aqueous solution of $NaOH$. The dilution would specifically affect the protonation of free MEA in solution, where excess MEA would be deprotonated by the water, thereby changing the $MEAH^+$ concentration throughout the dilution. The $MEAH^+$ concentration determined from the dilution would then not reflect the amount of $MEAH^+$ formed during reaction and would not equal the concentration of carbamate formed in the reaction.

The carbamate calibration procedure used in this work was verified by plotting predicted HCO_3^- concentration against measured absorbance at 1360 cm^{-1}. The HCO_3^- concentration was calculated from a mass balance involving CO_2 and carbamate. Good fit of the data to a straight line would verify the assumptions of negligible CO_3^{2-} formation and 100% conversion of CO_2 to either carbamate or HCO_3^-. The plot of $[HCO_3^-]$ vs. absorbance for one experiment at 25°C is given in Figure 43, where the data do fit well to a straight line, thus verifying the carbamate calibration calculations.

Data points where 100% conversion of CO_2 to carbamate was assumed are not included in the figure. These data points would correspond to 0% conversion of CO_2 to HCO_3^-. At these data points, the absorbance measured at 1360 cm^{-1} was less than 0.0005 a.u. Absorbance measured up to 0.0005 a.u. has been shown to be an artefact created by MEA dissolving in water (Section 4.3). Excluding absorbance of less than 0.0005 a.u. therefore does not introduce significant error to the analysis. Plots of calculated carbamate and HCO_3^- concentration against measured absorbance are given in Appendix E for all experiments conducted.

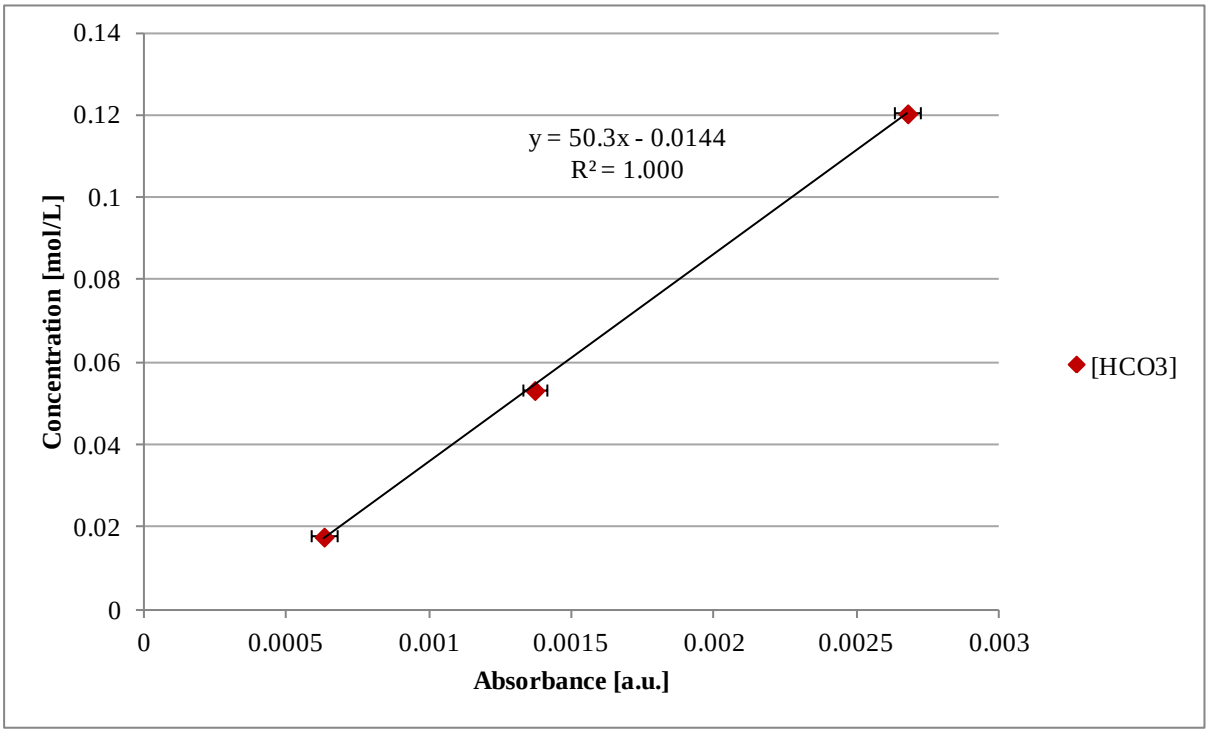

Figure 43 : Verification of carbamate calibration – [HCO_3^-] at 25°C (25_B)

The two CO_2-containing products, carbamate and HCO_3^-, were the two species with the highest measured absorbance. The carbamate and HCO_3^- absorbance therefore could be measured with the highest accuracy among all the species absorbance measured. Their concentrations at each CO_2 loading were used to derive the concentrations of $MEAH^+$ and MEA. $MEAH^+$ was calculated from a charge balance between $MEAH^+$, carbamate and HCO_3^- (Equation 56), and MEA was calculated from mole balance on the total amount of MEA added to the reactor (Equation 57).

$$[MEAH^+] = [Carb^-] + [HCO_3^-] \quad (56)$$

$$[MEA] = [MEA]_{fed} - [MEAH^+] - [Carb^-] \quad (57)$$

The validity of the calculated $MEAH^+$ and MEA concentrations is illustrated in Figures 44 and 45, respectively. These figures show the calculated $MEAH^+$ and MEA concentrations plotted against the measured absorbance. Good fit of the data to a straight line indicates the data obey Lambert-Beer's law, and that the species concentrations calculated from the carbamate calibration calculations are reliable. For both MEA and protonated $MEAH^-$ concentrations, deviation from Lambert-Beer's law was observed for concentrations corresponding to CO_2 loadings above 0.5 mol CO_2/mol MEA. The deviation could be caused by increasing uncertainty when both carbamate and HCO_3^- form in significant concentrations, where large errors in the concentrations of both species may be present. The calibration factor calculated for MEA for the experimental data shown in Figure 45 is in agreement with the MEA calibration factors determined for the kinetic experiments (Section 3.3.2.2). Plots of [$MEAH^+$] and [MEA] against absorbance for the other experiments are given in Appendix E.

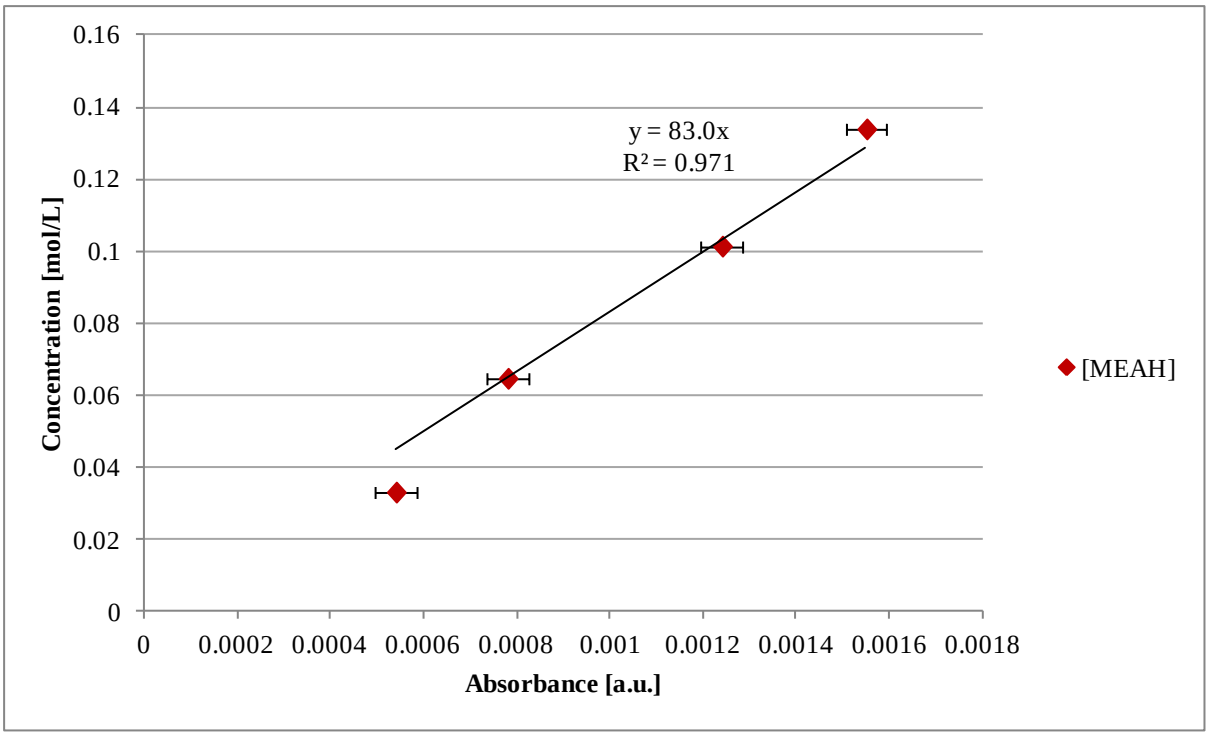

Figure 44 : Verification of carbamate calibration – [MEAH$^+$] at 25°C (25_B)

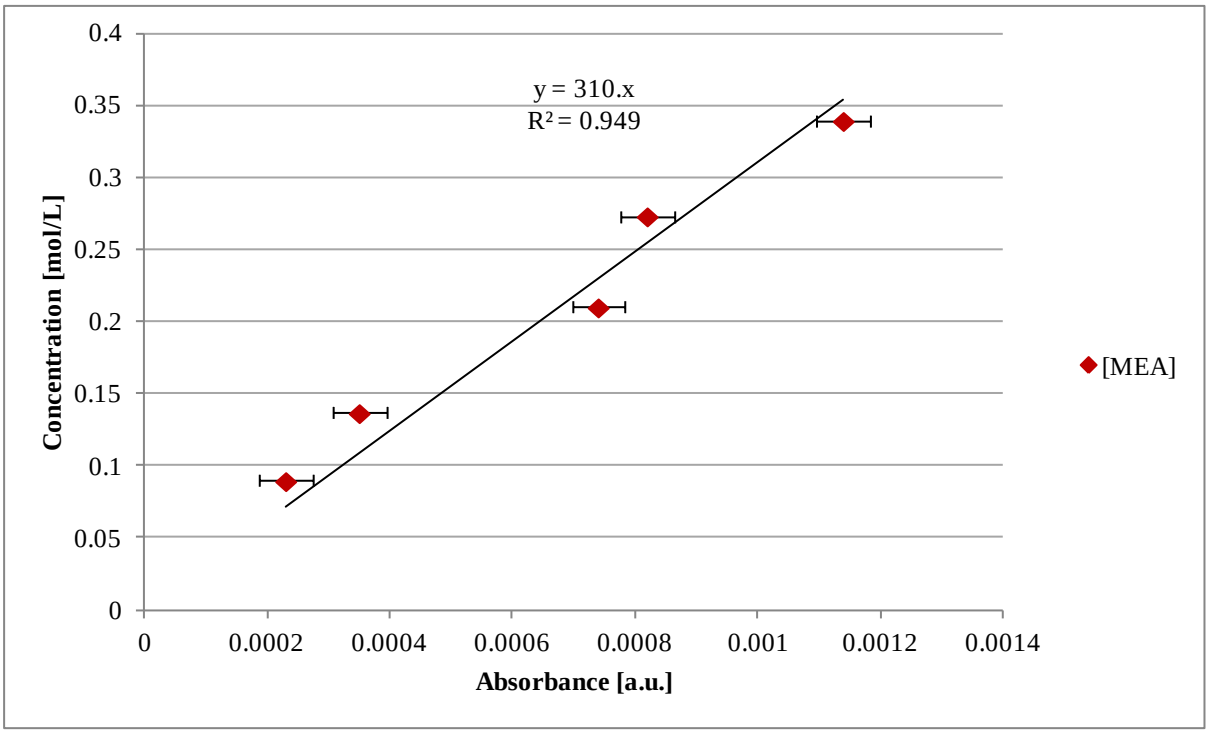

Figure 45 : Verification of carbamate calibration – [MEA] at 25°C (25_B)

5.4 Species concentration-CO_2 loading profiles

The species concentrations derived from the carbamate calibration calculations are plotted against CO_2 loading in Figures 46 to 50. These species concentrations were derived for 0.33 mol/L MEA solutions at 20 to 30°C. Curves representing model predictions of species

concentrations in 5 mol/L MEA solutions at 40°C (Austgen *et al.*, 1989) have been superimposed on Figures 46 to 50. 5 mol/L MEA solutions and 40°C represent typical industrial absorption column operating conditions. Experimental data collected from this work were compared to model predictions representing industrial absorption column conditions so that the trends in species concentrations over CO_2 loadings could be compared. General agreement between the species concentrations at the two MEA concentrations would indicate a similar reaction mechanisms in both solutions.

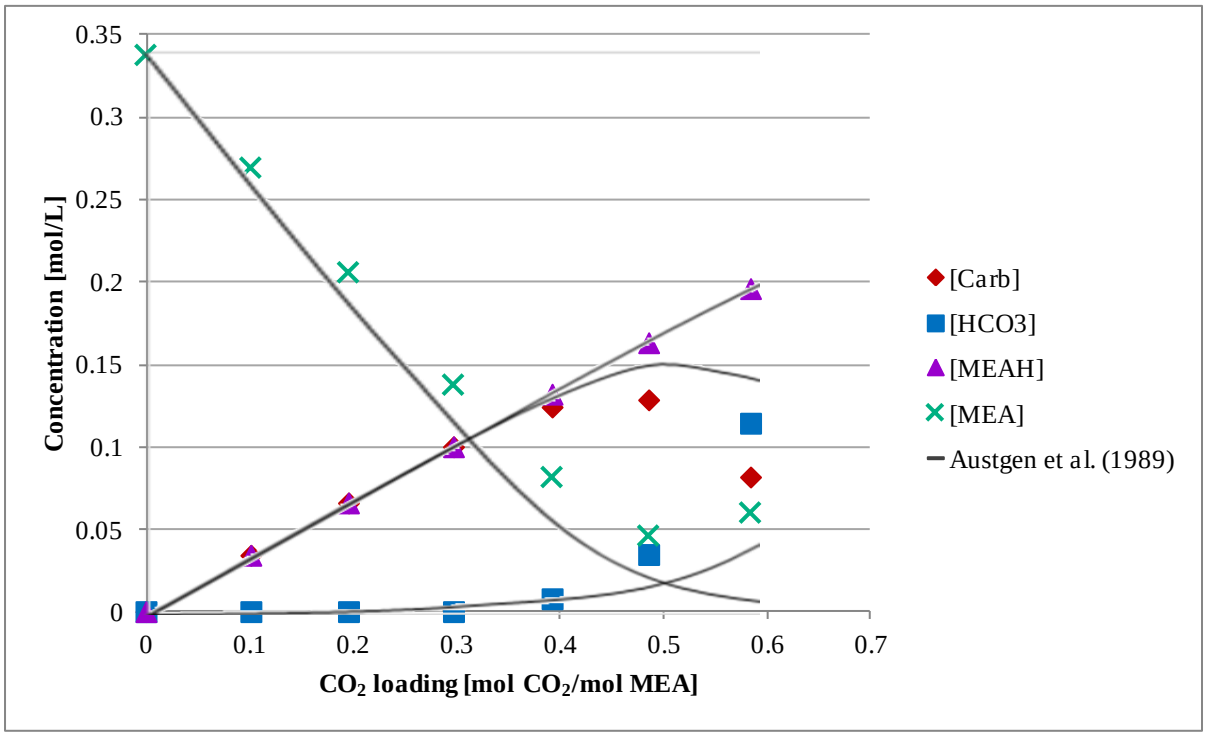

Figure 46 : Species concentrations as a function of CO_2 at 0.337 mol MEA/L at 20°C; the model predictions by Austgen *et al.* (1989) for 5 mol/L MEA solutions at 40°C are superimposed

The experimental data show trends similar to the literature profiles: at CO_2 loading less than 0.4 mol CO_2/mol MEA, [Carb] and [$MEAH^+$] increase at the same rate with increasing CO_2 loading; at CO_2 loadings higher than 0.4 mol CO_2/mol MEA, [Carb] decreases while [HCO_3^-] increases rapidly with increasing CO_2 loading. At CO_2 loadings less than 0.4 mol CO_2/mol MEA, the rate of MEA consumption is twice as fast as the rate of carbamate formation, and most of the MEA is consumed when the CO_2 loading reaches 0.5 mol CO_2/mol MEA.

Based on these observations, carbamate formation was predominant at CO_2 loadings less than 0.4 mol CO_2/mol MEA, and hydration of CO_2 to form HCO_3^- was predominant at CO_2 loadings greater than 0.4 mol CO_2/mol MEA. A similar conclusion was made for measurements in solutions of 5 mol MEA/L and is discussed in the literature review (Section 2.5.2). Therefore, the mechanism of the aqueous CO_2-MEA reaction at MEA concentrations as high as 5 mol/L is valid at MEA concentrations as low as 0.33 mol/L as well. The elementary reaction steps for the mechanism are given in Equations 58 to 65, where the carbamate formation and HCO_3^- formation steps are given separately.

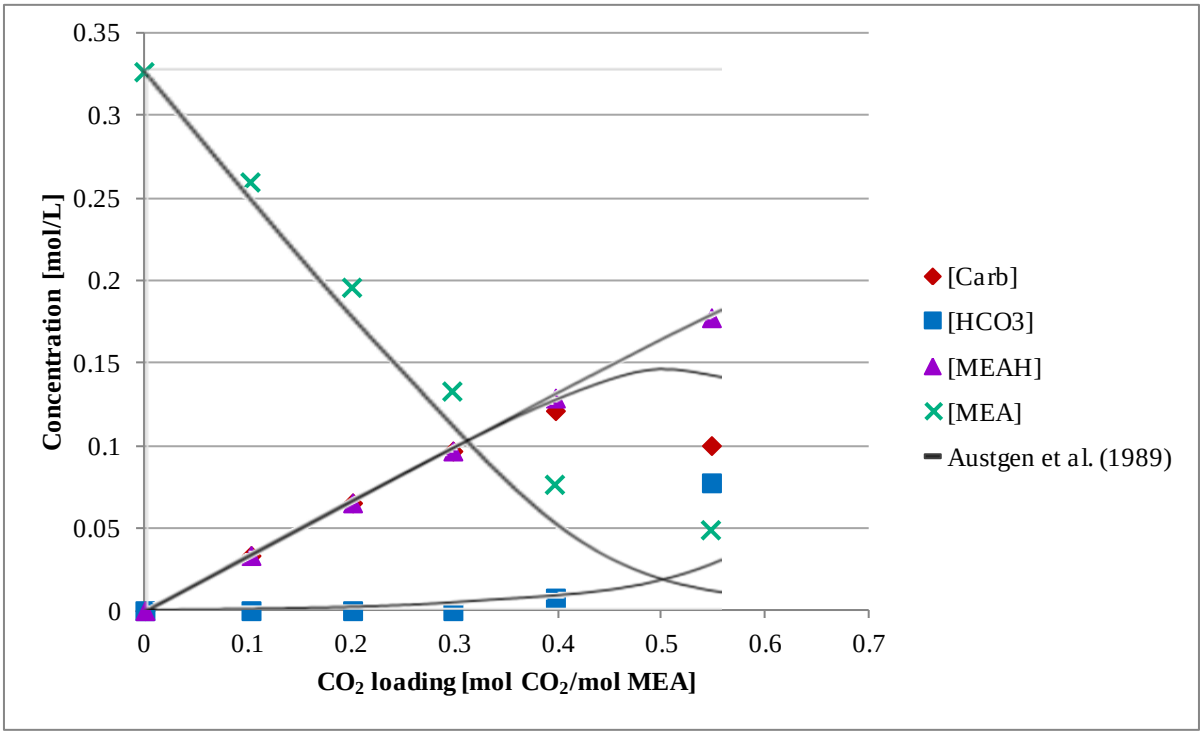

Figure 47 : Species concentrations as a function of CO_2 at 0.326 mol MEA/L at 25°C; the model predictions by Austgen *et al*. (1989) for 5 mol/L MEA solutions at 40°C are superimposed

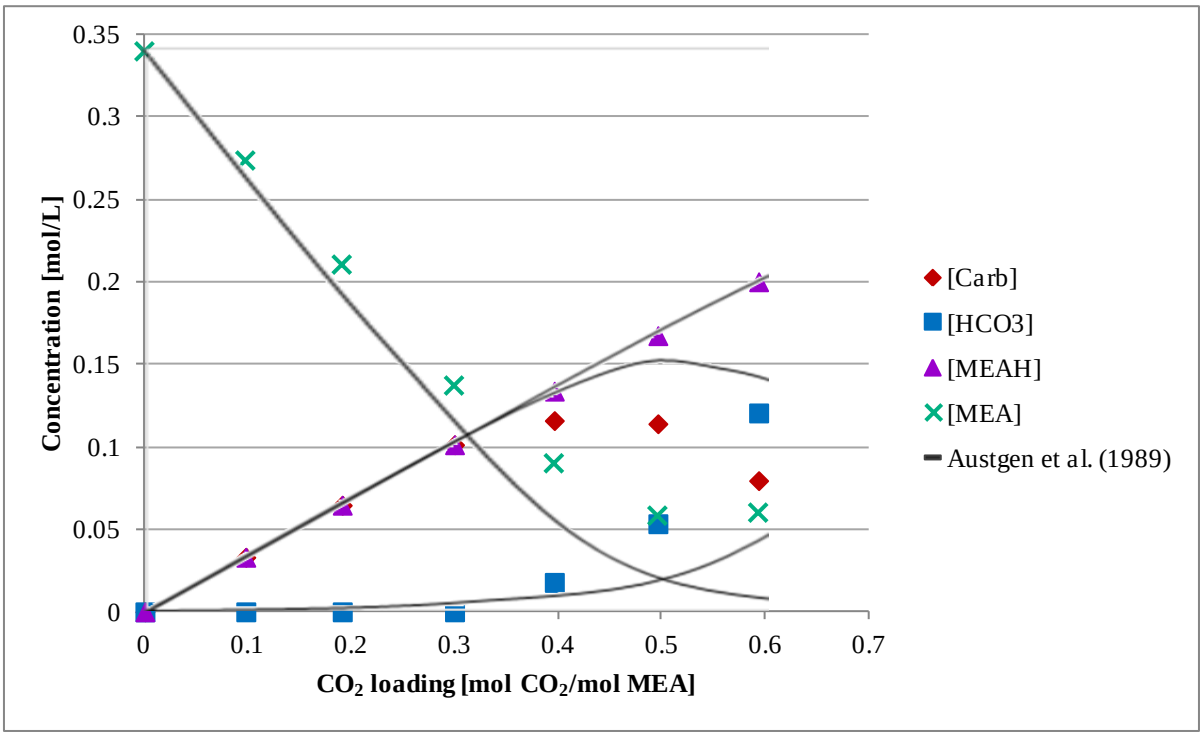

Figure 48 : Species concentrations as a function of CO_2 at 0.340 mol MEA/L at 25°C (25_B) ; the model predictions by Austgen *et al*. (1989) for 5 mol/L MEA solutions at 40°C are superimposed

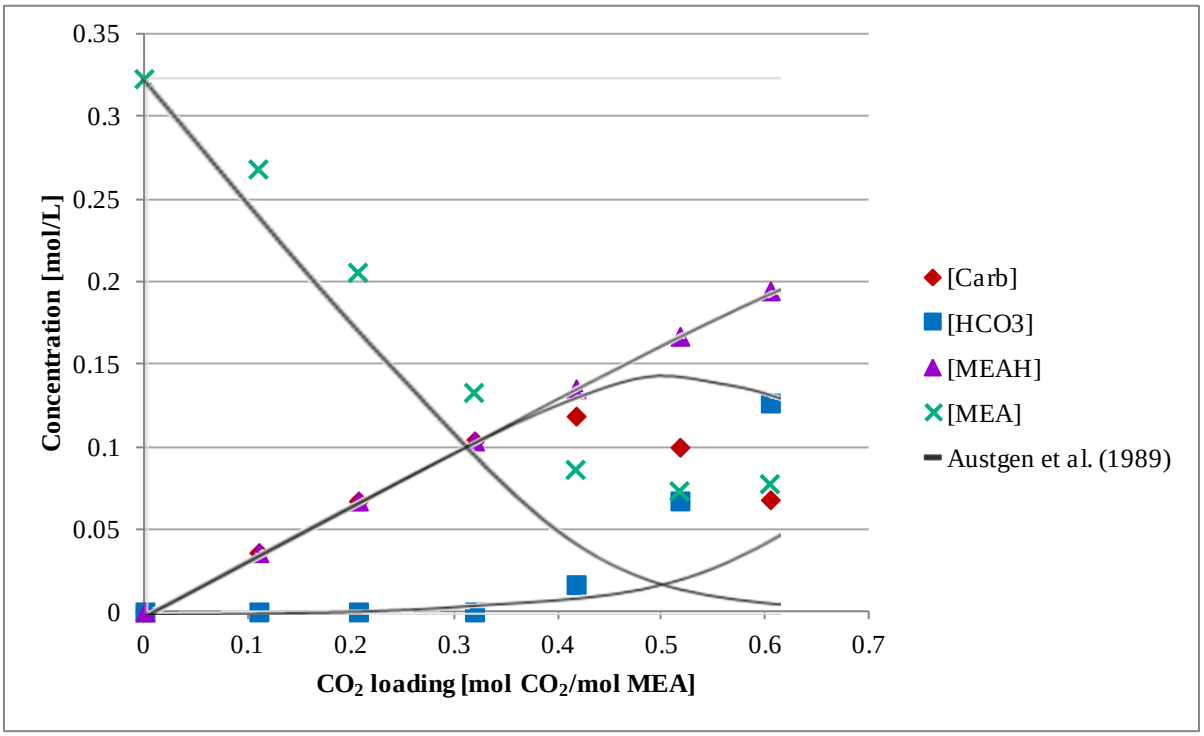

Figure 49 : Species concentrations as a function of CO_2 at 0.323 mol MEA/L at 25°C (25_C) ; the model predictions by Austgen *et al*. (1989) for 5 mol/L MEA solutions at 40°C are superimposed

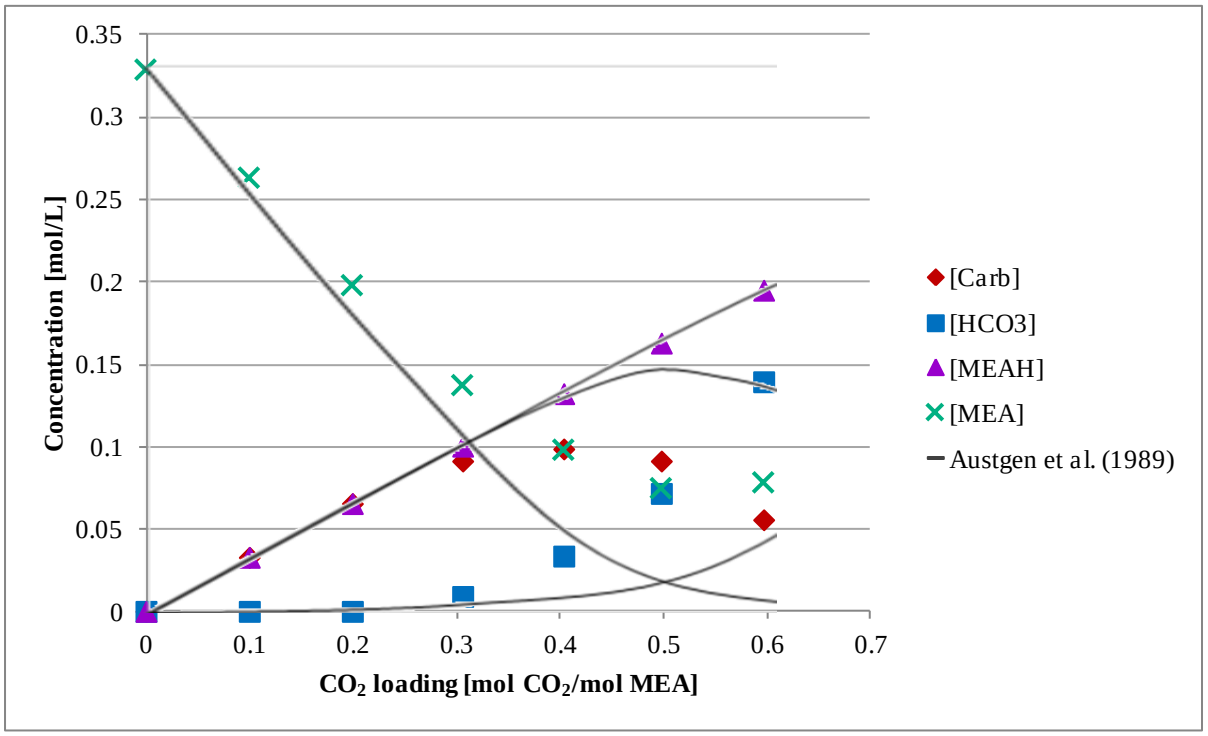

Figure 50 : Species concentrations as a function of CO_2 at 0.328 mol MEA/L at 30°C; the model predictions by Austgen *et al*. (1989) for 5 mol/L MEA solutions at 40°C are superimposed

Carbamate formation reactions:

$$CO_2 + MEA \leftrightarrow Zwitterion \quad (58)$$

$$Zwitterion + MEA \leftrightarrow Carb^- + MEAH^+ \quad (59)$$

HCO_3^- formation with carbamate decomposition reactions:

$$2H_2O \leftrightarrow 2OH^- + 2H^+ \quad (60)$$
$$CO_2 + OH^- \leftrightarrow HCO_3^- \quad (61)$$
$$Carb^- + H^+ \leftrightarrow Zwitterion \quad (62)$$
$$Zwitterion \leftrightarrow MEA + CO_2 \quad (63)$$
$$MEA + H^+ \leftrightarrow MEAH^+ \quad (64)$$
$$CO_2 + OH^- \leftrightarrow HCO_3^- \quad (65)$$

Figures 46 to 50 show similar trends in the species concentrations. When comparing 5 mol/L MEA solutions and 0.33 mol/L MEA solutions, the effect of decreasing MEA concentration is a decrease in the CO_2 loading at which [Carb] and $[HCO_3^-]$ are equal. For 5 mol/L MEA solutions, this CO_2 loading is near 0.7 mol CO_2/mol MEA; in 0.33 mol/L MEA solutions, it is near 0.5 mol CO_2/mol MEA. At the low MEA concentration solutions, increasing temperature from 20 – 30°C shifts the CO_2 loading from 0.56 – 0.52 mol CO_2/mol MEA.

The values of rate constants determined in a reaction kinetics study will be affected by the MEA concentration (Luo *et al*., 2014). Most of the second order rate constants reported to date are from experiments conducted in low MEA concentration solutions. In these experiments, CO_2 loadings were typically less than 0.3 mol CO_2/mol MEA. At these loadings, carbamate can be expected to be the only CO_2-containing product, as confirmed by the carbamate calibration calculations in this work. Experiments at less than 0.3 mol CO_2/mol MEA would not lead to HCO_3^- formation.

In Luo *et al*. (2014)'s experiments conducted at CO_2 loadings up to 0.4 mol CO_2/mol MEA, HCO_3^- would have formed. However, since the reaction was monitored using the inlet and outlet CO_2 gas flow rate, any HCO_3^- forming in the reaction solution was not detected. Based on published equilibrium species concentrations, HCO_3^- is expected to form in significant amounts above 0.3 mol CO_2/mol MEA. Significant amounts of HCO_3^- forming would be the cause of the reported systematic deviation in the reaction rate predicted by two of Luo *et al*. (2014)'s proposed reaction models. One of these models was a second order rate model. The systematic deviations were reported in both 1 and 5 mol/L MEA solutions and only above 0.3 mol CO_2/mol MEA.

5.5 Carbamate-HCO_3^- equilibrium

A carbamate-HCO_3^- equilibrium constant was calculated from the data collected using Equation 66. For each set of experimental measurements, K_{eq} was calculated at each CO_2 loading, considering only CO_2 loadings above 0.3 mol CO_2/mol MEA. Only CO_2 loadings above 0.3 mol CO_2/mol MEA were considered because negligible amounts of HCO_3^- formed at CO_2 loadings less than 0.3 mol CO_2/mol MEA. The average value of the constant calculated from each experiment is plotted in Figure 51 and given in Table 11.

$$K_{eq} = \frac{[Carb^-]}{[HCO_3^-][MEA]} \quad (66)$$

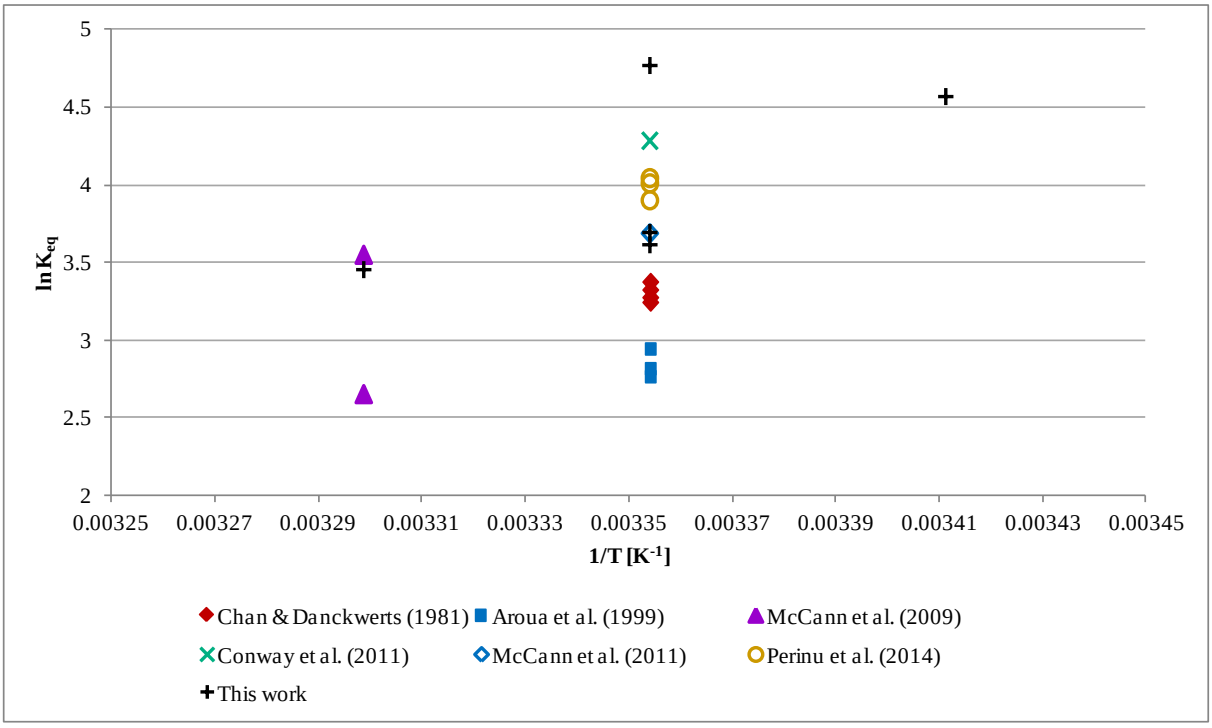

Figure 51 : Carbamate-HCO_3^- equilibrium constant at various temperatures

Table 11 : Carbamate-HCO_3^- equilibrium constants at various temperatures

T [°C]	K_{eq} [L/mol]	Analysis method	Reference
25	29.2	Titration	Chan & Danckwerts (1981)
25	27.8		
25	26.5		
25	25.6		
25	15.89	Titration	Aroua *et al.* (1999)
25	19		
25	16.73		
30	14.1	^{1}H-NMR spectroscopy	McCann *et al.* (2009)
30	34.7	Titration	
25	72.3	^{1}H-NMR spectroscopy	Conway *et al.* (2011)
25	39.8	Titration calorimetry	McCann *et al.* (2011)
25	49.3	^{13}C NMR spectroscopy	Perinu *et al.* (2014)
25	56.8		
25	54.9		
20	96.1	ATR-FTIR spectroscopy	This work
25 (A)	117.4		
25 (B)	40.0		
25 (C)	37.0		
30	31.5		

At 25°C, the values of K_{eq} calculated for the three experiments conducted are 117.4, 40.0 and 37.0 L/mol. Literature data at 25°C varies between 15.89 and 72.3 L/mol. The scatter in the data is due to the different analytical methods that were used to determine the equilibrium

constant. The analytical methods are given in Table 11. The scatter in the equilibrium constant values determined in this work is caused by the calculation method used to calculate the equilibrium constant. The values in this work were calculated from the average of individual measurements. In the individual measurements, low values of $[HCO_3^-]$ and [MEA] at CO_2 loadings between 0.3 and 0.6 mol CO_2/mol MEA would contribute towards a bias in K_{eq}, increasing the calculated value.

A more robust method to calculate K_{eq} would be through a thermodynamic model describing all the chemical species in the reaction system. K_{eq} would be a regressed parameter that would be optimized so as to minimize the errors between predicted and actual species concentrations. In the literature data given in Figure 51 and Table 11, only the values corresponding to ^{1}H-NMR spectroscopy were determined by regression (McCann *et al.*, 2009; Conway *et al.*, 2011). However, there is reasonable agreement between K_{eq} values determined in this work and all literature values.

5.6 Chapter summary

Equilibrium absorbance measurements on the aqueous CO_2-MEA reaction mixture were presented. The measurements were made at CO_2 loadings between 0 and 0.6 mol CO_2/mol MEA at an MEA concentration of 0.33 mol/L. Implicit calibration calculations were used to generate species concentrations at each CO_2 loading. The concentrations for MEA, and the products carbamate, HCO_3^- and protonated MEA were plotted against CO_2 loading at 20, 25 and 30°C. The concentration-CO_2 loading plots had similar trends to trends in published data collected at 5 mol/L MEA and 40°C. Carbamate-HCO_3^- equilibrium constants calculated from the experimental data were in agreement with published equilibrium constants. The measurements provided the first equilibrium species concentration measurements made using FTIR spectroscopy in low MEA concentration solutions, and novel conclusions could be made regarding the mechanism of the reaction at low MEA concentrations.

6. Kinetic experimental results

This chapter describes the results of the kinetic experiments, starting with verification of the semi-batch method for use in monitoring the aqueous CO_2-MEA reaction. The species absorbance- and molar-time profiles are then discussed, followed by an analysis of the reagent species conversions at equilibrium. The absorbance measurements provide the first recorded use of FTIR spectroscopy to monitor the reaction. The chapter ends with a discussion of calculated reaction rate constants.

6.1 Verification of kinetic control under semi-batch reactor operation

Using a semi-batch reactor setup to monitor a rapid reaction creates the possibility of conducting the reaction under equilibrium limitation. That is, the measured reaction rate is lower than the actual reaction rate because the reaction reaches equilibrium essentially instantaneously. This results in a measured "reaction rate" that is determined by the rate at which the second reagent is fed. The measured species concentrations would then only reflect a moving equilibrium, and would not be suitable for determining kinetic rate constants.

The efficiency of semi-batch operation was verified in this work by conducting kinetic experiments at different MEA molar flow rates. The amount of CO_2 used in all experiments was kept at approximately 0.5 g dissolved in 0.5 L of water and all experiments were conducted at 25°C. The CO_2 absorbances measured over time in the experiments are shown in Figure 52. The actual amounts of CO_2 and MEA added to the reactor in each experiment are given in Table 12.

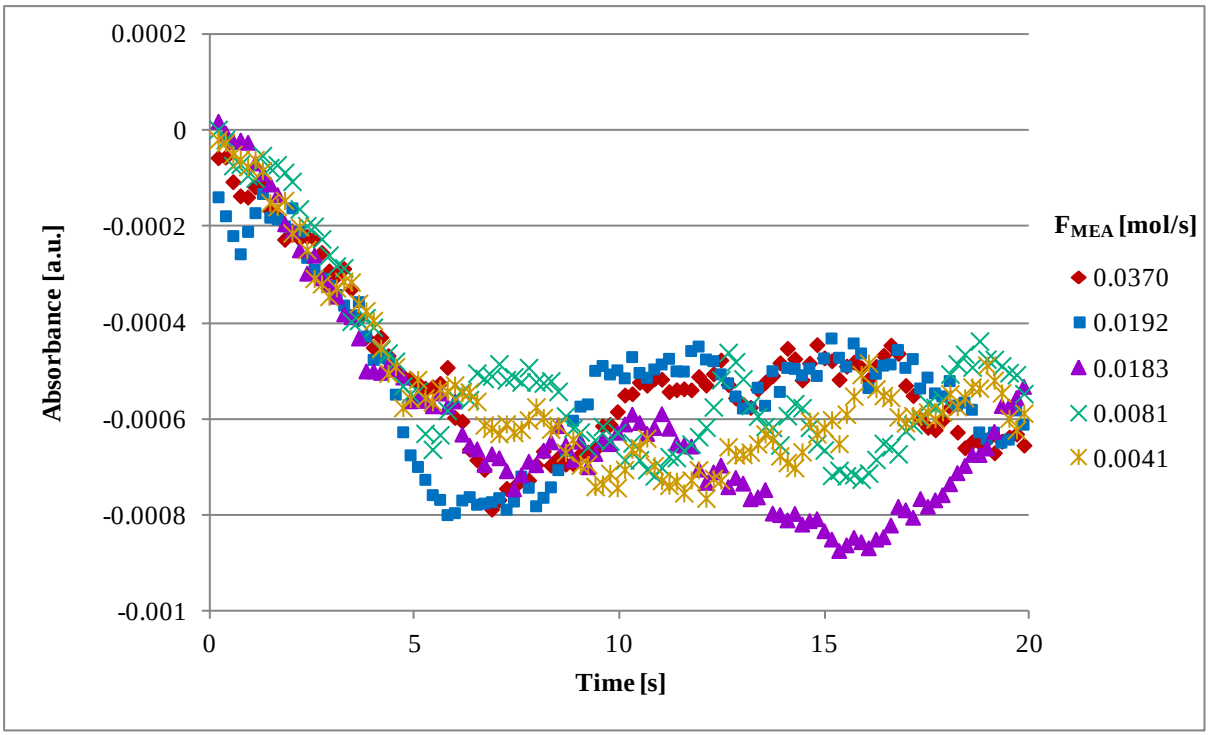

Figure 52 : CO_2 absorbance measured at 2342 cm^{-1} for various MEA molar flow rates at 25°C; initial CO_2 solutions have concentrations of approximately 0.022 mol CO_2/L (0.011 mol in 0.5 L)

Table 12 : Details of semi-batch operation verification experiments: molar flow rate of MEA solution into reactor, total moles of MEA added and total moles of CO_2 added

F_{MEA} [mol/s]	N_{MEA} [mol]	N_{CO_2} [mol]
0.0370	0.553	0.0108
0.0192	0.562	0.0112
0.0183	0.272	0.0108
0.0081	0.292	0.0115
0.0041	0.160	0.0115

The absorbances plotted in Figure 52 are directly proportional to the concentration of CO_2 in solution. The slopes of the absorbance graphs are therefore directly proportional to the rate of consumption of CO_2 in each experiment. The slopes of the graphs between 0 to 10 s can be used to determine whether the reaction was under kinetic or equilibrium control for the range of MEA flow rates considered: if the reaction was under equilibrium control, the measured absorbance would reflect an established equilibrium position at each point in time. Higher molar flow rates of MEA into the reactor would then cause the CO_2 to be consumed faster, giving a steeper slope in the absorbance graph.

Figure 52 shows that the slopes of the absorbance graphs from each experiment are not dependent on the molar flow rate of MEA into the reactor. The slopes are approximately equal, indicating that the rate of consumption of the CO_2 was not dependent on the MEA flow rate. This proves that the measured absorbances do not reflect a moving equilibrium position. The reaction did not achieve equilibrium instantaneously and the consumption of CO_2 could be monitored. The absorbances plotted in Figure 52 show the rate of consumption of CO_2 reached equilibrium only near 7 s.

6.2 Reagent species-time profiles

The absorbance-time profiles for two kinetic experiments are shown in Figures 53 and 54. The two MEA concentration settings used in the kinetic experiments are represented by the two figures. Figure 53 shows data collected at the higher MEA concentration setting (0.52 mol/L, corresponding to about 0.26 mol MEA added to the reactor). This experiment was conducted at 30°C, with a MEA molar flow rate of 0.00887 mol/s. 0.265 mol MEA in total was added to the reactor. The experiment represented by Figure 54 was conducted at the lower MEA concentration setting (0.26 mol/L, corresponding to about 0.13 mol MEA added to the reactor). The experiment was conducted at 25°C, with a MEA molar flow rate of 0.00420 mol/s. 0.137 mol MEA in total was added to the reactor during the experiment. The mass of reagents and MEA flow rates used in individual experiments are given in Appendix D.

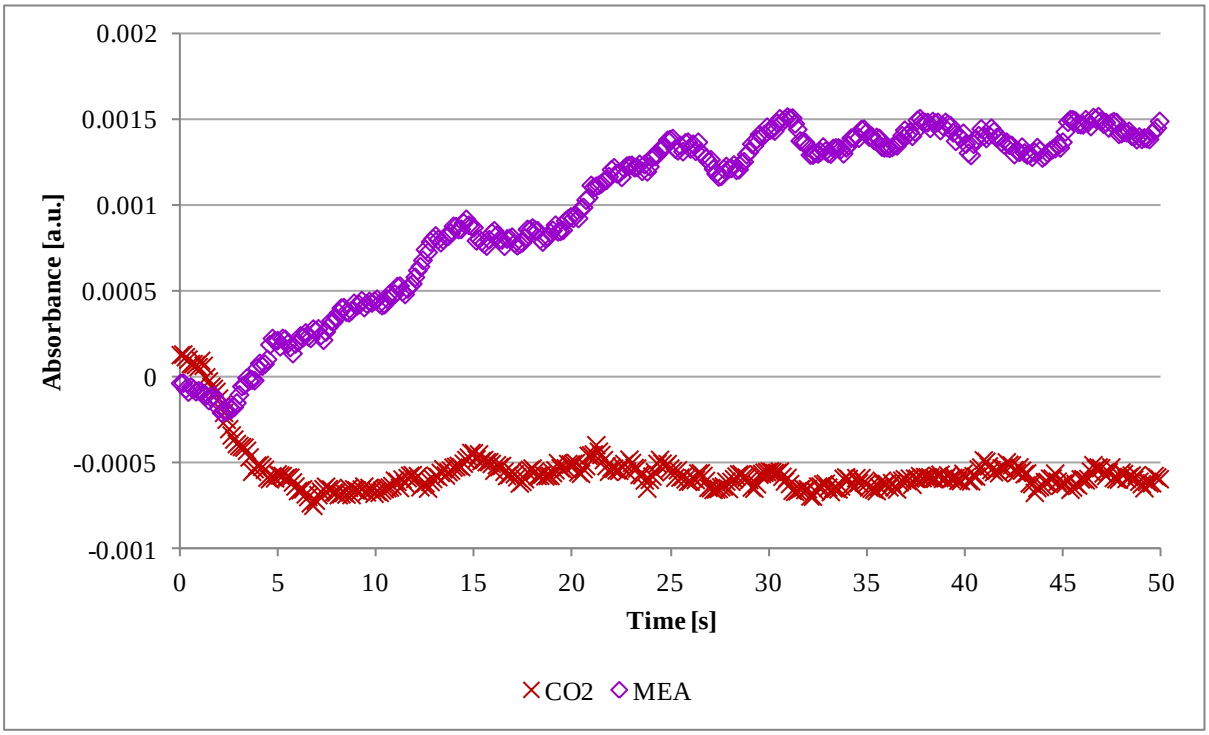

Figure 53 : Smoothed absorbance-time profiles for experiment 20_30_3, conducted with 0.265 mol MEA at 0.00887 mol MEA/s and 30°C

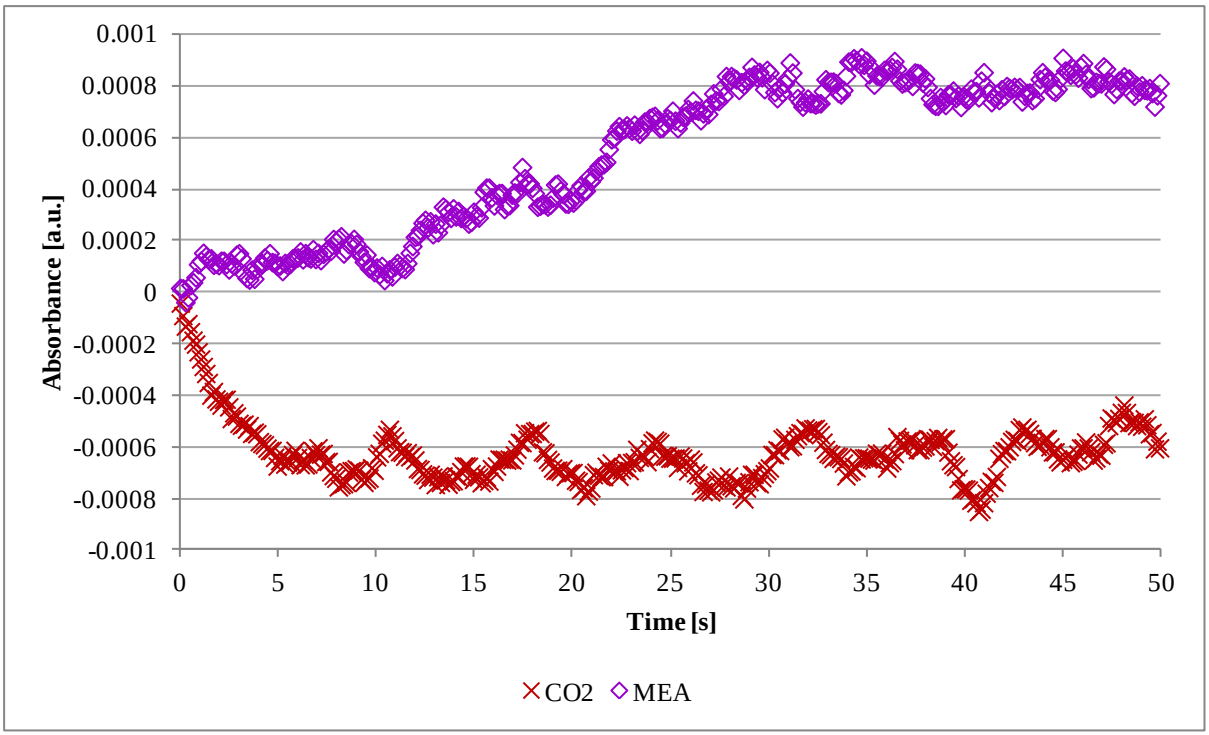

Figure 54 : Smoothed absorbance-time profiles for experiment 10_25_1, conducted with 0.137 mol MEA at 0.00420 mol MEA/s and 25°C

In both Figures 53 and 54, the CO_2 absorbance decreases rapidly once feed of MEA to the reactor is started. The CO_2 absorbance reaches the equilibrium value within the first 10 s, indicating complete conversion of the CO_2 within 10 s of adding MEA to the reactor. For the higher MEA concentration setting (Figure 53), there is little increase in the MEA absorbance during the first 5 s of the adding MEA to the reactor. The little increase in MEA absorbance indicates little increase in MEA concentration in the reactor. Little increase in MEA concentration would be expected due to direct reaction of the MEA with any free CO_2 in solution. The MEA absorbance increases only after most of the CO_2 has been consumed, as indicated by the decreasing CO_2 absorbance.

For the experiment conducted at the lower MEA concentration setting (Figure 54), the delay before MEA absorbance increases significantly extends to 10 s. The longer delay in the case of the lower MEA concentration experiment can be explained by the extent of the reaction between CO_2 and free MEA in solution. At the lower MEA concentration, less free MEA is added to the reactor per second. There is then less free available to react with CO_2, and once the stoichiometric amount of MEA has reacted with CO_2, a lower concentration of MEA is left behind in solution. For both the low and high MEA concentration settings, the MEA concentration in solution increases significantly after the CO_2 has completely reacted. Pumping of MEA into the reactor continued until 30 s, and the corresponding increase in MEA concentration is indicated by increasing MEA absorbance.

The molar-time profiles corresponding to Figures 53 and 54 are shown in Figures 55 and 56, respectively. The molar-time profiles show the same trends as the absorbance-time profiles: CO_2 is completely consumed within 10 s and little MEA accumulates during the first few

seconds of adding MEA to the reactor. N_{MEA} was calculated directly as the product of the measured MEA absorbance and the MEA calibration factor. N_{CO_2} was calculated from the negative CO_2 absorbance as follows: the amount of CO_2 consumed ($N_{CO_2,consumed}$) was calculated as the product of the measured CO_2 absorbance and the CO_2 calibration factor; the actual amount of CO_2 in the reactor was the difference between the initial amount of CO_2 added ($N_{CO_2,0}$) and the amount of CO_2 consumed (Equation 67).

$$N_{CO_2} = N_{CO_2,0} - N_{CO_2,consumed} \quad (67)$$

The uncertainty in N_{CO_2} and N_{MEA} plotted in the species profiles is given in Table 13 at each temperature. The uncertainty in the molar amounts was calculated as the product of two standard deviations of the absorbance measurements and the calibration factor at each temperature (Taylor, 1997). The 95% confidence interval in the molar amounts can be obtained by adding and subtracting the uncertainty values given in Table 13.

Table 13 : Error in calculated molar amounts, based on the average of 20 absorbance measurements

	CO_2			MEA		
T [°C]	$k_{CO_2,2342}$	Absorbance error [a.u]	N_{CO_2} error [mol]	$k_{MEA,1024}$	Absorbance error [a.u]	N_{MEA} error [mol]
20	32.960	$1.34x10^4$	0.00442	284.8	$1.57x10^4$	0.0446
25	29.948		0.00402	267.98		0.0419
30	34.725		0.00466	274.47		0.0430

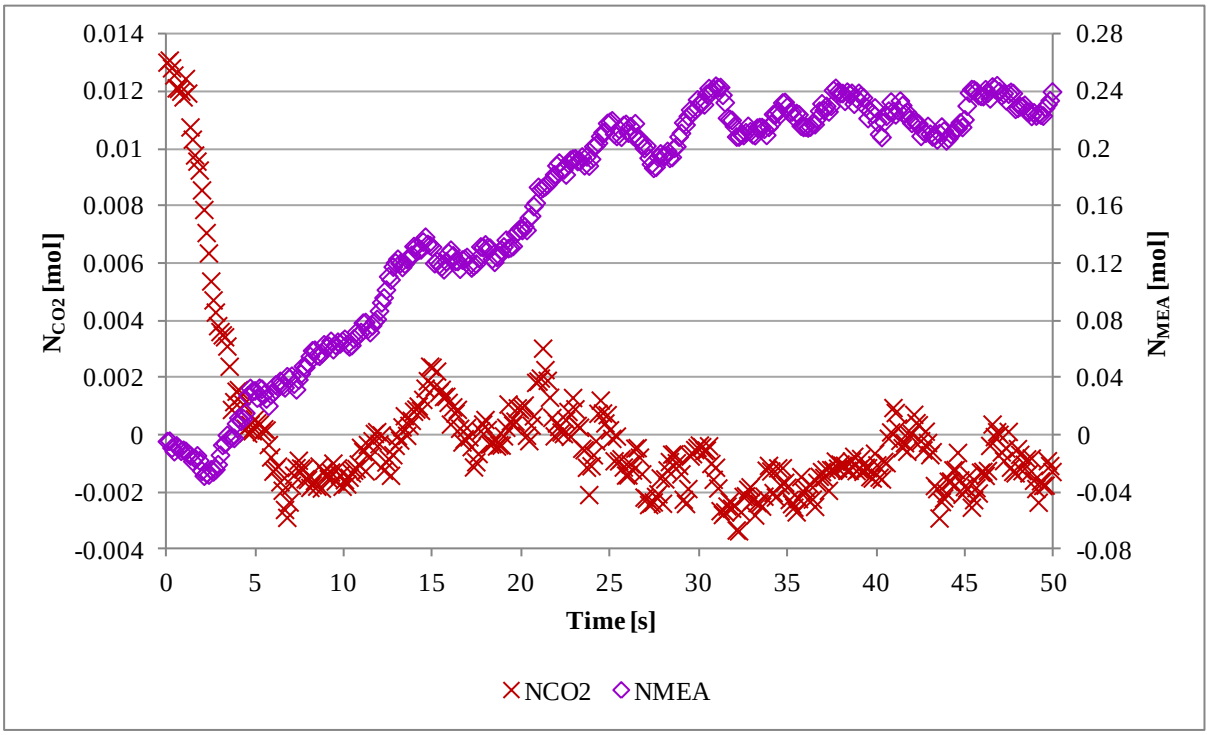

Figure 55 : CO_2 and MEA mole amount-time profiles for experiment 20_30_3, conducted with 0.265 mol MEA at 0.00887 mol MEA/s and 30°C

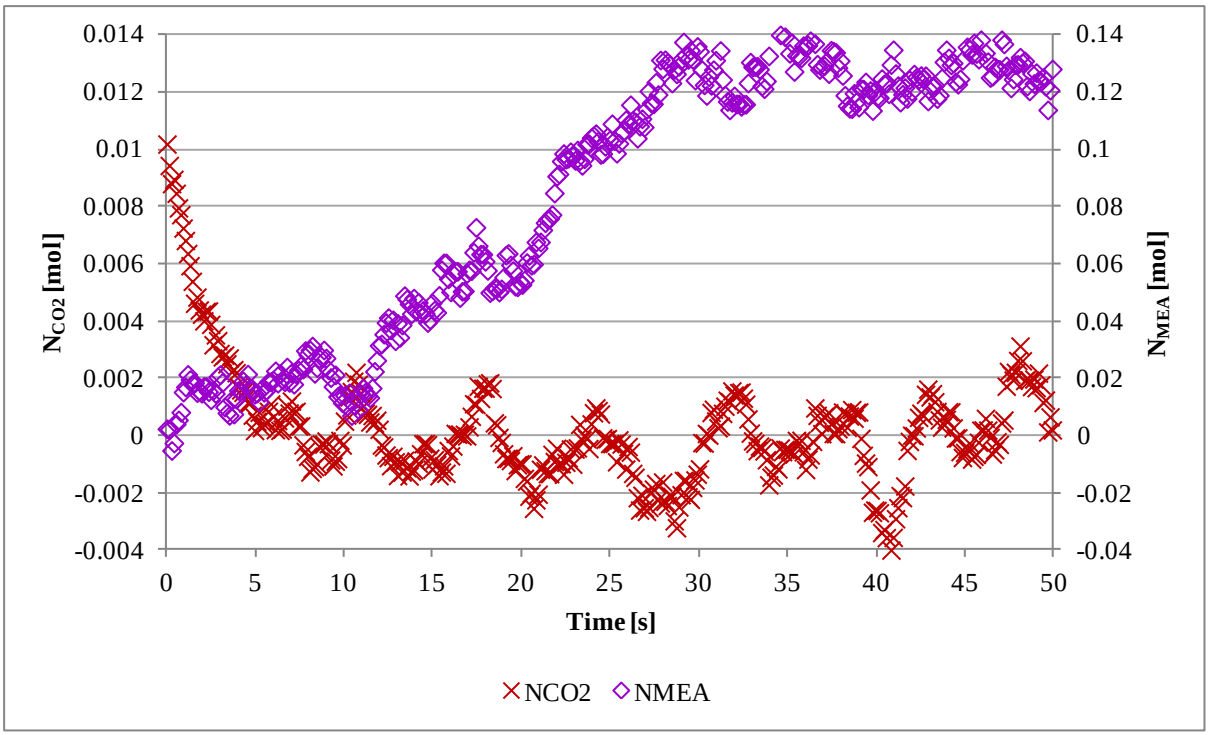

Figure 56 : CO_2 and MEA mole amount-time profiles for experiment 10_25_1, conducted with 0.137 mol MEA at 0.00420 mol MEA/s and 25°C

Once the reaction had reached equilibrium, the reagent species conversions and stoichiometric ratio were calculated for each experiment. These are given in Table 14 for the 18 experiments conducted. The species conversions and stoichiometric ratios were calculated from 700 data points recorded once the reaction had reached equilibrium. For the two MEA concentration levels considered, both reagent conversions and stoichiometric ratios show large scatter and no clear dependence on temperature can be observed. The CO_2 conversion varies between 95.0 to 135.3%; the MEA conversion varies between 8.6 to 18.0% at the low MEA concentration setting (0.13 mol), and between 3.2 to 12.9% at the high MEA concentration setting (0.26 mol); the stoichiometric ratios varies between 1.1 to 3.1. For both CO_2 conversion and stoichiometric ratio, the ranges are near the theoretical values of 100% and 2, respectively.

Table 14 : Equilibrium conversion and stoichiometric ratio for the kinetic experiments

0.13 mol MEA									
T [°C]	20			25			30		
Run #	10-20-1	10-20-2	10-20-3	10-25-1	10-25-2	10-25-3	10-30-1	10-30-2	10-30-3
F_{MEA} [mol/s]	0.00513	0.00531	0.00480	0.00420	0.00508	0.00448	0.00470	0.00541	0.00443
x_{CO_2}	135.3%	105.8%	116.4%	101.4%	103.0%	108.6%	117.2%	109.6%	109.0%
avg	119.2%			104.3%			111.9%		
x_{MEA}	12.6%	10.5%	10.6%	8.6%	14.3%	14.6%	18.0%	11.6%	12.7%
avg	11.2%			12.5%			14.1%		
Stoich. ratio	1.4	1.3	1.2	1.1	2.1	1.8	2.1	1.5	1.5
avg	1.3			1.6			1.7		

Table 14 (continued)

0.26 mol MEA									
T [°C]	20			25			30		
Run #	20-20-1	20-20-2	20-20-3	20-25-1	20-25-2	20-25-3	20-30-1	20-30-2	20-30-3
F_{MEA} [mol/s]	0.00944	0.00928	0.01006	0.01019	0.01017	0.00963	0.00957	0.00871	0.00887
x_{CO_2}	95.0%	119.1%	115.5%	108.3%	96.3%	116.1%	112.7%	118.9%	110.3%
avg	109.9%			106.9%			113.9%		
x_{MEA}	3.2%	5.4%	12.9%	7.8%	8.1%	12.8%	7.3%	7.8%	11.9%
avg	7.2%			9.6%			9.0%		
Stoich. ratio	1.0	1.2	3.0	2.2	2.0	3.1	1.7	1.6	2.7
avg	1.7			2.4			2.0		

The range in reagent conversions and stoichiometric ratios cannot be explained by the error of the average of 700 absorbance measurements. The absorbance errors for CO_2 and MEA based on 700 data points are 2.27×10^{5} and 2.65×10^{5}, respectively. Using the approach given in Table 13, the error in N_{CO_2} at 20, 25 and 30°C is 0.000747, 0.000679 and 0.000787 mol, respectively. The corresponding error in N_{MEA} is 0.00754, 0.00709 and 0.00726 mol. In a typical experiment, the amount of CO_2 added to the reactor was 0.011 mol. Using the error values, the expected error in CO_2 conversion is approximately 7%, and the expected percentage error in the amount of MEA consumed is 33%. The expected range in CO_2 conversions would then be 93 to 107% for a theoretical 100% CO_2 conversion and the range in stoichiometric ratios would be between 1.6 and 2.5. Both these ranges do not cover the ranges reported in Table 14.

The reason the calculated uncertainties do not explain the ranges reported in Table 14 may be due to the values of the calibration factors used. Single values of the CO_2 and MEA calibration factors at each temperature were used to calculate concentrations and molar amounts from measured absorbance. However, using the single values of the calibration factors does not take the uncertainty in the calibration factors into account. The uncertainty in the calculated reagent conversions and stoichiometric ratios would, therefore, be underestimated, leading to conservative estimates of expected ranges.

Better estimates of the ranges in reagent conversions and stoichiometric ratios can be obtained by taking the uncertainty in CO_2 and MEA calibration factors into account. However, reasonable estimates of the uncertainty in the calibration factors would require more calibration experiments than those that were conducted. For purposes of this work, it was sufficient to conduct at least three calibration experiments for each reagent and temperature combination. Three calibration experiments were sufficient to prove repeatability of the measured data. Conducting more calibration experiments will be considered in future work.

Kinetic experiments similar to those presented in this work have been conducted in non-aqueous solvents (du Preez, 2014). In the non-aqueous solvents, a ZnSe ATR element was attached to the FTIR spectrometer when monitoring the reaction. When using a ZnSe element,

the evanescent wave transmitted from the element to the reaction solution can penetrate the solution to a greater depth than a Ge element (PIKE Technologies, 2011). A greater penetration depth results in higher values of measured absorbance, leading to less noise in the measured data. This can easily be seen by comparing the range in stoichiometric ratios obtained for the CO_2-MEA reaction. Using a ZnSe element du Preez (2014) obtained stoichiometric ratios between 1.9 to 2.1, whereas in this work the range was 1.0 to 3.1.

In the experiments conducted in aqueous solutions, a Ge ATR element is preferred to ZnSe. This is because Ge has a wider operating pH range of 1 to14 pH units; ZnSe has an operating pH range of 5 to 9 pH units (PIKE Technologies, 2011). In water, the pH of CO_2 and MEA solutions can reach 4 and 11 respectively (Chuang & Johannsen, 2009; Kohl & Nielsen, 1997), making the ZnSe element unsuitable for use. An alternative ATR element material is diamond, which also has a pH range of 1 to 14. The diamond ATR element has been used successfully to monitor the aqueous CO_2-MEA reaction (Jackson *et al*., 2009; Richner & Puxty, 2012). However, diamond absorbs IR radiation near the absorption band of CO_2 and is not recommended for monitoring CO_2 absorption (Richner & Puxty, 2012).

Although the kinetic results obtained with the Ge ATR element have large errors, they can be used to qualitatively comment on the aqueous CO_2-MEA reaction: the semi-batch setup confirms that the reaction is rapid at ambient conditions; and the assumptions of 100% CO_2 conversion and 2:1 MEA: CO_2 stoichiometric ratio are reasonable at low CO_2 concentrations. The N_{CO_2}- and N_{MEA}-time profiles discussed in this section were modelled to determine the reaction rate constants. The results of the reaction modelling are discussed next.

6.3 Reaction modelling

The species molar amounts collected over the duration of the reaction were modelled using reaction rate equations published in literature. The modelling was performed in an attempt to determine which rate equation represented the experimental data best. For each rate equation, the optimum rate constants were found by minimizing the error between the predicted species amounts and the experimental amounts for each model.

6.3.1 Semi-batch reactor design equations

The equations used in the modelling procedure were the species mole balances as defined by semi-batch reactor design equations. The species mole balances are given in Equations 68 and 69 for the case where MEA solution is pumped at a constant flow rate into a CO_2 solution. Product species were not included in the reaction modelling because of errors encountered when measuring the product species (Section 4.3). A reaction stoichiometry of 2 was imposed, resulting in the reaction rate of MEA being twice the rate of CO_2 (Equation 70).

$$\frac{dN_{CO_2}}{dt} = r_{CO_2}V \qquad (68)$$

$$\frac{dN_{\mathrm{MEA}}}{dt} = F_{\mathrm{MEA}_{in}} + r_{\mathrm{MEA}}V \quad (69)$$

$$r_{\mathrm{MEA}} = 2 * r_{\mathrm{CO}_2} \quad (70)$$

The MEA solution was pumped into the reactor over a specific time interval. Therefore, the MEA molar flow rate ($F_{\mathrm{MEA}_{in}}$) and reactor volume (V) were piece-wise defined functions. The flow of MEA into the reactor was started at t = 0 s and stopped at time t_f. With this notation, the variation of $F_{\mathrm{MEA}_{in}}$ and V over time were given by Equations 71 and 72, respectively. V_0 was the initial reactor volume and v_{in} the volumetric flow rate into the reactor.

$$F_{\mathrm{MEA}_{in}} = \begin{Bmatrix} 0 & t \leq 0 \\ F_{\mathrm{MEA}_{in}} & 0 < t < t_f \\ 0 & t \geq t_f \end{Bmatrix} \quad (71)$$

$$V = \begin{Bmatrix} V_0 & t \leq 0 \\ V_0 + v_{in} \cdot t & 0 < t < t_f \\ V_0 + v_{in} \cdot t_f & t \geq t_f \end{Bmatrix} \quad (72)$$

6.3.2 Modelling procedure

The modelling procedure used was adapted from du Preez (2014). The two species mole balances given by Equations 68 and 69 form a set of ordinary differential equations (ODEs). In each species balance, the reaction rate expression (r) for a particular reaction mechanism is defined by the species concentrations $\left(\frac{N}{V}\right)$ and rate constants (k_i). The aim of the modelling procedure was to optimize these rate constants so as to minimize the error between the predicted and experimental species molar amounts. Mathematically, the prediction error was defined for each species as the sum of squares of the differences between the corresponding predicted and experimental values (Equation 73). The subscript i represents CO_2 or MEA.

$$error = \sum\left(N_{pred} - N_{exp}\right)_i^2 \quad (73)$$

Equations 68 and 69 contain the reaction rate expressions and therefore are linear in the rate constants that are to be optimized. However, the rate expressions have concentration terms based on molar amounts, whereas the mole balance equations represent the first derivatives of the molar amounts. Therefore, to calculate a prediction error, a differential or integral method is necessary to solve the modelling problem. A differential method would require that the derivatives of the experimental data be calculated, but numerical differentiation would increase the noise in the data. Therefore, an integral method is preferred.

The MATLAB ordinary differential equation (ODE) solver, ode23s, was used to perform numerical integration in this work. The ode23s solver is suitable for systems where at least one system variable increases or decreases rapidly compared to other variables in the system (Shampine & Reichelt, 1997). In this work, ode23s was suitable because N_{CO_2} decreased to almost zero within 10 s while N_{MEA} increased over 30 s. Most N_{MEA} values were also an order of magnitude higher than N_{CO_2} values.

A multi-objective goal attainment algorithm was necessary to simultaneously minimize prediction errors in both N_{CO_2} and N_{MEA}. The MATLAB algorithm, *fgoalattain*, was used for this purpose. The prediction errors (Equation 73) were set as the objective functions. The goal of each objective was 10% of the sum of squares of the corresponding experimental measurements (Equation 74). The subscript in Equation 74 represents CO_2 or MEA. The achievement of the overall goal was evaluated using an attainment factor, with the best achievement of the goal having the attainment factor closest to zero.

$$goal = \sum(0.1N_{exp})_i^2 \quad (74)$$

Because the experimental data modelled (N_{CO_2} and N_{MEA}) were of different orders of magnitude, one objective function could have had a greater influence on the solution of optimized rate constants. To avoid this, the contribution of each species' experimental data to the solution was given the same priority. In *fgoalattain*, equal priority was given by setting the weight parameter equal to the absolute value of the goal (Equation 75).

$$weight = |goal| \quad (75)$$

Local minima were encountered on the optimization error surface. To avoid taking a local minimum for a global minimum, 20 rate constant estimation trials were performed for each optimization case. In each trial, random scaled initial estimates for the rate constants were used. Unique initial estimates would result in a better indication of the global minimum. The optimized rate constants that gave the lowest attainment factor from the 20 trials were assumed to correspond to the global minimum.

A bootstrapping method was used to estimate the confidence interval of the optimized rate constants. For each of the 20 rate estimation trials, a subset of the experimental data was used for modelling the reaction. The subset contained 90% of the experimental data selected at random. The result of each estimation trial was the optimized rate constants and the corresponding attainment factor. From the 20 optimized rate constants, the 5^{th} and 95^{th} percentile and the median were determined. These are reported with the best case optimized rate constants in Section 6.3.5.

The bootstrapping method described above to determine the 5^{th} and 95^{th} percentiles gives an approximate estimate of the rate constant confidence intervals. A better estimate of the confidence intervals can be determined from multiple executions of the optimization algorithm using the probability distribution of the experimental measurements. At each measured instant in time (t), the corresponding species molar amount used in the optimization algorithm (N_i) is a data point randomly chosen from within the confidence interval represented by the measured value's probability distribution. The optimization algorithm is then executed multiple times with different sets of randomly chosen values of N_i at corresponding t to give a range of optimized rate constants. The rate constant confidence interval is taken as the standard deviation of the set of optimized rate constants. For this study,

the confidence interval determined using the bootstrapping method was sufficient for comparing the calculated rate constants to published literature values.

A flow diagram for the modelling procedure used is given in Figure 57. In a typical execution of the modelling algorithm, the experimental data and the initial rate constant estimates are loaded. The numerical solution to the differential equations given by Equations 68 and 69 is then calculated using the initial values of the rate constants. Afterwards the value of the prediction error is calculated using Equation 73, and the value of the prediction error is compared to the goal as defined by Equation 74. If the prediction error goal is not reached, the rate constants are changed and the solution to the differential equations is calculated again. If the prediction error goal is reached, the solution to the differential equations with the optimized rate constants is returned. The rate expressions that were used in the modelling algorithm are described next.

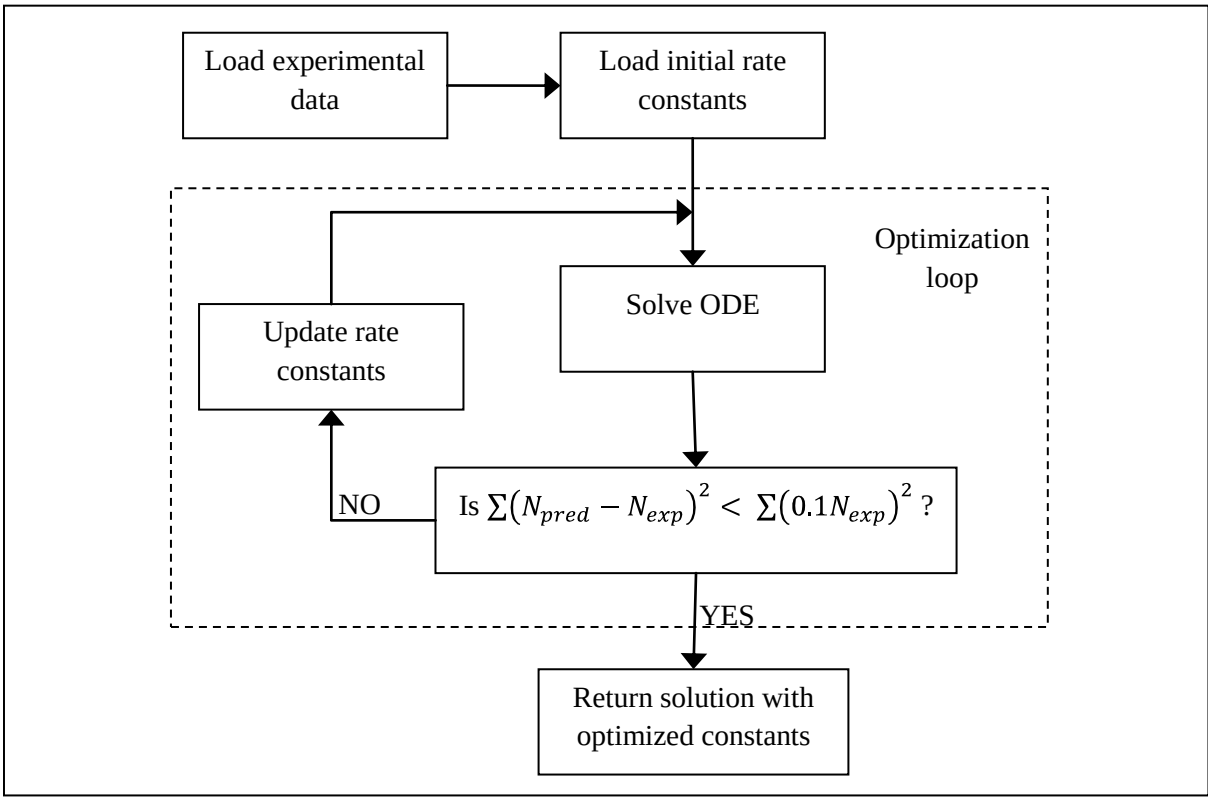

Figure 57 : Flow diagram of modelling procedure

6.3.3 Rate expressions used

Four rate expression were chosen for modelling the aqueous CO_2-MEA reaction: pseudo-first order (Equation 76), overall second order (Equation 77), overall third order (Equation 78) and termolecular (Equation 79). These are the rate expressions that have been proposed in literature for modelling the CO_2-MEA reaction. Only the forward expressions of the rate equation were considered because no product species could be measured (Section 4.3). The rate expressions used assume that CO_2 reaches 100% conversion, which is a reasonable

assumption when excess MEA is used. The assumption of 100% CO_2 conversion was validated by the equilibrium species measurements in Chapter 5.

$$-r_{CO_2} = k_1[CO_2] \quad (76)$$

$$-r_{CO_2} = k_2[CO_2][MEA] \quad (77)$$

$$-r_{CO_2} = k_3[CO_2][MEA]^2 \quad (78)$$

$$-r_{CO_2} = [CO_2][MEA] \cdot (k_{MEA}[MEA] + k_{H_2O}[H_2O]) \quad (79)$$

The pseudo-first order model (Equation 76) assumes that the concentration of MEA in solution does not change significantly over the course of the reaction. This assumption is not valid for the experimental results modelled in this work because the MEA concentration increases from zero at the beginning of each experiment, to a value 10 or 20 times the initial concentration of CO_2 in solution. However, the pseudo-first order model was considered so that the reaction rate of CO_2 could be modelled separately from MEA. Because the model is simple, it can be used in practice to provide a quick estimate of the reaction rate.

The second order model (Equation 77) is the model most used for describing the aqueous CO_2-MEA reaction (Versteeg *et al.*, 1996; Vaidya & Kenig, 2007). The third order model (Equation 78) is based on the molecularity of the reaction at CO_2 loadings below 0.3 mol CO_2/mol MEA, where 2 MEA molecules react with 1 CO_2 molecule. The termolecular model (Equation 79) is similar to the third order model, but assumes that both MEA and water deprotonate the reaction intermediate. The equilibrium results support deprotonation by only the MEA (Chapter 5). However, the termolecular model was considered because it is reported to successfully describe the reaction in both low and high MEA concentration solutions (Aboudheir *et al.*, 2003; Luo *et al.*, 2012).

The four models given above are only empirical models. A more realistic model for the reaction would incorporate the effect of CO_2 loading on the reaction, and the different products that form at each CO_2 loading. The CO_2 loading can possibly be incorporated by adding a term based on the ratio of CO_2 concentration to the MEA concentration. The importance of including the effect of CO_2 loading is supported by measurements of the reaction rate that decrease with increasing CO_2 loading (Aboudheir *et al.*, 2003).

6.3.4 Selecting appropriate time segment for modelling kinetic data

The recorded kinetic experimental data can be divided into three segments. The first occurs during the first 5 to 10 s of adding MEA into the reactor, where essentially all the CO_2 in the reactor is consumed. The second segment occurs after all the CO_2 has been consumed, during the period when MEA is still being added to the reactor (~10 to 30 s). The last segment occurs after all MEA has been added to the reactor and equilibrium of both CO_2 and MEA has been reached. The time segments are divided by the vertical dashed lines as shown in Figure 58.

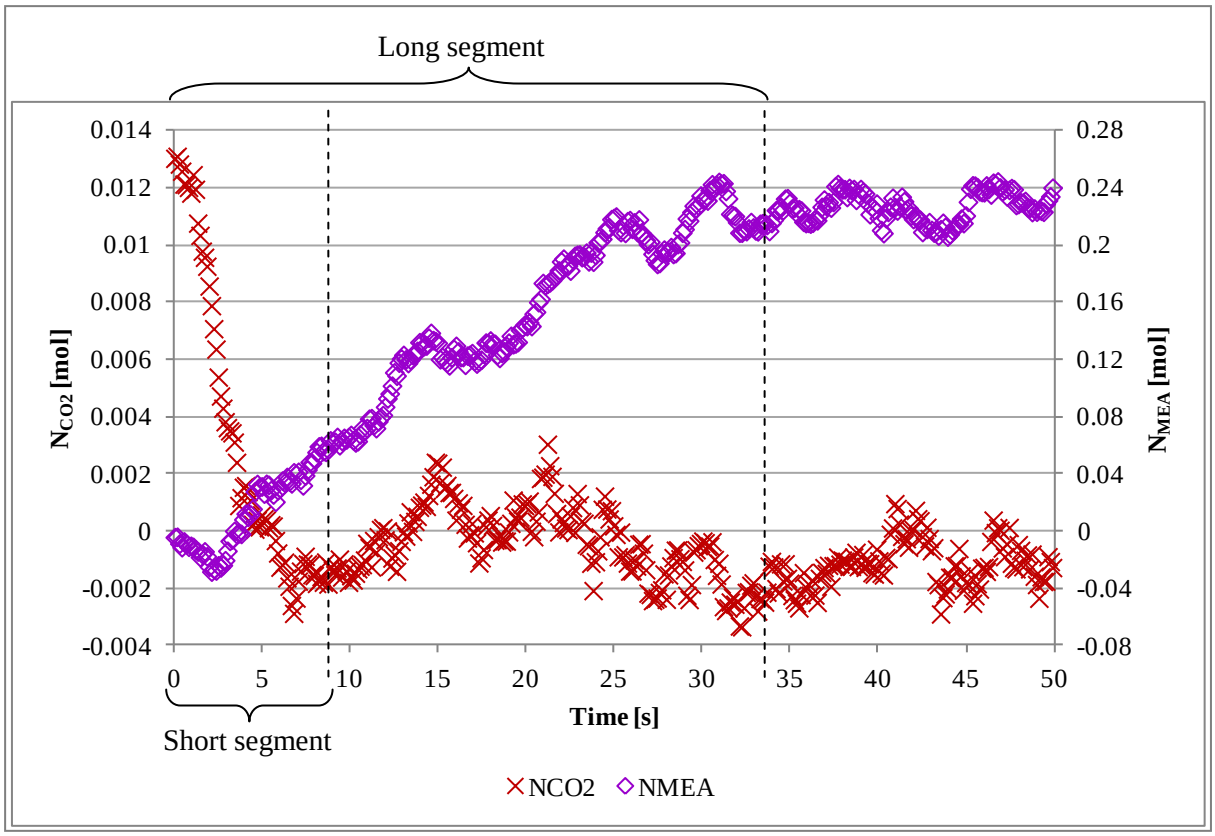

Figure 58 : Time segments used in modelling experimental data, indicated for experiment 20_30_3 conducted with 0.265 mol MEA at 0.00887 mol MEA/s and 30°C

For modelling the kinetic experimental data, only the time segments when CO_2 was reacting and MEA was added to the reactor were considered. This is because the last segment (beyond ~30 s) only reflected the reaction equilibrium that had been reached and would not add any value to modelling of the kinetic data. Two time segments were used in modelling the kinetic data. One was a "short" time segment, reflecting only the region where CO_2 is reacting. The other time segment was a "long" time segment which reflected the entire duration of adding MEA to the reactor. The short- and long-time segments are also indicated in Figure 58.

Using the short-time segments had the advantage of prioritizing the consumption rate of CO_2. Since the reaction takes place during the first 5 to 10 s of adding MEA to the reactor, this segment would be more suited to use for modelling the reaction and obtaining the kinetic rate constants. However, negligible free MEA is present in the reactor during the first 5 to 10 s of the reaction. This results in large fractional errors in N_{MEA}, which could significantly contribute to the prediction errors in the reaction rate models.

The long-time segments allow the MEA concentration to reach values that are significant compared to the noise in the data. However, the reaction only takes place during a short portion of the long-time segment. Only a third of the duration of the time segment represents the actual reaction of CO_2, whereas the rest of the time segment represents only adding of MEA to the reactor. Therefore, in modelling data in the long-time segment, adding MEA to the reactor will have a higher influence on the value of the rate constant than the reaction of CO_2.

This is because a greater percentage of the prediction error will be calculated in the region where only pumping in of MEA into the reactor is taking place, with the reaction already at completion.

The rate constants for individual experiments are given in the Appendices, with the short-time segment data in Appendix F and the long-time segment data in Appendix G. However, the two time segments gave rate constants with similar confidence intervals. The confidence intervals calculated for the second order and termolecular models from both time segments were also in agreement with published literature values. The following discussion of the optimized rate constants is limited to the rate constants determined using the short time segments. Results from the short-time segment were preferred over results from the long-time segment because short-time segment emphasized the consumption of CO_2 instead of the pumping of MEA into the reactor.

6.3.5 Optimized rate constants

The results of the reaction modelling are given in this section. The fit of the models to the experimental data is discussed first and, afterwards, the optimized rate constants for each model are presented.

6.3.5.1 Comparison of the fit of the reaction models

The plots in Figures 59 to 62 show the fit of the four reaction models considered to data collected in an experiment conducted with 0.266 mol MEA, at a MEA flow rate of 0.00871 mol/s and 30°C. The plots shown in the figures represent a typical good fit of the models to experimental data. The pseudo-first order model fit is shown in Figure 59, the second order model fit in Figure 60, the third order model fit in Figure 61, and the termolecular model fit in Figure 62. The optimized rate constants and the corresponding model mean sum of squared errors (MSE) are given in Table 15. The best CO_2 profile is predicted by the termolecular model (Figure 62), which also gives the lowest MSE in CO_2. The best MEA profile is predicted by the second order and third order models. The predicted MSE in MEA for the second and third order models has the same value of 66.

The fit of the termolecular model to the experimental MEA values is similar to the fit by the second order and third order models. This is reflected by a MSE of 68 for the termolecular model, and a MSE of 66 for the second and third order models. Graphically, the termolecular model predicts a steeper slope between 0 and 3 s for the N_{MEA} profile, where there is negligible N_{MEA} in the reaction solution. For the experimental data under consideration, the termolecular model gives the best prediction of N_{CO_2} and the worst fit of N_{MEA}. This suggests the modelling algorithm placed priority on minimizing errors in either N_{CO_2} or N_{MEA} while the overall model error was reduced (Section 6.3.2).

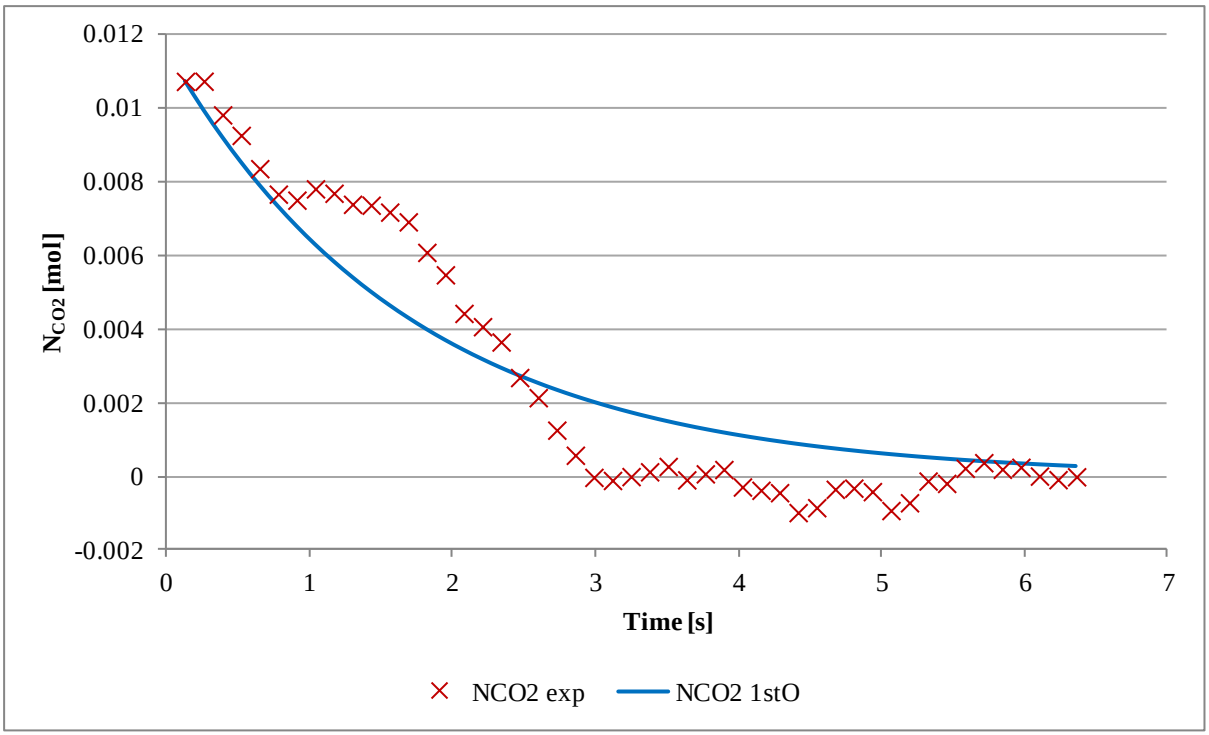

Figure 59 : Pseudo-first order model fit to experimental data collected for experiment 20-30-2 conducted with 0.266 mol MEA at 0.00871 mol MEA/s and 30°C

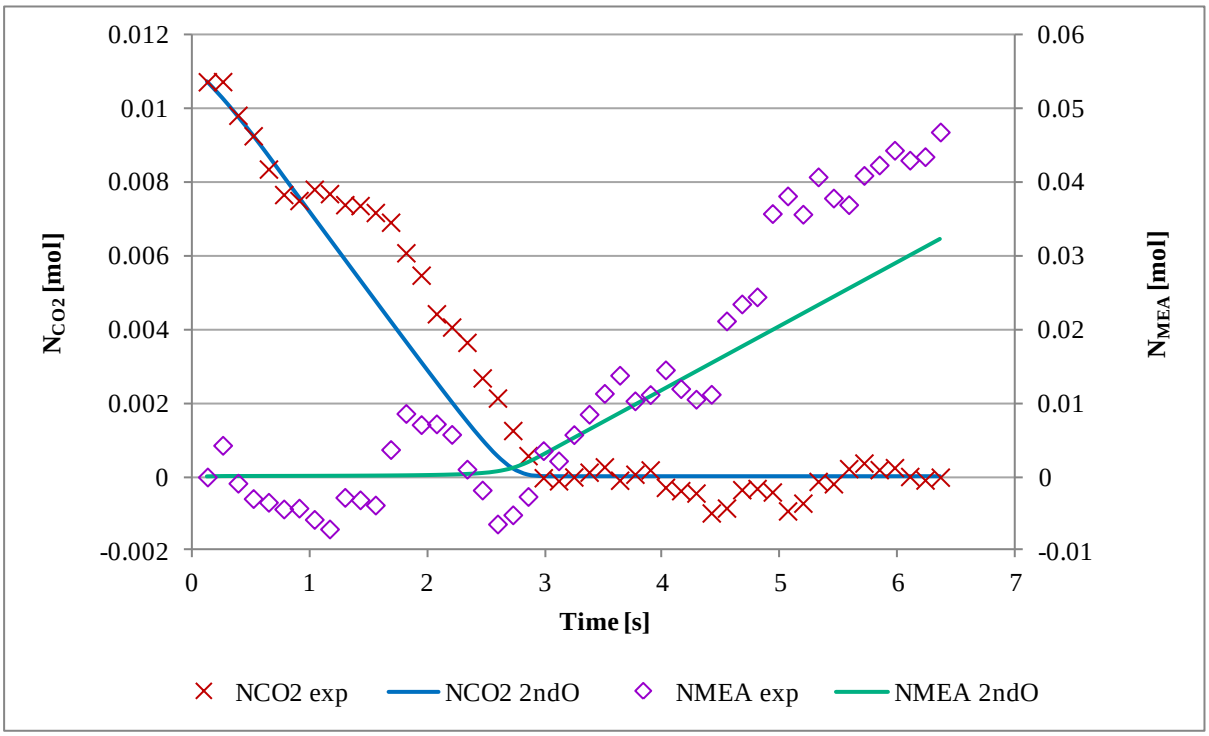

Figure 60 : Second order model fit to experimental data collected for experiment 20-30-2 conducted with 0.266 mol MEA at 0.00871 mol MEA/s and 30°C

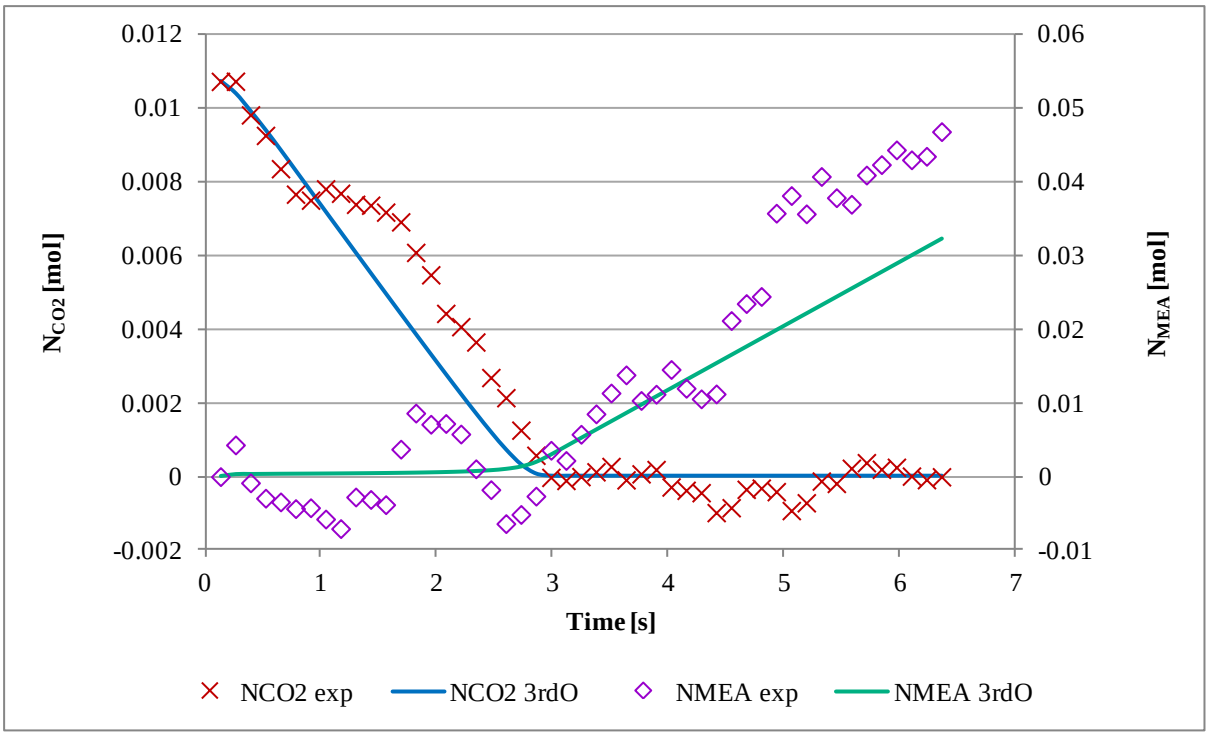

Figure 61 : Third order model fit to experimental data collected for experiment 20-30-2 conducted with 0.266 mol MEA at 0.00871 mol MEA/s and 30°C

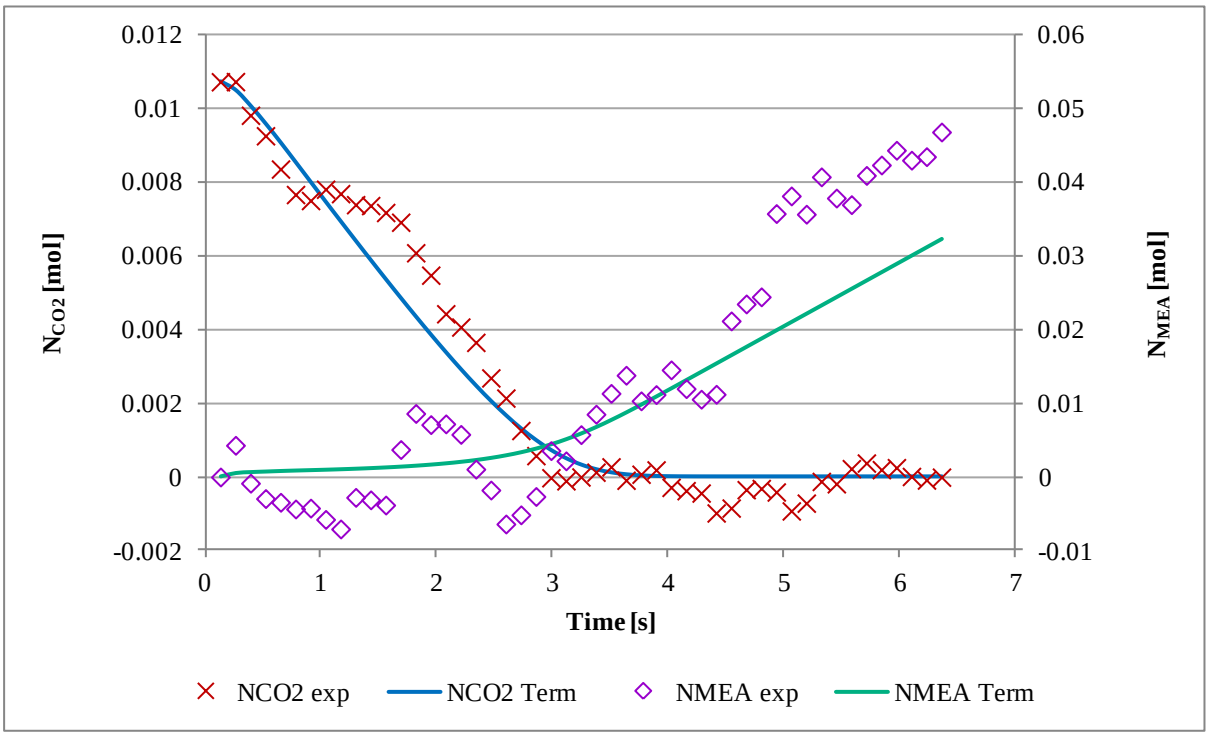

Figure 62 : Termolecular model fit to experimental data collected for experiment 20-30-2 conducted with 0.266 mol MEA at 0.00871 mol MEA/s and 30°C

Table 15 : Optimized rate constants for model fits to experimental data collected for experiment 20-30-2 conducted with 0.266 mol MEA at 0.00871 mol MEA/s and 30°C

	Estimated Rate Constants		MSE CO_2 x 10^6	MSE MEA x 10^6
Pseudo-first order	k_1 [s^{-1}]			
	0.30		1.73	–
Second order	k_2 [L/mol.s]			
	4099		1.15	66
Third order	k_3 [$L^2/mol^2.s$]			
	1318607		1.00	66
Termolecular	k_{MEA} [$L^2/mol^2.s$]	k_{H_2O} [$L^2/mol^2.s$]		
	343	2.85	0.59	68

In Figures 63 to 66, the fit of the reaction models to data collected in an experiment conducted with 0.147 mol MEA, at a MEA flow rate of 0.00508 mol/s and 25°C is shown. The plots shown in the figures represent a typical poor fit of the models to experimental data. The pseudo-first order model fit is shown in Figure 63, the second order model fit in Figure 64, the third order model fit in Figure 65, and the termolecular model fit in Figure 66. The optimized rate constants and the corresponding model MSE are given in Table 16.

The pseudo-first order model fit to the data collected at 0.147 mol MEA and 25°C is given in Figure 63. For this experiment, N_{CO_2} is under-predicted for the entire time segment chosen. The amount of CO_2 immediately drops from the initial value to zero within less than 1 s of pumping MEA into the reactor. The predicted N_{CO_2} remains zero for the rest of the reaction time plotted. This means that at the optimized rate constant value, the reaction is essentially instantaneous. The value of the rate constant is 897 s^{-1}, and is near the estimated value of 1000 s^{-1}. The MSE for CO_2 has a similar value to the MSE predicted by the third order and termolecular models (Table 16). The second order model predicts a lower MSE. However, all the models give a poor fit to N_{CO_2} even at different values of the MSE. The pseudo-first order model under-predicts N_{CO_2}, whereas the second order, third order and termolecular models over-predict N_{CO_2}.

A model fit to experimental N_{CO_2} data by the pseudo-first order model similar to Figure 63 was often encountered. The poor model fit given by the pseudo-first order model was a result of the optimized rate constant's insensitivity to the error between predicted and experimental N_{CO_2}. For experimental data from individual experiments, optimized rate constants of different orders of magnitude gave similar prediction errors. The pseudo-first order model rate constants are discussed further in Section 6.3.5.2.

In the case of Figures 64 to 66, poor fit of three of the models to experimental data was caused by errors in experimental N_{MEA}. For the second order model (Figure 64), the experimental values of N_{MEA} in the time segment plotted are higher than expected. Instead of oscillating around 0 mol, the data points oscillate around 0.025 mol, leading to the poor model fit. In all the model predictions, the initial value of N_{MEA} was set to zero because no MEA was

present in the reactor at the beginning of each experiment. Hence, the predicted MEA profile shows the plotted N_{MEA} starting at 0 mol, and then increasing to 0.025 mol when CO_2 is completely consumed. The predicted MEA profile is similar to the typical trend in experimental N_{MEA} values for experiments conducted at the 0.13 mol MEA setting: the value of N_{MEA} does not increase significantly during the first 5 to 10 s of adding MEA to the reactor. The experimental values of N_{MEA} are therefore at a constant offset from their expected values.

Other data sets that gave poor model fits showed similar constant offsets in either CO_2 or MEA. However, the data set shown in Figures 63 to 66 had the highest offset from the expected experimental amount. Therefore, model fits to this data set provided the poorest visual fit to experimental data. The optimized second order rate constant for this experiment is 16.1 L/mol.s, which is much lower than the literature average of 6 000 L/mol.s. The relatively low estimate of the rate constant may have also contributed to the poor fit of the model to the experimental data. The third order and termolecular models predicted the smallest MSE in MEA, and the largest MSE in CO_2. This observation again points to a tendency of the modelling algorithm to prioritize minimizing errors in one species above the other.

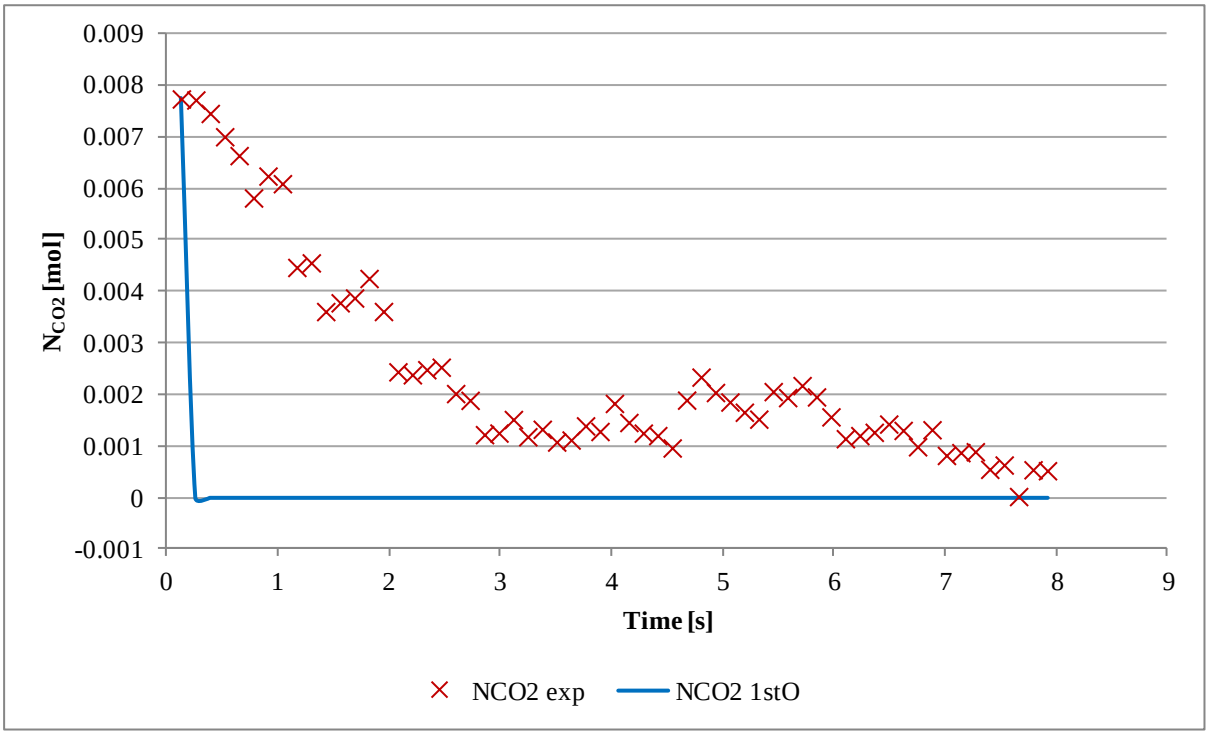

Figure 63 : Pseudo-first order model fit to experimental data collected for experiment 10-25-2 conducted with 0.147 mol MEA at 0.00508 mol MEA/s and 25°C

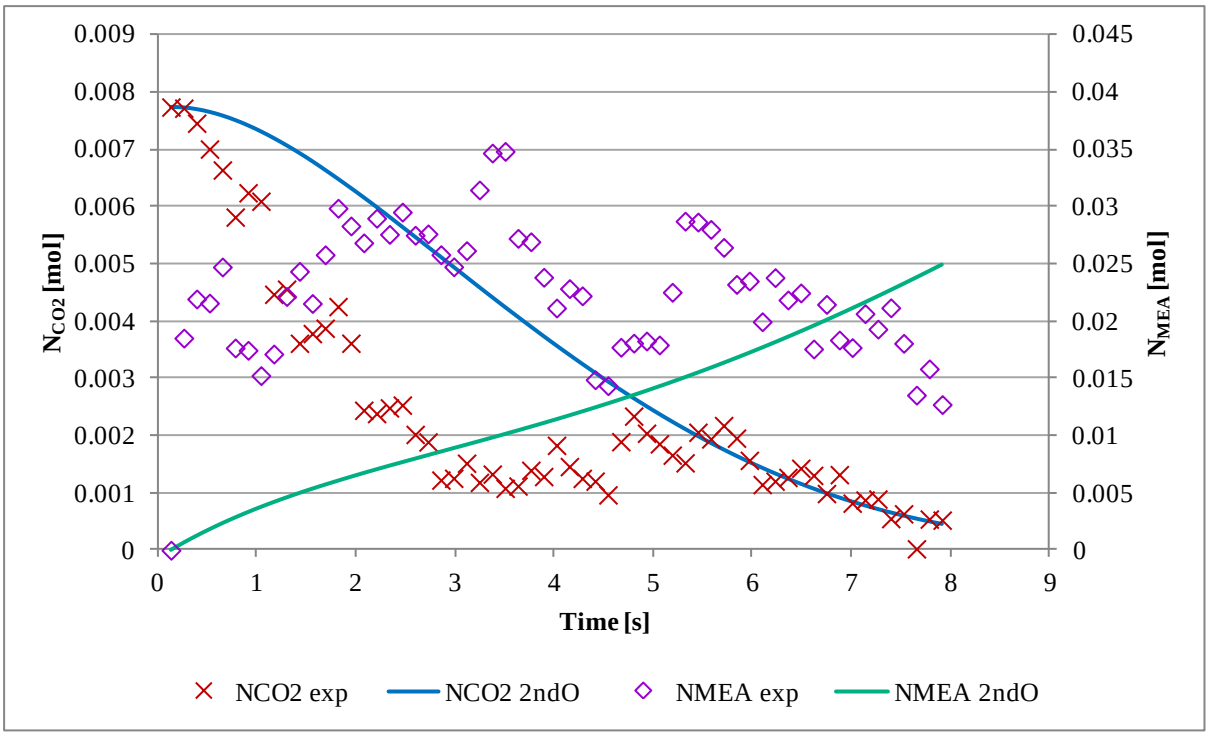

Figure 64 : Second order model fit to experimental data collected for experiment 10-25-2 conducted with 0.147 mol MEA at 0.00508 mol MEA/s and 25°C

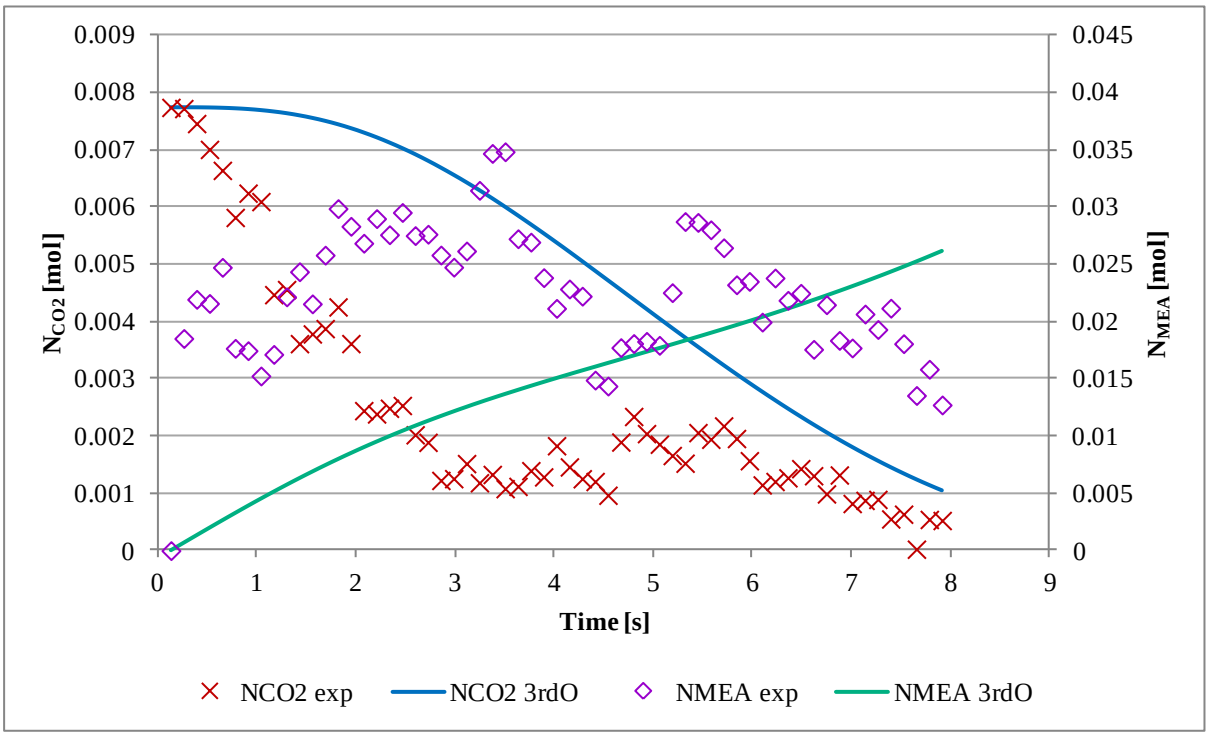

Figure 65 : Third order model fit to experimental data collected for experiment 10-25-2 conducted with 0.147 mol MEA at 0.00508 mol MEA/s and 25°C

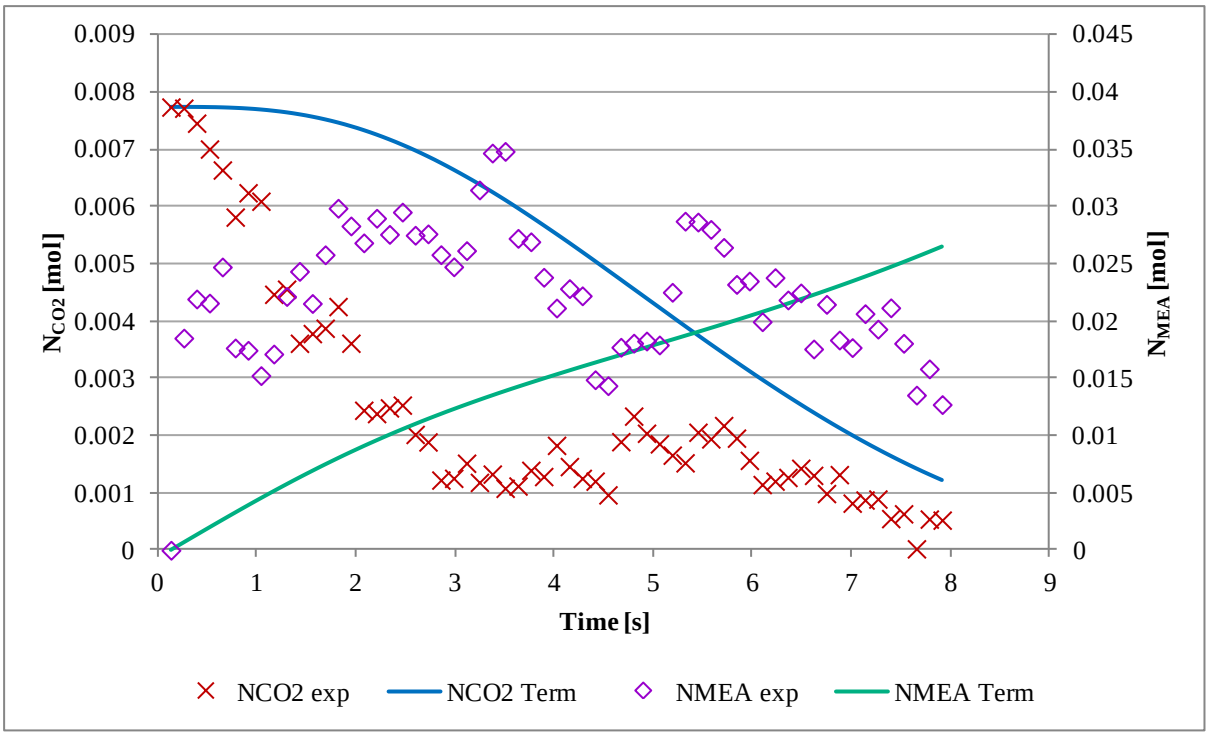

Figure 66 : Termolecular model fit to experimental data collected for experiment 10-25-2 conducted with 0.147 mol MEA at 0.00508 mol MEA/s and 25°C

Table 16 : Optimized rate constants for model fits to experimental data collected for experiment 10-25-2 conducted with 0.147 mol MEA at 0.00508 mol MEA/s and 25°C

	Estimated Rate Constants		MSE CO_2 x 10^6	MSE MEA x 10^6
Pseudo-first order	k_1 [s^{-1}]			
	897		8.92	–
Second order	k_2 [L/mol.s]			
	16.1		4.00	199
Third order	k_3 [$L^2/mol^2.s$]			
	280		9.38	156
Termolecular	k_{MEA} [$L^2/mol^2.s$]	k_{H_2O} [$L^2/mol^2.s$]		
	133	0.00	9.92	155

In general, better fit to experimental N_{MEA} was found with experimental data collected at the higher MEA concentration setting, when using short-time segments for modelling the data. This is because at the higher concentration, the amount of MEA in solution increased significantly from near 5 s after adding MEA to the reactor. At the higher values of N_{MEA}, the ratio of N_{MEA} to experimental noise would be higher than for the low MEA concentration data. The lower relative error at higher MEA concentrations would then lead to better model predictions of the experimental data.

6.3.5.2 Pseudo-first order rate constants

The pseudo-first order model is valid under experimental conditions where N_{MEA} is in great excess compared to N_{CO_2}. Under these conditions, the initial estimate of k_1 would be given by

Equation 80. The initial estimate of k_1 is based on the average value for the literature second order rate constant and the MEA concentration used in experimental work. For experiments in the semi-batch reactor, the value of [MEA] in the reactor changed from zero when feed of MEA to the reactor was started, to the final value at the end of the experiment. This means that a range of [MEA] values between zero and approximately 0.52 mol/L were encountered during the kinetic experiments.

$$k_{1,expected} = k_{2,avg} \cdot [\text{MEA}] = 6\,000\ \text{L/mol.s} \times 0.2\ \text{mol/L} = 1\,200\ \text{s}^{-1} \quad (80)$$

The value of [MEA] used in Equation 80 was 0.2 mol/L, which is the average concentration calculated over the time during which MEA is pumped into the reactor for both concentration settings. The value of the initial rate constant was then k_1 = 1 000 s^{-1} when rounded off to one significant figure.

Results from modelling the experimental data with the pseudo-first order model are given in Table 17. The values given in the table are the averages calculated from the three experiments conducted at each MEA concentration and temperature setting. The table gives the best estimate of the rate constants, with the confidence interval in the rate constant values given by the 5th and 95th percentiles. The prediction error in the model is given by the mean sum of squares of the error between experimental and predicted molar amounts of CO_2 (MSE CO_2). The MSE values given for each concentration-temperature setting are also the averages of the three experiments conducted at each setting.

Table 17 : Optimized pseudo-first order rate constants

	0.13 mol MEA		
T [°C]		k_1 [s^{-1}]	**MSE CO_2 x 10^6**
20	Best fit	61.5	10.98
	Upper bound (95%)	931	16.89
	Median	576	16.89
	Lower bound (5%)	76.8	16.89
25	Best fit	827	13.55
	Upper bound (95%)	908	13.55
	Median	422	13.55
	Lower bound (5%)	57.5	13.55
30	Best fit	46.3	9.76
	Upper bound (95%)	932	18.31
	Median	488	18.31
	Lower bound (5%)	43.4	14.05

From Table 17, the MSE values show little sensitivity to the values of the rate constants. For example, for the experiments conducted with 0.13 mol MEA at 25°C, the range of rate constants is 57.5 to 908 s^{-1}, showing an increase of almost 20-fold. However, the MSE for this range of rate constants is constant at 13.55.

Table 17 (continued)

	0.26 mol MEA		
T [°C]		k_1 [1/s]	**MSE CO_2 x 10^6**
20	Best fit	337	8.04
	Upper bound (95%)	834	14.32
	Median	446	14.32
	Lower bound (5%)	54.6	14.31
25	Best fit	222	19.50
	Upper bound (95%)	943	26.04
	Median	610	26.04
	Lower bound (5%)	109	19.50
30	Best fit	355	17.16
	Upper bound (95%)	917	23.02
	Median	555	23.02
	Lower bound (5%)	61.7	23.02

The MSE likely does not change significantly with the different values of the rate constants because of the noise in the experimental data. Visually, the MSE represents the average distance between the predicted model species molar amounts and the experimental values. The position of the predicted profile relative to the experimental data points can be changed by changing the model rate constants. However, when considering noisy experimental data, a change in the position of the predicted profile may decrease the distance between the predicted profile and some experimental data points, while simultaneously increasing the distance between the predicted profile and other experimental data points. The overall effect then is that the average distance between the predicted profile and the experimental data is not changed significantly. Hence, the MSE may appear to not change significantly with changing values of the rate constants.

The Arrhenius plots for the best case pseudo-first order rate constants are given in Figures 67 and 68. The low MEA concentration data (0.013 mol) and the high MEA concentration data (0.26 mol) are plotted separately in Figures 67 and 68, respectively. Both data sets give Pearson's R^2 values that are less than 0.1, indicating poor fit of the rate constants to the Arrhenius relationship (Equation 81). The activation energy in Equation 81 represents the minimum energy needed to initiate the reaction, and a realistic value of the activation energy would be positive for an elementary reaction (Silberberg, 2007). The slope of the Arrhenius plot $\left(-\frac{E}{R}\right)$ would also be negative. The slope in Figure 67 is positive, suggesting that the CO_2-MEA reaction is not fundamentally a pseudo-first order reaction. However, the low Pearson's R^2 value for the plot also suggests that the positive slope may be a result of the error in the experimental data: scatter in the experimental measurements lead to rate constants with a large degree of scatter, leading to an Arrhenius plot with a low Pearson's R^2 value.

$$\ln(k) = \ln(A) - \frac{E}{R} \cdot \frac{1}{T} \qquad (81)$$

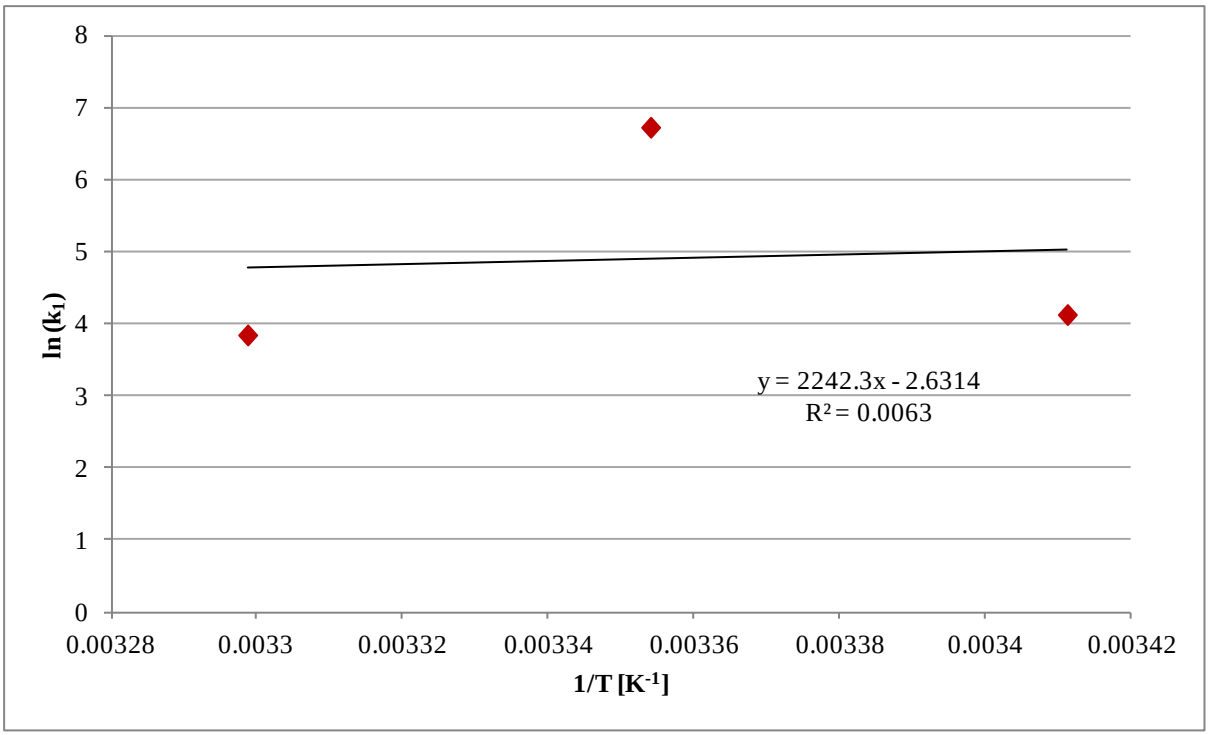

Figure 67 : Arrhenius plot of k_1 for the 0.13 mol MEA series data

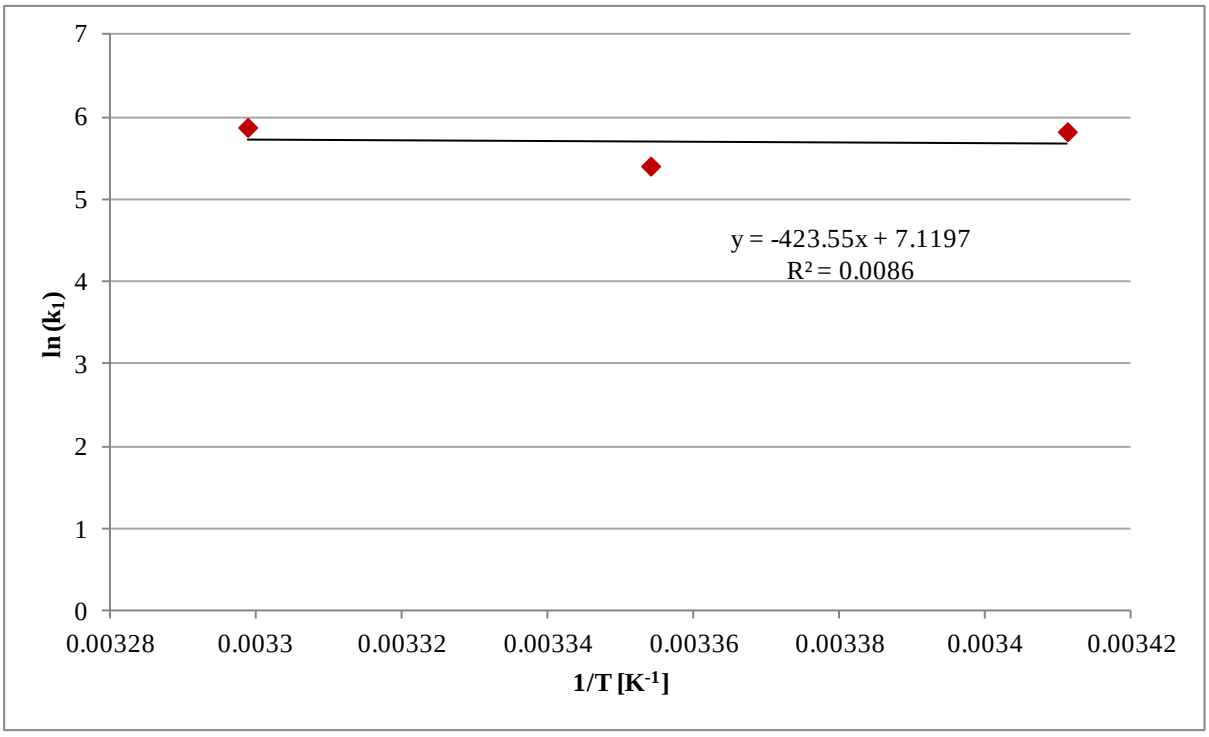

Figure 68 : Arrhenius plot of k_1 for the 0.26 mol MEA series data

6.3.5.3 Second order rate constants

The optimized rate constants for the second order model are given in Table 18. The values given in the table are the averages values calculated from the three experiments conducted at each MEA concentration and temperature setting. The initial rate constant estimate was k_2 = 6 000 L/mol.s. This value of the initial estimate is the average rate constant value reported in

literature for experiments conducted at 25°C. The values reported in Table 18 are the best estimate of the rate constants, as well as the 95th percentile, median and 5th percentile. The model prediction error is given as the mean sum of squares of the error (MSE) between experimental and predicted molar amounts of each species.

Table 18 : Optimized second order rate constants

	0.13 mol MEA			
T [°C]		k_2 [L/mol.s]	**MSE CO_2 x 10^6**	**MSE MEA x 10^6**
20	Best fit	23367	6.82	248
	Upper bound (95%)	39774	3.84	293
	Median	3742	3.86	292
	Lower bound (5%)	944	6.71	249
25	Best fit	276	2.90	151
	Upper bound (95%)	6343	1.06	224
	Median	3545	1.05	224
	Lower bound (5%)	429	2.37	158
30	Best fit	3377	1.98	156
	Upper bound (95%)	39489	3.41	160
	Median	3121	3.46	161
	Lower bound (5%)	790	1.98	156
	0.26 mol MEA			
T [°C]		k_2 [L/mol.s]	**MSE CO_2 x 10^6**	**MSE MEA x 10^6**
20	Best fit	3192	2.90	259
	Upper bound (95%)	5352	3.12	258
	Median	2557	3.02	258
	Lower bound (5%)	883	2.74	260
25	Best fit	530	1.45	81
	Upper bound (95%)	5687	5.23	90
	Median	3464	5.15	90
	Lower bound (5%)	252	1.33	81
30	Best fit	3044	3.01	117
	Upper bound (95%)	5585	3.24	114
	Median	3418	3.18	114
	Lower bound (5%)	377	2.55	115

For the best case optimized rate constants, the model does not simultaneously give the lowest MSE in both CO_2 and MEA. The squared errors in CO_2 and MEA could not be minimized simultaneously, even when equal weight was given to both minimization goals. This means that in each execution of the modelling algorithm, the solution was biased to minimizing either the CO_2 squared errors or the MEA squared errors. The reason for the bias could be that the CO_2 experimental values decreased over time, while the MEA experimental values increased. The opposing trends could then have forced the modelling algorithm to place more emphasis on minimizing errors in one species over the other.

The optimized rate constants are compared to the literature values in Figures 69 and 70, where the error bars indicate the 95% confidence interval of the rate constants. Figure 69 shows the rate constants from the low MEA concentration setting (0.13 mol MEA), and Figure 70 the rate constants from the high MEA concentration setting (0.26 mol MEA). Published models are plotted in Figures 69 and 70 without including published data points as well. In both figures, the range in rate constants is in agreement with the models, with most of the published values falling within the range specified by the confidence interval at each temperature. The published models plotted in the figures were determined from data collected from different experimental methods. Agreement between the calculated rate constants and the literature values means that the semi-batch reactor is valid for use in investigating the aqueous CO_2-MEA reaction.

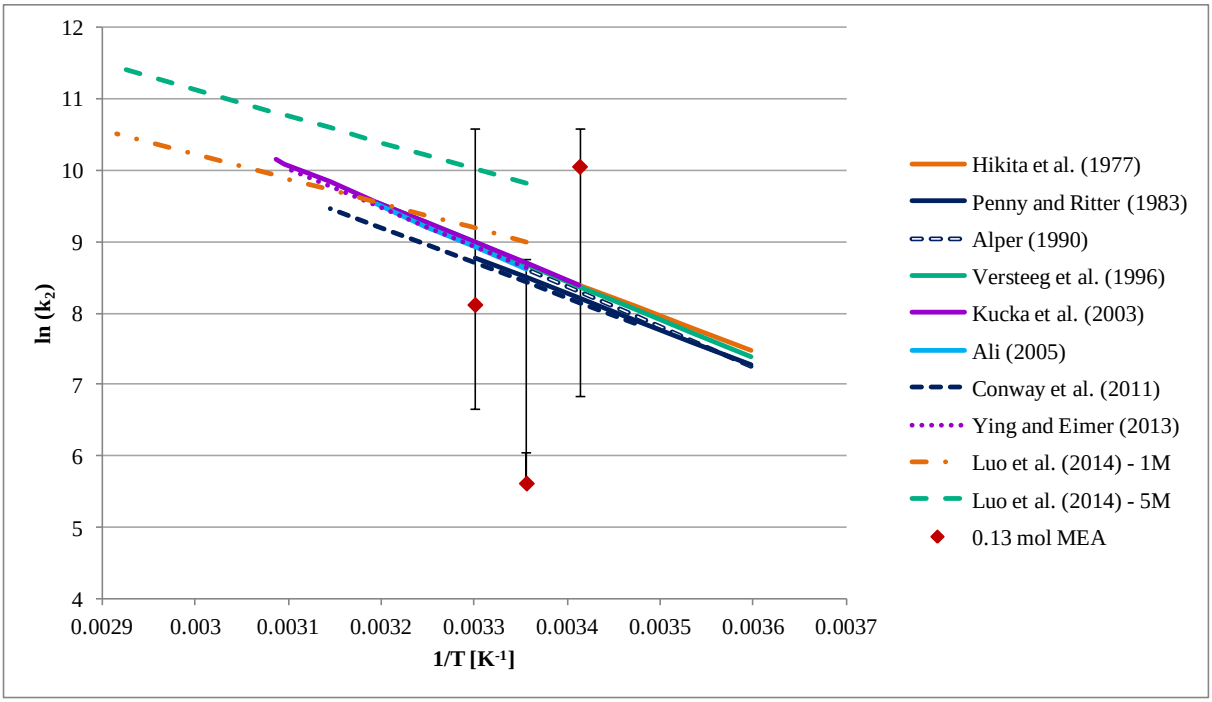

Figure 69 : Comparison of optimized second order rate constants for the 0.13 mol MEA series with literature models

Although the rate constant values generated are in general agreement with literature, the large spread in rate constant values at each temperature is proof of the large uncertainty in the calculated rate constants. The rate constants are, therefore, not suitable for use in design or modelling of absorption columns. The uncertainty in the rate constants can be reduced by modelling experimental data with less noise. For the existing experimental setup, experimental data with reduced noise can be generated by increasing the chemical species concentrations, as well as increasing data collection time for recording sample spectra.

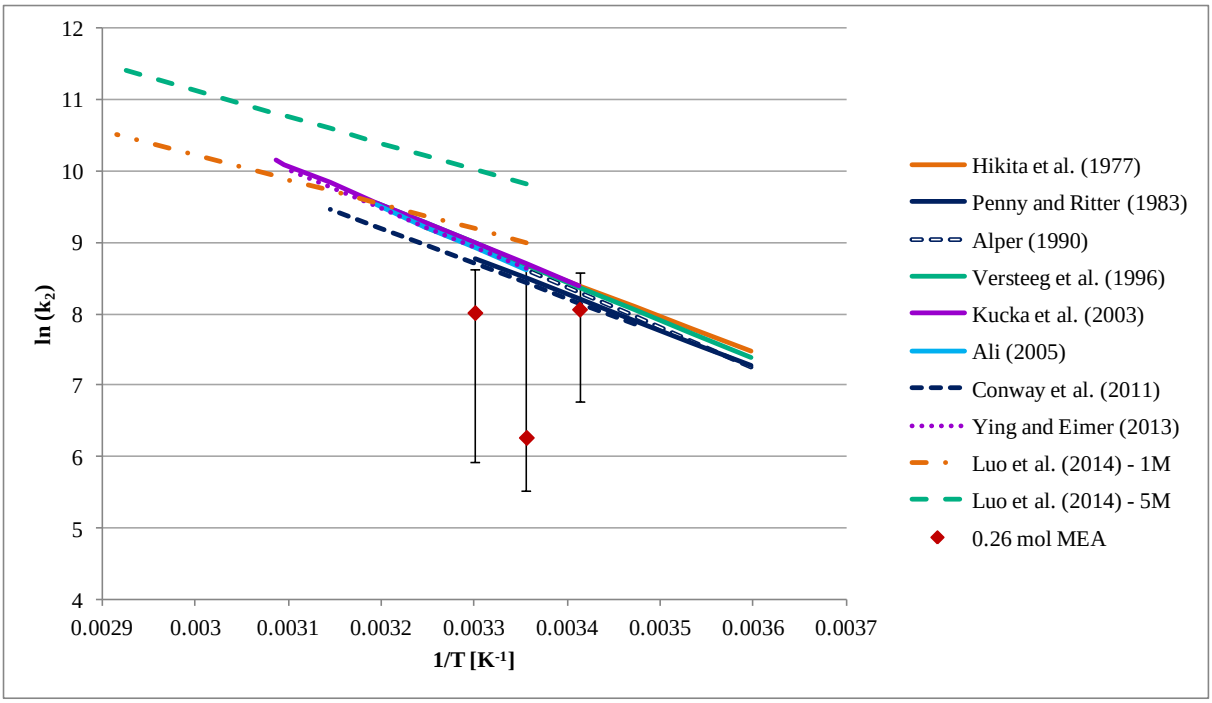

Figure 70 : Comparison of optimized second order rate constants for the 0.26 mol MEA series with literature models

Reduction of noise in experimental measurements using both these techniques was demonstrated in the previous chapter for measurements made at equilibrium. In these measurements, the species absorbances' uncertainty was decreased by increasing the data collection time. The product species absorbances' uncertainty was also decreased by increasing the product species concentration, through increasing the total amount of reagents added to the reactor. For the kinetic experiments, the data collection time was kept low in order to generate as many data points as possible in each experiment. The concentrations of product species could not be detected accurately (Section 4.3), and the concentrations could not be increased above the detection limits due to the small amounts of CO_2 dissolved in water for each experiment.

The Arrhenius plots for the best case second order rate constants are given in Figures 71 and 72. The low MEA concentration data (0.013 mol) are plotted in Figure 71 and the high MEA concentration data (0.26 mol) in Figure 72. The Pearson's R^2 value for the data sets are 0.1968 for the low MEA concentration series and 0.0011 for the high MEA concentration series. The low R^2 values are proof of a poor fit of the rate constants to the Arrhenius relationship, and support the unreliability of the individual rate constants. Furthermore, the slopes of both plots are positive, indicating a predicted negative reaction activation energy. A negative activation energy suggests the reaction is not fundamentally of second order.

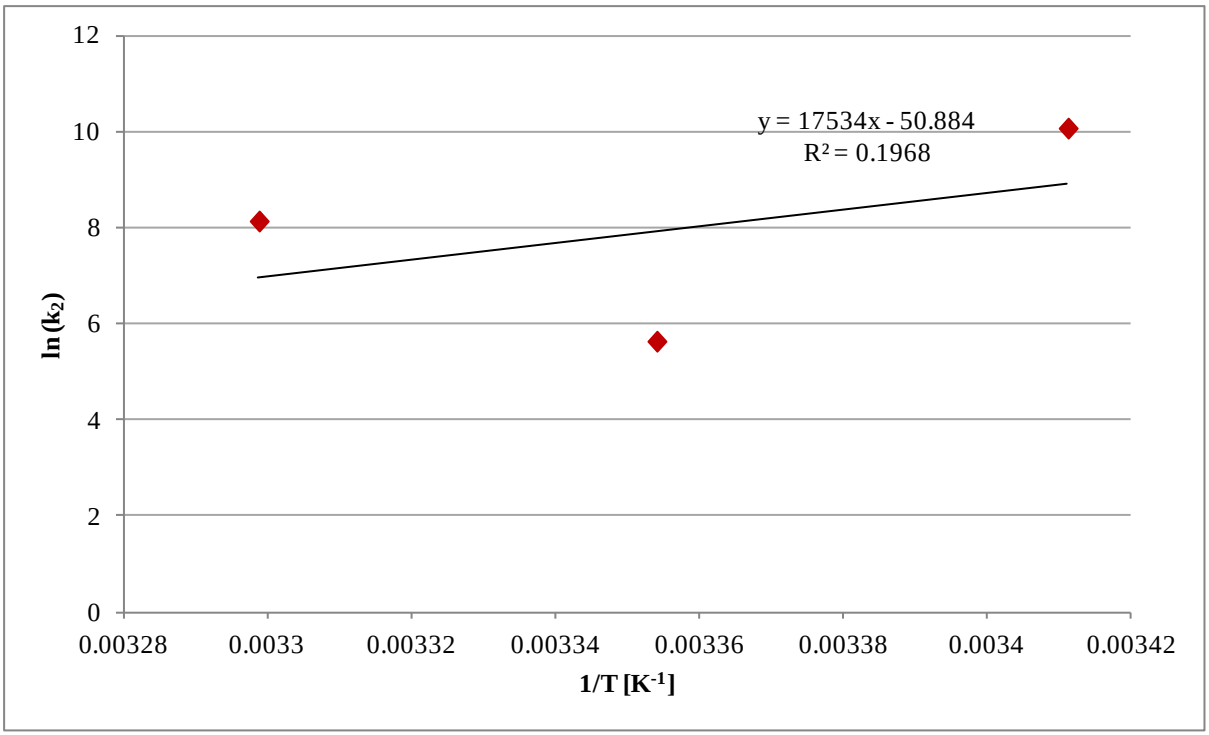

Figure 71 : Arrhenius plot of the second order rate constants for the 0.13 mol MEA series data

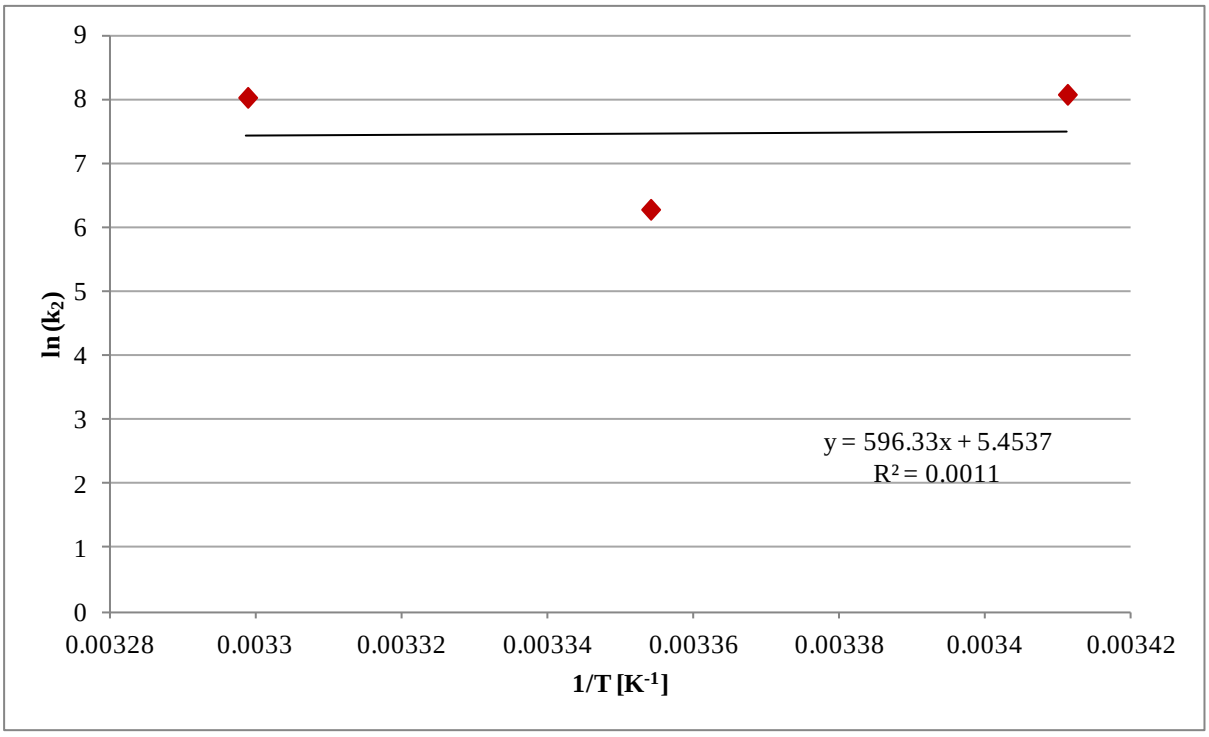

Figure 72 : Arrhenius plot of the second order rate constants for the 0.26 mol MEA series data

6.3.5.4 Third order rate constants

The optimized rate constants for the third order model are given in Table 19. The values given in the table are the average values calculated from the three experiments conducted at each MEA concentration and temperature setting. The initial rate constant estimate was k_3 = 10 000 $L^2/mol^2.s$. The initial estimate was based on the average value for the literature second

order rate constant, and the average MEA concentration used in experimental work (Equation 82). An order of magnitude estimate (k_1 = 10 000 $L^2/mol^2.s$) was used rather than the actual calculated value of k_1 = 30 000 $L^2/mol^2.s$. The lower value was to take into account the lower MEA concentrations that were present in the reactor during the first 10 s of the reaction.

$$k_{3,expected} = \frac{k_{2,average}}{[\text{MEA}]} = \frac{6000\ \text{L/mol.s}}{0.2\ \text{mol/L}} = 30\ 000\ \text{L}^2/\text{mol}^2.\text{s} \qquad (82)$$

Table 19 gives the best estimate of the rate constants, with the confidence interval in the rate constant values given by the 5th and 95th percentiles. The prediction error in the model is given by the mean sum of squares of the error between experimental and predicted molar amounts of CO_2 (MSE CO_2). The values given for each concentration-temperature setting are the averages of the three experiments conducted at each setting.

Table 19 : Optimized third order rate constants

	0.13 mol MEA			
T [°C]		k_3 [$L^2/mol^2.s$]	**MSE CO_2 x 10^6**	**MSE MEA x 10^6**
20	Best fit	1431099	7.38	246
	Upper bound (95%)	4030389	5.30	267
	Median	589946	6.24	263
	Lower bound (5%)	217036	7.05	262
25	Best fit	381953	4.78	137
	Upper bound (95%)	1135990	1.63	185
	Median	5066	2.46	166
	Lower bound (5%)	3057	3.49	154
30	Best fit	3273771	2.13	157
	Upper bound (95%)	14945529	2.86	157
	Median	904965	2.58	157
	Lower bound (5%)	31605	4.05	181
	0.26 mol MEA			
T [°C]		k_3 [$L^2/mol^2.s$]	**MSE CO_2 x 10^6**	**MSE MEA x 10^6**
20	Best fit	732795	3.11	280
	Upper bound (95%)	1168479	2.43	260
	Median	104091	1.76	265
	Lower bound (5%)	4383	2.01	290
25	Best fit	104203	1.41	82
	Upper bound (95%)	139549	2.38	88
	Median	5747	1.34	97
	Lower bound (5%)	2160	0.73	101
30	Best fit	534779	2.58	114
	Upper bound (95%)	448630	2.62	113
	Median	7356	2.02	132
	Lower bound (5%)	2802	2.70	151

The optimized rate constants are larger than the expected value of k_3 = 30 000 $L^2/mol^2.s$. All the best case rate constants are larger than the expected value by 1 or 2 orders of magnitude. The 0.13 mol MEA data at 25°C, and the 0.26 mol MEA data at all three temperatures have confidence intervals that include k_3 = 15 000 $L^2/mol^2.s$. The general overestimation of rate constants at especially the low MEA concentration setting could be due to selecting the short-time segment for modelling the experimental data. The short-time segment included the first 10 of the reaction. Insignificant concentrations of MEA were measured during the first 10 s of the reaction for the 0.13 mol MEA setting, and during the first 5 s of the reaction for the 0.26 mol MEA setting. In the third order model rate expression (Equation 83), the MEA concentration term is squared, and the already small MEA concentration values become even smaller. A high rate constant may then be predicted by the modelling algorithm to overcompensate for low MEA concentration values in order to match the predicted reaction rate with the experimental reaction rate.

$$-r_{CO_2} = k_3[CO_2][MEA]^2 \quad (83)$$

The Arrhenius plots for the best case third order rate constants are given in Figures 73 and 74. The low MEA concentration data (0.013 mol) are plotted in Figure 73 and the high MEA concentration data (0.26 mol) in Figure 74. The Pearson's R^2 values for the data sets are 0.139 for the low MEA concentration series and 0.0256 for the high MEA concentration series. The low R^2 values indicate poor dependence of the rate constants on temperature, and poor fit to the Arrhenius relationship. The low R^2 values also suggest the individual third order rate constants calculated are unreliable.

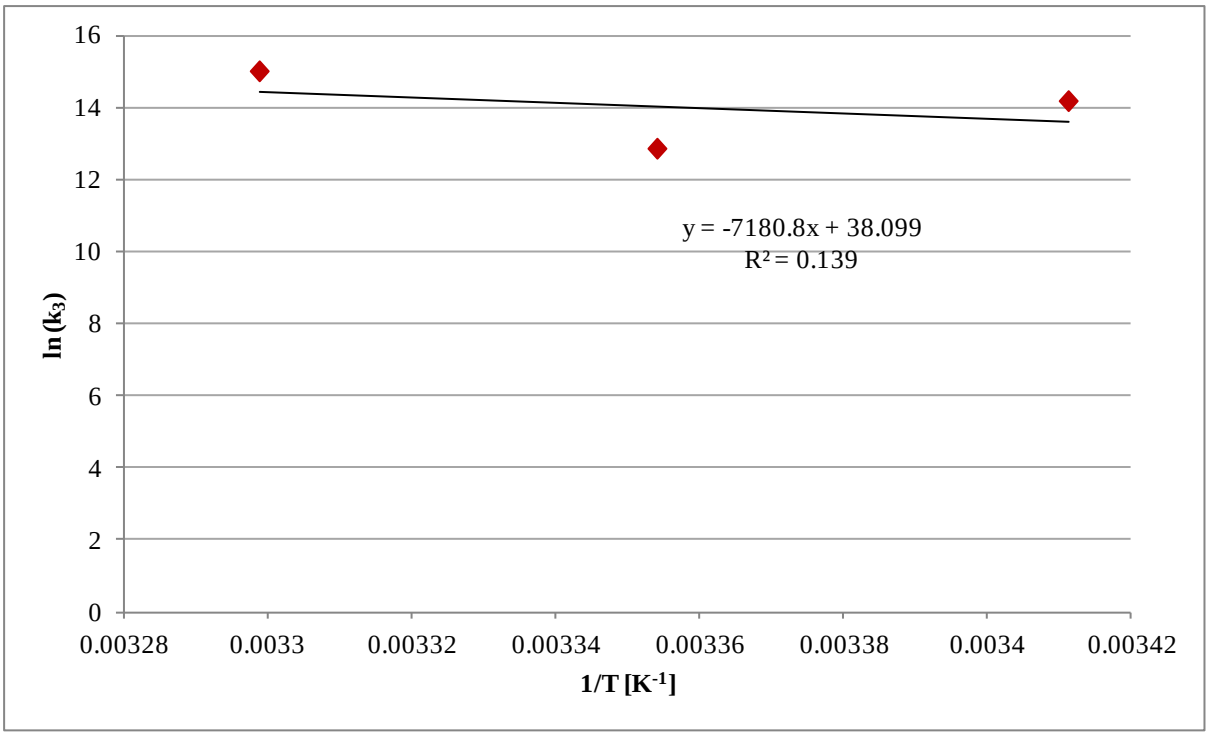

Figure 73 : Arrhenius plot of the third order rate constant for the 0.13 mol MEA series data

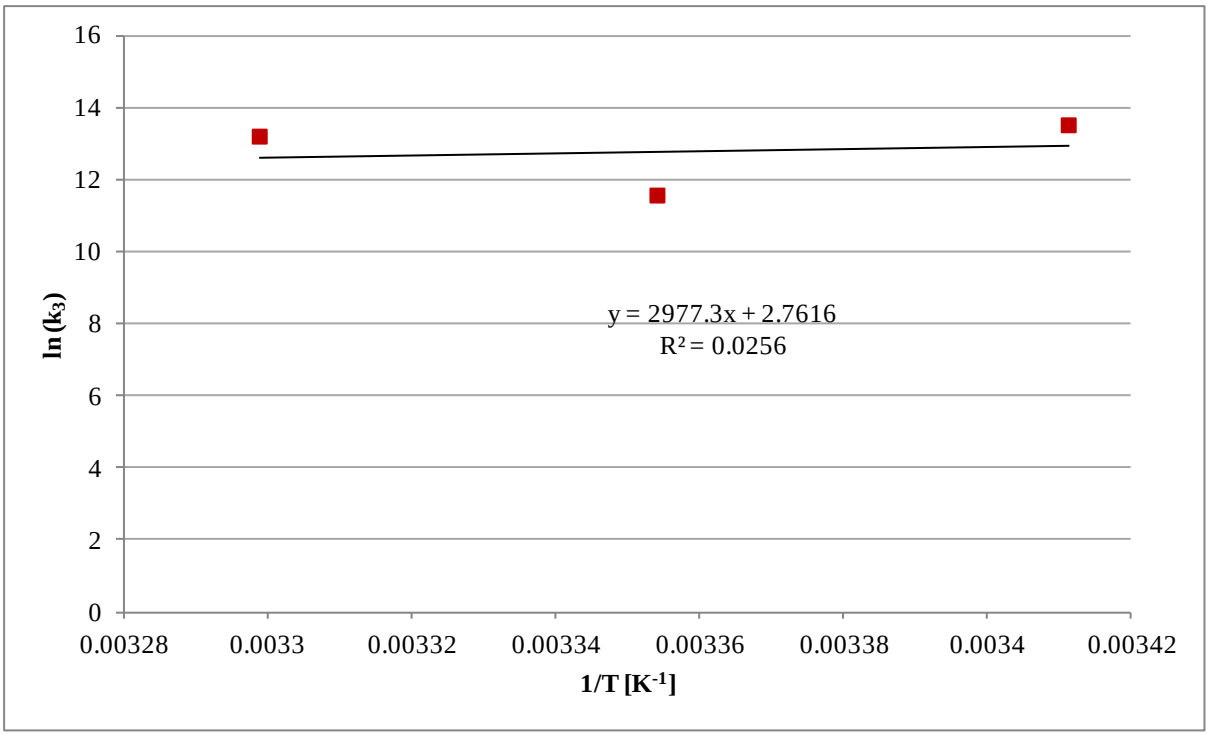

Figure 74 : Arrhenius plot of the third order rate constant for the 0.26 mol MEA series data

6.3.5.5 Termolecular rate constants

The optimized rate constants for the termolecular model are given in Table 20. The values given in the table are the average values calculated from the three experiments conducted at each MEA concentration and temperature setting. The optimized termolecular rate constants are given in Table 20. The initial rate constant estimates were k_{MEA} = 2 000 $L^2/mol^2.s$ and $k_{\mathrm{H_2O}}$ = 90 $L^2/mol^2.s$. These estimates were based on the results of Aboudheir *et al*. (2003) and Luo *et al*. (2012). The values reported in the table are the best estimate of the rate constants, as well as the 95th percentile, median and 5th percentile. The model prediction error is given as the mean sum of squares of the error (MSE) between experimental and predicted molar amounts of each species.

The best case optimized rate constants in Table 20 for deprotonation by MEA (k_{MEA}) are all lower than the initial estimate of 2 000 $L^2/mol^2.s$. For the water deprotonation rate constants ($k_{\mathrm{H_2O}}$), all the high MEA concentration (0.26 mol) rate constant values are near the initial estimate. At the low MEA concentration setting (0.13 mol), the k_{MEA} value at only 25°C is similar to the initial estimate. The value at 30°C is three times the initial estimate, and the value at 20°C is three orders of magnitude higher.

Table 20 : Optimized termolecular rate constants

	0.13 mol MEA				
T [°C]		k_{MEA} [L^2/mol^2.s]	k_{H_2O} [L^2/mol^2.s]	**MSE CO_2 x 10^6**	**MSE MEA x 10^6**
20	Best fit	212	86174.0	6.58	250
	Upper bound (95%)	1538	44318	5.58	262
	Median	628	372.0	6.67	249
	Lower bound (5%)	51.0	113.18	10.44	226
25	Best fit	588	14.751	4.99	135
	Upper bound (95%)	1466	106.2	1.07	224
	Median	467	21.8	2.66	154
	Lower bound (5%)	28	12.107	13.16	125
30	Best fit	1251	61.0	1.88	155
	Upper bound (95%)	5735	24712.4	3.42	160
	Median	868	151.3	3.42	160
	Lower bound (5%)	64	41.21	22.27	183
	0.26 mol MEA				
T [°C]		k_{MEA} [L^2/mol^2.s]	k_{H_2O} [L^2/mol^2.s]	**MSE CO_2 x 10^6**	**MSE MEA x 10^6**
20	Best fit	838	25.5	3.03	260
	Upper bound (95%)	1813	408.6	3.19	258
	Median	917	53.2	3.12	258
	Lower bound (5%)	31	5.22	2.59	262
25	Best fit	1376	27.171	1.45	80
	Upper bound (95%)	2597	734.4	5.34	89
	Median	970	29.6	5.06	90
	Lower bound (5%)	96.1	2.252	2.65	100
30	Best fit	902	24.294	2.72	112
	Upper bound (95%)	2809	118.2	2.95	112
	Median	859	28.1	2.90	112
	Lower bound (5%)	189	6.811	6.66	117

The optimized rate constants are compared to published literature values in Figures 75 to 78. Figures 75 and 76 give the MEA deprotonation rate constants at the 0.13 and 0.26 mol MEA settings, respectively, and Figures 77 and 78 give the water deprotonation rate constants at the 0.13 and 0.26 mol MEA settings, respectively. In all the figures, error bars represent the 95% confidence interval for each rate constant value. The range of rate constants represented by the confidence intervals are in general agreement with the literature values. Agreement between the rate constant confidence intervals and the literature values validates the rate constants calculated in this work.

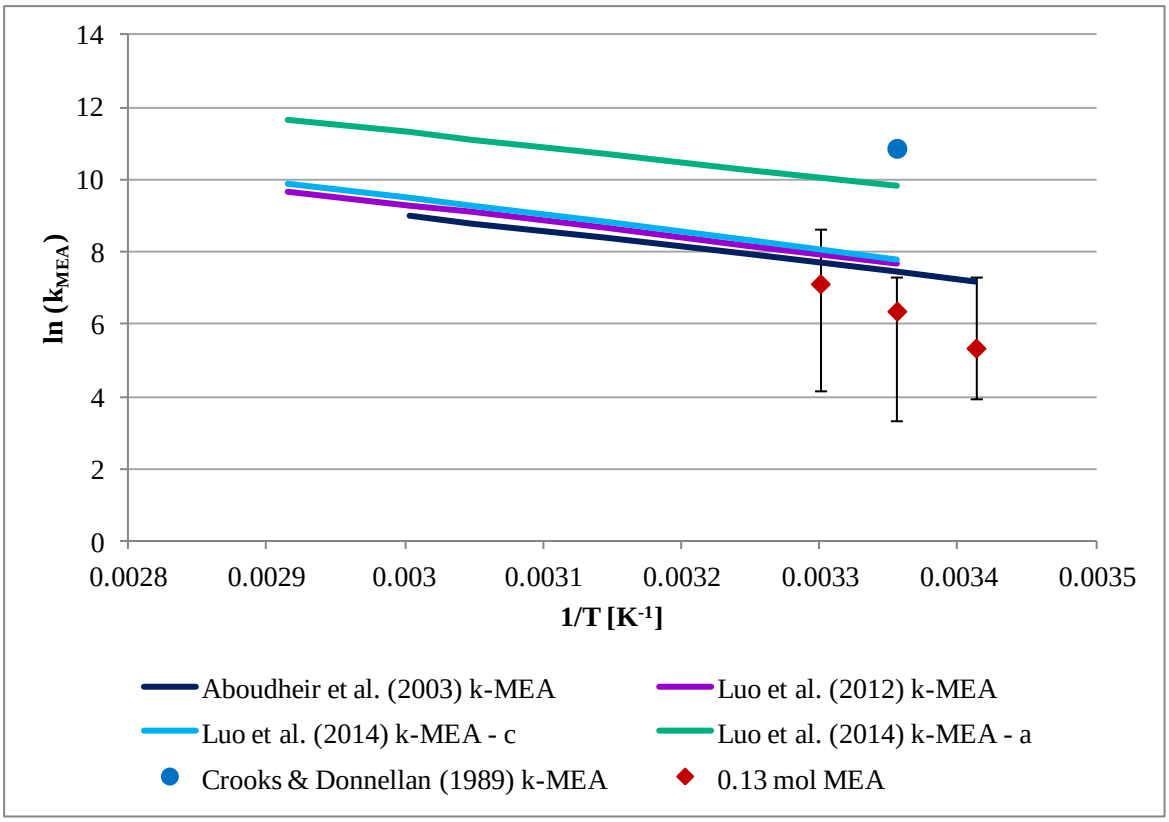

Figure 75 : Comparison of optimized MEA deprotonation rate constants for the termolecular model for the 0.13 mol MEA series with literature data

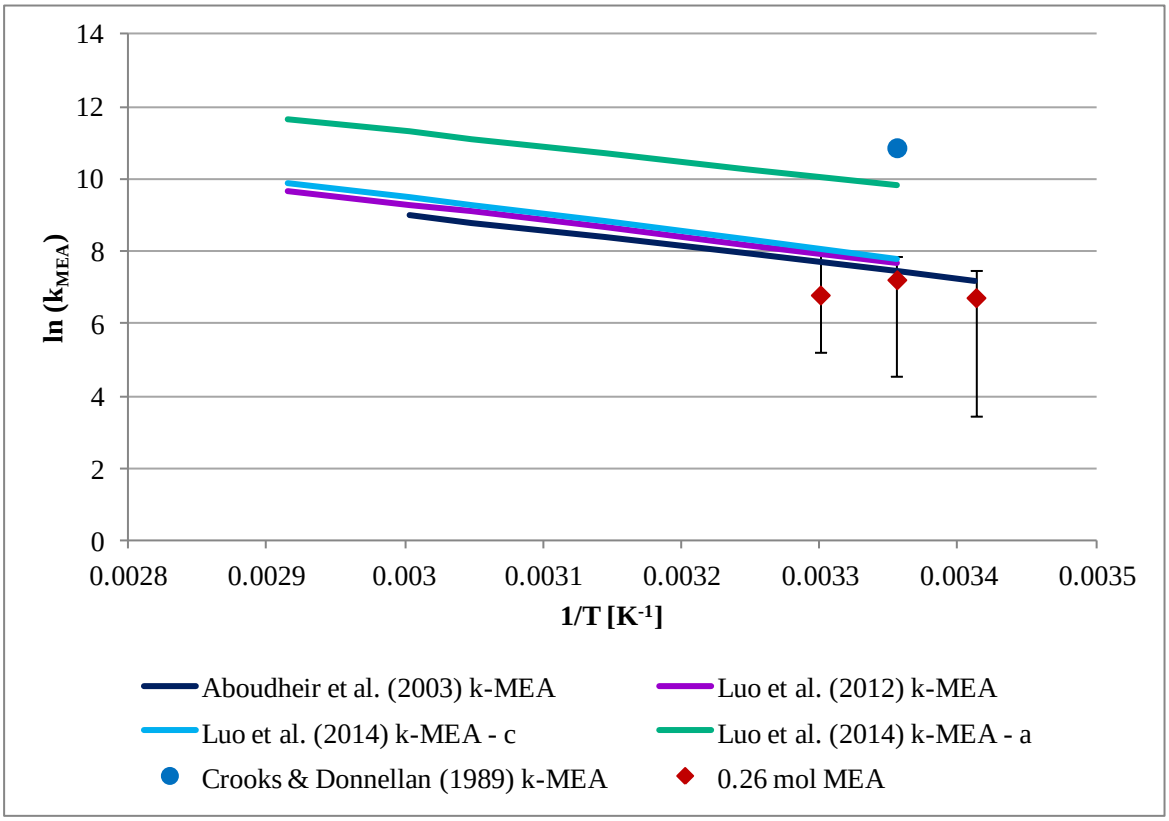

Figure 76 : Comparison of optimized MEA deprotonation rate constants for the termolecular model for the 0.26 mol MEA series with literature data

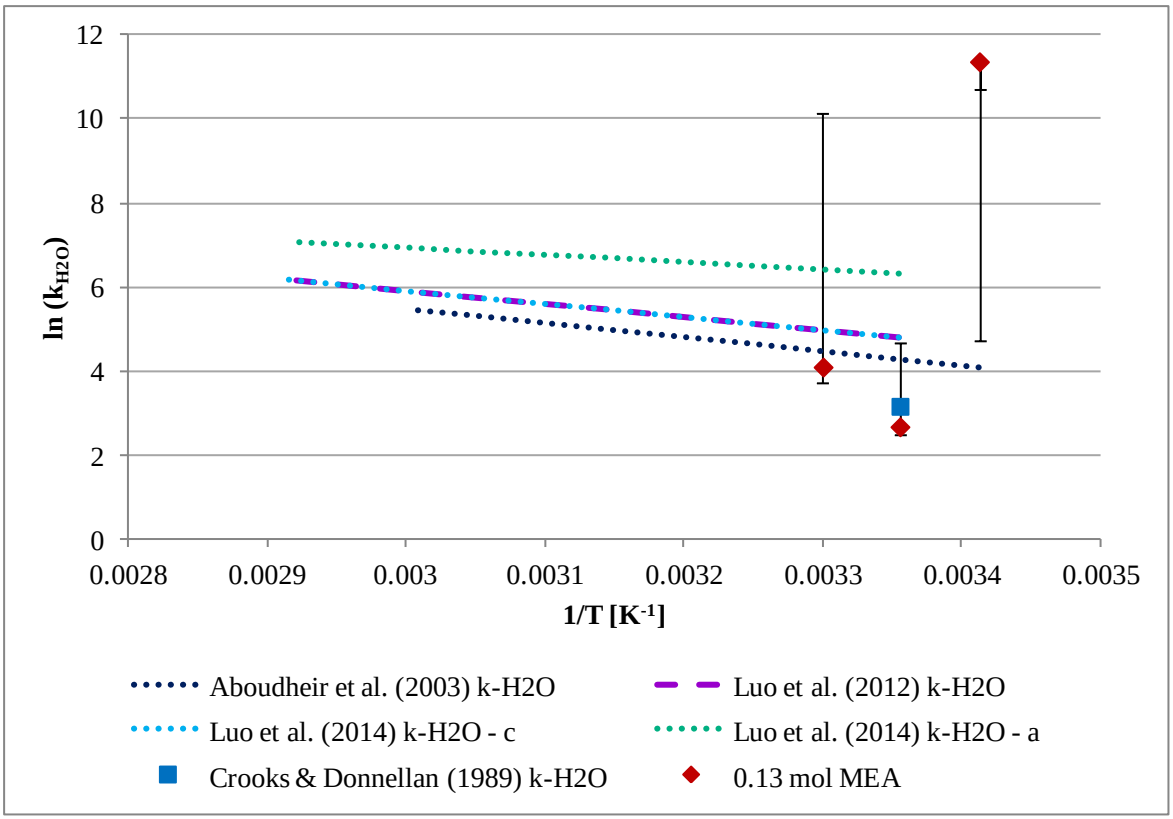

Figure 77 : Comparison of optimized water deprotonation rate constants for the termolecular model for the 0.13 mol MEA series with literature data

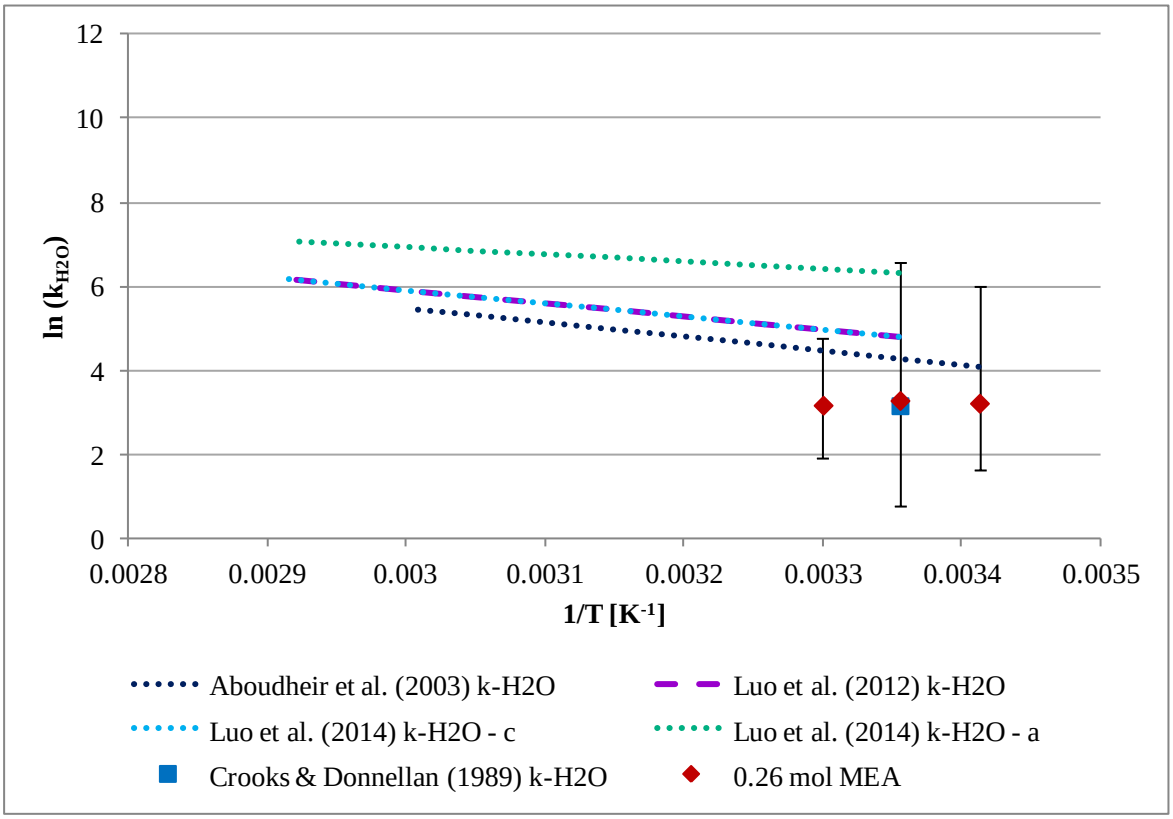

Figure 78 : Comparison of optimized water deprotonation rate constants for the termolecular model for the 0.26 mol MEA series with literature data

The Arrhenius plots for the best case termolecular rate constants are given in Figures 79 to 82. Figures 79 and 80 correspond to the MEA deprotonation rate constants at the 0.13 and 0.26 mol MEA settings, respectively, and Figures 81 and 82 correspond to the water deprotonation rate constants at the 0.13 and 0.26 mol MEA settings, respectively. Most of the Arrhenius plots given show poor dependence on temperature, with Pearson's R^2 values between 0.0216 to 0.6173. Only the MEA deprotonation rate constant plot for the 0.13 mol MEA series data (Figure 79) shows a strong dependence on temperature. The corresponding Pearson's R^2 value for the Arrhenius plot is 0.9941.

The water deprotonation rate constant plots have positive slopes. Positive slopes on Arrhenius plots correspond to negative activation energies. The activation energy represents the minimum amount of energy to be added to a reactive system before a reaction occurs (Silberberg, 2007). Therefore, negative activation energies may suggest that little energy is needed to initiate deprotonation by water. However, the equilibrium species distribution results indicate that only the MEA can be regarded as a deprotonating base (Chapter 5). This would suggest the termolecular model is not fundamentally correct. The model has been used by other researchers to successfully represent experimental data in both low and high MEA concentration solutions (Aboudheir *et al*., 2003; Luo *et al*., 2012).

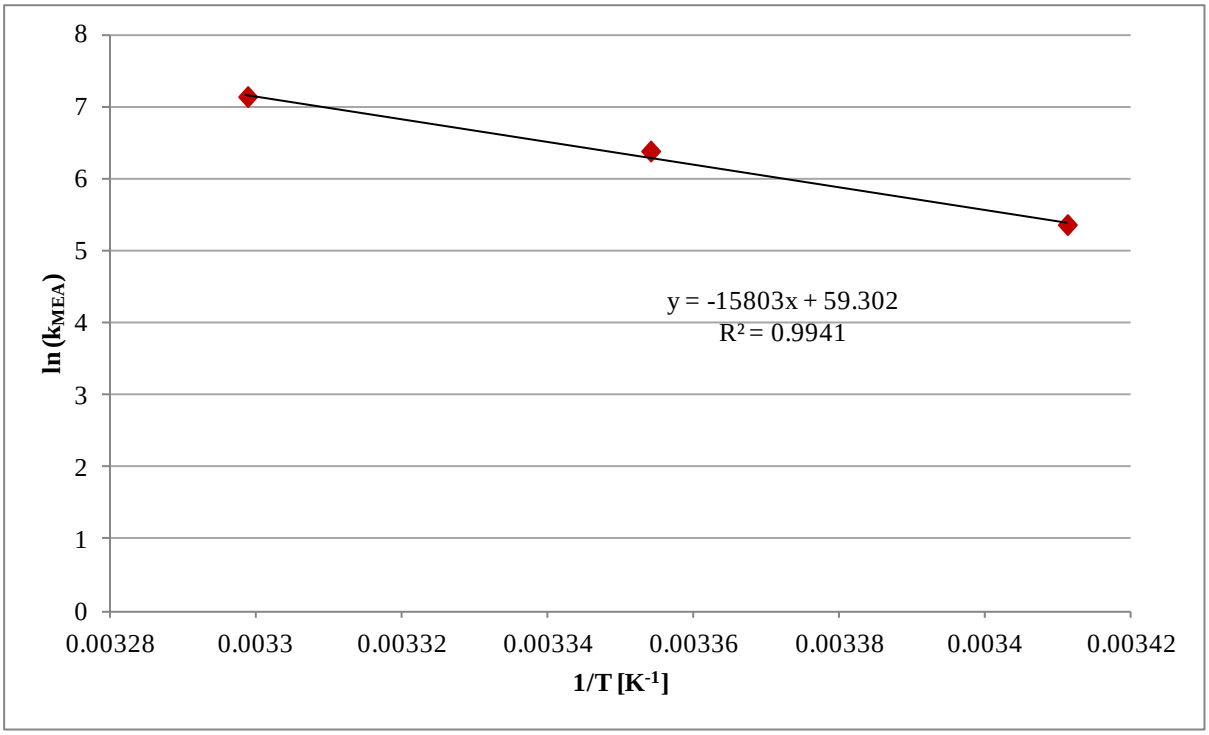

Figure 79 : Arrhenius plot of the MEA deprotonation termolecular model rate constants for the 0.13 mol MEA series data

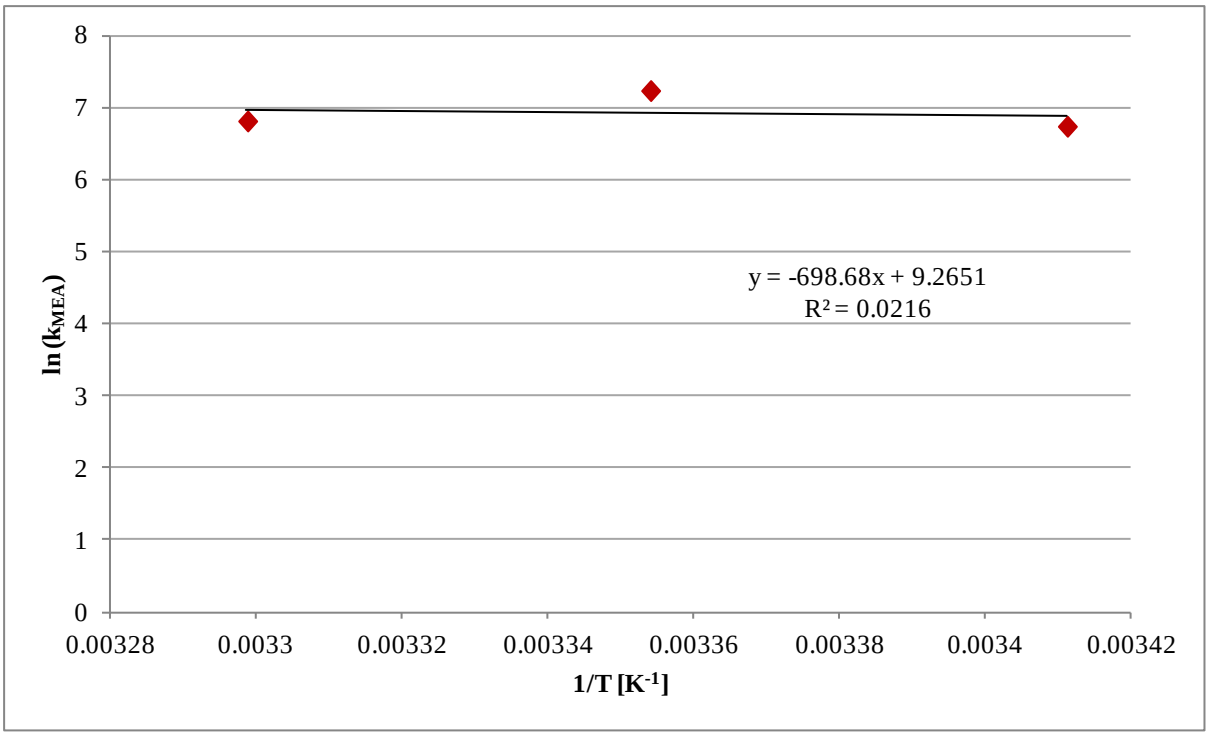

Figure 80 : Arrhenius plot of the MEA deprotonation termolecular model rate constants for the 0.26 mol MEA series data

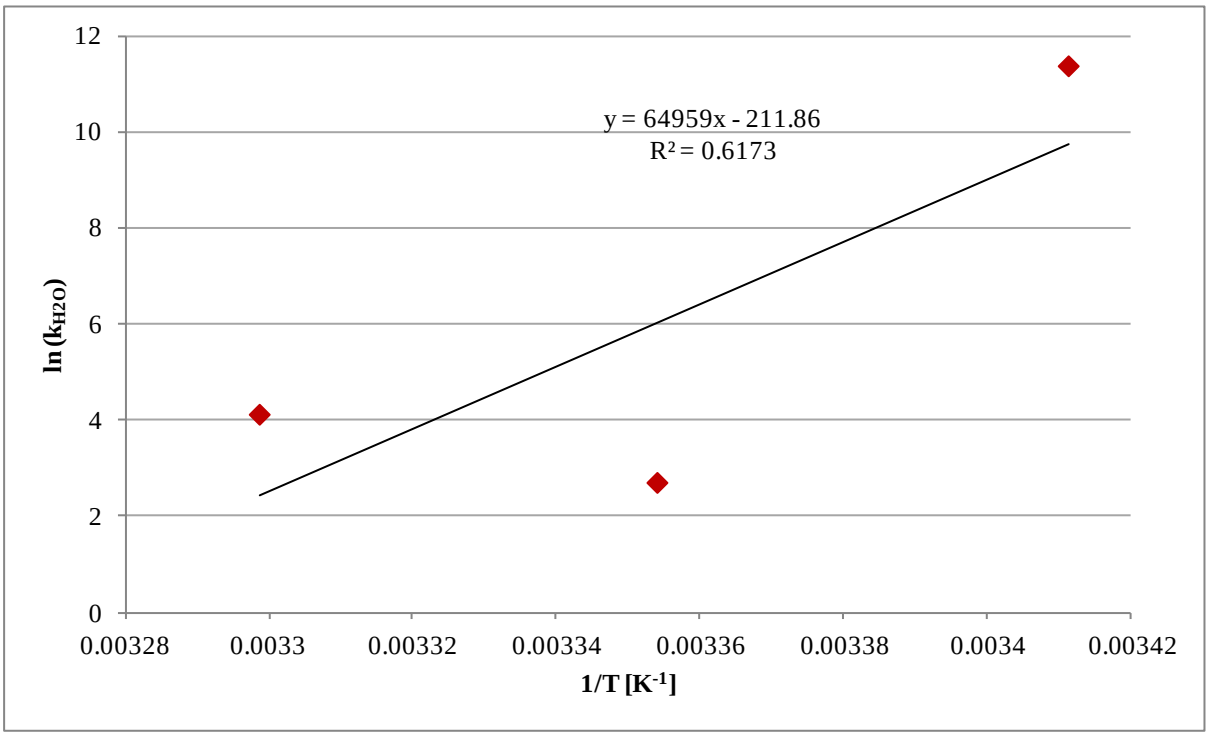

Figure 81 : Arrhenius plot of the water deprotonation termolecular model rate constants for the 0.13 mol MEA series data

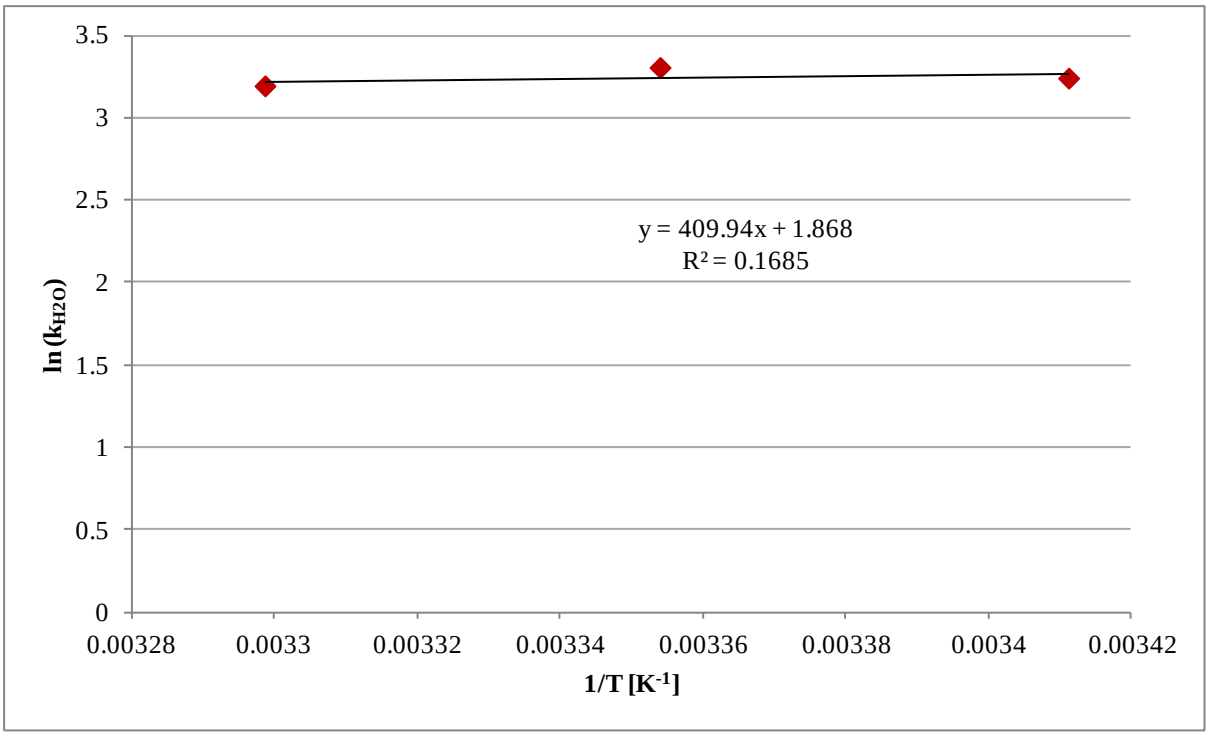

Figure 82 : Arrhenius plot of the water deprotonation termolecular model rate constants for the 0.26 mol MEA series data

The activation energy (E_a) for the MEA deprotonation rate constants for the 0.13 mol MEA series data is given in Table 21. The value of E_a calculated in this work is approximately four times the values reported in literature. The activation energy was calculated from the best case rate constants at the 0.13 mol MEA setting. The large difference between the calculated activation energy and literature values reflects the unreliability of the calculated individual rate constants.

Table 21 : Comparison of activation energies for the optimized MEA deprotonation rate constants from the termolecular model: experimental data is from the 0.13 mol MEA series

Reference	E_a [kJ/mol]
Aboudheir *et al.* (2003)	36.7
Luo *et al.* (2012)	37.4
Luo *et al.* (2014) – concentration model	39.4
Luo *et al.* (2014) – activity coefficient model	34.2
This work	131.4

6.4 Chapter summary

In this chapter, real-time kinetic data collected from a semi-batch experimental setup were presented. Kinetic control under semi-batch operation was proven. Reagent species profiles confirmed that the CO_2-MEA reaction is rapid when conducted in water. The species profiles provided the first FTIR measurements on the aqueous CO_2-MEA reaction collected for purposes of monitoring the kinetics of the reaction.

Due to error in the experimental measurements, the actual CO_2 conversion calculated varied between 95.0 to 135.3%, and the stoichiometric ratio between 1.0 to 3.1. The MEA conversion varied between 8.6 to 18.0% for experiments conducted with low MEA concentrations (0.26 mol/L), and between 3.2 to 12.9% for experiments conducted with high MEA concentrations (0.52 mol/L). The experimental data was modelled using published reaction models. The rate constants obtained were in general agreement with literature within the confidence interval specified. Most of the published values were within the range of rate constants given by the confidence interval.

7. Conclusions and recommendations

7.1 Conclusions

A semi-batch-FTIR experimental setup was used to generate new data for the aqueous CO_2-MEA reaction system. Equilibrium and kinetic experiments were conducted. The data generated in the equilibrium experiments were species absorbances measured in 0.33 mol/L MEA solutions, at CO_2 loadings between 0 and 0.6 mol CO_2/mol MEA. The measurements provided the first equilibrium species concentration measurements made using FTIR spectroscopy in low MEA concentration solutions. Implicit calibration calculations were used to calculate MEA, carbamate, HCO_3^- and protonated MEA concentrations at all CO_2 loadings considered. The plots of concentration vs. CO_2 loading showed similar trends to those found in literature for 5 mol/L MEA solutions, indicating that the reaction mechanism is the same in both low and high MEA concentration solutions.

The reaction mechanism consists of predominantly carbamate formation at CO_2 loadings less than 0.3 mol CO_2/mol MEA. Any CO_2 added to the solution completely reacts to form only carbamate. At CO_2 loadings higher than 0.3 mol CO_2/mol MEA, HCO_3^- forms in significant concentrations. The HCO_3^- formation is accompanied by consumption of the carbamate. Work by Luo *et al*. (2014) indirectly confirms the formation of HCO_3^- in significant concentrations at CO_2 loadings above 0.3 mol CO_2/mol MEA.

Real-time kinetic data collected from the semi-batch experimental setup confirmed that the reaction is rapid when conducted in water. The data provided the first FTIR spectroscopy measurements on the aqueous CO_2-MEA reaction. The experiments were conducted with low (0.26 mol/L) and high (0.52 mol/L) MEA concentrations, at 20 to 30°C. Due to measurement limitations, only CO_2 and MEA could be monitored accurately. The CO_2 conversion calculated from the experimental results varied between 95.0 to 135.3%, and the MEA conversion varied between 8.6 to 18.0% for experiments conducted with low MEA concentrations, and between 3.2 to 12.9% for experiments conducted with high MEA concentrations. The stoichiometric ratio varied between 1.0 to 3.1. The calculated values of CO_2 conversion and stoichiometric ratio suggest that essentially 100% conversion of CO_2 and a reaction stoichiometry of 2 moles MEA/mol CO_2 were achieved in each experiment. The assumption of 100% CO_2 conversion and reaction stoichiometry of 2 moles MEA/mol CO_2 are supported by results from the equilibrium experiments.

The kinetic data was modelled using published reaction models. The models considered were the pseudo-first order, second order, third order and termolecular models. Because product species were not monitored during the reaction, only the forward reaction was modelled. The proposed carbamate-HCO_3^- mechanism could not be evaluated since it depends on knowledge of the carbamate and HCO_3^- product concentrations.

When modelling the reagent species, the second order and termolecular rate constants obtained were in general agreement with literature within the error specified. The second order model is most quoted for describing the CO_2-MEA reaction in both aqueous and non-aqueous solutions. The range of optimized second order rate constants obtained at 25°C, as represented by a 95% confidence interval, was k_2 = 252 to 6343. This range includes the typical literature value of 6 000 L/mol.s. The relatively large range in the rate constant was due to measurement limitations. The values of the rate constants from the pseudo-first order model were insensitive to the model error predicted. The second order, third order and termolecular models represented the CO_2 and MEA data equally well. Because of the comparable fit of the models, an appropriate reaction mechanism could not be recommended based on the kinetic experimental data.

7.2 Recommendations

Overall second order reaction models are not suitable for prediction of the reaction rate in industrial absorption columns operating at 0.4-0.5 mol CO_2/mol MEA (Luo *et al.*, 2014). Equilibrium species concentrations such as those reported in this work point to a change in reaction mechanism as the reason for the inadequacy in overall second order reaction models. Suitable reaction models should include both carbamate formation and HCO_3^- formation as a function of CO_2 loading.

Reaction rate models that incorporate both carbamate and HCO_3^- formation can be derived from experiments with high MEA concentration solutions in a heterogeneous reactor. An experimental setup for this purpose could be a wetted wall column reactor with ATR-FTIR spectroscopy. The heterogeneous operation would allow use of MEA and CO_2 concentrations representative of values used in industrial absorption columns, as well as operation at CO_2 loadings between 0-0.5 mol CO_2/mol MEA. At these concentrations and CO_2 loadings, both reagent and product species concentrations will be sufficiently high that accurate detection with a germanium ATR element will be possible.

The heterogeneous reactor setup will also be suitable for testing the carbamate-HCO_3^- reaction mechanism proposed in this work with kinetic data. A pH meter connected to the experimental setup will also allow direct correlation of the solution pH with concentrations of chemical species in solution.

8. References

Aaron, D. & Tsouris, C. 2005, “Separation of CO_2 from Flue Gas: A Review”, *Separation Science and Technology*, vol. 30, no. 1-3, pp. 321-348.

Aboudheir, A., Tontiwachwuthikul, P., Chakma, A. & Idem, R. 2003, "Kinetics of the reactive absorption of carbon dioxide in high CO_2-loaded, concentrated aqueous monoethanolamine solutions", *Chemical Engineering Science*, vol. 58, no. 23-24, pp. 5195-5210.

Aboudheir, A., Tontiwachwuthikul, P., Chakma, A. & Idem, R. 2004, "Novel Design for the Nozzle of a Laminar Jet Absorber", *Industrial and Engineering Chemistry Research*, vol. 43, no. 10, pp. 2568-2574.

Ali, S.H. 2005, "Kinetics of the Reaction of Carbon Dioxide with Blends of Amines in Aqueous Media Using the Stopped-Flow Technique", *International Journal of Chemical Kinetics*, vol. 37, no. 7, pp. 391-405.

Alper, E. 1990, "Reaction Mechanism and Kinetics of Aqueous Solutions of 2-Amino-2-methyl-1-propanol and Carbon Dioxide", *Industrial and Engineering Chemistry Research*, vol. 29, no. 8, pp. 1725-1728.

Alvarez-Fuster, C., Midoux, N., Laurent, A. & Charpentier, J. 1980, "Chemical kinetics of the reaction of carbon dioxide with amines in pseudo m-nth order conditions in aqueous and organic solutions", *Chemical Engineering Science*, vol. 35, no. 8, pp. 1717-1723.

Aroua, M.K., Benamor, A. & Haji-Sulaiman, M. 1999, "Equilibrium Constant for Carbamate Formation from Monoethanolamine and Its Relationship with Temperature", *Journal of Chemical & Engineering Data*, vol. 44, no. 5, pp. 887-891.

Arstad, B., Blom, R. & Swang, O. 2007, "CO_2 Absorption in Aqueous Solutions of Alkanolamines: Mechanistic Insight from Quantum Chemical Calculations", *Journal of Physical Chemistry A*, vol. 111, no. 7, pp. 1222-1228.

Aruldhas, G. 2001, *Molecular Structure and Spectroscopy*, 1st edn, Prentice Hall, New Delhi.

Astarita, G. 1961, "Carbon dioxide absorption in aqueous monoethanolamine solutions", *Chemical Engineering Science*, vol. 16, no. 3-4, pp. 202-207.

Astarita, G., Marrucci, G. & Gioia, F. 1964, "The influence of carbonation ratio and total amine concentration on carbon dioxide absorption in aqueous monoethanolamine solutions", *Chemical Engineering Science*, vol. 19, no. 2, pp. 95-103.

Austgen, D.M., Rochelle, G.T., Peng, X. & Chen, C.C. 1989, "Model of Vapor-Liquid Equilibria for Aqueous Acid Gas-Alkanolamine Systems Using the Electrolyte-NRTL Equation", *Industrial & Engineering Chemistry Research*, vol. 28, no. 7, pp. 1060-1073.

Barth, D., Tondre, C. & Delpuech, J.J. 1986, "Stopped-flow Investigations of the Reaction Kinetics of Carbon Dioxide with some Primary and Secondary Alkanolamines in Aqueous Solutions", *International Journal of Chemical Kinetics*, vol. 18, no. 4, pp. 445-457.

Bhown, A.S. & Freeman, B.C. 2011, "Analysis and Status of Post-Combustion Carbon Dioxide Capture Technologies", *Environmental Science and & Technology*, vol. 45, no. 20, pp. 8624-8632.

Böttinger, W., Maiwald, M. & Hasse, H. 2008, "Online NMR Spectroscopic Study of Species Distribution in MEA–H_2O–CO_2 and DEA–H_2O–CO_2", *Fluid Phase Equilibria*, vol. 263, no. 2, pp. 131-143.

Caplow, M. 1968, "Kinetics of Carbamate Formation and Breakdown", *Journal of the American Chemical Society*, vol. 90, no. 24, pp. 6795-6803.

Chan, H.M. & Danckwerts, P.V. 1981, "Equilibrium of MEA and DEA with Bicarbonate and Carbamate", *Chemical Engineering Science*, vol. 36, no. 1, pp. 229-230.

Chuang, M.-H. & Johannsen, M. 2009, *Characterization of pH in Aqueous CO_2-Systems*. Available: www.isasf.net/fileadmin/files/Docs/Arcachon/posters/p4-P46%20ISSF2009_Johannsen_P46.pdf [2013, 15 May]

Clarke, J.K.A. 1964, "Kinetics of Absorption of Cardon Dioxide in Monoethanolamine Solutions at Short Contact Times", *Industrial & Engineering Chemistry Fundamentals*, vol. 3, no. 3, pp. 239-245.

Conway, W., Wang, X., Fernandes, D., Burns, R., Lawrance, G., Puxty, G. & Maeder, M. 2011, "Comprehensive Kinetic and Thermodynamic Study of the Reactions of CO_2(aq) and HCO_3^- with Monoethanolamine (MEA) in Aqueous Solution", *Journal of Physical Chemistry A*, vol. 115, no. 50, pp. 14340-14349.

Crooks, J.E. & Donnellan, J.P. 1989, "Kinetics and Mechanism of the Reaction between Carbon Dioxide and Amines in Aqueous Solution", *Journal of the Chemical Society*, vol. Perkin Transactions 2, no. 4, pp. 331-333.

Cummings, A.L., Veatch, F.C., Keller, A.E., Mecum, S.M. & Kammiller, R.M. 1990, "An Analytical Method for Determining Bound and Free Alkanolamines in Heat Stable Salt Contaminated Solutions", *AIChE 1990 Summer National Meeting*, Ponca City, 21 August.

Da Silva, E.F. & Svendsen, H.F. 2004, "Ab Initio Study of the Reaction of Carbamate Formation from CO_2 and Alkanolamines", *Industrial & Engineering Chemistry Research*, vol. 43, no. 13, pp. 3413-3418.

Da Silva, E.F. & Svendsen, H.F. 2007, "Computational Chemistry Study of Reactions, Equilibrium and Kinetics of Chemical CO_2 Absorption", *International Journal of Greenhouse Gas Control*, vol. 1, no. 2, pp. 151-157.

Danckwerts, P.V. 1970, *Gas-Liquid Reactions*, 1st edn, McGraw-Hill.

Danckwerts, P.V. 1979, "The Reaction of CO_2 with Ethanolamines", *Chemical Engineering Science*, vol. 34, no. 4, pp. 443-446.

Danckwerts, P.V. & McNeil, K.M. 1967, "The Effects of Catalysis on Rates of Absorption of CO_2 into Aqueous Amine-Potash Solutions", *Chemical Engineering Science*, vol. 22, no. 7, pp. 925-930.

Davis, A.R. & Oliver, B.G. 1972, "A Vibrational-Spectroscopic Study of the Species Present in the CO_2-H_2O System", *Journal of Solution Chemistry*, vol. 1, no. 4, pp. 329-339.

Diab, F., Provost, E., Laloué, N., Alix, P., Souchon, V., Delpoux, O. & Fürst, W. 2012, "Quantitative Analysis of the Liquid Phase by FT-IR Spectroscopy in the System CO_2/Diethanolamine (DEA)/H_2O", *Fluid Phase Equilibria*, vol. 325, pp. 90-99.

Diab, F., Provost, E., Laloué, N., Alix, P. & Fürst, W. 2013, "Effect of the Incorporation of Speciation Data in the Modeling of CO_2-DEA-H_2O System", *Fluid Phase Equilibria*, vol. 353, pp. 22-30.

Donaldson, T.L. & Quinn, J.A. 1974, "Kinetic Constants Determined from Membrane Transport Measurements: Carbonic Anhydrase Activity at High Concentrations", *Proceedings of the National Academy of Sciences*, vol. 71, no. 12, pp. 4995-4999.

Donaldson, T.L. & Quinn, J.A. 1975, "Carbon Dioxide Transport through Enzymatically Active Synthetic Membranes", *Chemical Engineering Science*, vol. 30, no. 1, pp. 103-115.

Donaldson, T.L. & Nguyen, Y.N. 1980, "Carbon Dioxide Reaction Kinetics and Transport in Aqueous Amine Membranes", *Industrial & Engineering Chemistry Fundamentals*, vol. 19, no. 3, pp. 260-266.

Du Preez, L.J. 2014, *Reactive Absorption Kinetics of CO_2 in Alcoholic Solutions of MEA: Fundamental Knowledge for Determining Effective Interfacial Mass Transfer Area*, Stellenbosch University.

Ewing, S.P., Lockshon, D. & Jencks, W.P. 1980, "Mechanism of Cleavage of Carbamate Anions", *Journal of the American Chemical Society*, vol. 102, no. 9, pp. 3072-3084.

Falk, M. & Miller, A.G. 1992, "Infrared Spectrum of Carbon Dioxide in Aqueous Solution", *Vibrational Spectroscopy*, vol. 4, no. 1, pp. 105-108.

Fan, G.-J., Wee, A.G.H., Idem, R. & Tontiwachwuthikul, P. 2009, "NMR Studies of Amine Species in MEA-CO_2-H_2O System: Modification of the Model of Vapor-Liquid Equilibrium (VLE)", *Industrial & Engineering Chemistry Research*, vol. 48, no. 5, pp. 2717-2720.

Freguia, S. & Rochelle, G.T. 2003, "Modeling of CO_2 Capture by Aqueous Monoethanolamine", *AIChE Journal*, vol. 49, no. 7, pp. 1676-1686.

Guido, C.A., Pietrucci, F., Gallet, G.A. & Andreoni, W. 2013, "The Fate of a Zwitterion in Water from *ab Initio* Molecular Dynamics: Monoethanolamine (MEA)-CO_2", *Journal of Chemical Theory and Computation,* vol. 9, no. 1, pp. 28-32.

Han, B., Zhou, C., Wu, J., Tempel, D.J. & Cheng, H. 2011, "Understanding CO_2 Capture Mechanisms in Aqueous Monoethanolamine via First Principles Simulations", *The Journal of Physical Chemistry Letters,* vol. 2, no. 6, pp. 522-526.

Han, J., Jin, J., Eimer, D.A. & Melaaen, M.C. 2012, "Density of Water (1) Monoethanolamine (2) CO_2 (3) from (298.15 to 413.15) K and Surface Tension of Water (1) Monoethanolamine (2) from (303.15 to 333.15) K", *Journal of Chemical & Engineering Data,* vol. 57, no. 4, pp. 1095-1103.

Hartridge, H. & Roughton, F.J.W. 1923, "A Method of Measuring the Velocity of Very Rapid Chemical Reactions", *Proceedings of the Royal Society of London.Series A,* vol. 104, no. 726, pp. 376-394.

Hikita, H., Asai, S., Ishikawa, H. & Honda, M. 1977, "The Kinetics of Reactions of Carbon Dioxide with Monoethanolamine, Diethanolamine and Triethanolamine by a Rapid Mixing Method", *The Chemical Engineering Journal,* vol. 13, no. 1, pp. 7-12.

Hsu, C.-P.S. 1997, "Infrared Spectroscopy" in *Handbook of Instrumental Techniques for Analytical Chemistry*, ed. F.A. Settle, 1st edn, Prentice Hall, , pp. 247.

Iida, K. & Sato, H. 2012, "Proton Transfer Step in the Carbon Dioxide Capture by Monoethanol Amine: A Theoretical Study at the Molecular Level", *The Journal of Physical Chemistry B,* vol. 116, no. 7, pp. 2244-2248.

Jackson, P., Robinson, K., Puxty, G. & Attalla, M. 2009, "*In Situ* Fourier Transform-Infrared (FT-IR) Analysis of Carbon Dioxide Absorption and Desorption in Amine Solutions", *9th International Conference on Greenhouse Gas Control Technologies*, eds. J. Gale, H. Herzog & J. Braitsch, Elsevier, 16–20 November 2008, pp. 985.

Jakobsen, J.P., Krane, J. & Svendsen, H.F. 2005, "Liquid-Phase Composition Determination in CO_2-H_2O-Alkanolamine Systems: An NMR Study", *Industrial & Engineering Chemistry Research,* vol. 44, no. 26, pp. 9894-9903.

Johnson, S.L. & Morrison, D.L. 1972, "Kinetics and Mechanism of Decarboxylation of N-arylcarbamates. Evidence for Kinetically Important Zwitterionic Carbamic Acid Species of Short Lifetime", *Journal of the American Chemical Society,* vol. 94, no. 4, pp. 1323-1334.

Kohl, A.L. & Nielsen, R.B. 1997, *Gas Purification,* 5th edn, Gulf, Houston, Tex.

Kreulen, H., Versteeg, G.F., Smolders, C.A., & Van Swaaij, W.P.M. 1993, "Selective Removal of H_2S from Sour Gases with Microporous Membranes. Part II. A Liquid Membrane of Water-Free Tertiary Amines", *Journal of Membrane Science,* vol. 82, no. 1-2, pp. 185-197.

Kucka, L., Richter, J., Kenig, E.Y. & Górak, A. 2003, "Determination of Gas–liquid Reaction Kinetics with a Stirred Cell Reactor", *Separation and Purification Technology,* vol. 31, no. 2, pp. 163-175.

Laddha, S. & Danckwerts, P. 1981, "Reaction of CO_2 with ethanolamines: kinetics from gas-absorption", *Chemical Engineering Science,* vol. 36, no. 3, pp. 479-482.

Levine, I.N. 2009, *Quantum Chemistry,* 6th edn, Pearson Prentice Hall, Upper Saddle River, N.J.

Littel, R., Versteeg, G.F. & Van Swaaij, W.P.M. 1992, "Kinetics of CO_2 with Primary and Secondary Amines in Aqueous Solutions - II. Influence of Temperature on Zwitterion Formation and Deprotonation Rates", *Chemical Engineering Science,* vol. 47, no. 8, pp. 2037-2045.

Luo, X., Hartono, A. & Svendsen, H.F. 2012, "Comparative Kinetics of Carbon Dioxide Absorption in Unloaded Aqueous Monoethanolamine Solutions using Wetted Wall and String of Discs Columns", *Chemical Engineering Science,* vol. 82, pp. 31-43.

Luo, X., Hartono, A., Hussain, S. & Svendsen, H.F. 2014, "Mass Transfer and Kinetics of Carbon Dioxide Absorption into Loaded Aqueous Monoethanolamine Solutions", *Chemical Engineering Science,* Manuscript submitted for publication. http://dx.doi.org/10.1016/j.ces.2014.10.013

Ma, C., Pietrucci, F. & Andreoni, W. 2014, "Capturing CO_2 in Monoethanolamine (MEA) Aqueous Solutions: Fingerprints of Carbamate Formation Assessed with First-Principles Simulations", *The Journal of Physical Chemistry Letters,* pp. 1672-1677.

Machinga, P. 2012, *Carbon Dioxide Reaction in Aqueous Amine Solutions,* Stellenbosch University.

McCann, N., Phan, D., Wang, X., Conway, W., Burns, R., Attalla, M., Puxty, G. & Maeder, M. 2009, "Kinetics and Mechanism of Carbamate Formation from CO_2 (aq), Carbonate Species, and Monoethanolamine in Aqueous Solution", *Journal of Physical Chemistry A,* vol. 113, no. 17, pp. 5022-5029.

McCann, N., Maeder, M. & Hasse, H. 2011, "A Calorimetric Study of Carbamate Formation", *The Journal of Chemical Thermodynamics,* vol. 43, no. 5, pp. 664-669.

Mimura, T., Suda, T., Iwaki, I., Honda, A. & Kumazawa, H. 1998, "Kinetics of Reaction between Carbon Dioxide and Stericaly Hindered Amines for Carbon Dioxide Recovery from Power Plant Flue Gases", *Chemical Engineering Communications,* vol. 170, no. 1, pp. 245-260.

Montgomery, D.C. 2013, *Design and Analysis of Experiments,* 8th edn, John Wiley and Sons, Hoboken, NJ.

Moore, J.C., Battino, R., Rettich, T.R., Handa, Y.P. & Wilhelm, E. 1982, "Partial Molar Volumes of Gases at Infinite Dilution in Water at 298.15 K", *Journal of Chemical and Engineering Data,* vol. 27, no. 1, pp. 22-24.

Motang, N. 2012, *Improvement and Testing of Carbon Dioxide Sequestration Reactor for Kinetic Measurements*, Stellenbosch University.

Nakamoto, K. 1986, *Infrared and Raman Spectra on Inorganic and Coordination Compounds*, 4th edn, John Wiley and Sons, Inc., New York.

Parkinson, W.J. & De Nevers, N.J. 1969, "Partial Molal Volume of Carbon Dioxide in Water Solutions", *Industrial & Engineering Chemistry Fundamentals*, vol. 8, no. 4, pp. 709-713.

National Energy Technology Laboratory, 2007, *Carbon Dioxide Capture from Existing Coal-Fired Power Plants*. Available: www.netl.doe.gov/File%20Library/Research/Energy%20Analysis/Publications/CO2-Retrofit-From-Existing-Plants-Revised-November-2007.pdf [2014, 05 December].

Penny, D.E. & Ritter, T.J. 1983, "Kinetic study of the reaction between carbon dioxide and primary amines", *Journal of the Chemical Society, Faraday Transactions 1*, vol. 79, no. 9, pp. 2103-2109.

Perinu, C., Arstad, B., Bouzga, A.M., Svendsen, J.A. & Jens, K.J. 2014, "NMR-Based Carbamate Decomposition Constants of Linear Primary Alkanolamines for CO_2 Capture", *Industrial & Engineering Chemistry Research*, vol. 53, no. 38, pp. 14571-14578.

Perry, R.H. & Green, D.W. 2008, *Perry's Chemical Engineers' Handbook*, 8th edn, McGraw-Hill, New York.

PIKE Technologies, 2011, *ATR – Theory and Applications*. Available: www.piketech.com/files/pdfs/ATRAN611.pdf [2013, 06 May].

Puxty, G., Rowland, R. & Attalla, M. 2010, "Comparison of the Rate of CO_2 Absorption into Aqueous Ammonia and Monoethanolamine", *Chemical Engineering Science*, vol. 65, no. 2, pp. 915-922.

Richner, G. & Puxty, G. 2012, "Assessing the Chemical Speciation during CO_2 Absorption by Aqueous Amines Using *in Situ* FTIR", *Industrial & Engineering Chemistry Research*, vol. 51, no. 44, pp. 14317-14324.

Roberts, G.W. 2009, *Chemical Reactions and Chemical Reactors*, John Wiley and Sons, Hoboken, NJ.

Roughton, F.J.W. 1934, "The Kinetics of Haemoglobin VI--The Competition of Carbon Monoxide and Oxygen for Haemoglobin", *Proceedings of the Royal Society of London B*, vol. 115, no. 795, pp. 473-495.

Sada, E., Kumazawa, H. & Butt, M.A. 1976, "Chemical Absorption Kinetics over a Wide Range of Contact Time: Absorption of Carbon Dioxide into Aqueous Solutions of Monoethanolamine", *AIChE Journal*, vol. 22, no. 1, pp. 196-198.

Sada, E., Kumazawa, H., Butt, M. & Hayashi, D. 1976, "Simultaneous Absorption of Carbon Dioxide and Hydrogen Sulfide into Aqueous Monoethanolamine Solutions", *Chemical Engineering Science*, vol. 31, no. 9, pp. 839-841.

Sada, E., Kumazawa, H., Han, Z.Q. & Matsuyama, H. 1985, "Chemical Kinetics of the Reaction of Carbon Dioxide with Ethanolamines in Nonaqueous Solvents", *AIChE Journal*, vol. 31, no. 8, pp. 1297-1303.

Setameteekul, A., Aroonwilas, A. & Veawab, A. 2008, "Statistical Factorial Design Analysis for Parametric Interaction and Empirical Correlations of CO_2 Absorption Performance in MEA and Blended MEA/MDEA Processes", *Separation and Purification Technology*, vol. 64, no. 1, pp. 16-25.

Shampine, L.F. & Reichelt, M.W. 1997, "The MALAB ODE Suite", *SIAM Journal on Scientific Computing*, vol. 18, no. 1, pp. 1-22.

Sharma, M. 1965, "Kinetics of Reactions of Carbonyl Sulphide and Carbon Dioxide with Amines and Catalysis by Brönsted Bases of the Hydrolysis of COS", *Transactions of the Faraday Society*, vol. 61, pp. 681-688.

Sharma, M. & Danckwerts, P. 1963, "Catalysis by Brönsted bases of the reaction between CO_2 and water", *Transactions of the Faraday Society*, vol. 59, pp. 386-395.

Shim, J.-G., Kim, J.-H., Jhon, Y.H., Kim, J. & Cho, K.-. 2009, "DFT Calculations on the Role of Base in the Reaction between CO_2 and Monoethanolamine", *Industrial and Engineering Chemistry Research*, vol. 48, no. 4, pp. 2172-2178.

Silberberg, M.S. 2007, *Principles of General Chemistry*, McGraw-Hill.

Smith, B.C. 2011, *Fundamentals of Fourier Transform Infrared Spectroscopy*, 2nd edn, CRC Press.

Socrates, G. 1994, *Infrared Characteristics Group Frequencies: Tables and Charts*, 2nd edn, Wiley.

Taylor, J.R. 1997, *An Introduction to Error Analysis: the Study of Uncertainties in Physical Measurements*, 2nd edn, University Science Books.

Tseng, Y.-M. & Thompson, A.R. 1964, "Densities and Refractive Indices of Aqueous Monoethanolamine, Diethanolamine, Triethanolamine", *Journal of Chemical & Engineering Data*, vol. 9, no. 2, pp. 264-267.

Vaidya, P.D. & Kenig, E.Y. 2007, "CO_2-Alkanolamine Reaction Kinetics: A Review of Recent Studies", *Chemical Engineering and Technology*, vol. 30, no. 11, pp. 1467-1474.

Vaidya, P.D. & Kenig, E.Y. 2007, "Gas–Liquid Reaction Kinetics: A Review of Determination Methods", *Chemical Engineering Communications*, vol. 194, no. 12, pp. 1543-1565.

Versteeg, G.F., Van Dijck, L.A.J. & Van Swaaij, W.P.M. 1996, "On the Kinetics between CO_2 and Alkanolamines both in Aqueous and Non-aqueous Solutions: An Overview", *Chemical Engineering Communications,* vol. 144, no. 1, pp. 113-158.

Xie, H.-B., Zhou, Y., Zhang, Y. & Johnson, J.K. 2010, "Reaction Mechanism of Monoethanolamine with CO_2 in Aqueous Solution from Molecular Modeling", *Journal of Physical Chemistry A,* vol. 114, no. 43, pp. 11844-11852.

Yang, Q., Bown, M., Ali, A., Winkler, D., Puxty, G. & Attalla, M. 2009, "A Carbon-13 NMR Study of Carbon Dioxide Absorption and Desorption with Aqueous Amine Solutions", *Energy Procedia,* vol. 1, no. 1, pp. 955-962.

Ying, J. & Eimer, D.A. 2013, "Determination and Measurements of Mass Transfer Kinetics of CO_2 in Concentrated Aqueous Monoethanolamine Solutions by a Stirred Cell", *Industrial & Engineering Chemistry Research,* vol. 52, no. 7, pp. 2548-2559.

Appendices

Appendix A Valve and fitting specifications

Table A. 1 : Valve specifications

Valve	Specifications				
	Valve type	**Primary material**	**Valve size**	**Media temp.**	**Connection type**
SS-14DKM4-S4	Needle	316 Stainless steel	0.25 inch	-29 – 93°C	Male NPT
SS-16DKM4-F4	Needle	316 Stainless steel	0.25 inch	-29 – 93°C	Male NPT
SS-20VM4	Needle	316 Stainless steel	0.25 inch	-54 – 232°C	Male NPT
SS-RL3S4	Relief	316 Stainless steel	0.25 inch	-12 – 135°C	Compression tube fitting

Table A. 2 : Fitting specifications

Fitting	Specifications			
	Fitting type	Connection type	**Material**	**Dimensions**
SS-4-VCO-9	Elbow	Male O-ring face seal (x2)	316 Stainless steel	0.25 inch
SS-4-WVCO-7-4	Straight	Female O-ring face seal; Female NPT	316 Stainless steel	0.25 inch
SS-400-1-4	Straight	Compression tube fitting; Male NPT	316 Stainless steel	0.25 inch
SS-400-3-4TTM	Tee	Compression tube fitting (x2); Male NPT	316 Stainless steel	0.25 inch

Appendix B Calibration factors for kinetic experiments

B.1. CO_2 calibration curves

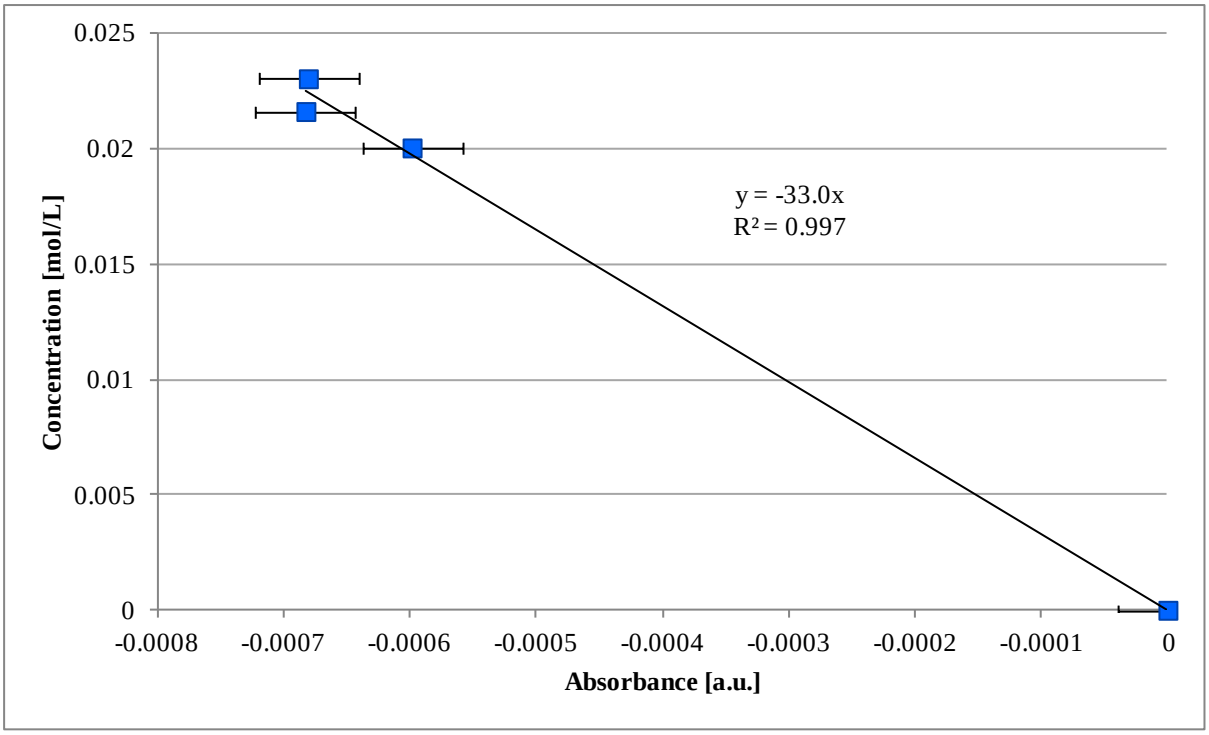

Figure B. 1 : CO_2 calibration data at 20°C

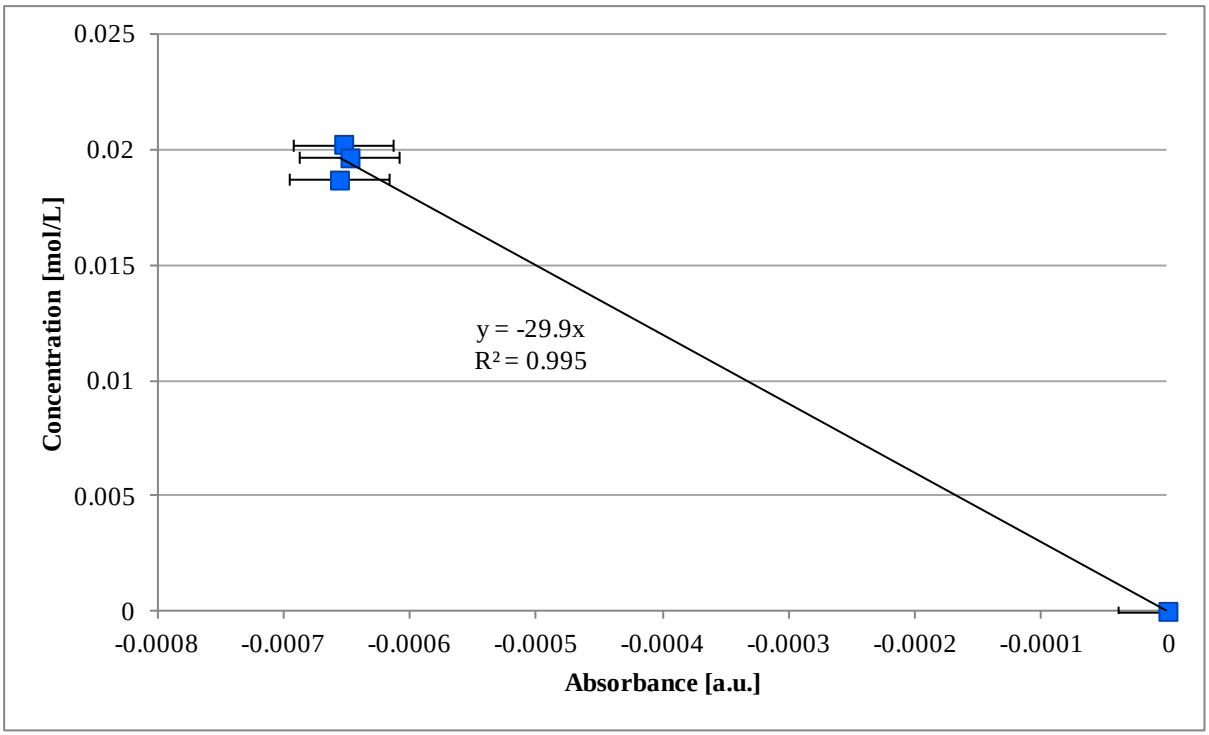

Figure B. 2 : CO_2 calibration data at 25°C

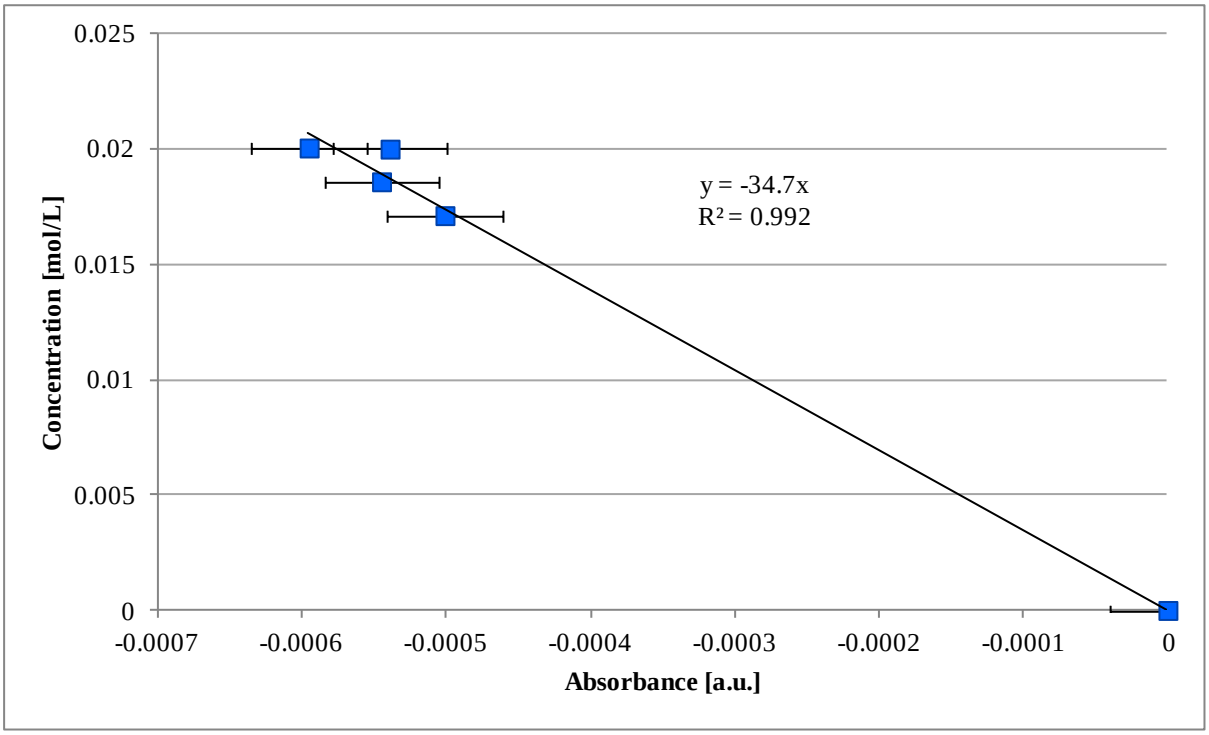

Figure B. 3 : CO_2 calibration data at 30°C

B.2. MEA calibration curves

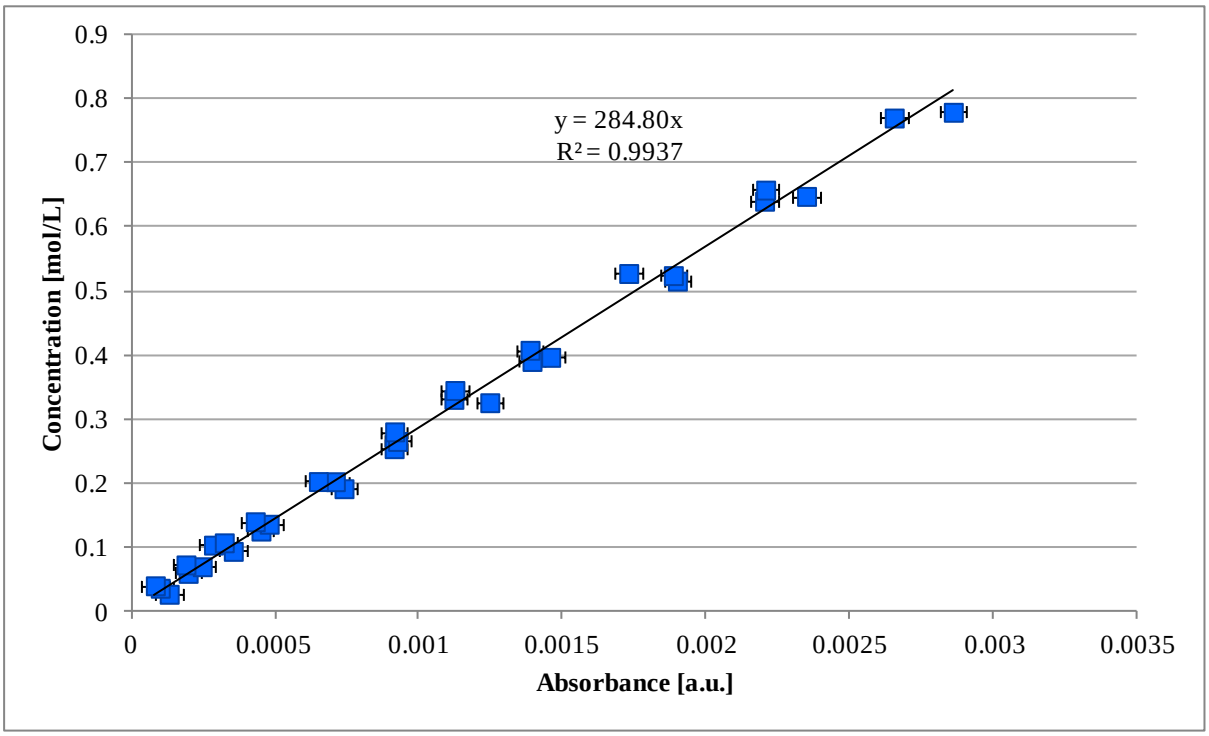

Figure B. 4 : MEA calibration data at 20°C

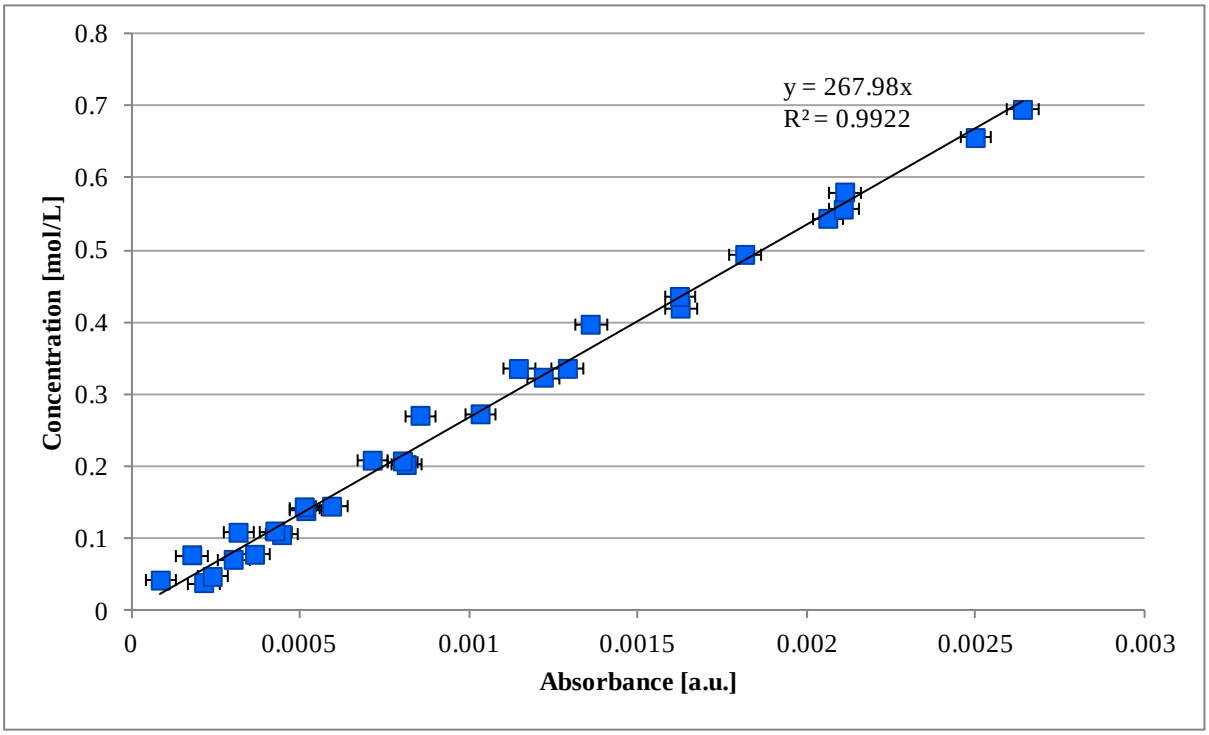

Figure B. 5 : MEA calibration data at 25°C

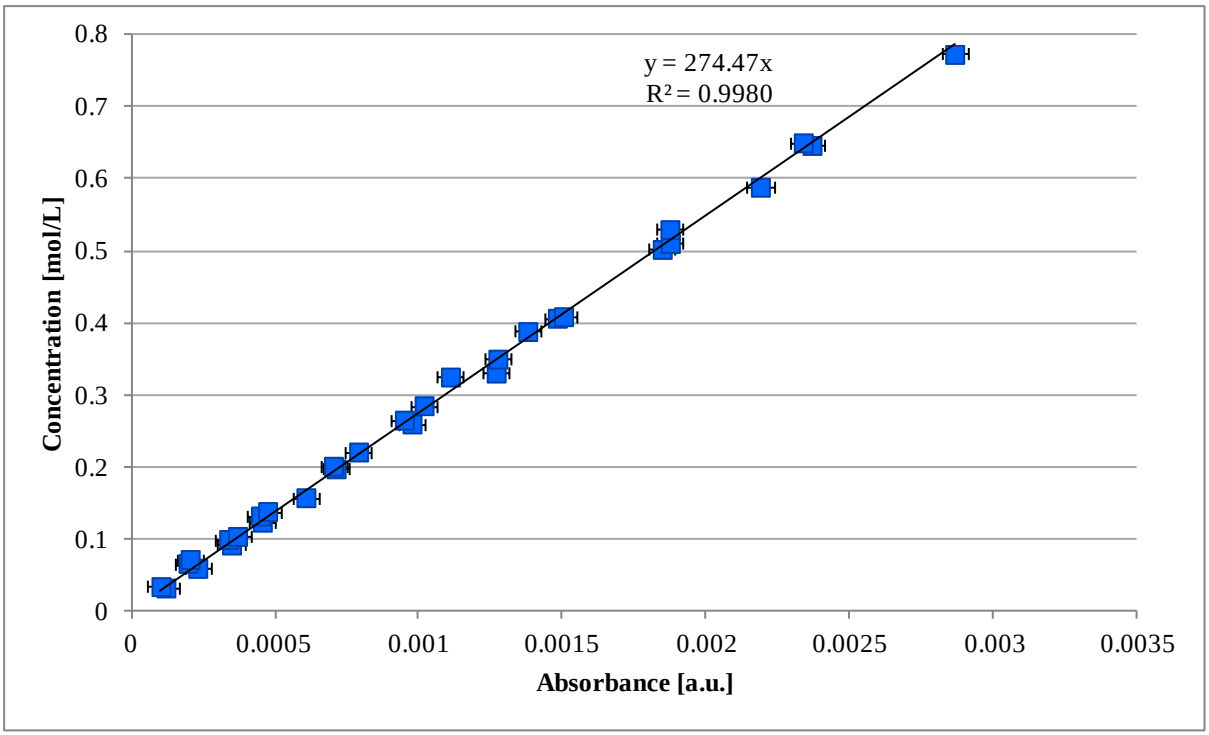

Figure B. 6 : MEA calibration data at 30°C

Appendix C Proof of normally distributed data

Normal distribution of the measured experimental data is illustrated using measurements made during a MEA calibration experiment at 25°C. Measurements were made in a solution containing 22.264 g MEA and 500.569 g H_2O at 25°C. The absorbance measured is given in Figure C. 1, showing the 230 data points that were recorded. The average absorbance is 0.0026383 a.u.

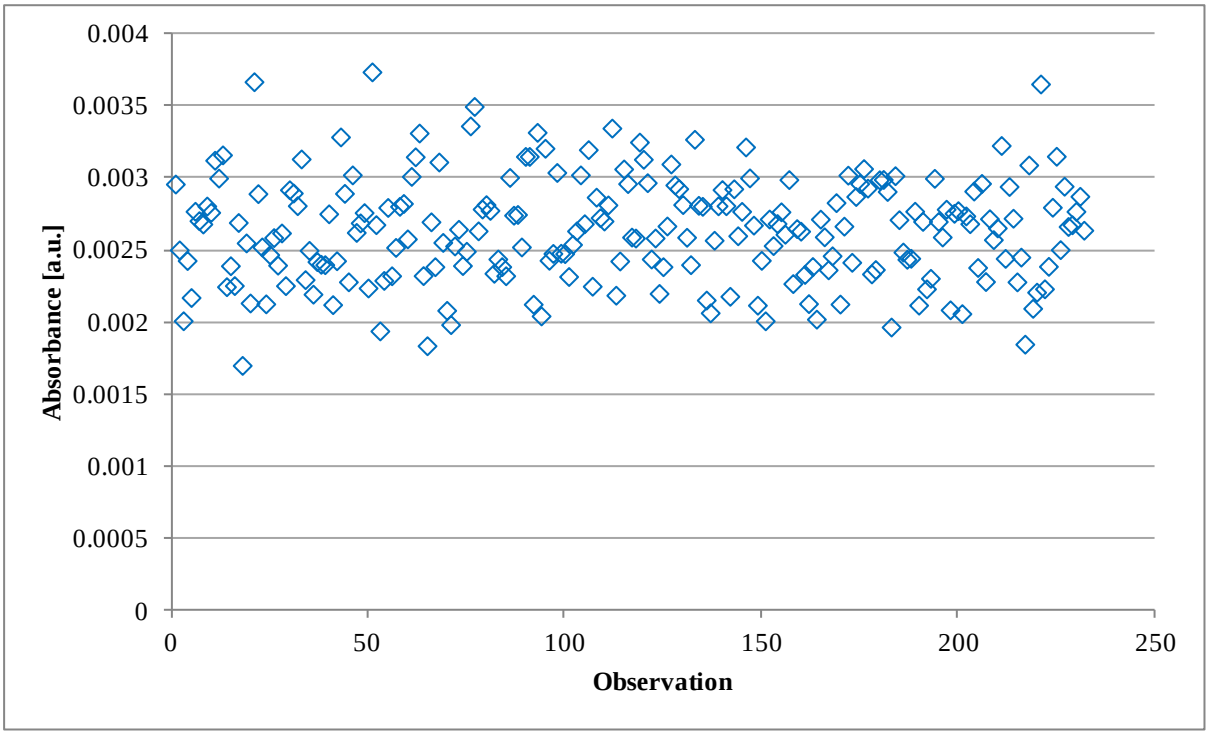

Figure C. 1 : Measured absorbance for a MEA solution containing 22.264 g MEA and 500.569 g H_2O at 25°C

Normal distribution of the data can be proven by constructing a histogram from the measured absorbance. If the data plotted in the histogram approaches a bell curve shape, normal distribution of the data is valid (Taylor, 1997). The histogram of the measured absorbance is given in Figure C. 2, showing how the data approaches the bell curve shape. The shape of the histogram proves the validity of the assumption of normally distributed data, verifying the use of the standard deviation to quantify uncertainty in measurements.

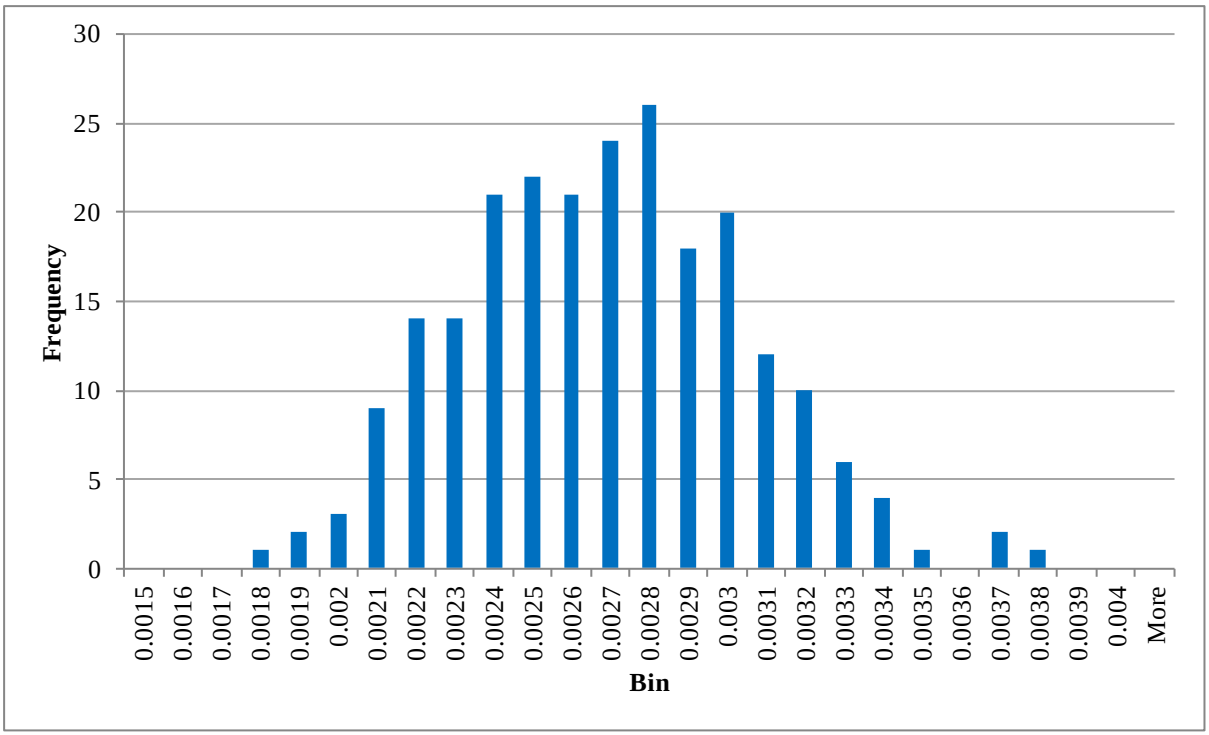

Figure C. 2 : Histogram of measured absorbance for a MEA solution containing 22.264 g MEA and 500.569 g H_2O at 25°C

Appendix D Mass of reagents used in experiments

Table D. 1 : Mass of reagents and flow rates used in kinetic experiments

	0.13 mol MEA								
T [°C]	20			25			30		
Run #	10-20-1	10-20-2	10-20-3	10-25-1	10-25-2	10-25-3	10-30-1	10-30-2	10-30-3
Reactor:									
m_{H_2O}[g]	501.454	499.306	499.457	506.957	505.268	498.210	500.464	500.650	501.299
m_{CO_2}[g]	0.432	0.431	0.467	0.476	0.438	0.461	0.441	0.456	0.458
Syringe:									
m_{H_2O}[g]	89.951	90.880	90.318	87.356	89.143	91.575	90.068	90.422	91.121
m_{MEA}[g]	11.008	10.133	10.384	10.346	11.377	10.930	10.659	11.335	10.011
$m_{sol.in}$[g]	80.729	79.508	80.179	79.295	79.589	80.179	80.584	80.374	80.398
F_{MEA} [mol/s]	0.00513	0.00531	0.00480	0.00420	0.00508	0.00448	0.00470	0.00541	0.00443
	0.26 mol MEA								
T [°C]	20			25			30		
Run #	20-20-1	20-20-2	20-20-3	20-25-1	20-25-2	20-25-3	20-30-1	20-30-2	20-30-3
Reactor:									
m_{H_2O}[g]	501.213	501.444	499.724	505.271	501.162	498.428	500.569	501.169	501.524
m_{CO_2}[g]	0.421	0.453	0.430	0.441	0.507	0.443	0.446	0.468	0.469
Syringe:									
m_{H_2O}[g]	81.085	81.359	81.010	77.700	80.354	80.111	81.356	81.335	81.998
m_{MEA}[g]	20.966	20.471	20.341	22.723	21.042	21.701	21.052	20.575	20.586
$m_{sol.in}$[g]	80.683	81.153	80.380	80.836	80.974	80.762	80.845	80.604	80.656
F_{MEA} [mol/s]	0.00944	0.00928	0.01006	0.01019	0.01017	0.00963	0.00957	0.00871	0.00887

Table D. 2 : Mass of reagents used in equilibrium experiments

T [°C]	20	25 (A)	25 (B)	25 (C)	30
m_{H_2O}[g]	500.069	498.940	502.843	499.114	499.268
m_{MEA}[g]	10.538	10.174	10.685	10.062	10.265
m_{CO_2}[g]	0.770	0.752	0.751	0.799	0.739
	0.717	0.720	0.718	0.698	0.737
	0.771	0.711	0.836	0.814	0.789
	0.724	0.727	0.743	0.712	0.723
	0.709	1.106	0.771	0.728	0.698
	0.748		0.750	0.634	0.732

Appendix E Calibration factors for equilibrium experiments

E.1. Carbamate concentration-absorbance plots

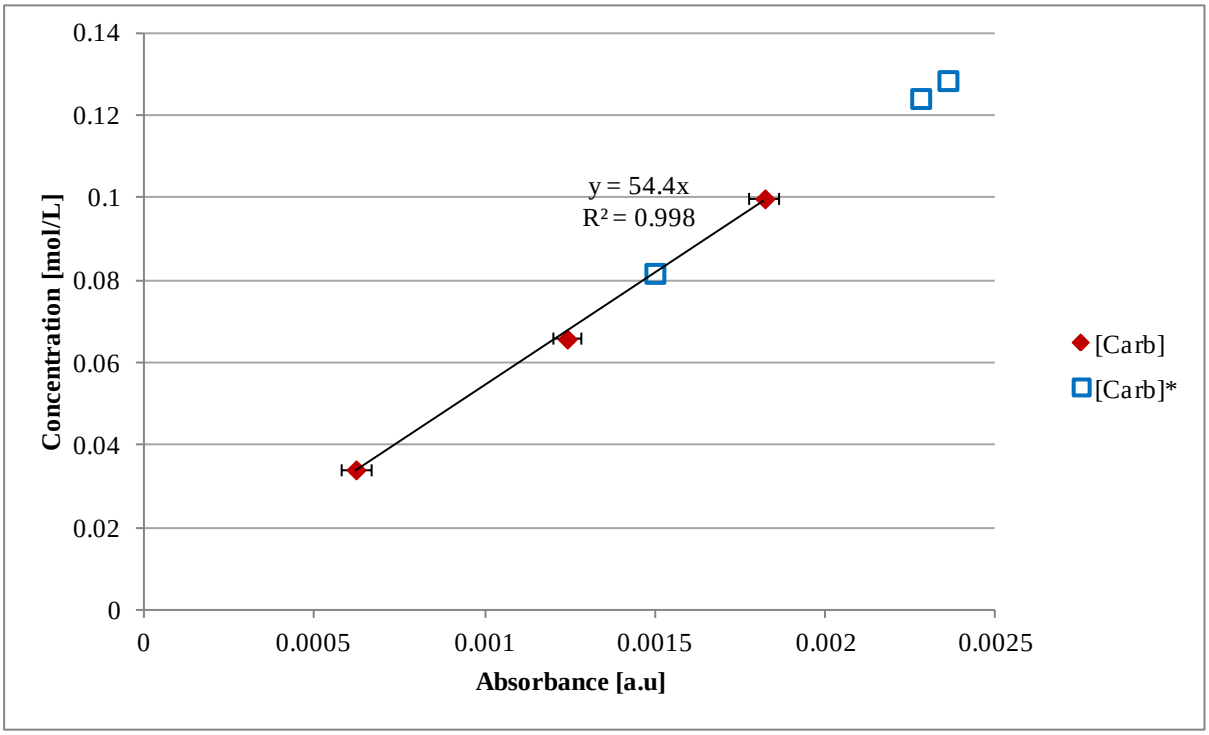

Figure E. 1 : Carbamate calibration curve for at 20°C

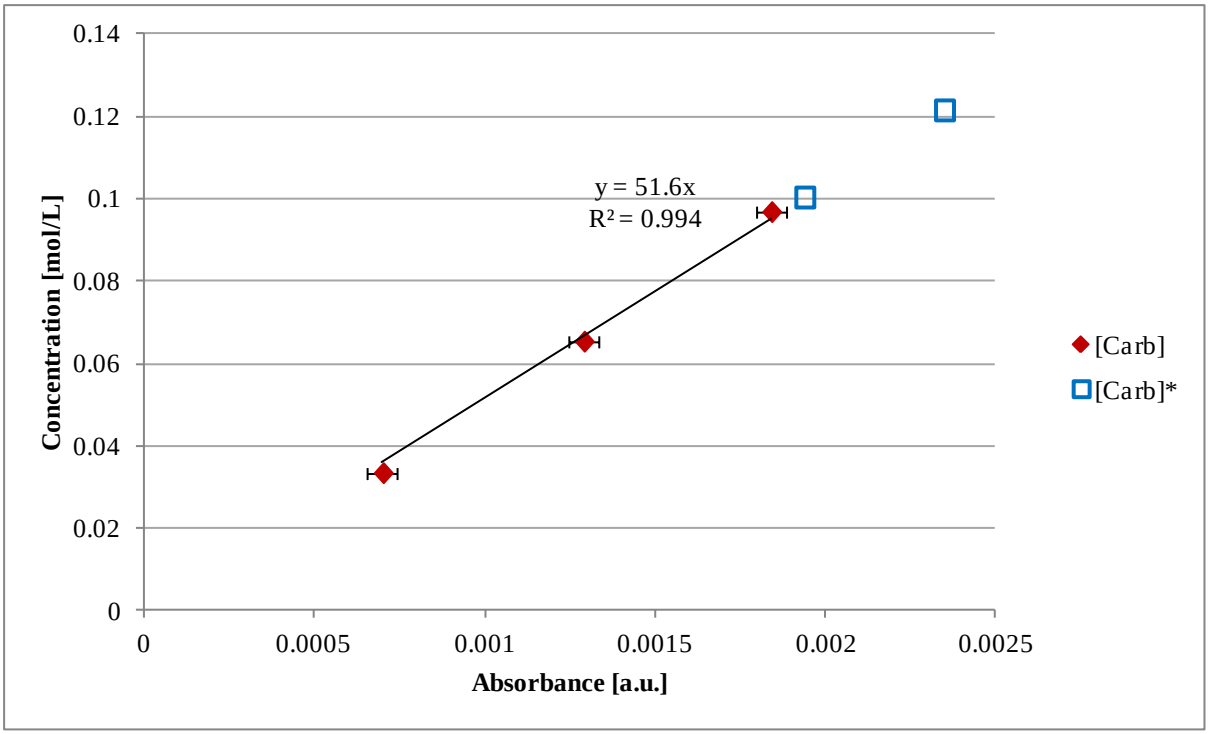

Figure E. 2 : Carbamate calibration curve for at 25°C (25_A)

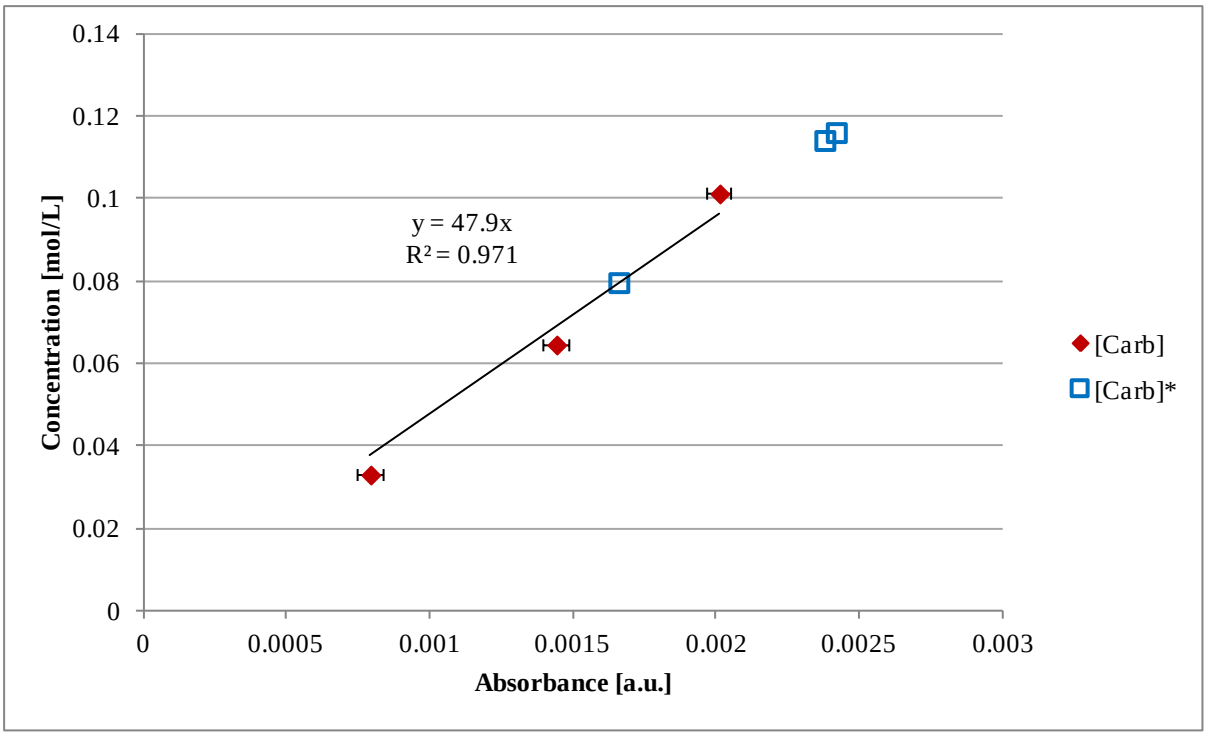

Figure E. 3 : Carbamate calibration curve for at 25°C (25_B)

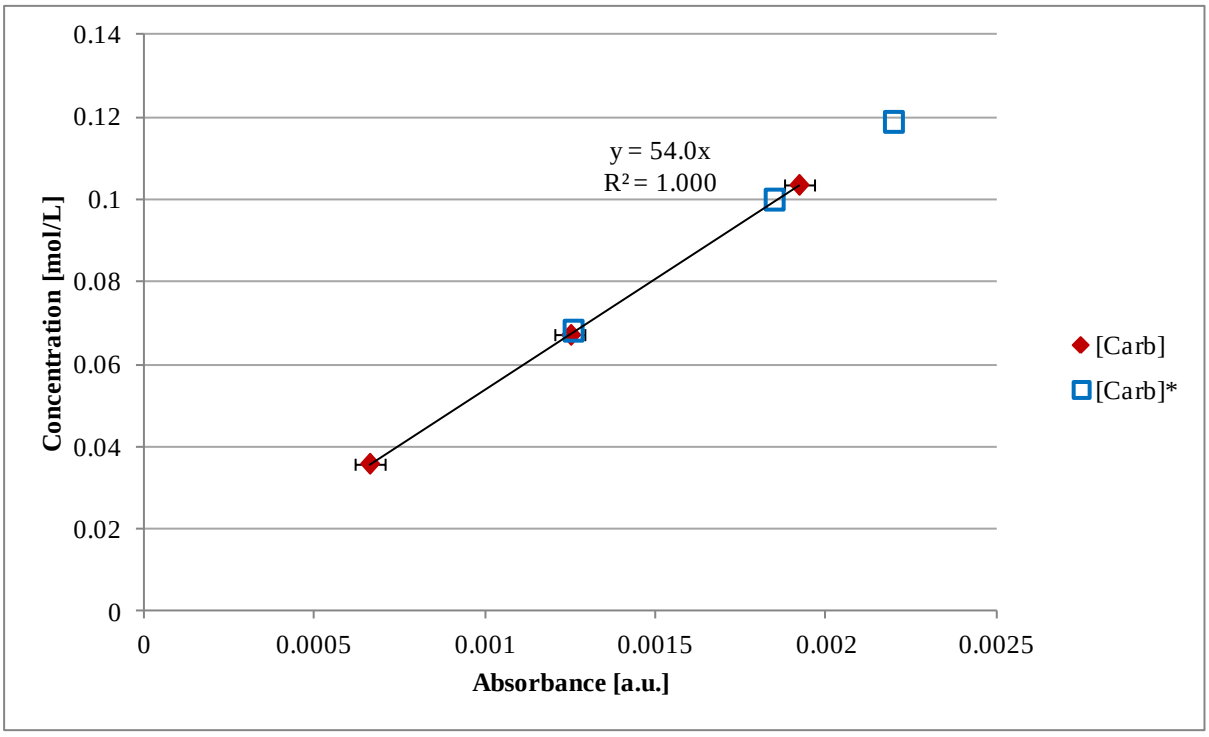

Figure E. 4 : Carbamate calibration curve for at 25°C (25_C)

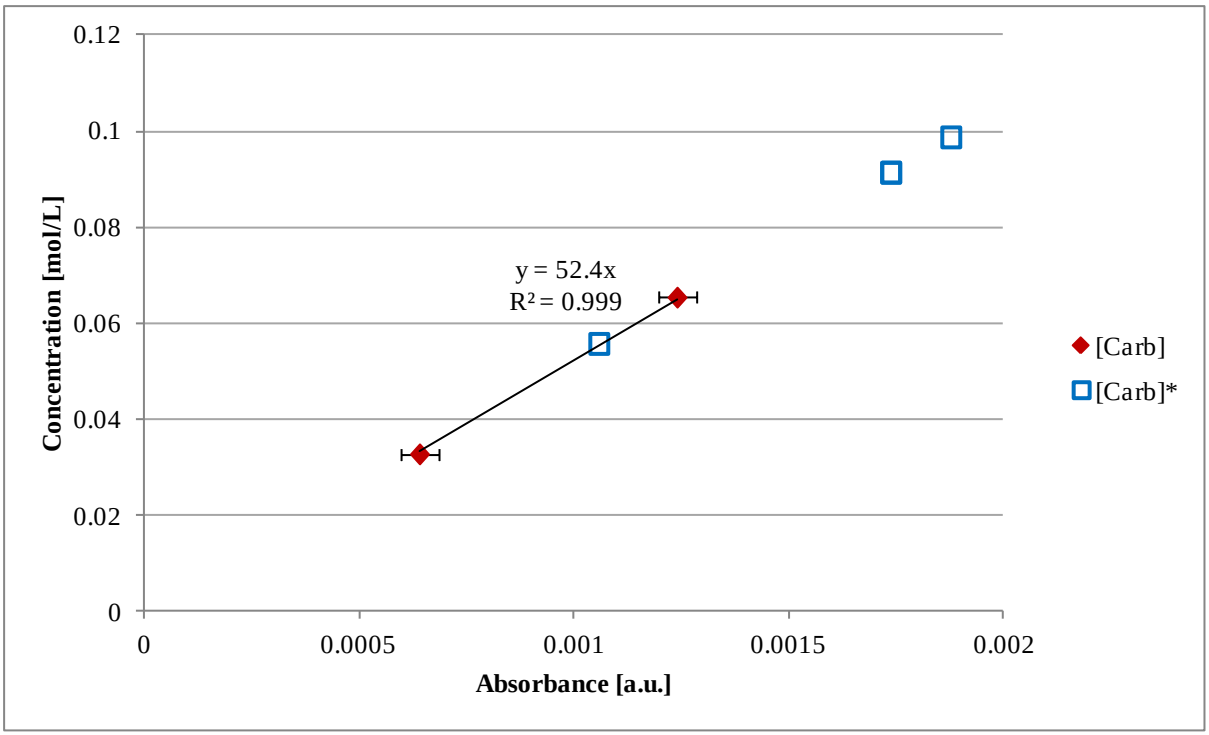

Figure E. 5 : Carbamate calibration curve for at 30°C

E.2. HCO_3^- concentration-absorbance plots

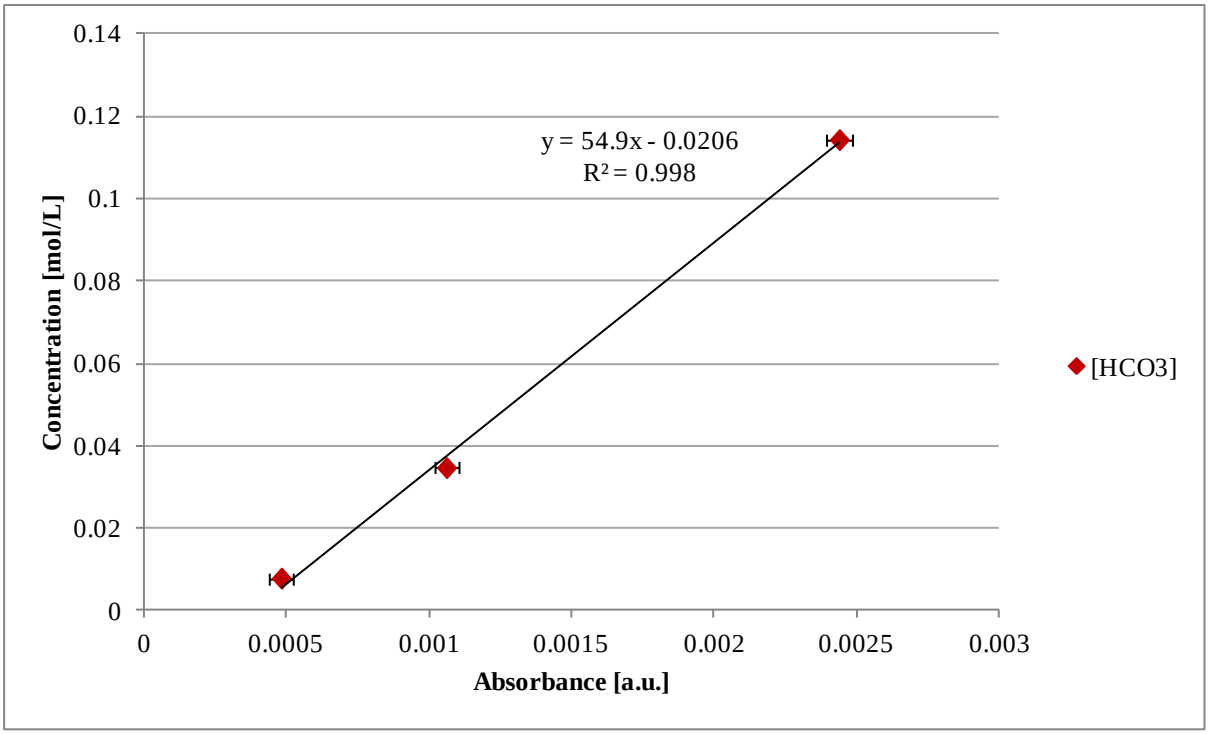

Figure E. 6 : Verification of carbamate calibration – [HCO_3^-] at 20°C

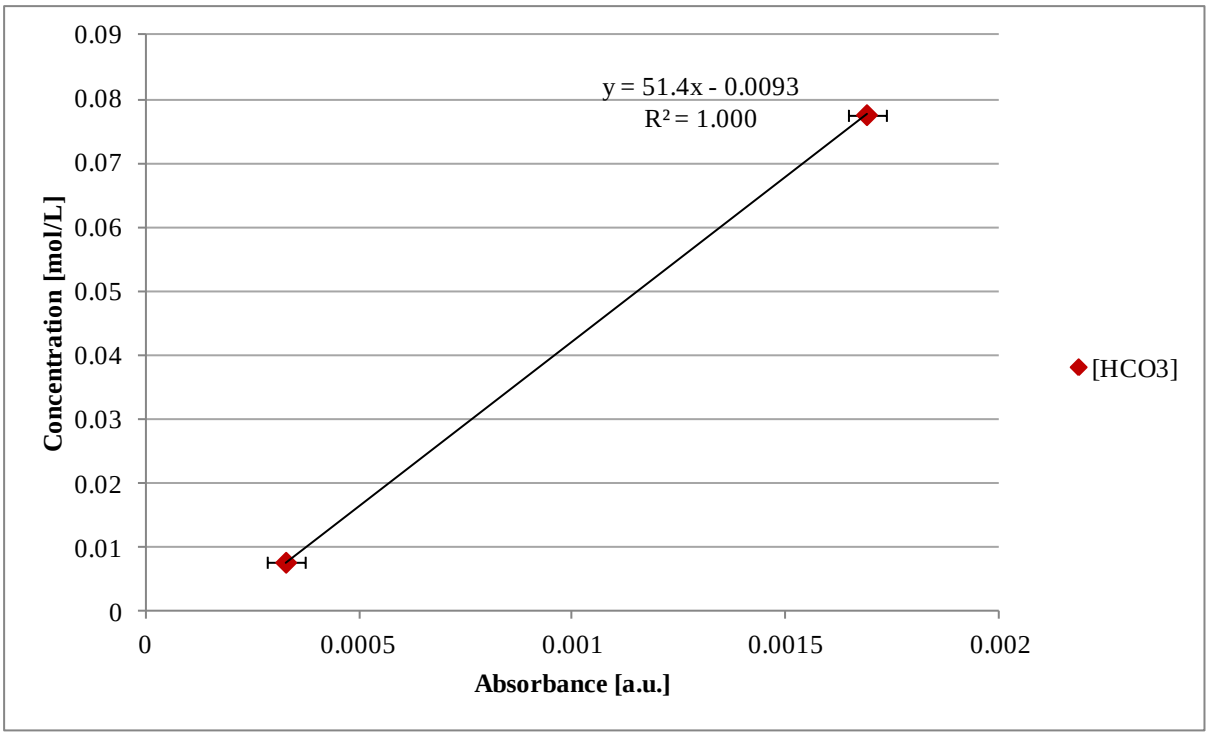

Figure E. 7 : Verification of carbamate calibration – [HCO_3^-] at 25°C (25_A)

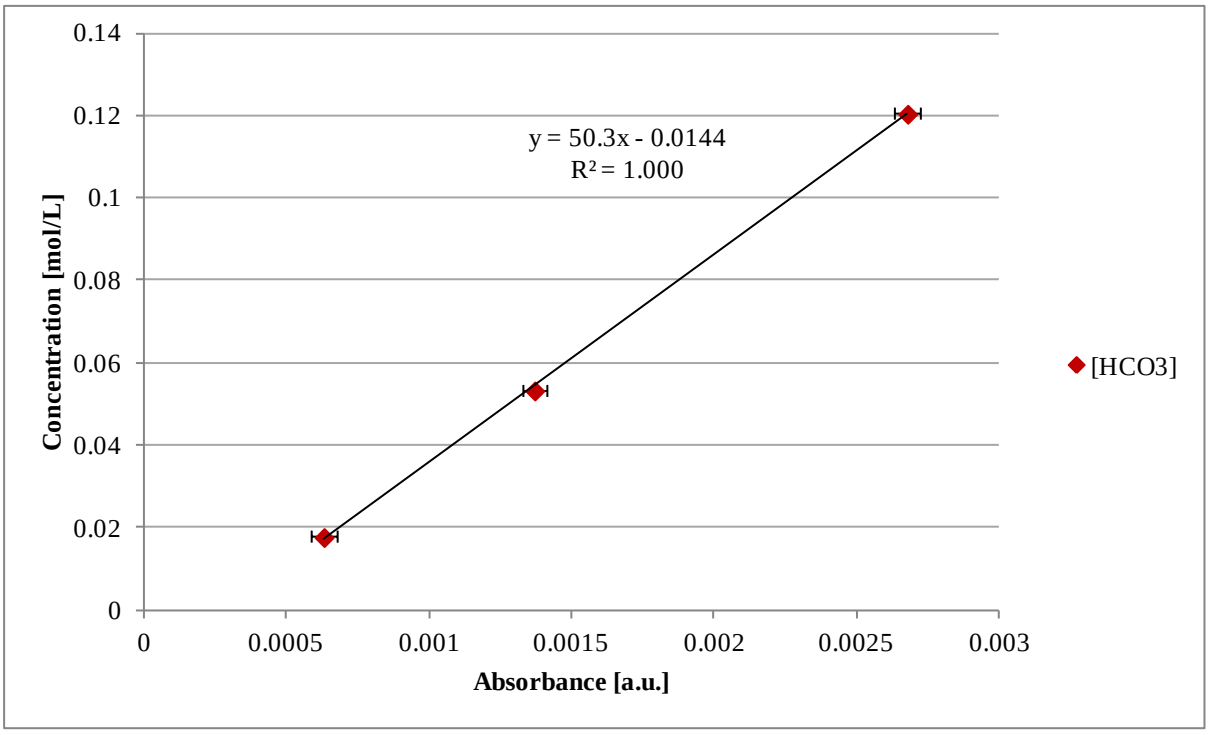

Figure E. 8 : Verification of carbamate calibration – [HCO_3^-] at 25°C (25_B)

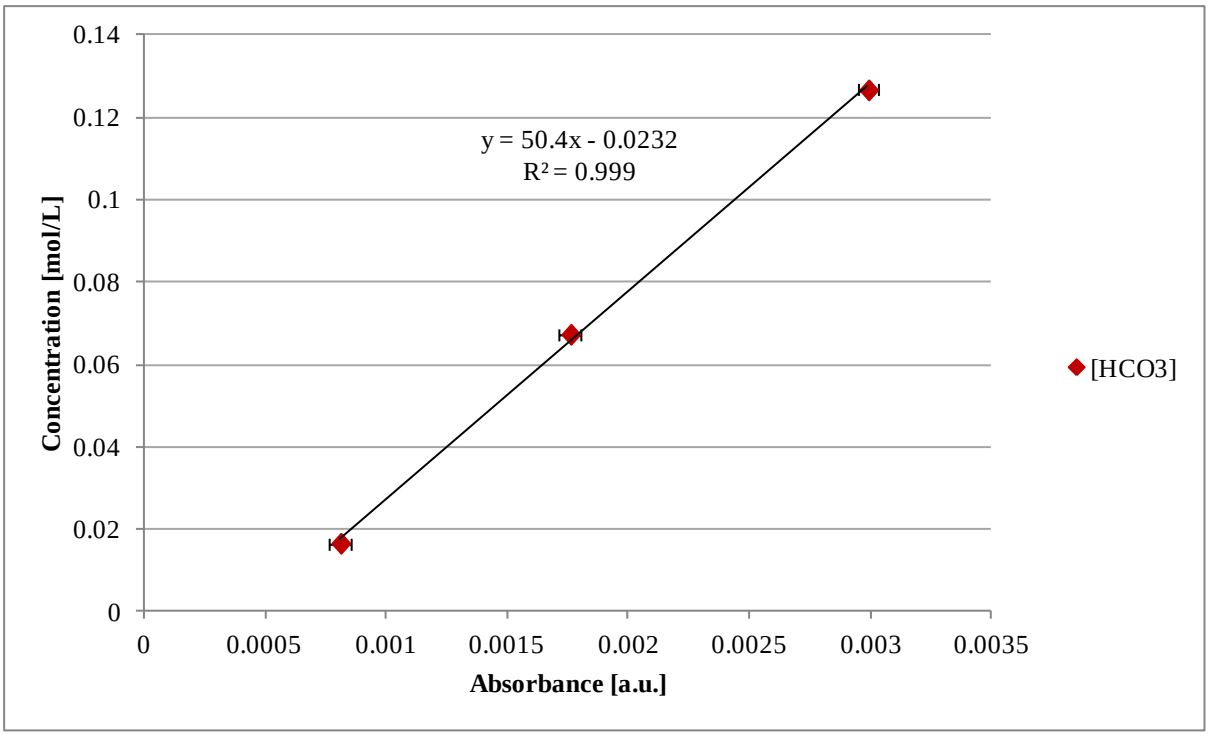

Figure E. 9 : Verification of carbamate calibration – [HCO_3^-] at 25°C (25_C)

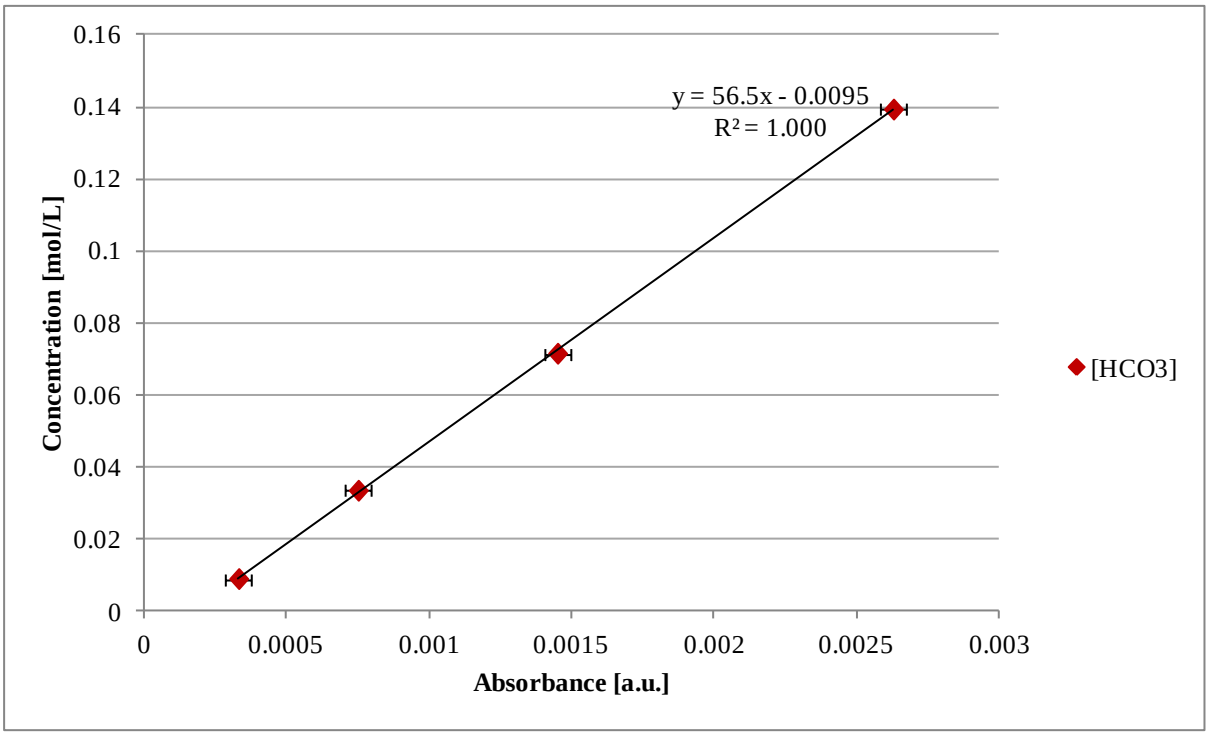

Figure E. 10 : Verification of carbamate calibration – [HCO_3^-] at 30°C

E.3. $MEAH^+$ concentration-absorbance plots

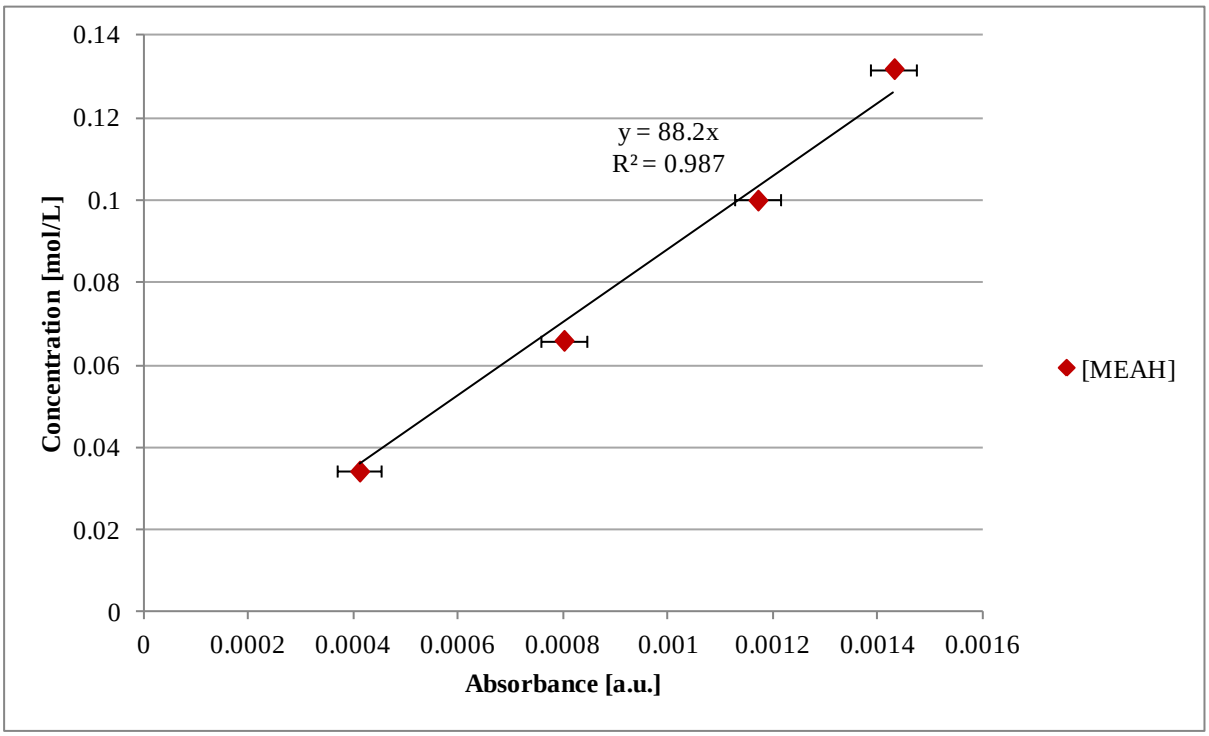

Figure E. 11 : Verification of carbamate calibration – [$MEAH^+$] at 20°C

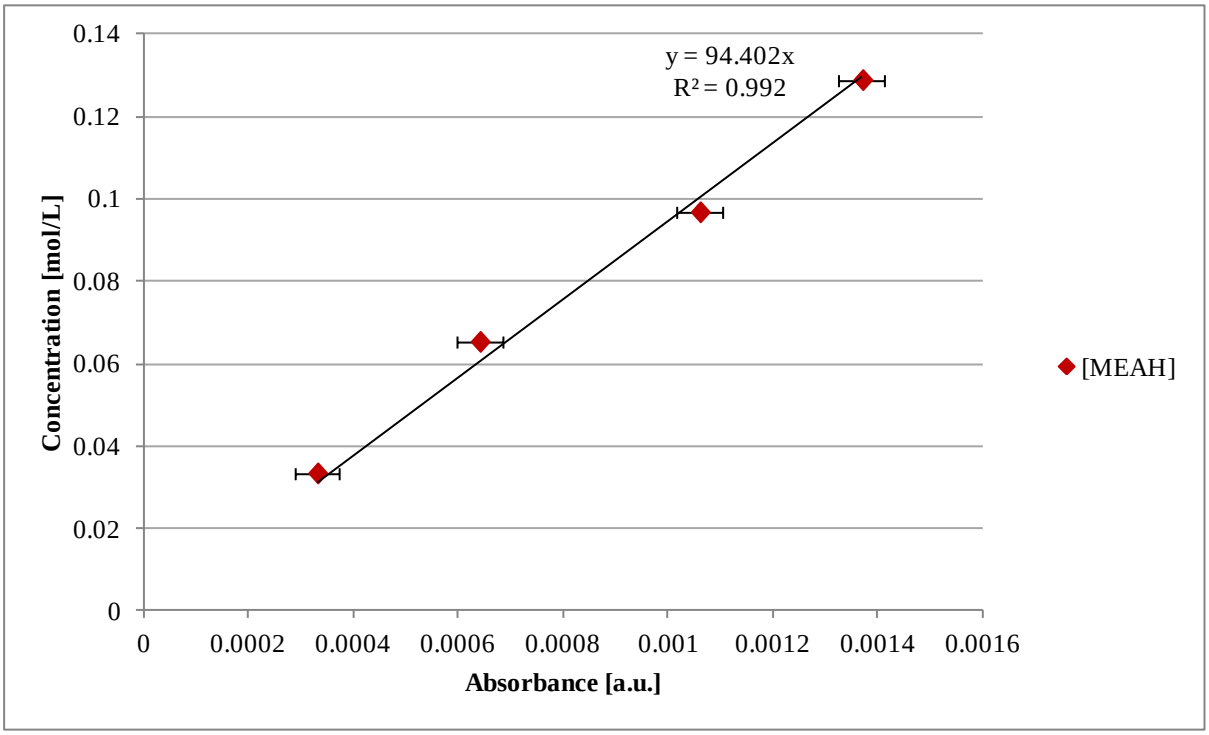

Figure E. 12 : Verification of carbamate calibration – [$MEAH^+$] at 25°C (25_A)

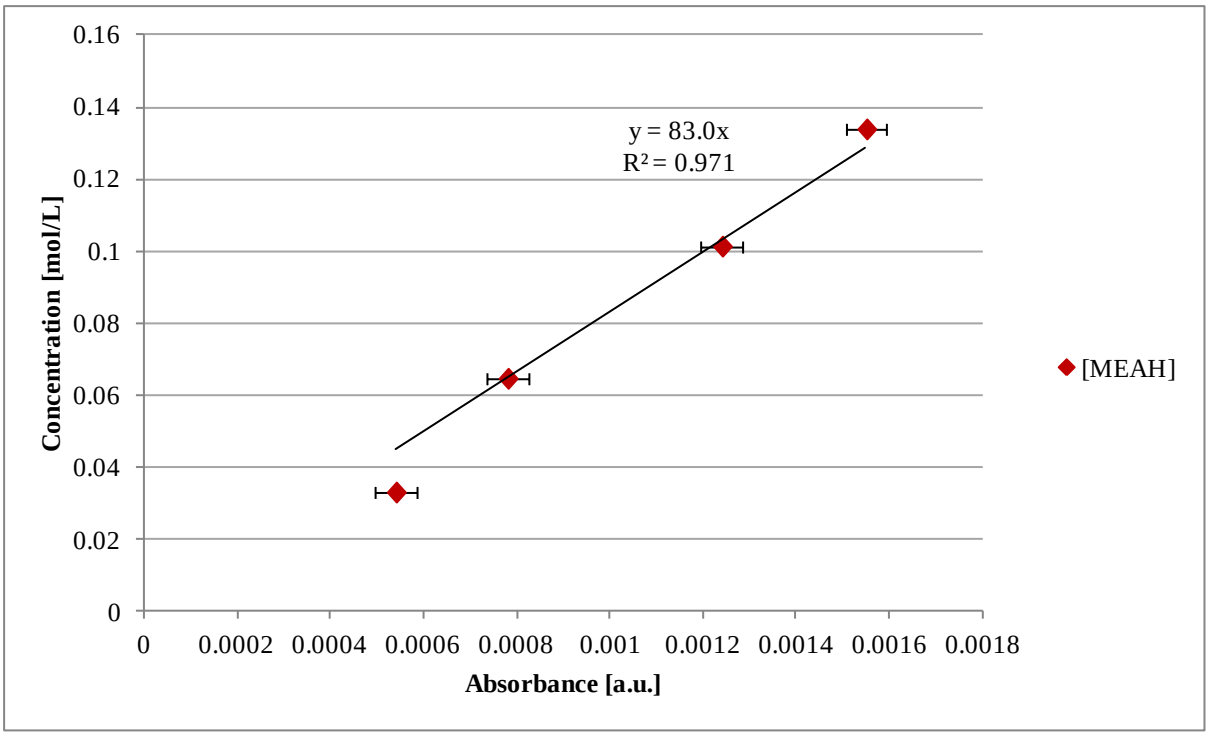

Figure E. 13 : Verification of carbamate calibration – [MEAH$^+$] at 25°C (25_B)

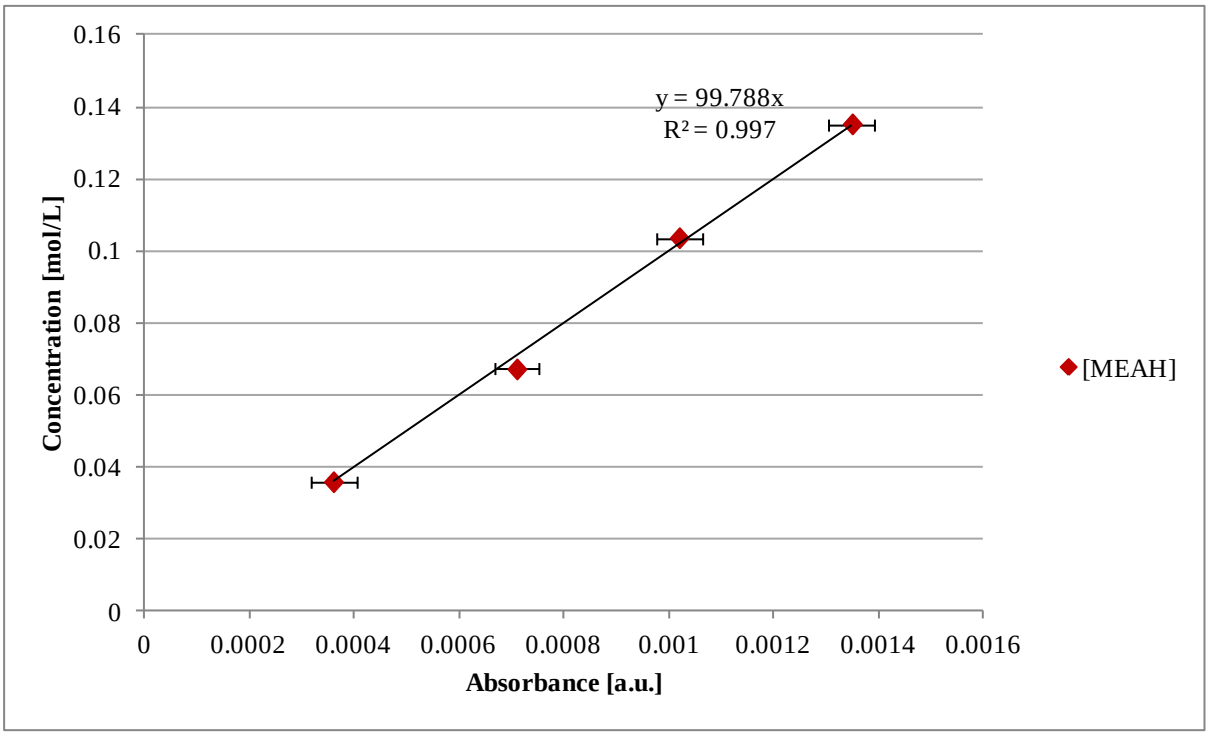

Figure E. 14 : Verification of carbamate calibration – [MEAH$^+$] at 25°C (25_C)

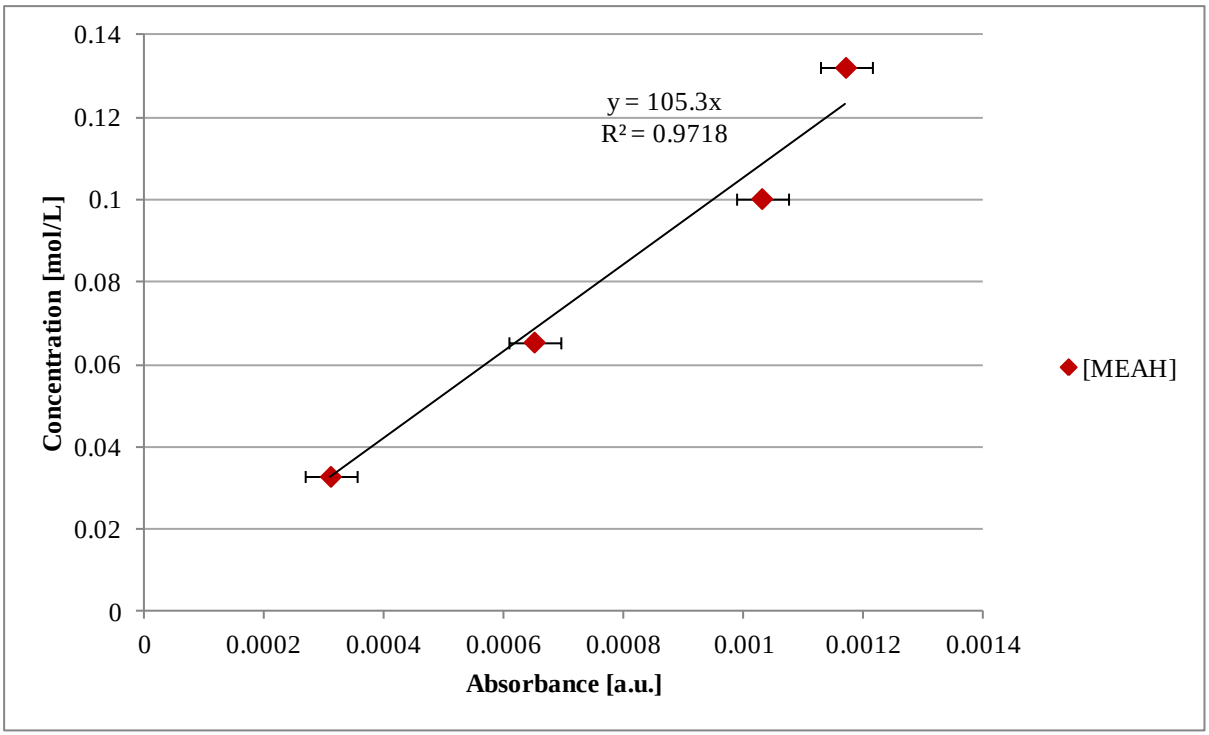

Figure E. 15 : Verification of carbamate calibration – [MEAH$^+$] at 30°C

E.4. MEA concentration-absorbance plots

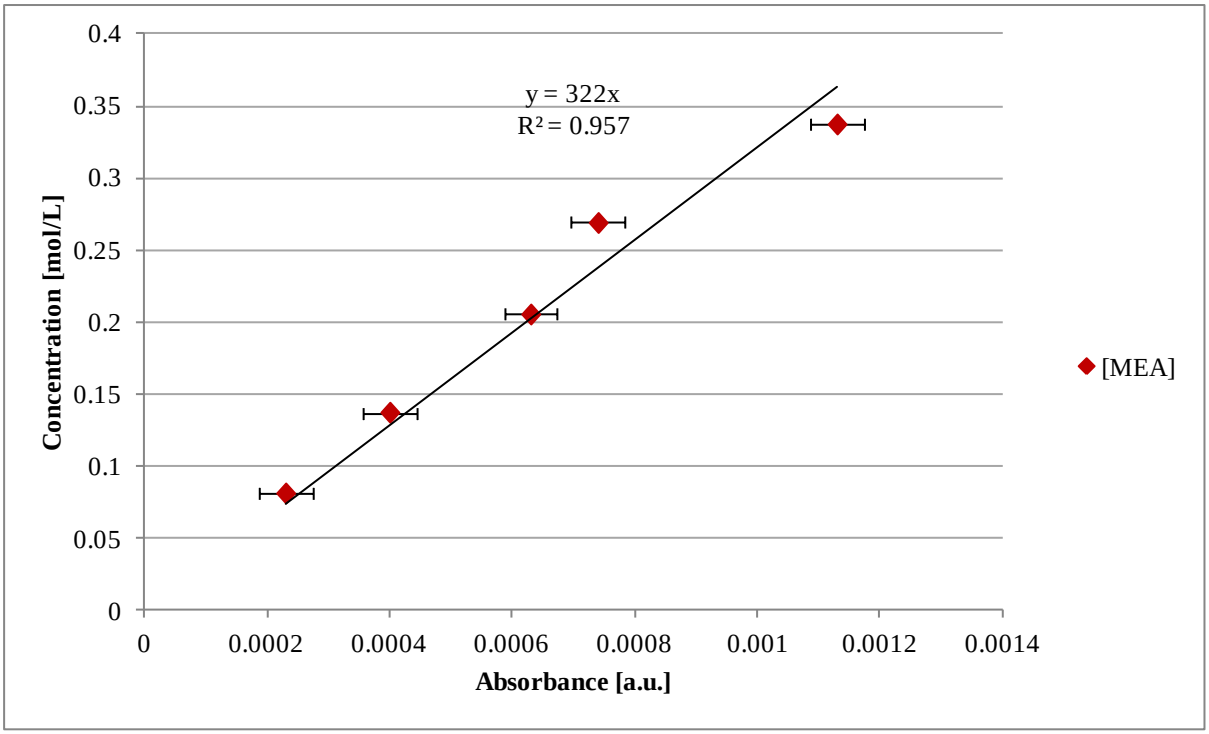

Figure E. 16 : Verification of carbamate calibration – [MEA] at 20°C

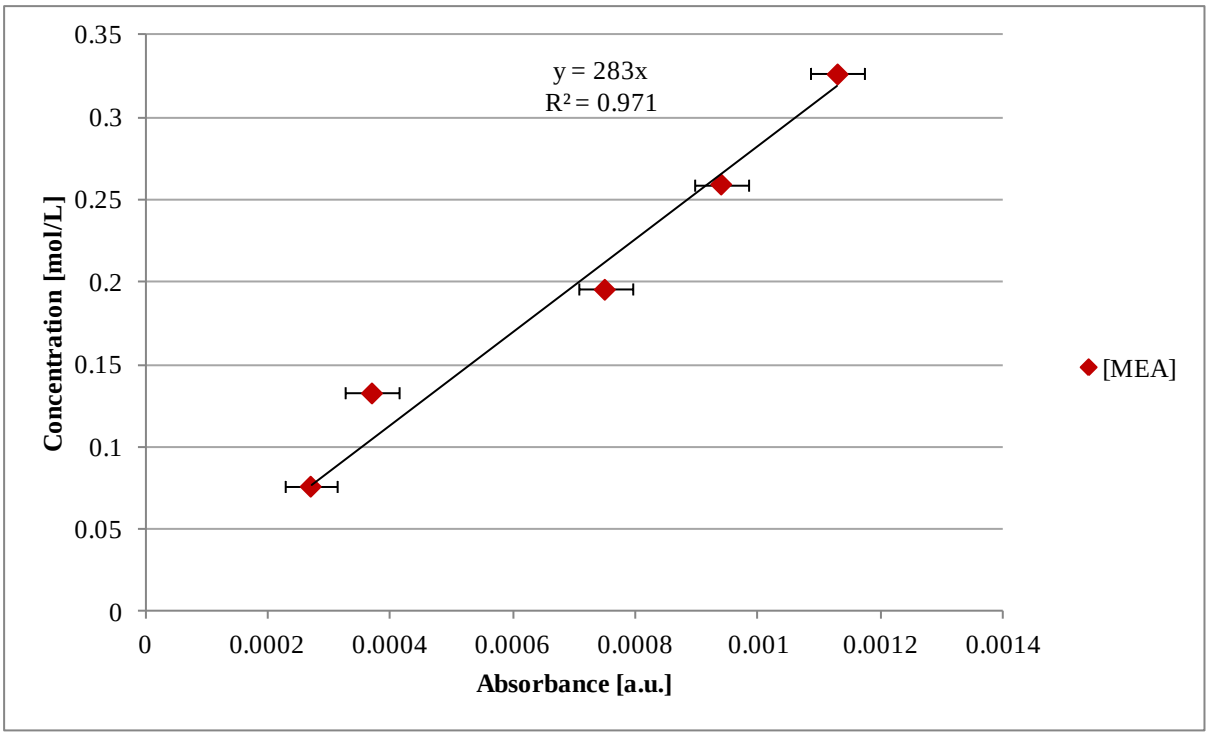

Figure E. 17 : Verification of carbamate calibration – [MEA] at 25°C (25_A)

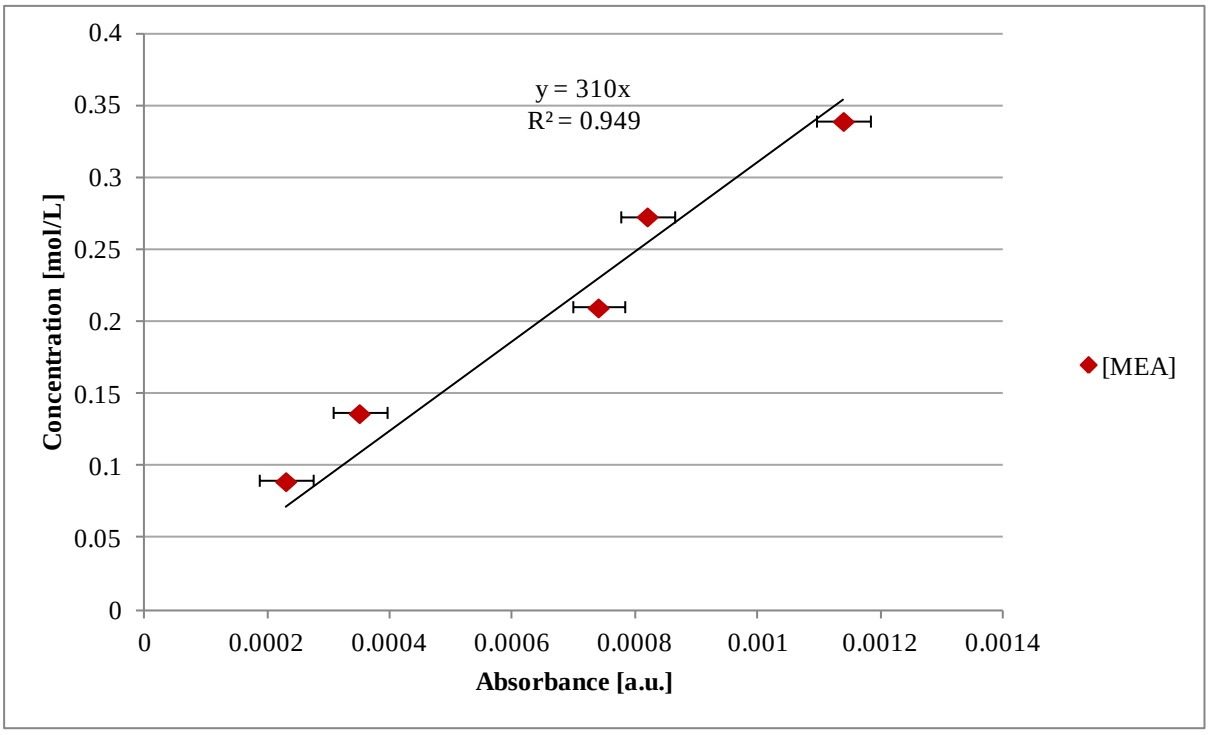

Figure E. 18 : Verification of carbamate calibration – [MEA] at 25°C (25_B)

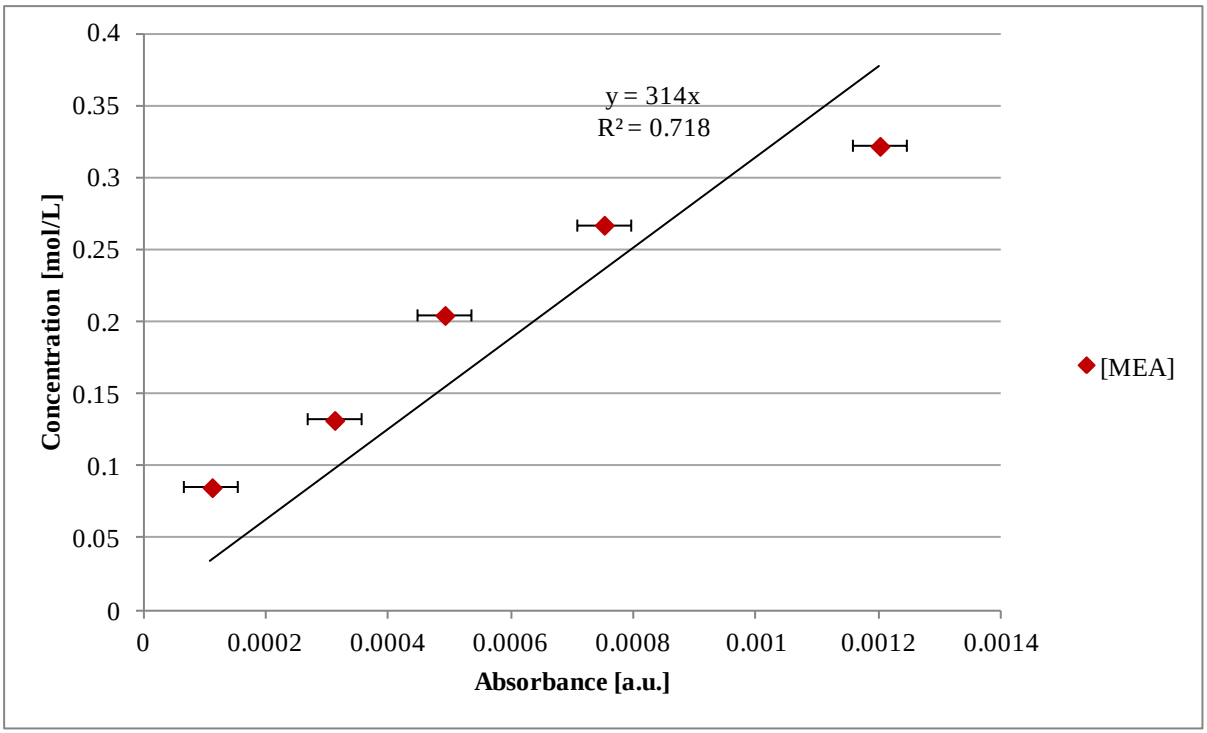

Figure E. 19 : Verification of carbamate calibration – [MEA] at 25°C (25_C)

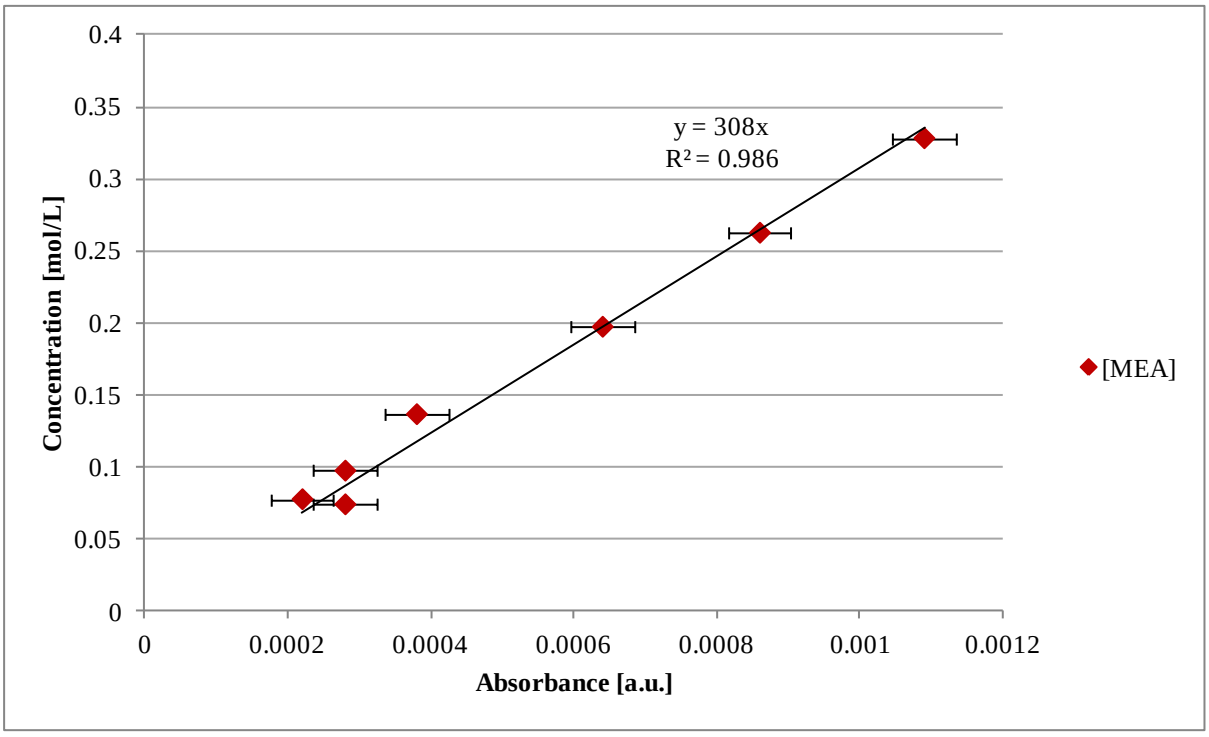

Figure E. 20 : Verification of carbamate calibration – [MEA] at 30°C

Appendix F Individual rate constants – short-time segments

Table F. 1 : Experiment 10-20-1 conducted with 0.144 mol MEA at 0.00513 mol MEA/s and 20°C

Pseudo-first order rate constants				
	k_1 [s^{-1}]		**MSE CO_2 x 10^6**	
Best fit	158		8.98	
Upper bound (95%)	968		8.98	
Median	796		8.98	
Lower bound (5%)	112		8.98	
Second order rate constants				
	k_2 [L/mol.s]		**MSE CO_2 x 10^6**	**MSE MEA x 10^6**
Best fit	66388		7.26	421
Upper bound (95%)	107682		7.25	421
Median	5048		7.33	419
Lower bound (5%)	2146		7.42	418
Third order rate constants				
	k_3 [$L^2/mol^2.s$]		**MSE CO_2 x 10^6**	**MSE MEA x 10^6**
Best fit	3931629		7.36	418
Upper bound (95%)	4061230		7.36	418
Median	1758144		7.42	417
Lower bound (5%)	645259		7.54	415
Termolecular rate constants				
	k_{MEA} [$L^2/mol^2.s$]	k_{H_2O} [$L^2/mol^2.s$]	**MSE CO_2 x 10^6**	**MSE MEA x 10^6**
Best fit	85.0	258491	5.63	436
Upper bound (95%)	1847	132828	7.25	421
Median	1025	1047	7.25	421
Lower bound (5%)	33.8	314	7.26	421

Table F. 2 : Experiment 10-20-2 conducted with 0.131 mol MEA at 0.00531 mol MEA/s and 20°C

Pseudo-first order rate constants				
	k_1 [s^{-1}]		**MSE CO_2 x 10^6**	
Best fit	0.177		2.23	
Upper bound (95%)	904		19.97	
Median	495		19.97	
Lower bound (5%)	29.3		19.97	
Second order rate constants				
	k_2 [L/mol.s]		**MSE CO_2 x 10^6**	**MSE MEA x 10^6**
Best fit	3688		1.66	130
Upper bound (95%)	5924		1.68	130
Median	2893		1.63	130
Lower bound (5%)	659		1.40	133
Third order rate constants				
	k_3 [$L^2/mol^2.s$]		**MSE CO_2 x 10^6**	**MSE MEA x 10^6**
Best fit	359837		1.36	134
Upper bound (95%)	8021091		1.64	130
Median	8676		0.63	163
Lower bound (5%)	3821		0.82	180
Termolecular rate constants				
	k_{MEA} [$L^2/mol^2.s$]	k_{H_2O} [$L^2/mol^2.s$]	**MSE CO_2 x 10^6**	**MSE MEA x 10^6**
Best fit	550	30.6	1.65	130
Upper bound (95%)	1928	127	1.72	129
Median	859	68.4	1.69	130
Lower bound (5%)	119	25.4	1.63	130

Table F. 3 : Experiment 10-20-3 conducted with 0.135 mol MEA at 0.00480 mol MEA/s and 20°C

Pseudo-first order rate constants				
	k_1 [s^{-1}]		**MSE CO_2 x 10^6**	
Best fit	26.6		21.72	
Upper bound (95%)	921		21.73	
Median	435		21.73	
Lower bound (5%)	88.7		21.73	
Second order rate constants				
	k_2 [L/mol.s]		**MSE CO_2 x 10^6**	**MSE MEA x 10^6**
Best fit	25.3		11.55	192
Upper bound (95%)	5714		2.59	328
Median	3285		2.63	327
Lower bound (5%)	26.0		11.32	194
Third order rate constants				
	k_3 [$L^2/mol^2.s$]		**MSE CO_2 x 10^6**	**MSE MEA x 10^6**
Best fit	1830		13.42	185
Upper bound (95%)	8845		6.91	252
Median	3018		10.66	210
Lower bound (5%)	2029		12.79	191
Termolecular rate constants				
	k_{MEA} [$L^2/mol^2.s$]	k_{H_2O} [$L^2/mol^2.s$]	**MSE CO_2 x 10^6**	**MSE MEA x 10^6**
Best fit	0.18	0.21	12.47	184
Upper bound (95%)	840	0.31	7.76	235
Median	0.02	0.25	11.08	196
Lower bound (5%)	0.00	0.10	22.43	126

Table F. 4 : Experiment 10-25-1 conducted with 0.137 mol MEA at 0.00420 mol MEA/s and 25°C

Pseudo-first order rate constants				
	k_1 [s^{-1}]		**MSE CO_2 x 10^6**	
Best fit	902		10.59	
Upper bound (95%)	964		10.59	
Median	486		10.59	
Lower bound (5%)	38.8		10.59	
Second order rate constants				
	k_2 [L/mol.s]		**MSE CO_2 x 10^6**	**MSE MEA x 10^6**
Best fit	29.8		3.58	105
Upper bound (95%)	5924		0.56	173
Median	2893		0.56	172
Lower bound (5%)	55.2		1.90	127
Third order rate constants				
	k_3 [$L^2/mol^2.s$]		**MSE CO_2 x 10^6**	**MSE MEA x 10^6**
Best fit	2958		3.82	107
Upper bound (95%)	9756		1.91	132
Median	3561		3.41	111
Lower bound (5%)	2400		4.35	102
Termolecular rate constants				
	k_{MEA} [$L^2/mol^2.s$]	k_{H_2O} [$L^2/mol^2.s$]	**MSE CO_2 x 10^6**	**MSE MEA x 10^6**
Best fit	0.00	0.27	3.74	103
Upper bound (95%)	1694	57.6	0.56	173
Median	367	0.28	2.98	112
Lower bound (5%)	0.00	0.03	30.36	57

Table F. 5 : Experiment 10-25-2 conducted with 0.147 mol MEA at 0.00508 mol MEA/s and 25°C

Pseudo-first order rate constants				
	k_1 [s^{-1}]		**MSE CO_2 x 10^6**	
Best fit	897		8.92	
Upper bound (95%)	870		8.92	
Median	426		8.92	
Lower bound (5%)	67.6		8.92	
Second order rate constants				
	k_2 [L/mol.s]		**MSE CO_2 x 10^6**	**MSE MEA x 10^6**
Best fit	16.1		4.00	199
Upper bound (95%)	5681		1.31	352
Median	3831		1.30	351
Lower bound (5%)	16.1		4.02	199
Third order rate constants				
	k_3 [$L^2/mol^2.s$]		**MSE CO_2 x 10^6**	**MSE MEA x 10^6**
Best fit	280		9.38	156
Upper bound (95%)	9577		1.74	278
Median	1809		3.45	218
Lower bound (5%)	737		5.50	182
Termolecular rate constants				
	k_{MEA} [$L^2/mol^2.s$]	k_{H_2O} [$L^2/mol^2.s$]	**MSE CO_2 x 10^6**	**MSE MEA x 10^6**
Best fit	132	0.00	9.92	155
Upper bound (95%)	888	44.2	1.30	352
Median	0.00	0.17	3.68	204
Lower bound (5%)	0.00	0.07	7.81	171

Table F. 6 : Experiment 10-25-3 conducted with 0.140 mol MEA at 0.00448 mol MEA/s and 25°C

Pseudo-first order rate constants				
	k_1 [s^{-1}]		**MSE CO_2 x 10^6**	
Best fit	681		21.14	
Upper bound (95%)	891		21.14	
Median	355		21.14	
Lower bound (5%)	66.2		21.14	
Second order rate constants				
	k_2 [L/mol.s]		**MSE CO_2 x 10^6**	**MSE MEA x 10^6**
Best fit	784		1.11	150
Upper bound (95%)	7424		1.33	147
Median	3912		1.30	147
Lower bound (5%)	1214		1.18	149
Third order rate constants				
	k_3 [$L^2/mol^2.s$]		**MSE CO_2 x 10^6**	**MSE MEA x 10^6**
Best fit	1142619		1.15	148
Upper bound (95%)	3388637		1.24	147
Median	9829		0.53	169
Lower bound (5%)	6035		0.63	177
Termolecular rate constants				
	k_{MEA} [$L^2/mol^2.s$]	k_{H_2O} [$L^2/mol^2.s$]	**MSE CO_2 x 10^6**	**MSE MEA x 10^6**
Best fit	1630	44.0	1.31	147
Upper bound (95%)	1817	216	1.36	146
Median	1034	65.0	1.32	147
Lower bound (5%)	84.8	36.2	1.30	147

Table F. 7 : Experiment 10-30-1 conducted with 0.140 mol MEA at 0.00470 mol MEA/s and 30°C

Pseudo-first order rate constants			
	k_1 [s^{-1}]	**MSE CO_2 x 10^6**	
Best fit	0.30	1.05	
Upper bound (95%)	977	13.82	
Median	512	13.82	
Lower bound (5%)	0.31	1.04	
Second order rate constants			
	k_2 [L/mol.s]	**MSE CO_2 x 10^6**	**MSE MEA x 10^6**
Best fit	4248	2.02	231
Upper bound (95%)	107910	1.94	229
Median	3251	2.04	232
Lower bound (5%)	1695	2.12	234
Third order rate constants			
	k_3 [$L^2/mol^2.s$]	**MSE CO_2 x 10^6**	**MSE MEA x 10^6**
Best fit	9605621	2.05	231
Upper bound (95%)	44201983	1.99	230
Median	2492230	2.16	234
Lower bound (5%)	5928	7.49	302
Termolecular rate constants			
	k_{MEA} [$L^2/mol^2.s$]	k_{H_2O} [$L^2/mol^2.s$]	**MSE CO_2 x 10^6**	**MSE MEA x 10^6**
Best fit	1907	175	1.96	230
Upper bound (95%)	13313	73972	1.94	229
Median	993	380	1.95	229
Lower bound (5%)	0.00	118	1.97	230

Table F. 8 : Experiment 10-30-2 conducted with 0.147 mol MEA at 0.00541 mol MEA/s and 30°C

Pseudo-first order rate constants				
	k_1 [s^{-1}]		**MSE CO_2 x 10^6**	
Best fit	0.10		2.74	
Upper bound (95%)	929		15.61	
Median	465		15.61	
Lower bound (5%)	57.3		15.61	
Second order rate constants				
	k_2 [L/mol.s]		**MSE CO_2 x 10^6**	**MSE MEA x 10^6**
Best fit	5.06		2.63	103
Upper bound (95%)	4912		7.00	118
Median	3568		6.97	118
Lower bound (5%)	6.74		2.20	104
Third order rate constants				
	k_3 [$L^2/mol^2.s$]		**MSE CO_2 x 10^6**	**MSE MEA x 10^6**
Best fit	293		2.57	107
Upper bound (95%)	9297		5.05	108
Median	2093		3.80	104
Lower bound (5%)	285		2.57	107
Termolecular rate constants				
	k_{MEA} [$L^2/mol^2.s$]	k_{H_2O} [$L^2/mol^2.s$]	**MSE CO_2 x 10^6**	**MSE MEA x 10^6**
Best fit	0.00	0.08	2.12	103
Upper bound (95%)	1962	82.4	7.03	118
Median	630	38.3	6.99	118
Lower bound (5%)	0.00	0.00	63.20	186

Table F. 9 : Experiment 10-30-3 conducted with 0.130 mol MEA at 0.00443 mol MEA/s and 30°C

Pseudo-first order rate constants				
	k_1 [s^{-1}]		**MSE CO_2 x 10^6**	
Best fit	139		25.50	
Upper bound (95%)	890		25.50	
Median	487		25.50	
Lower bound (5%)	72.7		25.50	
Second order rate constants				
	k_2 [L/mol.s]		**MSE CO_2 x 10^6**	**MSE MEA x 10^6**
Best fit	5877		1.30	133
Upper bound (95%)	5646		1.30	133
Median	2544		1.36	132
Lower bound (5%)	667		1.62	132
Third order rate constants				
	k_3 [$L^2/mol^2.s$]		**MSE CO_2 x 10^6**	**MSE MEA x 10^6**
Best fit	215400		1.78	133
Upper bound (95%)	625306		1.55	133
Median	220572		1.77	133
Lower bound (5%)	88603		2.11	134
Termolecular rate constants				
	k_{MEA} [$L^2/mol^2.s$]	k_{H_2O} [$L^2/mol^2.s$]	**MSE CO_2 x 10^6**	**MSE MEA x 10^6**
Best fit	1845	7.68	1.56	132
Upper bound (95%)	1931	82.9	1.28	133
Median	981	35.8	1.33	132
Lower bound (5%)	193	5.68	1.66	132

Table F. 10 : Experiment 20-20-1 conducted with 0.271 mol MEA at 0.00944 mol MEA/s and 20°C

Pseudo-first order rate constants				
	k_1 [s^{-1}]		**MSE CO_2 x 10^6**	
Best fit	0.25		2.42	
Upper bound (95%)	788		21.26	
Median	477		21.26	
Lower bound (5%)	19.9		21.23	
Second order rate constants				
	k_2 [L/mol.s]		**MSE CO_2 x 10^6**	**MSE MEA x 10^6**
Best fit	548		2.51	64
Upper bound (95%)	4979		3.13	62
Median	1826		2.96	63
Lower bound (5%)	559		2.52	64
Third order rate constants				
	k_3 [$L^2/mol^2.s$]		**MSE CO_2 x 10^6**	**MSE MEA x 10^6**
Best fit	208597		2.47	63
Upper bound (95%)	424239		2.67	63
Median	33275		1.72	67
Lower bound (5%)	5252		1.27	80
Termolecular rate constants				
	k_{MEA} [$L^2/mol^2.s$]	k_{H_2O} [$L^2/mol^2.s$]	**MSE CO_2 x 10^6**	**MSE MEA x 10^6**
Best fit	5.21	16.6	2.95	63
Upper bound (95%)	1713	88.4	3.19	62
Median	875	40.5	3.12	62
Lower bound (5%)	17.8	2.94	2.18	65

Table F. 11 : Experiment 20-20-2 conducted with 0.267 mol MEA at 0.00928 mol MEA/s and 20°C

Pseudo-first order rate constants				
	k_1 [s^{-1}]		**MSE CO_2 x 10^6**	
Best fit	151		7.12	
Upper bound (95%)	802		7.12	
Median	435		7.12	
Lower bound (5%)	84.5		7.12	
Second order rate constants				
	k_2 [L/mol.s]		**MSE CO_2 x 10^6**	**MSE MEA x 10^6**
Best fit	3682		2.46	276
Upper bound (95%)	5678		2.47	276
Median	2953		2.45	277
Lower bound (5%)	1095		2.41	280
Third order rate constants				
	k_3 [$L^2/mol^2.s$]		**MSE CO_2 x 10^6**	**MSE MEA x 10^6**
Best fit	1989386		2.44	277
Upper bound (95%)	3047838		2.45	277
Median	271858		2.40	282
Lower bound (5%)	5557		3.92	335
Termolecular rate constants				
	k_{MEA} [$L^2/mol^2.s$]	k_{H_2O} [$L^2/mol^2.s$]	**MSE CO_2 x 10^6**	**MSE MEA x 10^6**
Best fit	548	7.40	2.40	281
Upper bound (95%)	1737	759	2.51	274
Median	593	62.8	2.48	275
Lower bound (5%)	22.7	5.50	2.40	284

Table F. 12 : Experiment 20-20-3 conducted with 0.264 mol MEA at 0.01006 mol MEA/s and 20°C

Pseudo-first order rate constants				
	k_1 [s^{-1}]		**MSE CO_2 x 10^6**	
Best fit	860		14.59	
Upper bound (95%)	911		14.59	
Median	426		14.59	
Lower bound (5%)	59.5		14.59	
Second order rate constants				
	k_2 [L/mol.s]		**MSE CO_2 x 10^6**	**MSE MEA x 10^6**
Best fit	5345		3.74	436
Upper bound (95%)	5399		3.74	436
Median	2893		3.63	436
Lower bound (5%)	996		3.29	437
Third order rate constants				
	k_3 [$L^2/mol^2.s$]		**MSE CO_2 x 10^6**	**MSE MEA x 10^6**
Best fit	402		4.41	501
Upper bound (95%)	33360		2.16	441
Median	7140		1.17	446
Lower bound (5%)	2340		0.84	454
Termolecular rate constants				
	k_{MEA} [$L^2/mol^2.s$]	k_{H_2O} [$L^2/mol^2.s$]	**MSE CO_2 x 10^6**	**MSE MEA x 10^6**
Best fit	1962	52.4	3.75	436
Upper bound (95%)	1987	379	3.88	437
Median	1283	56.2	3.76	436
Lower bound (5%)	53.7	7.21	3.18	437

Table F. 13 : Experiment 20-25-1 conducted with 0.299 mol MEA at 0.01019 mol MEA/s and 25°C

Pseudo-first order rate constants				
	k_1 [s^{-1}]		**MSE CO_2 x 10^6**	
Best fit	356		15.65	
Upper bound (95%)	947		15.65	
Median	609		15.65	
Lower bound (5%)	82.9		15.65	
Second order rate constants				
	k_2 [L/mol.s]		**MSE CO_2 x 10^6**	**MSE MEA x 10^6**
Best fit	66.0		1.44	122
Upper bound (95%)	5940		5.10	92
Median	3154		4.99	92
Lower bound (5%)	64.4		1.40	123
Third order rate constants				
	k_3 [$L^2/mol^2.s$]		**MSE CO_2 x 10^6**	**MSE MEA x 10^6**
Best fit	4022		1.23	129
Upper bound (95%)	9555		2.09	115
Median	4547		1.35	126
Lower bound (5%)	1475		0.47	151
Termolecular rate constants				
	k_{MEA} [$L^2/mol^2.s$]	k_{H_2O} [$L^2/mol^2.s$]	**MSE CO_2 x 10^6**	**MSE MEA x 10^6**
Best fit	1900	0.12	1.37	125
Upper bound (95%)	1940	304	5.22	92
Median	1004	15.0	4.79	93
Lower bound (5%)	83.8	0.10	0.49	170

Table F. 14 : Experiment 20-25-2 conducted with 0.275 mol MEA at 0.01017 mol MEA/s and 25°C

Pseudo-first order rate constants			
	k_1 [s^{-1}]	**MSE CO_2 x 10^6**	
Best fit	310	41.56	
Upper bound (95%)	964	41.56	
Median	565	41.56	
Lower bound (5%)	244	41.56	
Second order rate constants			
	k_2 [L/mol.s]	**MSE CO_2 x 10^6**	**MSE MEA x 10^6**
Best fit	15.5	1.02	51
Upper bound (95%)	5369	8.47	109
Median	3552	8.39	109
Lower bound (5%)	15.6	1.00	51
Third order rate constants			
	k_3 [$L^2/mol^2.s$]	**MSE CO_2 x 10^6**	**MSE MEA x 10^6**
Best fit	552	1.38	48
Upper bound (95%)	8704	3.38	78
Median	5035	2.42	71
Lower bound (5%)	533	1.46	48
Termolecular rate constants			
	k_{MEA} [$L^2/mol^2.s$]	k_{H_2O} [$L^2/mol^2.s$]	**MSE CO_2 x 10^6**	**MSE MEA x 10^6**
Best fit	397	0.00	0.83	49
Upper bound (95%)	1967	83.5	8.57	110
Median	940	25.0	8.29	109
Lower bound (5%)	110	0.00	5.84	60

Table F. 15 : Experiment 20-25-3 conducted with 0.282 mol MEA at 0.00963 mol MEA/s and 25°C

Pseudo-first order rate constants				
	k_1 [s^{-1}]		**MSE CO_2 x 10^6**	
Best fit	0.26		1.30	
Upper bound (95%)	917		20.90	
Median	656		20.90	
Lower bound (5%)	0.26		1.30	
Second order rate constants				
	k_2 [L/mol.s]		**MSE CO_2 x 10^6**	**MSE MEA x 10^6**
Best fit	1509		1.88	69
Upper bound (95%)	5751		2.12	68
Median	3688		2.06	68
Lower bound (5%)	675		1.59	71
Third order rate constants				
	k_3 [$L^2/mol^2.s$]		**MSE CO_2 x 10^6**	**MSE MEA x 10^6**
Best fit	308037		1.60	71
Upper bound (95%)	400387		1.67	70
Median	7660		0.25	96
Lower bound (5%)	4470		0.24	105
Termolecular rate constants				
	k_{MEA} [$L^2/mol^2.s$]	k_{H_2O} [$L^2/mol^2.s$]	**MSE CO_2 x 10^6**	**MSE MEA x 10^6**
Best fit	1833	81.4	2.16	67
Upper bound (95%)	3885	1815	2.23	67
Median	967	48.7	2.11	68
Lower bound (5%)	94.3	6.66	1.62	70

Table F. 16 : Experiment 20-30-1 conducted with 0.272 mol MEA at 0.00957 mol MEA/s and 30°C

Pseudo-first order rate constants				
	k_1 [s^{-1}]		**MSE CO_2 x 10^6**	
Best fit	421		21.13	
Upper bound (95%)	970		21.13	
Median	628		21.13	
Lower bound (5%)	95.7		21.13	
Second order rate constants				
	k_2 [L/mol.s]		**MSE CO_2 x 10^6**	**MSE MEA x 10^6**
Best fit	4450		4.75	128
Upper bound (95%)	5802		4.78	128
Median	3603		4.73	128
Lower bound (5%)	137		3.83	121
Third order rate constants				
	k_3 [$L^2/mol^2.s$]		**MSE CO_2 x 10^6**	**MSE MEA x 10^6**
Best fit	13690		3.62	119
Upper bound (95%)	14922		3.62	119
Median	8673		3.70	118
Lower bound (5%)	3234		4.60	118
Termolecular rate constants				
	k_{MEA} [$L^2/mol^2.s$]	k_{H_2O} [$L^2/mol^2.s$]	**MSE CO_2 x 10^6**	**MSE MEA x 10^6**
Best fit	529	1.11	3.80	121
Upper bound (95%)	4592	1.18	3.80	122
Median	447	0.92	3.82	120
Lower bound (5%)	213	0.00	15.84	131

Table F. 17 : Experiment 20-30-2 conducted with 0.266 mol MEA at 0.00871 mol MEA/s and 30°C

Pseudo-first order rate constants			
	k_1 [s^{-1}]	**MSE CO_2 x 10^6**	
Best fit	0.30	1.73	
Upper bound (95%)	926	19.32	
Median	566	19.32	
Lower bound (5%)	31.9	19.32	
Second order rate constants			
	k_2 [L/mol.s]	**MSE CO_2 x 10^6**	**MSE MEA x 10^6**
Best fit	4099	1.15	66
Upper bound (95%)	5297	1.18	66
Median	3303	1.13	66
Lower bound (5%)	369	0.64	67
Third order rate constants			
	k_3 [$L^2/mol^2.s$]	**MSE CO_2 x 10^6**	**MSE MEA x 10^6**
Best fit	1318607	1.00	66
Upper bound (95%)	760352	0.93	66
Median	5773	1.03	79
Lower bound (5%)	3737	1.62	83
Termolecular rate constants			
	k_{MEA} [$L^2/mol^2.s$]	k_{H_2O} [$L^2/mol^2.s$]	**MSE CO_2 x 10^6**	**MSE MEA x 10^6**
Best fit	343	2.85	0.59	68
Upper bound (95%)	1896	270	1.25	66
Median	1026	27.1	1.11	66
Lower bound (5%)	137	2.65	0.57	68

Table F. 18 : Experiment 20-30-3 conducted with 0.265 mol MEA at 0.00887 mol MEA/s and 30°C

Pseudo-first order rate constants			
	k_1 [s^{-1}]	**MSE CO_2 x 10^6**	
Best fit	644	28.62	
Upper bound (95%)	854	28.62	
Median	470	28.62	
Lower bound (5%)	57.5	28.62	
Second order rate constants			
	k_2 [L/mol.s]	**MSE CO_2 x 10^6**	**MSE MEA x 10^6**
Best fit	584	3.13	157
Upper bound (95%)	5655	3.76	149
Median	3350	3.68	150
Lower bound (5%)	627	3.17	156
Third order rate constants			
	k_3 [$L^2/mol^2.s$]	**MSE CO_2 x 10^6**	**MSE MEA x 10^6**
Best fit	272041	3.11	158
Upper bound (95%)	570616	3.32	155
Median	7622	1.33	200
Lower bound (5%)	1436	1.88	251
Termolecular rate constants			
	k_{MEA} [$L^2/mol^2.s$]	k_{H_2O} [$L^2/mol^2.s$]	**MSE CO_2 x 10^6**	**MSE MEA x 10^6**
Best fit	1834	68.9	3.77	149
Upper bound (95%)	1938	83.5	3.79	148
Median	1105	56.1	3.76	149
Lower bound (5%)	219	17.8	3.58	151

Appendix G Individual rate constants – long time-segments

Table G. 1 : Experiment 10-20-1 conducted with 0.144 mol MEA at 0.00513 mol MEA/s and 20°C

Pseudo-first order rate constants				
	k_1 [s^{-1}]		**MSE CO_2 x 10^6**	
Best fit	632		10.68	
Upper bound (95%)	968		10.68	
Median	796		10.68	
Lower bound (5%)	112		10.68	
Second order rate constants				
	k_2 [L/mol.s]		**MSE CO_2 x 10^6**	**MSE MEA x 10^6**
Best fit	5349		10.02	474
Upper bound (95%)	41789		10.00	475
Median	3178		10.04	474
Lower bound (5%)	1338		10.10	473
Third order rate constants				
	k_3 [$L^2/mol^2.s$]		**MSE CO_2 x 10^6**	**MSE MEA x 10^6**
Best fit	5440071		10.03	474
Upper bound (95%)	3477933		10.04	474
Median	265385		10.18	472
Lower bound (5%)	8482		11.44	462
Termolecular rate constants				
	k_{MEA} [$L^2/mol^2.s$]	k_{H_2O} [$L^2/mol^2.s$]	**MSE CO_2 x 10^6**	**MSE MEA x 10^6**
Best fit	649	1024	10.00	475
Upper bound (95%)	1952	2145	9.99	474
Median	867	89.4	10.01	474
Lower bound (5%)	22.5	3.02	10.37	470

Table G. 2 : Experiment 10-20-2 conducted with 0.131 mol MEA at 0.00531 mol MEA/s and 20°C

Pseudo-first order rate constants				
	k_1 [s^{-1}]		**MSE CO_2 x 10^6**	
Best fit	205		10.65	
Upper bound (95%)	997		10.65	
Median	590		10.65	
Lower bound (5%)	61.9		10.65	
Second order rate constants				
	k_2 [L/mol.s]		**MSE CO_2 x 10^6**	**MSE MEA x 10^6**
Best fit	66.9		1.05	145
Upper bound (95%)	5561		1.55	129
Median	2517		1.52	129
Lower bound (5%)	67.1		1.05	145
Third order rate constants				
	k_3 [$L^2/mol^2.s$]		**MSE CO_2 x 10^6**	**MSE MEA x 10^6**
Best fit	8525		1.03	145
Upper bound (95%)	9376		1.03	145
Median	6317		1.04	149
Lower bound (5%)	2321		1.34	161
Termolecular rate constants				
	k_{MEA} [$L^2/mol^2.s$]	k_{H_2O} [$L^2/mol^2.s$]	**MSE CO_2 x 10^6**	**MSE MEA x 10^6**
Best fit	743	0.48	1.04	146
Upper bound (95%)	1947	561	1.58	129
Median	718	55.9	1.55	129
Lower bound (5%)	116	0.54	1.06	147

Table G. 3 : Experiment 10-20-3 conducted with 0.135 mol MEA at 0.00480 mol MEA/s and 20°C

Pseudo-first order rate constants				
	k_1 [s^{-1}]		**MSE CO_2 x 10^6**	
Best fit	0.25		2.01	
Upper bound (95%)	975		8.04	
Median	350		8.04	
Lower bound (5%)	0.26		2.01	
Second order rate constants				
	k_2 [L/mol.s]		**MSE CO_2 x 10^6**	**MSE MEA x 10^6**
Best fit	4321		2.38	349
Upper bound (95%)	11097		2.36	349
Median	3895		2.38	349
Lower bound (5%)	1422		2.41	348
Third order rate constants				
	k_3 [$L^2/mol^2.s$]		**MSE CO_2 x 10^6**	**MSE MEA x 10^6**
Best fit	427579		2.52	345
Upper bound (95%)	1875812		2.43	348
Median	204751		2.59	344
Lower bound (5%)	9582		3.59	327
Termolecular rate constants				
	k_{MEA} [$L^2/mol^2.s$]	k_{H_2O} [$L^2/mol^2.s$]	**MSE CO_2 x 10^6**	**MSE MEA x 10^6**
Best fit	1309	89.9	2.36	349
Upper bound (95%)	1769	7774	2.36	350
Median	1067	88.3	2.36	349
Lower bound (5%)	116	53.1	2.37	349

Table G. 4 : Experiment 10-25-1 conducted with 0.137 mol MEA at 0.00420 mol MEA/s and 25°C

Pseudo-first order rate constants			
	k_1 [s^{-1}]	**MSE CO_2 x 10^6**	
Best fit	0.23	1.26	
Upper bound (95%)	881	4.71	
Median	454	4.71	
Lower bound (5%)	20.5	4.71	
Second order rate constants			
	k_2 [L/mol.s]	**MSE CO_2 x 10^6**	**MSE MEA x 10^6**
Best fit	3015	1.34	227
Upper bound (95%)	8744	1.34	228
Median	4120	1.34	227
Lower bound (5%)	1185	1.34	225
Third order rate constants			
	k_3 [$L^2/mol^2.s$]	**MSE CO_2 x 10^6**	**MSE MEA x 10^6**
Best fit	156700	1.39	224
Upper bound (95%)	660709	1.36	225
Median	114377	1.41	223
Lower bound (5%)	3027	2.42	205
Termolecular rate constants			
	k_{MEA} [$L^2/mol^2.s$]	k_{H_2O} [$L^2/mol^2.s$]	**MSE CO_2 x 10^6**	**MSE MEA x 10^6**
Best fit	1675	19.7	1.34	227
Upper bound (95%)	1958	147	1.34	228
Median	1259	48.3	1.34	227
Lower bound (5%)	167	14.3	1.34	227

Table G. 5 : Experiment 10-25-2 conducted with 0.147 mol MEA at 0.00508 mol MEA/s and 25°C

Pseudo-first order rate constants				
	k_1 [s^{-1}]		**MSE CO_2 x 10^6**	
Best fit	0.22		1.02	
Upper bound (95%)	889		3.51	
Median	434		3.51	
Lower bound (5%)	19.9		3.51	
Second order rate constants				
	k_2 [L/mol.s]		**MSE CO_2 x 10^6**	**MSE MEA x 10^6**
Best fit	4791		1.26	171
Upper bound (95%)	5100		1.26	171
Median	2859		1.25	171
Lower bound (5%)	205		1.22	161
Third order rate constants				
	k_3 [$L^2/mol^2.s$]		**MSE CO_2 x 10^6**	**MSE MEA x 10^6**
Best fit	144438		1.24	165
Upper bound (95%)	461967		1.24	168
Median	77058		1.24	163
Lower bound (5%)	4202		1.56	141
Termolecular rate constants				
	k_{MEA} [$L^2/mol^2.s$]	k_{H_2O} [$L^2/mol^2.s$]	**MSE CO_2 x 10^6**	**MSE MEA x 10^6**
Best fit	0.00	0.12	2.38	124
Upper bound (95%)	1972	72.9	1.26	172
Median	775	2.35	1.22	163
Lower bound (5%)	0.00	0.12	2.40	124

Table G. 6 : Experiment 10-25-3 conducted with 0.140 mol MEA at 0.00448 mol MEA/s and 25°C

Pseudo-first order rate constants				
	k_1 [s^{-1}]		**MSE CO_2 x 10^6**	
Best fit	0.16		1.49	
Upper bound (95%)	972		8.69	
Median	461		8.69	
Lower bound (5%)	0.16		1.49	
Second order rate constants				
	k_2 [L/mol.s]		**MSE CO_2 x 10^6**	**MSE MEA x 10^6**
Best fit	79.8		1.06	116
Upper bound (95%)	5452		1.35	107
Median	2703		1.34	107
Lower bound (5%)	70.9		1.06	117
Third order rate constants				
	k_3 [$L^2/mol^2.s$]		**MSE CO_2 x 10^6**	**MSE MEA x 10^6**
Best fit	12724		1.06	114
Upper bound (95%)	13700		1.06	114
Median	11651		1.06	114
Lower bound (5%)	4313		1.16	121
Termolecular rate constants				
	k_{MEA} [$L^2/mol^2.s$]	k_{H_2O} [$L^2/mol^2.s$]	**MSE CO_2 x 10^6**	**MSE MEA x 10^6**
Best fit	1249	0.53	1.06	116
Upper bound (95%)	1901	87.7	1.36	107
Median	1126	0.56	1.06	116
Lower bound (5%)	107	0.41	1.12	121

Table G. 7 : Experiment 10-30-1 conducted with 0.140 mol MEA at 0.00470 mol MEA/s and 30°C

Pseudo-first order rate constants				
	k_1 [s^{-1}]		**MSE CO_2 x 10^6**	
Best fit	920		7.21	
Upper bound (95%)	923		7.21	
Median	516		7.21	
Lower bound (5%)	62.4		7.21	
Second order rate constants				
	k_2 [L/mol.s]		**MSE CO_2 x 10^6**	**MSE MEA x 10^6**
Best fit	3507		3.75	188
Upper bound (95%)	34358		3.73	187
Median	3516		3.75	188
Lower bound (5%)	1150		3.80	188
Third order rate constants				
	k_3 [$L^2/mol^2.s$]		**MSE CO_2 x 10^6**	**MSE MEA x 10^6**
Best fit	6998317		3.76	187
Upper bound (95%)	4058892		3.77	188
Median	116089		4.04	192
Lower bound (5%)	443		11.09	232
Termolecular rate constants				
	k_{MEA} [$L^2/mol^2.s$]	k_{H_2O} [$L^2/mol^2.s$]	**MSE CO_2 x 10^6**	**MSE MEA x 10^6**
Best fit	378	174	3.73	187
Upper bound (95%)	1691	38169	3.72	187
Median	467	96.7	3.73	187
Lower bound (5%)	14.1	47.6	3.74	187

Table G. 8 : Experiment 10-30-2 conducted with 0.147 mol MEA at 0.00541 mol MEA/s and 30°C

Pseudo-first order rate constants				
	k_1 [s^{-1}]		**MSE CO_2 x 10^6**	
Best fit	0.10		2.20	
Upper bound (95%)	920		11.22	
Median	379		11.22	
Lower bound (5%)	0.10		2.20	
Second order rate constants				
	k_2 [L/mol.s]		**MSE CO_2 x 10^6**	**MSE MEA x 10^6**
Best fit	5.2		2.10	211
Upper bound (95%)	5263		5.17	221
Median	2194		5.11	221
Lower bound (5%)	6.60		1.80	210
Third order rate constants				
	k_3 [$L^2/mol^2.s$]		**MSE CO_2 x 10^6**	**MSE MEA x 10^6**
Best fit	117		2.54	217
Upper bound (95%)	8871		3.77	214
Median	1572		2.73	210
Lower bound (5%)	195		2.14	213
Termolecular rate constants				
	k_{MEA} [$L^2/mol^2.s$]	k_{H_2O} [$L^2/mol^2.s$]	**MSE CO_2 x 10^6**	**MSE MEA x 10^6**
Best fit	0.00	0.08	1.73	210
Upper bound (95%)	1677	84.5	5.19	221
Median	522	56.8	5.18	221
Lower bound (5%)	0.00	0.00	69.91	192

Table G. 9 : Experiment 10-30-3 conducted with 0.130 mol MEA at 0.00443 mol MEA/s and 30°C

Pseudo-first order rate constants				
	k_1 [s^{-1}]		**MSE CO_2 x 10^6**	
Best fit	0.21		3.15	
Upper bound (95%)	920		10.68	
Median	437		10.68	
Lower bound (5%)	71.2		10.68	
Second order rate constants				
	k_2 [L/mol.s]		**MSE CO_2 x 10^6**	**MSE MEA x 10^6**
Best fit	953		2.54	117
Upper bound (95%)	8166		2.46	117
Median	3391		2.48	117
Lower bound (5%)	932		2.55	117
Third order rate constants				
	k_3 [$L^2/mol^2.s$]		**MSE CO_2 x 10^6**	**MSE MEA x 10^6**
Best fit	1199641		2.52	118
Upper bound (95%)	931895		2.53	118
Median	146377		2.67	118
Lower bound (5%)	2923		4.75	129
Termolecular rate constants				
	k_{MEA} [$L^2/mol^2.s$]	k_{H_2O} [$L^2/mol^2.s$]	**MSE CO_2 x 10^6**	**MSE MEA x 10^6**
Best fit	1025	101	2.46	117
Upper bound (95%)	1799	761	2.45	118
Median	636	76.6	2.46	117
Lower bound (5%)	59.8	43.1	2.47	117

Table G. 10 : Experiment 20-20-1 conducted with 0.271 mol MEA at 0.00944 mol MEA/s and 20°C

Pseudo-first order rate constants				
	k_1 [s^{-1}]		**MSE CO_2 x 10^6**	
Best fit	965		7.67	
Upper bound (95%)	949		7.67	
Median	698		7.67	
Lower bound (5%)	83.5		7.67	
Second order rate constants				
	k_2 [L/mol.s]		**MSE CO_2 x 10^6**	**MSE MEA x 10^6**
Best fit	73.8		2.10	95
Upper bound (95%)	5787		2.59	90
Median	3163		2.57	90
Lower bound (5%)	76.1		2.10	94
Third order rate constants				
	k_3 [$L^2/mol^2.s$]		**MSE CO_2 x 10^6**	**MSE MEA x 10^6**
Best fit	6523		2.05	94
Upper bound (95%)	8548		2.06	94
Median	7081		2.05	94
Lower bound (5%)	4157		2.09	96
Termolecular rate constants				
	k_{MEA} [$L^2/mol^2.s$]	k_{H_2O} [$L^2/mol^2.s$]	**MSE CO_2 x 10^6**	**MSE MEA x 10^6**
Best fit	1384	0.36	2.08	95
Upper bound (95%)	1658	84.6	2.60	90
Median	996	0.67	2.09	94
Lower bound (5%)	139	0.31	2.27	99

Table G. 11 : Experiment 20-20-2 conducted with 0.267 mol MEA at 0.00928 mol MEA/s and 20°C

Pseudo-first order rate constants				
	k_1 [s^{-1}]		**MSE CO_2 x 10^6**	
Best fit	0.57		4.11	
Upper bound (95%)	978		5.21	
Median	297		5.21	
Lower bound (5%)	0.57		4.11	
Second order rate constants				
	k_2 [L/mol.s]		**MSE CO_2 x 10^6**	**MSE MEA x 10^6**
Best fit	621		4.00	342
Upper bound (95%)	5587		4.02	340
Median	3385		4.01	340
Lower bound (5%)	606		4.00	342
Third order rate constants				
	k_3 [$L^2/mol^2.s$]		**MSE CO_2 x 10^6**	**MSE MEA x 10^6**
Best fit	138369		4.00	343
Upper bound (95%)	262588		4.00	343
Median	55958		4.02	344
Lower bound (5%)	8163		4.26	352
Termolecular rate constants				
	k_{MEA} [$L^2/mol^2.s$]	k_{H_2O} [$L^2/mol^2.s$]	**MSE CO_2 x 10^6**	**MSE MEA x 10^6**
Best fit	294	5.92	4.00	342
Upper bound (95%)	1886	86.9	4.02	340
Median	1049	39.3	4.02	340
Lower bound (5%)	39.5	1.56	4.08	347

Table G. 12 : Experiment 20-20-3 conducted with 0.264 mol MEA at 0.01006 mol MEA/s and 20°C

Pseudo-first order rate constants				
	k_1 [s^{-1}]		**MSE CO_2 x 10^6**	
Best fit	325		6.20	
Upper bound (95%)	910		6.20	
Median	317		6.20	
Lower bound (5%)	108		6.20	
Second order rate constants				
	k_2 [L/mol.s]		**MSE CO_2 x 10^6**	**MSE MEA x 10^6**
Best fit	46.7		1.74	297
Upper bound (95%)	5817		2.66	292
Median	3713		2.64	292
Lower bound (5%)	198		2.13	293
Third order rate constants				
	k_3 [$L^2/mol^2.s$]		**MSE CO_2 x 10^6**	**MSE MEA x 10^6**
Best fit	4515		1.74	296
Upper bound (95%)	9683		1.88	296
Median	5902		1.79	296
Lower bound (5%)	1630		1.76	299
Termolecular rate constants				
	k_{MEA} [$L^2/mol^2.s$]	k_{H_2O} [$L^2/mol^2.s$]	**MSE CO_2 x 10^6**	**MSE MEA x 10^6**
Best fit	736	0.19	1.71	298
Upper bound (95%)	1892	81.0	2.68	292
Median	1061	47.2	2.66	292
Lower bound (5%)	269	0.02	2.35	307

Table G. 13 : Experiment 20-25-1 conducted with 0.299 mol MEA at 0.01019 mol MEA/s and 25°C

Pseudo-first order rate constants				
	k_1 [s^{-1}]		**MSE CO_2 x 10^6**	
Best fit	947.7057		5.73	
Upper bound (95%)	954.1735		5.73	
Median	654.0171		5.73	
Lower bound (5%)	86.20765		5.73	
Second order rate constants				
	k_2 [L/mol.s]		**MSE CO_2 x 10^6**	**MSE MEA x 10^6**
Best fit	22.36456		0.55	182
Upper bound (95%)	5900.374		2.18	162
Median	3090.062		2.14	162
Lower bound (5%)	22.22086		0.55	182
Third order rate constants				
	k_3 [$L^2/mol^2.s$]		**MSE CO_2 x 10^6**	**MSE MEA x 10^6**
Best fit	974.7125		0.60	186
Upper bound (95%)	8857.007		1.15	170
Median	1027.52		0.60	185
Lower bound (5%)	942.8306		0.60	187
Termolecular rate constants				
	k_{MEA} [$L^2/mol^2.s$]	k_{H_2O} [$L^2/mol^2.s$]	**MSE CO_2 x 10^6**	**MSE MEA x 10^6**
Best fit	2.11	0.21	0.55	182
Upper bound (95%)	1959	85.5	2.20	162
Median	1238	33.1	2.15	162
Lower bound (5%)	0.00	0.00	83.89	609

Table G. 14 : Experiment 20-25-2 conducted with 0.275 mol MEA at 0.01017 mol MEA/s and 25°C

Pseudo-first order rate constants				
	k_1 [s^{-1}]		**MSE CO_2 x 10^6**	
Best fit	604		14.29	
Upper bound (95%)	981		14.29	
Median	462		14.29	
Lower bound (5%)	120		14.29	
Second order rate constants				
	k_2 [L/mol.s]		**MSE CO_2 x 10^6**	**MSE MEA x 10^6**
Best fit	22.0		1.62	139
Upper bound (95%)	5483		4.06	156
Median	1910		3.96	156
Lower bound (5%)	22.0		1.62	139
Third order rate constants				
	k_3 [$L^2/mol^2.s$]		**MSE CO_2 x 10^6**	**MSE MEA x 10^6**
Best fit	1086		1.64	138
Upper bound (95%)	9523		2.53	147
Median	4574		2.14	144
Lower bound (5%)	605		1.81	137
Termolecular rate constants				
	k_{MEA} [$L^2/mol^2.s$]	k_{H_2O} [$L^2/mol^2.s$]	**MSE CO_2 x 10^6**	**MSE MEA x 10^6**
Best fit	0.00	0.21	1.62	138
Upper bound (95%)	1599	73.2	4.09	156
Median	406	20.2	3.98	156
Lower bound (5%)	0.00	0.01	18.61	230

Table G. 15 : Experiment 20-25-3 conducted with 0.282 mol MEA at 0.00963 mol MEA/s and 25°C

Pseudo-first order rate constants				
	k_1 [s^{-1}]		**MSE CO_2 x 10^6**	
Best fit	0.26		2.99	
Upper bound (95%)	906		8.46	
Median	469		8.46	
Lower bound (5%)	0.27		2.99	
Second order rate constants				
	k_2 [L/mol.s]		**MSE CO_2 x 10^6**	**MSE MEA x 10^6**
Best fit	64.8		2.62	117
Upper bound (95%)	5563		3.17	108
Median	2817		3.15	109
Lower bound (5%)	51.1		2.64	119
Third order rate constants				
	k_3 [$L^2/mol^2.s$]		**MSE CO_2 x 10^6**	**MSE MEA x 10^6**
Best fit	4080		2.65	120
Upper bound (95%)	8989		2.66	116
Median	5472		2.64	118
Lower bound (5%)	2390		2.74	123
Termolecular rate constants				
	k_{MEA} [$L^2/mol^2.s$]	k_{H_2O} [$L^2/mol^2.s$]	**MSE CO_2 x 10^6**	**MSE MEA x 10^6**
Best fit	694	0.44	2.62	117
Upper bound (95%)	1785	128	3.19	108
Median	941	63.0	3.18	108
Lower bound (5%)	245	0.31	2.69	121

Table G. 16 : Experiment 20-30-1 conducted with 0.272 mol MEA at 0.00957 mol MEA/s and 30°C

Pseudo-first order rate constants				
	k_1 [s^{-1}]		**MSE CO_2 x 10^6**	
Best fit	0.38		2.82	
Upper bound (95%)	982		7.22	
Median	650		7.22	
Lower bound (5%)	46.1		7.22	
Second order rate constants				
	k_2 [L/mol.s]		**MSE CO_2 x 10^6**	**MSE MEA x 10^6**
Best fit	131		2.11	164
Upper bound (95%)	5705		2.40	165
Median	2273		2.36	165
Lower bound (5%)	75.5		2.19	163
Third order rate constants				
	k_3 [$L^2/mol^2.s$]		**MSE CO_2 x 10^6**	**MSE MEA x 10^6**
Best fit	9025		2.07	162
Upper bound (95%)	15247		2.05	163
Median	8479		2.08	163
Lower bound (5%)	2717		2.44	163
Termolecular rate constants				
	k_{MEA} [$L^2/mol^2.s$]	k_{H_2O} [$L^2/mol^2.s$]	**MSE CO_2 x 10^6**	**MSE MEA x 10^6**
Best fit	93.6	1.13	2.11	163
Upper bound (95%)	1965	85.9	2.41	166
Median	944	1.13	2.10	163
Lower bound (5%)	84.0	0.00	9.64	168

Table G. 17 : Experiment 20-30-2 conducted with 0.266 mol MEA at 0.00871 mol MEA/s and 30°C

Pseudo-first order rate constants				
	k_1 [s^{-1}]		**MSE CO_2 x 10^6**	
Best fit	529		8.85	
Upper bound (95%)	975		8.85	
Median	553		8.85	
Lower bound (5%)	146		8.85	
Second order rate constants				
	k_2 [L/mol.s]		**MSE CO_2 x 10^6**	**MSE MEA x 10^6**
Best fit	3844		5.00	71
Upper bound (95%)	5533		5.01	70
Median	3401		5.00	70
Lower bound (5%)	110		4.87	72
Third order rate constants				
	k_3 [$L^2/mol^2.s$]		**MSE CO_2 x 10^6**	**MSE MEA x 10^6**
Best fit	24065		4.85	72
Upper bound (95%)	26606		4.85	71
Median	14985		4.86	72
Lower bound (5%)	3766		5.10	74
Termolecular rate constants				
	k_{MEA} [$L^2/mol^2.s$]	k_{H_2O} [$L^2/mol^2.s$]	**MSE CO_2 x 10^6**	**MSE MEA x 10^6**
Best fit	1028	1.39	4.85	71
Upper bound (95%)	1838	86.0	5.01	71
Median	986	48.1	5.01	71
Lower bound (5%)	42.0	1.27	4.86	71

Table G. 18 : Experiment 20-30-3 conducted with 0.265 mol MEA at 0.00887 mol MEA/s and 30°C

Pseudo-first order rate constants				
	k_1 [s^{-1}]		**MSE CO_2 x 10^6**	
Best fit	0.23		2.10	
Upper bound (95%)	980		10.45	
Median	570		10.45	
Lower bound (5%)	35.8		10.45	
Second order rate constants				
	k_2 [L/mol.s]		**MSE CO_2 x 10^6**	**MSE MEA x 10^6**
Best fit	47.2		1.31	267
Upper bound (95%)	5877		2.13	246
Median	3323		2.10	246
Lower bound (5%)	48.7		1.31	266
Third order rate constants				
	k_3 [$L^2/mol^2.s$]		**MSE CO_2 x 10^6**	**MSE MEA x 10^6**
Best fit	3941		1.26	269
Upper bound (95%)	9510		1.35	262
Median	5265		1.28	267
Lower bound (5%)	3923		1.26	269
Termolecular rate constants				
	k_{MEA} [$L^2/mol^2.s$]	k_{H_2O} [$L^2/mol^2.s$]	**MSE CO_2 x 10^6**	**MSE MEA x 10^6**
Best fit	1626	0.07	1.27	269
Upper bound (95%)	1914	181	2.15	246
Median	1079	37.9	2.12	246
Lower bound (5%)	112	0.07	2.68	291